

# 1 Seeing through moving eyes - microsaccadic information sampling provides 2 *Drosophila* hyperacute vision

3  
4 Mikko Juusola<sup>1,2,\*‡</sup>, An Dau<sup>2‡</sup>, Zhuoyi Song<sup>2‡</sup>, Narendra Solanki<sup>2</sup>, Diana Rien<sup>1,2</sup>, David Jaciuch<sup>2</sup>,  
5 Sidhartha Dongre<sup>2</sup>, Florence Blanchard<sup>2</sup>, Gonzalo G. de Polavieja<sup>3</sup>, Roger C. Hardie<sup>4</sup> and Jouni  
6 Takalo<sup>2</sup>

7  
8 <sup>1</sup>National Key laboratory of Cognitive Neuroscience and Learning, Beijing, Beijing Normal  
9 University, Beijing 100875, China

10 <sup>2</sup>Department of Biomedical Science, University of Sheffield, Sheffield S10 T2N, UK

11 <sup>3</sup>Champalimaud Neuroscience Programme, Champalimaud Center for the Unknown, Lisbon,  
12 Portugal

13 <sup>4</sup>Department of Physiology Development and Neuroscience, Cambridge University, Cambridge CB2  
14 3EG, UK

15  
16 \*Correspondence to: [m.juusola@sheffield.ac.uk](mailto:m.juusola@sheffield.ac.uk)

17 ‡ Equal contribution

18  
19 **Small fly eyes should not see fine image details. Because flies exhibit saccadic visual behaviors**  
20 **and their compound eyes have relatively few ommatidia (sampling points), their photoreceptors**  
21 **would be expected to generate blurry and coarse retinal images of the world. Here we**  
22 **demonstrate that *Drosophila* see the world far better than predicted from the classic theories.**  
23 **By using electrophysiological, optical and behavioral assays, we found that R1-R6**  
24 **photoreceptors' encoding capacity *in time* is maximized to fast high-contrast bursts, which**  
25 **resemble their light input during saccadic behaviors. Whilst *over space*, R1-R6s resolve moving**  
26 **objects at saccadic speeds beyond the predicted motion-blur-limit. Our results show how**  
27 **refractory phototransduction and rapid photomechanical photoreceptor contractions jointly**  
28 **sharpen retinal images of moving objects *in space-time*, enabling hyperacute vision, and explain**  
29 **how such microsaccadic information sampling exceeds the compound eyes' optical limits. These**  
30 **discoveries elucidate how acuity depends upon photoreceptor function and eye movements.**

## 31 32 INTRODUCTION

33 The acuity of an eye is limited by its photoreceptor spacing, which provides the grain of the retinal  
34 image. To resolve two stationary objects, at least three photoreceptors are needed for detecting the  
35 intensity difference in between. To resolve two moving objects is harder, as vision becomes further  
36 limited by each photoreceptor's finite integration time and receptive field size (Srinivasan & Bernard,  
37 1975; Juusola & French, 1997; Land, 1997).

38 Nevertheless, animals - from insects to man - view the world by using saccades, fast  
39 movements, which direct their eyes to the surroundings, and fixation intervals between the saccades,  
40 during which gaze is held near stationary (Land, 1999). Because of photoreceptors' slow integration-  
41 time, saccades should blur image details and these are thought to be sampled when gaze is stabilized.  
42 Thus, information would be captured during fixations whilst during saccades animals would be  
43 effectively blind. This viewpoint, however, ignores fast photoreceptor adaptation, which causes  
44 perceptual fading during fixation (Ditchburn & Ginsborg, 1952; Riggs & Ratliff, 1952), reducing  
45 visual information. Therefore, to maximize information and acuity, it is plausible that evolution has  
46 optimized photoreceptor function in respect to visual behaviors and needs.

47 We have now devised a suite of new experimental and theoretical methods to study this  
48 question both in time and over space in *Drosophila* R1-R6 photoreceptors. The *Drosophila* compound  
49 eyes are composed of ~750 seemingly regular lens-capped modules called the ommatidia, which  
50 should provide the fly a panoramic visual field of low optical resolution (Barlow, 1952; Land, 1997).  
51 Each ommatidium contains eight photoreceptor cells (R1-R8), pointing to seven different directions.  
52 The ultraviolet and blue-green-sensitive outer photoreceptors, R1-R6, initiate the motion vision  
53 pathway, whilst the central R7 and R8, which lie on top of each other, detect different colors from one  
54 direction (Wardill *et al.*, 2012). Owing to the eye's neural superposition principle, R1, R2, R3, R4, R5

1 and R6, each from a separate neighboring ommatidium, also point to the same direction. By pooling  
2 their output for synaptic transmission, the photoreceptor spacing (spatial resolution) effectively  
3 matches the ommatidium spacing (average interommatidial angle,  $\Delta\phi = 4.5^\circ$  (Götz, 1964; Land, 1997;  
4 Gonzalez-Bellido *et al.*, 2011) but the signal-to-noise ratio of the transmitted image could improve by  
5  $\sqrt{6}$  (van Steveninck & Laughlin, 1996; Zheng *et al.*, 2006).

6 Here we show how evolution has improved *Drosophila* vision beyond these classic ideas,  
7 suggesting that light information sampling in R1-R6 photoreceptors is tuned to saccadic behavior.

8 Our intracellular recordings reveal that R1-R6s capture 2-to-4-times more information in time  
9 than previous maximum estimates (Juusola & Hardie, 2001a; Song *et al.*, 2012; Song & Juusola,  
10 2014) when responding to high-contrast bursts (periods of rapid light changes followed by quiescent  
11 periods) that resemble light input from natural scenes generated by saccadic viewing. Biophysically-  
12 realistic model simulations suggest that this improvement largely results from interspersed “fixation”  
13 intervals, which sensitize photoreceptors - by relieving their refractory microvilli (Song *et al.*, 2012;  
14 Song & Juusola, 2014; Juusola *et al.*, 2015) - to sample more information from phasic light changes.

15 Remarkably, over space, our intracellular recordings, high-speed microscopy and modeling  
16 further reveal how photomechanical photoreceptor contractions (Hardie & Franze, 2012) work  
17 together with refractory sampling to improve spatial acuity. We discover that by actively modulating  
18 light input and photoreceptor output, these processes reduce motion blur during saccades and  
19 adaptation during gaze fixation, which otherwise could fade vision (Ditchburn & Ginsborg, 1952;  
20 Riggs & Ratliff, 1952; Land, 1997). The resulting phasic responses sharpen retinal images by  
21 highlighting the times when visual objects cross a photoreceptor’s receptive field, thereby encoding  
22 space in time (see also: Ahissar & Arieli, 2001; Donner & Hemilä, 2007; Rucci *et al.*, 2007; Kuang *et*  
23 *al.*, 2012a; Kuang *et al.*, 2012b; Franceschini *et al.*, 2014; Viollet, 2014). Thus, neither saccades nor  
24 fixations blind the flies, but together improve vision.

25 Incorporation of this novel opto-mechano-electric mechanism into our ‘microsaccadic  
26 sampling’-model predicts that *Drosophila* can see >4-fold finer details than their eyes’ spatial  
27 sampling limit – a prediction directly confirmed by optomotor behavior experiments. By  
28 demonstrating how fly photoreceptors’ fast microsaccadic information sampling provides hyperacute  
29 vision of moving images, these results change our understanding of insect vision, whilst showing an  
30 important relationship between eye movements and visual acuity.

## 31 RESULTS

32 These results establish that *Drosophila* exploit image motion (through eye movements) to see spatial  
33 details, down to hyperacute resolution. A fly’s visual acuity is limited by how well its photoreceptors  
34 resolve different photon rate changes, and their receptive field sizes. However, because each  
35 photoreceptor’s signal-to-noise ratio and receptive field size adapt dynamically to light changes,  
36 acuity also depends upon the eye movements that cause them. To make these relationships clear, the  
37 results are presented in the following order:

38  
39 <sup>1st</sup> We show that photoreceptors capture most visual information from high-contrast bursts, and  
40 reveal how this is achieved by refractory photon sampling and connectivity (**Figures 1-5**).

41 <sup>2nd</sup> We show that saccades and gaze fixations in natural environment results in such high-contrast  
42 bursts, implying that eye movements work with refractory sampling to improve vision  
43 (**Figure 6**).

44 <sup>3rd</sup> We demonstrate that photoreceptors contract to light *in vivo* and explain how these  
45 microsaccades move and narrow their receptive fields (**Figures 7-8**) to sharpen light input and  
46 photoreceptor output in time.

47 <sup>4th</sup> Collectively, these dynamics predict that *Drosophila* see finer spatial details than their  
48 compound eyes’ optical resolution over a broad range of image velocities (**Figure 9**), and we  
49 verify this by optomotor behavior (**Figure 10**).

50 **Videos 1-4** and **Appendixes 1-10** explain in detail the new ideas, methods, experiments and theory  
51 behind these results.

## 52 Breaking the code by coupling experiments with theory

53 To work out how well a *Drosophila* R1-R6 photoreceptor can see the world, we compared  
54 intracellular recordings with realistic theoretical predictions from extensive quantal light information  
55

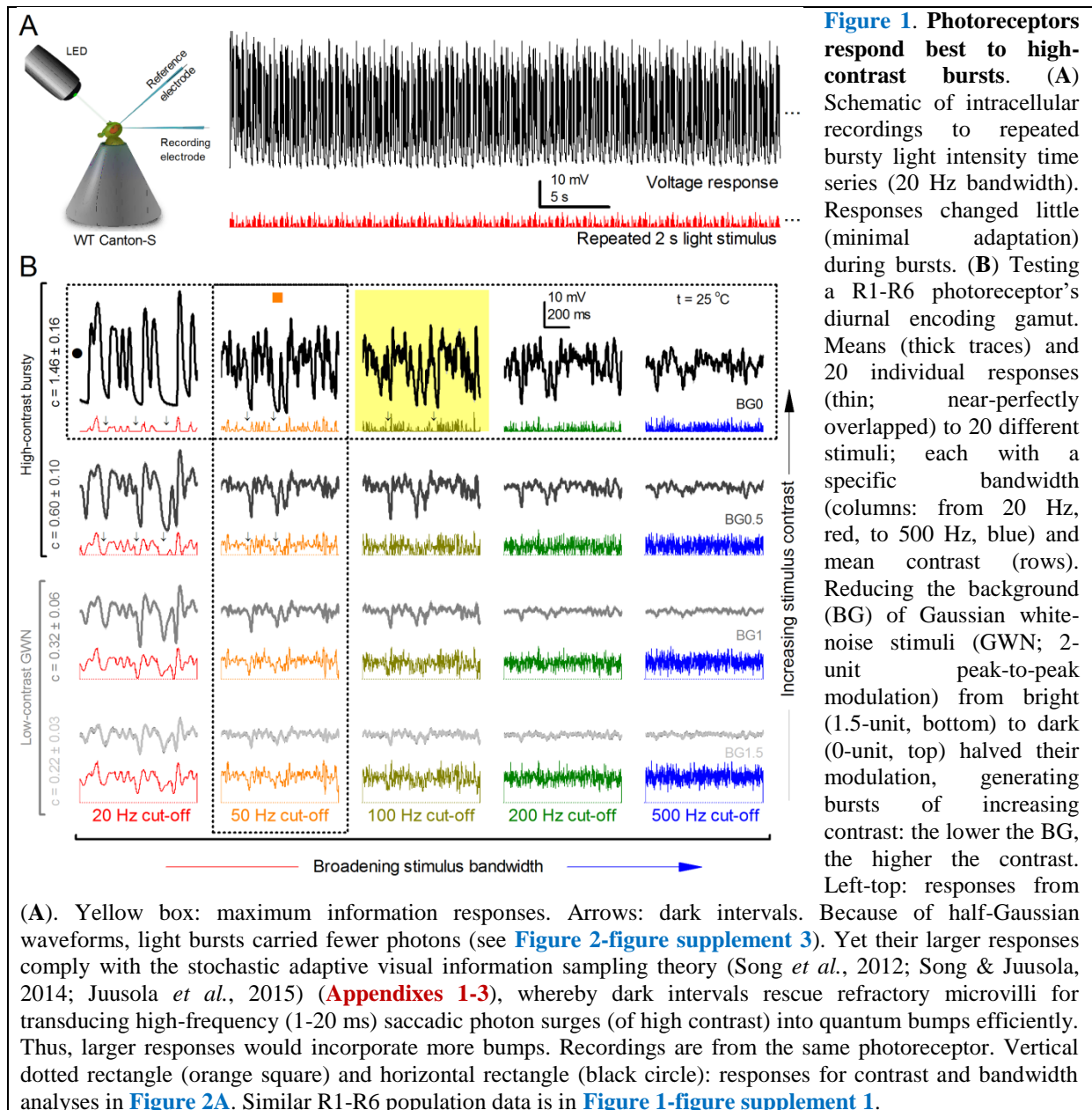
1 sampling simulations (**Appendixes 1-3**), having the following physical limits and properties (Song *et al.*, 2012; Song & Juusola, 2014; Juusola *et al.*, 2015; Song *et al.*, 2016):

- 3 • A photoreceptor counts photons and integrates these samples to an estimate, a macroscopic voltage response, of light changes within its receptive field.
- 4 • This estimate is counted by 30,000 microvilli, which form its light-sensor, the rhabdomere. Each microvillus is a photon sampling unit, capable of transducing a photon's energy to a unitary response (quantum bump or sample) (Henderson *et al.*, 2000; Juusola & Hardie, 2001a; Song *et al.*, 2012; Song & Juusola, 2014).
- 5 • Following each bump, the light-activated microvillus becomes *refractory* (Song *et al.*, 2012; Song & Juusola, 2014; Juusola *et al.*, 2015) for 50-300 ms. Therefore, with brightening light, a photoreceptor's sample rate gradually saturates, as fewer microvilli are available to generate bumps.
- 6 • Although refractory sampling makes photoreceptors imperfect photon counters, it benefits vision by representing a fast automatic adaptation mechanism, reducing sensitivity in proportion to background intensity (Song *et al.*, 2012; Song & Juusola, 2014), whilst accentuating responses to contrast changes (Song & Juusola, 2014).

17  
18 As previously described for a variety of other stimuli (Song *et al.*, 2012; Song & Juusola, 2014; Juusola *et al.*, 2015), we found a close correspondence between the recordings and simulations (waveforms, noise, adaptation dynamics and information transfer) for all the tested stimuli, establishing how refractory quantal sampling is tuned by light changes. Conversely, control models without refractoriness or based on the Volterra black-box method (Juusola & French, 1997) failed to predict R1-R6s' information sampling and adaptation dynamics. Nevertheless, these limitations and differences gave us vital clues into the hidden/combined mechanisms that underpin photoreceptor function (**Appendixes 2-9**). We now analyze and explain the key results step-by-step.

### 27 **High-contrast “saccadic” bursts maximize encoding**

28 A well-known trade-off of fast adaptation is that it causes perceptual fading during fixation (Ditchburn & Ginsborg, 1952; Riggs & Ratliff, 1952), and to see the world requires motion or self-motion: body, head and eye movements (Hengstenberg, 1971; Land, 1973; Franceschini & Chagneux, 1997; Schilstra & van Hateren, 1998; Blaj & van Hateren, 2004; Martinez-Conde *et al.*, 2013), which remove adaptation. However, it remains unclear whether or how the fly photoreceptors' information sampling dynamics is tuned to visual behaviors to see the world better. To start unravelling these questions, we first surveyed what kind of stimuli drove their information transfer maximally (**Figure 1**), ranging from high-contrast bursts, in which transient intensity fluctuations were briefer than *Drosophila*'s normal head/body-saccades (Fry *et al.*, 2003; Geurten *et al.*, 2014), to Gaussian white-noise (GWN). These stimuli tested systematically different contrast and bandwidth patterns over R1-R6s' diurnal encoding gamut.



1

2

3

4

5

6

7

8

9

10

11

12

13

14

15

16

17

Intracellular recordings (Figure 1A) revealed that photoreceptors responded most vigorously to high-contrast bursts, which contained fast transient events with darker intervals. Figure 1B shows the averages (signals; thick) and individual responses (thin) of a typical R1-R6, grouped by the stimulus bandwidth and mean contrast. For all the bandwidths (columns), the responses increased with contrast, while for all the contrasts (rows), the responses decreased with the increasing bandwidth (left). Therefore, the slowest high-contrast bursts (red; top-left) with the longest darker intervals, which theoretically (Song *et al.*, 2012; Song & Juusola, 2014; Juusola *et al.*, 2015) should relieve most refractory microvilli (Appendixes 1-3), evoked the largest peak-to-peak responses ( $43.4 \pm 5.6$  mV; mean  $\pm$  SD,  $n = 16$  cells; Figure 1-figure supplement 1). Whereas the fastest low-contrast GWN (blue; bottom-right), which would keep more microvilli refractory, evoked the smallest responses ( $3.7 \pm 1.1$  mV;  $n = 4$ ).

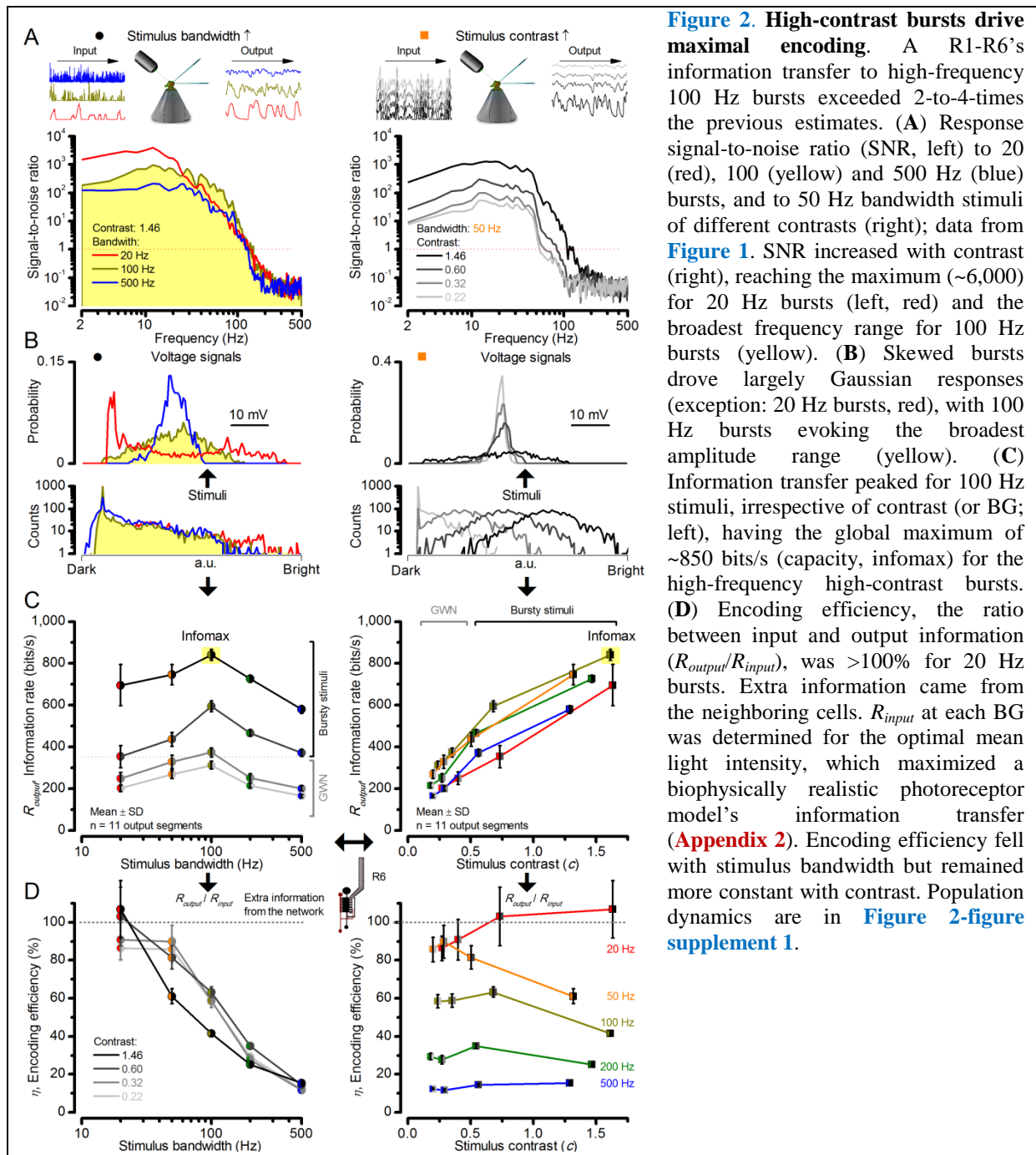
Notably, whilst all the stimuli were very bright, the largest responses (to bursts) were induced at the dimmest background (BG0, darkness) and the smallest responses (to GWN) at the brightest background (BG1.5) (Figure 1B). Thus, the mean emitted photon rate (and the signal-to-noise ratio) at the source was lower for the bursts and higher for the GWNs. However, in very bright stimulation, mean intensity is not critical for good vision. Photons galore are lost to intracellular pupil (Howard *et*

1 *al.*, 1987; Song & Juusola, 2014) and refractory microvilli (Song *et al.*, 2012), which reduce quantum  
2 efficiency. Although a R1-R6's receptive field could be bombarded by  $10^6$ – $10^9$  photons/s (in  
3 daylight), due to the dramatic drop in quantum efficiency, the photoreceptor could only count up  
4 ~80,000–800,000 quantum bumps/s (**Appendix 2**). More important for good vision are the stimulus  
5 contrast and bandwidth, which drive the dynamic quantum bump rate changes, summing up the  
6 photoreceptor output.

7 Information theoretical analysis (**Figure 2** and **Figure 2-figure supplement 1**) indicated that  
8 the response differences largely reflected differences in their quantum bump counts. The maximum  
9 signal power spectra to bursty stimuli could be up to ~6,000-times larger than that of the noise, which  
10 was effectively stimulus-invariant (**Figure 2-figure supplement 2A**). Because the noise power  
11 spectrum largely represents the average quantum bump's frequency composition (Wong *et al.*, 1982;  
12 Juusola & Hardie, 2001a; Song & Juusola, 2014), the bumps adapted to a similar size. Here, given the  
13 brightness of the stimuli, the bumps had light-adapted close to their minimum (Juusola & Hardie,  
14 2001a). Thereby, the larger responses simply comprised more bumps. Moreover, with Poisson light  
15 statistics, the response precision - how well it estimated photon flux changes - should increase with  
16 the square root of bump count until saturation; when more microvilli remained refractory (Song &  
17 Juusola, 2014). Accordingly, signaling performance (**Figures 2A, C**) increased both with the stimulus  
18 bandwidth (left) and contrast (right), until these became too fast to follow. Information transfer  
19 peaked at 100 Hz bursts, which allocated the R1-R6's limited bandwidth and amplitude range near-  
20 optimally, generating the broadest frequency (**Figure 2A** and **Figure 2-figure supplement 1A**) and  
21 (Gaussian) voltage distributions (**Figure 2B** and **Figure 2-figure supplement 1B**).

22 Thus, with the right mixture of bright “saccadic” bursts (to maximally activate microvilli) and  
23 darker “fixation” intervals (to recover from refractoriness) forming the high-contrast input, a  
24 photoreceptor's information transfer approached the capacity (Shannon, 1948), the theoretical  
25 maximum, where every symbol (voltage value) of a message (macroscopic voltage response) is  
26 transmitted equally often (**Figure 2C** and **Figure 2-figure supplement 1C**). Remarkably, this  
27 performance (610-850 bits/s) was 2-to-4-times of that for GWN (200-350 bits/s), which has often  
28 been used for characterizing maximal encoding (Juusola & Hardie, 2001a), and twice of that for rich  
29 naturalistic stimuli (380-510 bits/s) (Song & Juusola, 2014) (**Figure 2-figure supplement 3**). GWN,  
30 especially, lacks longer darker events, which should make microvilli refractory (Song & Juusola,  
31 2014) with fewer sampled photons limiting information transfer (**Appendixes 2-3**).

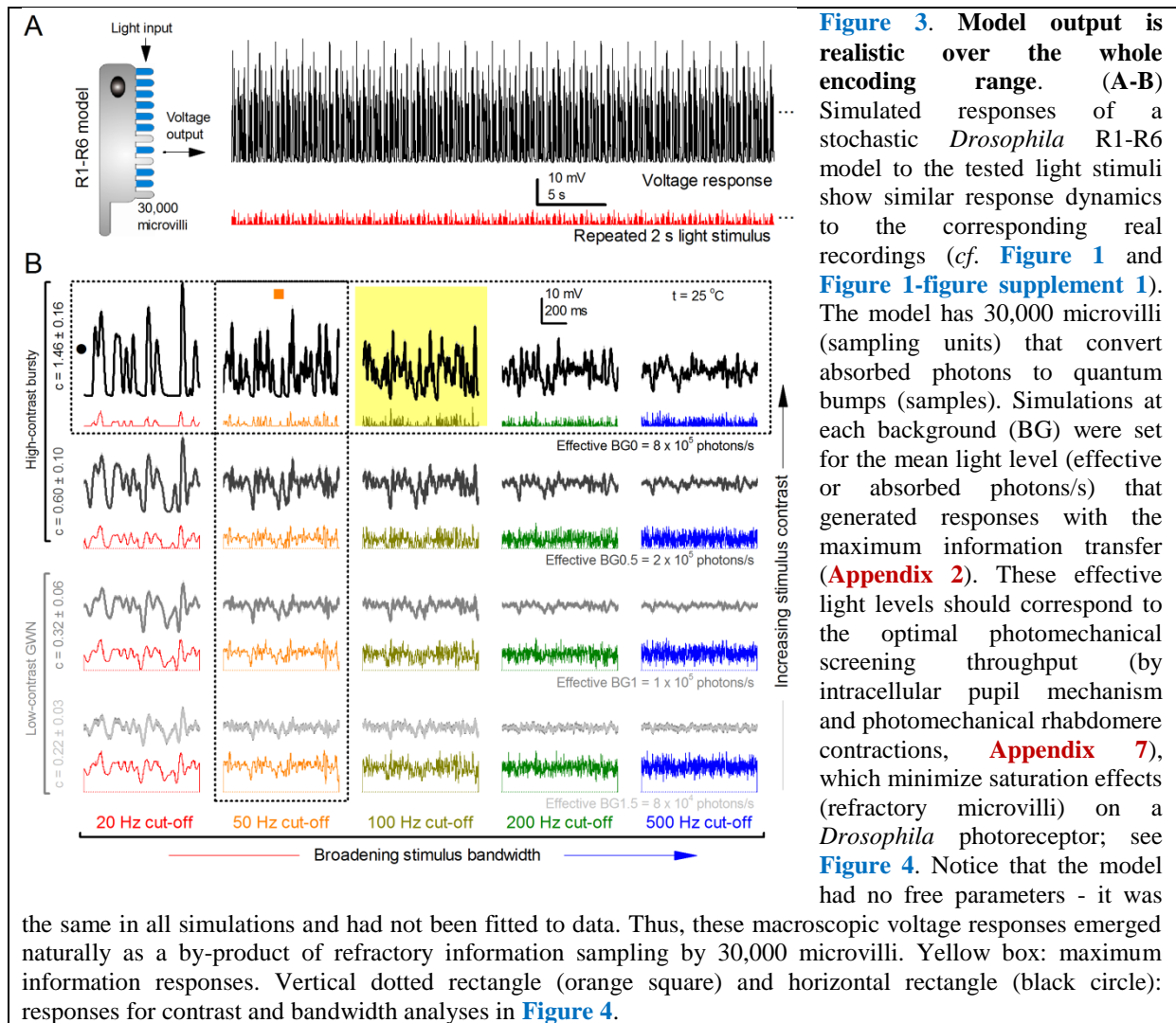
32 There are two reasons why these information rate estimates, which were calculated from  
33 equal-sized data chunks by the Shannon formula (**Eq. 1, Material and Methods**), should be robust  
34 and largely bias-free. First, apart from the responses to 20 Hz high-contrast bursts (**Figure 2B**, red  
35 trace), the responses to all the other stimuli had broadly Gaussian signal and noise distributions  
36 (**Figure 2-figure supplement 4**), obeying the Shannon formula's major assumptions (Shannon,  
37 1948). Second, our previous tests in comparing the Shannon formula to triple extrapolation method  
38 (Juusola & de Polavieja, 2003), which is directly derived from Shannon's information theory, have  
39 shown that for sufficiently large sets of data both these methods provide similar estimates even for  
40 this type of highly non-Gaussian responses (~5-20% maximal differences) (Song & Juusola, 2014;  
41 Dau *et al.*, 2016). Thus here, the Shannon formula should provide a sufficiently accurate information  
42 estimate also for the 20 Hz high-contrast burst responses, making this evaluation fair (see **Appendix**  
43 **2**).



1  
2  
3  
4  
5  
6  
7  
8  
9  
10  
11  
12  
13  
14

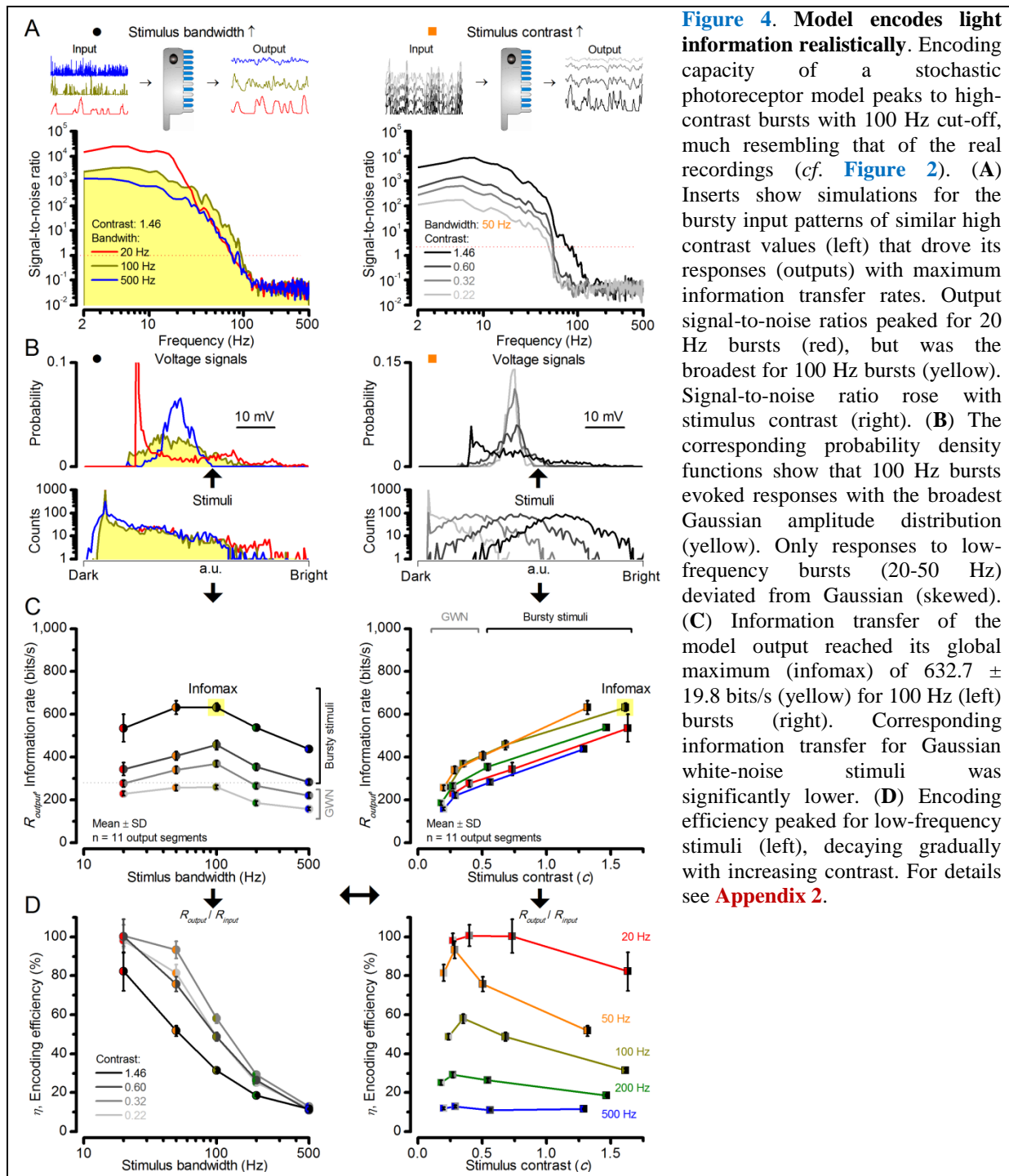
### Simulations reveal network contribution

These findings were largely replicated by stochastic simulations (**Figures 3-4**). A biophysically realistic photoreceptor model, which contains 30,000 microvilli (Song *et al.*, 2012), sampled light information much like a real R1-R6, generating authentic responses to all the test stimuli (**Figures 3A-B**). Yet, markedly, the model lacked the intracellular pupil (or any structural adaptation), which protects microvilli from saturation (Howard *et al.*, 1987; Song & Juusola, 2014), and network connections (Zheng *et al.*, 2006; Rivera-Alba *et al.*, 2011; Wardill *et al.*, 2012). In real photoreceptors, the pupil screens off excess light to maximize information transfer (Howard *et al.*, 1987; Song & Juusola, 2014). Similarly, in the simulations, the mean light intensity of each stimulus was optimized (**Appendix 2**) for maximum information (**Figures 4A-C**), establishing the photon absorption rate for a R1-R6 photoreceptor's best signaling performance (bits/s).



1  
2 At its peak, the model transferred  $633 \pm 20$  bits/s (mean  $\pm$  SD; **Figure 4C**) for 100 Hz bursts  
3 of  $8 \times 10^5$  photons/s, with further brightening reducing information as more microvilli became  
4 refractory. This performance matches that of many real R1-R6s (**Figure 2-figure supplement 1C**),  
5 but is  $\sim 200$  bits/s less than in some recordings (**Figure 2C**). The real R1-R6s, on balance, receive  
6 extra information from their neighbors (Rivera-Alba *et al.*, 2011; Wardill *et al.*, 2012), which through  
7 superposition (Zheng *et al.*, 2006) sample information from overlapping receptive fields. In other  
8 words, since our stimuli (from a white LED) were spatially homogenous, these synaptic feedbacks  
9 should be able to enhance the system's signal-to-noise by averaging the photoreceptors' independent  
10 photon count estimates from the same visual area, reducing noise (Zheng *et al.*, 2006; Juusola &  
11 Song, 2017).

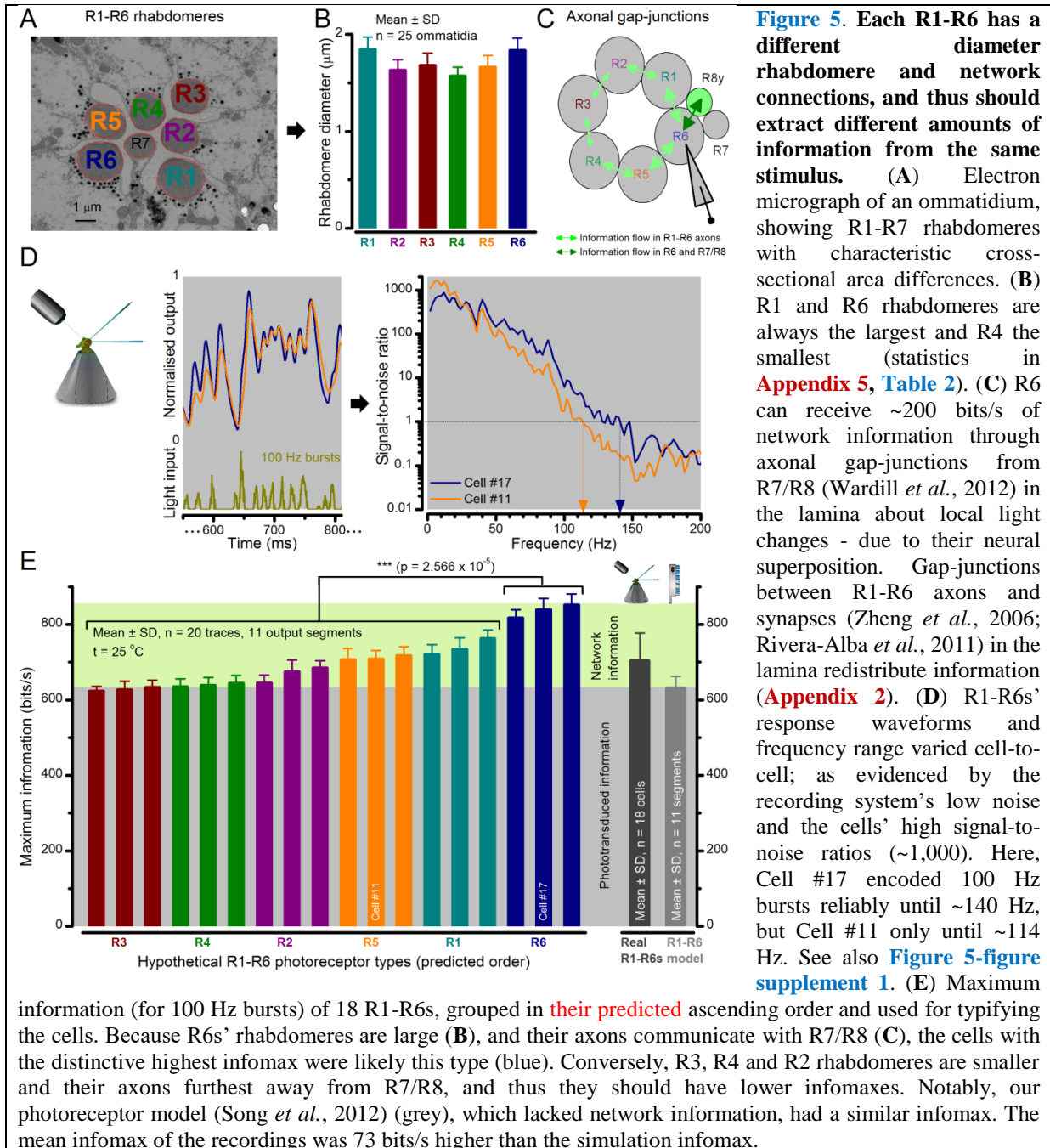
12 Moreover, as their rhabdomere sizes (**Figures 5A-B**) and connectivity vary systematically  
13 (Rivera-Alba *et al.*, 2011), each R1-R6 receives different amounts of information (**Figures 5C-D**)  
14 (see also: Wardill *et al.*, 2012). Here, R6s, with large rhabdomeres (**Figures 5B**) and gap-junctions to  
15 R8 (**Figure 5C**), should receive the most (Wardill *et al.*, 2012), suggesting that the best performing  
16 cells (e.g. **Figure 1** and **Figure 2**) might be of the R6-type (**Figure 5E**). And yet whilst R7s also share  
17 gap-junctions with R6s (Shaw *et al.*, 1989), our stimuli contained little UV component to drive them.  
18



1  
2  
3  
4  
5  
6  
7  
8  
9  
10  
11  
12

Encoding efficiency for the different stimuli (Figure 2D and Figure2-figure supplement 1D) was determined as the ratio between the related photoreceptor and light information rates ( $R_{output} / R_{input}$ ); with  $R_{input}$  estimated from the simulated Poisson stimulus repeats, which maximized information in R1-R6 model output (Figures 3B and 4C; Appendix 2). Thus, as  $R_{input}$  included the photon loss by the intracellular pupil and other structural adaptations (Howard *et al.*, 1987; Song & Juusola, 2014), it was less than at the light source. Moreover, *in vivo*, the combined stimulus information captured simultaneously by other photoreceptors in the retina network must be more than that by a single R1-R6 (Zheng *et al.*, 2006). *E.g.* as summation reduces noise, the signal-to-noise of a postsynaptic interneuron, LMC, which receives similar inputs from six R1-R6s, can be  $\sqrt{6}$ -times higher than that of a R1-R6 (van Steveninck & Laughlin, 1996; Zheng *et al.*, 2006), but lower than what is broadcasted from the source (Song & Juusola, 2014). Thus, information is lost during

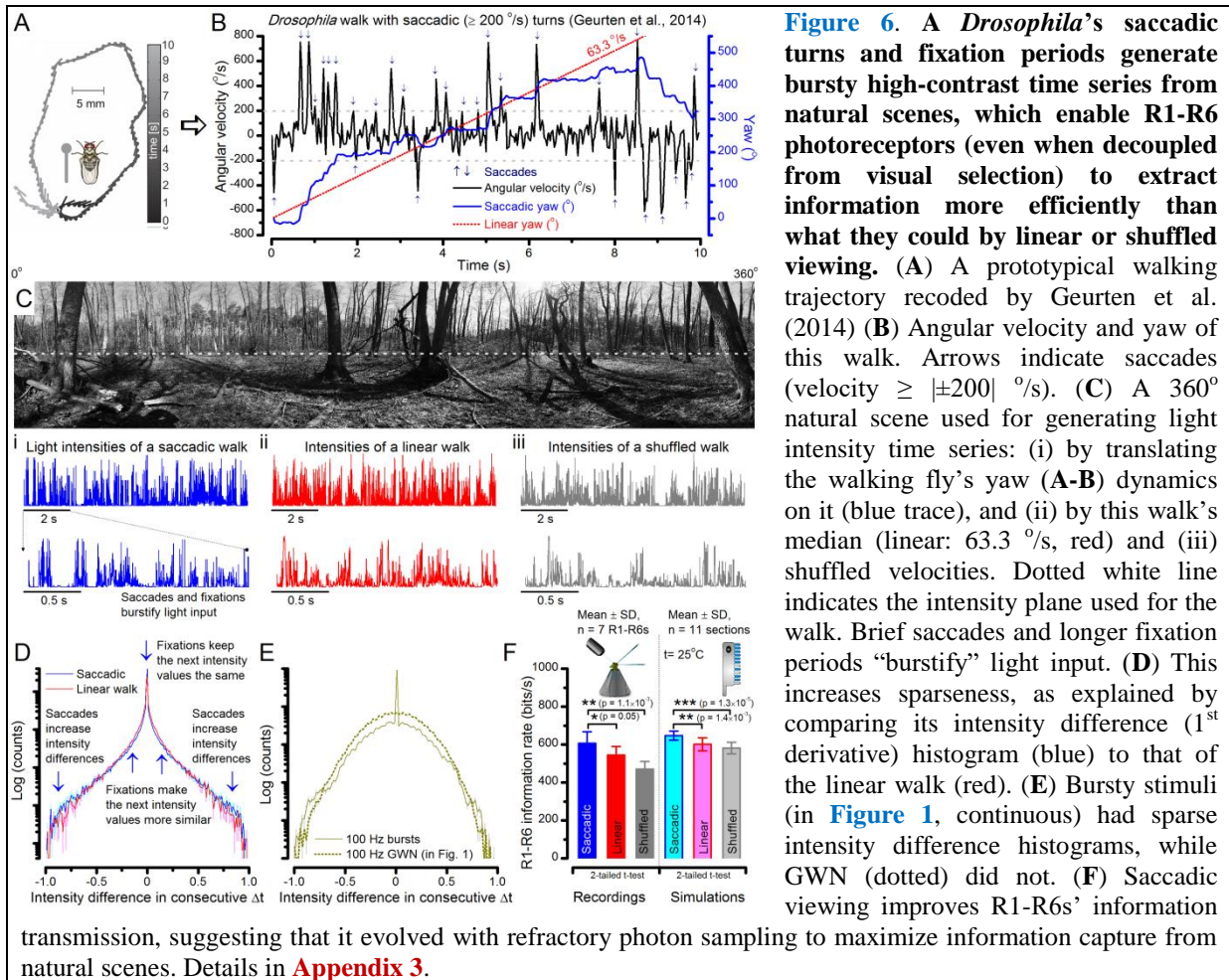
1 sampling and processing, with the analysis obeying data processing theorem (Shannon, 1948; Cover  
 2 & Thomas, 1991). Finally, as the LED light source's photon emission statistics were untested (if sub-  
 3 Poisson,  $R_{input}$  would be higher), the efficiency estimates represented the theoretical upper bounds.  
 4



5  
 6 We found that encoding efficiency for both the recordings (**Figure 2D** and **Figure 2-figure**  
 7 **supplement 1D**) and simulations (**Figure 4D**) weakened with the increasing bandwidth (left) but less  
 8 so with contrast (right). This was because  $R_{input}$  estimates (**Appendix 2**) increased monotonically with  
 9 bandwidth (Song & Jusuola, 2014) and contrast, while  $R_{output}$  for bandwidth did not (**Figure 2C**).  
 10 However, as predicted, some recordings showed >100% efficiency for 20 Hz bursts, presumably due  
 11 to their extra network information (**Figure 5** and **Figure 5-figure supplement 1**) (Zheng *et al.*, 2006;  
 12 Wardill *et al.*, 2012; Dau *et al.*, 2016).

13 A locomoting *Drosophila* generates ~1-5 head/body-saccades/s, which direct its gaze in high  
 14 velocities to the surroundings (Fry *et al.*, 2003; Geurten *et al.*, 2014). Here, our recordings and

1 simulations suggested that the refractoriness in R1-R6s' phototransduction, together with network  
 2 inputs, might be tuned for capturing information during such fast light changes in time.  
 3



4  
 5 **Saccades and fixations increase information capture from natural scenes**  
 6 To test this idea more directly, we used published body yaw velocities (Geurten *et al.*, 2014) of a  
 7 walking *Drosophila* (Figure 6A) to sample light intensity information from natural images (of  
 8 characteristic  $1/f^{\alpha}$ -statistics (van Hateren, 1997a)) (Figure 6B). This resulted in time series of  
 9 contrasts (Figure 6C, blue) that (i) mimicked light input to a R1-R6 photoreceptor during normal  
 10 visual behavior, containing fixations, translational movements and saccadic turns. As controls, we  
 11 further used light inputs resulting from corresponding (ii) linear median (red) and (iii) shuffled (gray)  
 12 velocity walks across the same images (Video 1). These stimuli were then played back to R1-R6s in  
 13 intracellular experiments and stochastic refractory model simulations.

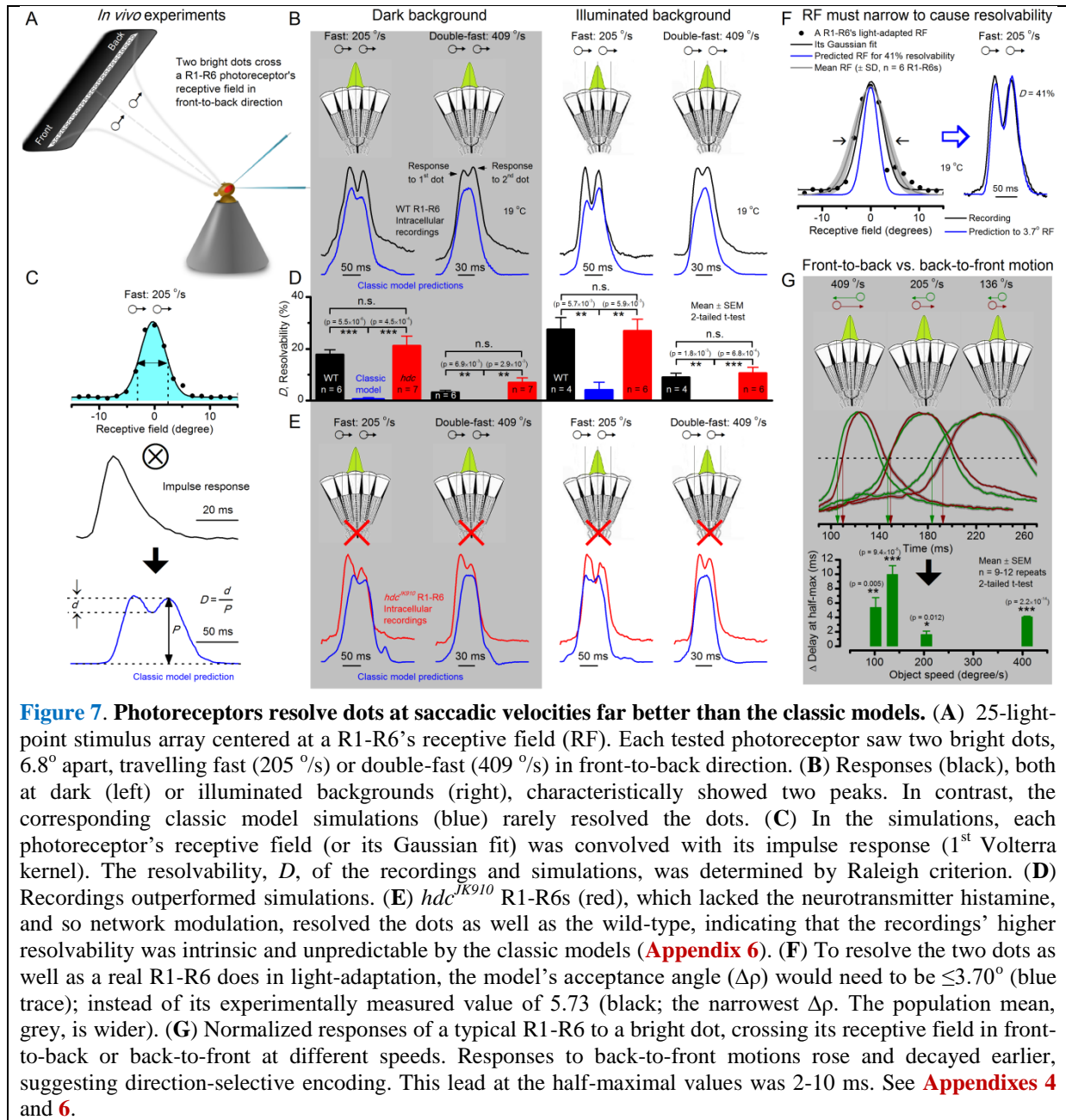
14 We found that saccadic viewing of natural images (Figure 6C, i), even without visual  
 15 selection (*i.e.* without the fly choosing what it gazes), transformed the resulting light input to resemble  
 16 the bursty high-contrast stimulation (Video1), which maximized photoreceptor information (Figures  
 17 1-2). Such inputs had increasingly sparse light intensity difference (1<sup>st</sup> derivative) distributions in  
 18 respect to those of the linear walks or GWN stimulation (Figures 6D-E; Appendix 3). Their  
 19 dynamics drove refractory sampling efficiently (Song & Juusola, 2014), enabling a R1-R6 to better  
 20 utilize its output range, and thus capture more information than through the median or shuffled  
 21 velocity viewing (Figure 6F; Figure 6-figure supplement 1; *cf.* Figure 2-figure supplement 3).

22 Altogether, these results (Figures 1-6) imply that saccades and fixations improve a R1-R6's  
 23 neural representation of the world in time. Furthermore, as behaviors modulate visual inputs in a  
 24 sensorimotor-loop, bursty spike trains from the brain (Franceschini *et al.*, 1991; Franceschini &  
 25 Chagneux, 1994; Tang & Juusola, 2010), which direct the gaze through self-motion, may have  
 26 evolved with photoreceptors' information sampling dynamics to better detect changes in the world. So

1 when a freely-moving fly directs its gaze to visual features that are relevant for its behavior, its R1-  
 2 R6's information capture may become optimized for the imminent task.

3  
 4 However, visual behaviors should also affect spatial acuity (Srinivasan & Bernard, 1975; Juusola &  
 5 French, 1997; Land, 1997; Geurten *et al.*, 2014). Hence, we next asked how R1-R6s see saccadic light  
 6 changes over space.

7



8

### 9 Testing acuity at saccadic velocities

10 A *Drosophila*'s head/body-saccades generate fast phasic photoreceptor movements, which ought to  
 11 blur retinal images (Srinivasan & Bernard, 1975; Juusola & French, 1997; Land, 1997). Moreover,  
 12 saccades – when dominated by axial rotation - provide little distance information (Land, 1999)  
 13 because objects, near and far, would move across the retina with the same speed. Therefore, it has  
 14 been long thought that visual information is mostly captured during translational motion and gaze  
 15 fixation, and less during saccades.

1 To test this hypothesis, we reasoned that object motion and self-motion shape a  
2 photoreceptor's light input the same way. Thus, the influence of eye movements (and motion blur) on  
3 a R1-R6's ability to resolve objects could be measured in experiments, where, instead of moving the  
4 eye, the objects were moved over its stationary receptive field (**Figure 7A**; **Appendixes 4-6**).

5 Using this approach, we recorded individual R1-R6s' voltage responses (**Figure 7B**; black  
6 traces) to a pair of bright dots (each  $1.7^\circ$  in size and  $6.8^\circ$  apart, as seen by the fly), moving at constant  
7 speed across their receptive field in front-to-back direction. The movements were either fast ( $205^\circ/\text{s}$ )  
8 or double-fast ( $409^\circ/\text{s}$ ), both within the head/body saccadic velocity range of a walking *Drosophila*  
9 (**Figures 6A-B**:  $200\text{-}800^\circ/\text{s}$ ) (Geurten *et al.*, 2014), and were presented against a dark or lit  
10 background (note: during a free flight (Fry *et al.*, 2003), saccadic velocities may reach  $2,000^\circ/\text{s}$ ).  
11 Importantly, the dots' angular separation was less than the half-width of a R1-R6's receptive field  
12 (**Figure 7C**) at the two backgrounds ( $\Delta\rho_{\text{dark}} = 9.47 \pm 1.57^\circ$ ,  $n = 19$  cells;  $\Delta\rho_{\text{light}} = 7.70 \pm 1.27^\circ$ ,  $n = 6$ ;  
13 mean  $\pm$  SD; **Figure 7-figure supplement 1** and **2**) and 1.5-times the average interommatidial angle  
14 ( $\Delta\phi \sim 4.5^\circ$ ), which should determine *Drosophila*'s visual acuity (Gonzalez-Bellido *et al.*, 2011). Thus,  
15 these fast-moving point objects tested the theoretical limit of what a R1-R6 should be able to resolve.

16 We further estimated each cell's respective impulse response (**Appendix 6**). Then following  
17 the classic theory of compound eyes' resolving power (Srinivasan & Bernard, 1975; Juusola &  
18 French, 1997; Land, 1997), we calculated each R1-R6's expected voltage output to the moving dots  
19 by convolving its impulse response with its measured dark- or light-adapted receptive field. These  
20 Volterra-model (Juusola & French, 1997) predictions (**Figures 7B-C**; blue) were then compared to  
21 the actual recordings (black).

### 22 **Eyesight beyond the motion blur-limit**

23 Remarkably in all these tests, the recordings showed distinctive responses to the two dots (**Figure**  
24 **7B**), as two peaks separated by a trough. The relative magnitude of this amplitude separation was  
25 quantified as resolvability, using the Raleigh criterion (Juusola & French, 1997) (**Figure 7C**).  
26 However, in marked contrast, the model predictions failed to resolve the double-fast dots, instead  
27 blurring into one broad response in both adapting states (**Figure 7D**; blue vs. black bars, respectively).  
28 The predictions for the fast dots were also poorer than the measured responses. Thus, a  
29 photoreceptor's real resolving power was significantly better and less affected by motion blur than  
30 predicted by classic theory (**Appendix 6**).

31 We next asked whether this better-than-expected resolving power resulted from synaptic  
32 interactions (Zheng *et al.*, 2006; Freifeld *et al.*, 2013) by using *hdc*<sup>JK910</sup> mutants (**Figure 7E**, red  
33 traces), in which photoreceptors lacked their neurotransmitter, histamine (Burg *et al.*, 1993)  
34 (**Appendixes 4-6**). Because *hdc*<sup>JK910</sup> R1-R6s cannot transmit information to their post-synaptic targets  
35 (Dau *et al.*, 2016) (LMCs, which initiate the motion detection pathways (Joesch *et al.*, 2010), and the  
36 amacrine cells), neither could these photoreceptors receive any light-driven interneuron feedback  
37 modulation (Dau *et al.*, 2016). Therefore, if the synaptic interactions improved the wild-type output to  
38 the moving dots, then *hdc*<sup>JK910</sup> R1-R6s, which lacked these interactions, should show diminished  
39 resolvability. But this was never observed. Instead, we found that *hdc*<sup>JK910</sup> R1-R6s resolved the dots at  
40 least equally well as the wild-type (**Figure 7D**, red). Thus, high acuity did not result from synaptic  
41 inputs but was intrinsic to photoreceptors.

42 We also calculated  $\Delta\rho$  needed to explain the spatial acuity of the recordings. The example  
43 (**Figure 7F**) is from a R1-R6, which had the narrowest light-adapted receptive field ( $\Delta\rho = 5.73^\circ$ )  
44 (**Figure 7-figure supplement 2**). Its response resolved the two fast-moving dots with a 40.5% dip.  
45 However, the Volterra model prediction, using its receptive field, only resolved the dots with a 12.5%  
46 dip (*cf.* **Figure 7D**). In fact, for 41.0% resolvability, its  $\Delta\rho$  would need to narrow to  $3.70^\circ$  (from  
47  $5.73^\circ$ ). Thus, for the prediction to match the recording, the receptive field would have to narrow at  
48 least by one-third. Because the required (predicted) acceptance angles of R1-R6s were always much  
49 narrower ( $\leq 4^\circ$ ) than the actual measurements ( $\Delta\rho_{\text{dark}} = 9.47$  and  $\Delta\rho_{\text{light}} = 7.70$ ; see above),  
50 measurement bias cannot explain this disparity.

51 We further discovered that R1-R6 recordings often showed phasic directional selectivity  
52 (**Figure 7G**), with the responses rising and decaying faster to back-to-front than to front-to-back  
53 moving dots. We asked whether these lag-time differences originated from asymmetric  
54 photomechanical photoreceptor contractions. Namely, atomic-force microscopy has revealed minute  
55

1 (<275 nm) vertical movements on the surface of dissected *Drosophila* eyes, generated by contraction  
 2 of individual microvilli as PIP<sub>2</sub> is hydrolyzed from the inner leaflet of the lipid bilayer (Hardie &  
 3 Franze, 2012). Here, instead, we reasoned that if the ommatidium lenses were effectively fixed and  
 4 R1-R8s levered to the retinal matrix, the contractions (Video 2) might be larger *in situ*, moving and  
 5 shaping the photoreceptors' receptive fields along some preferred direction. Such mechanical  
 6 feedback could then reduce light input to R1-R8s, making it more transient and directional.

7  
 8 **Microsaccadic sampling of retinal images**

9 To probe this idea, we recorded *in vivo* high-speed videos of photoreceptor rhabdomeres (viewed by  
 10 optical neutralization of the cornea) inside the eyes reacting to blue-green light flashes (470 + 560  
 11 nm) (Figure 8A). The recordings were performed under far-red (>720 nm) illumination, which is  
 12 nearly invisible to *Drosophila* (Appendix 7).  
 13

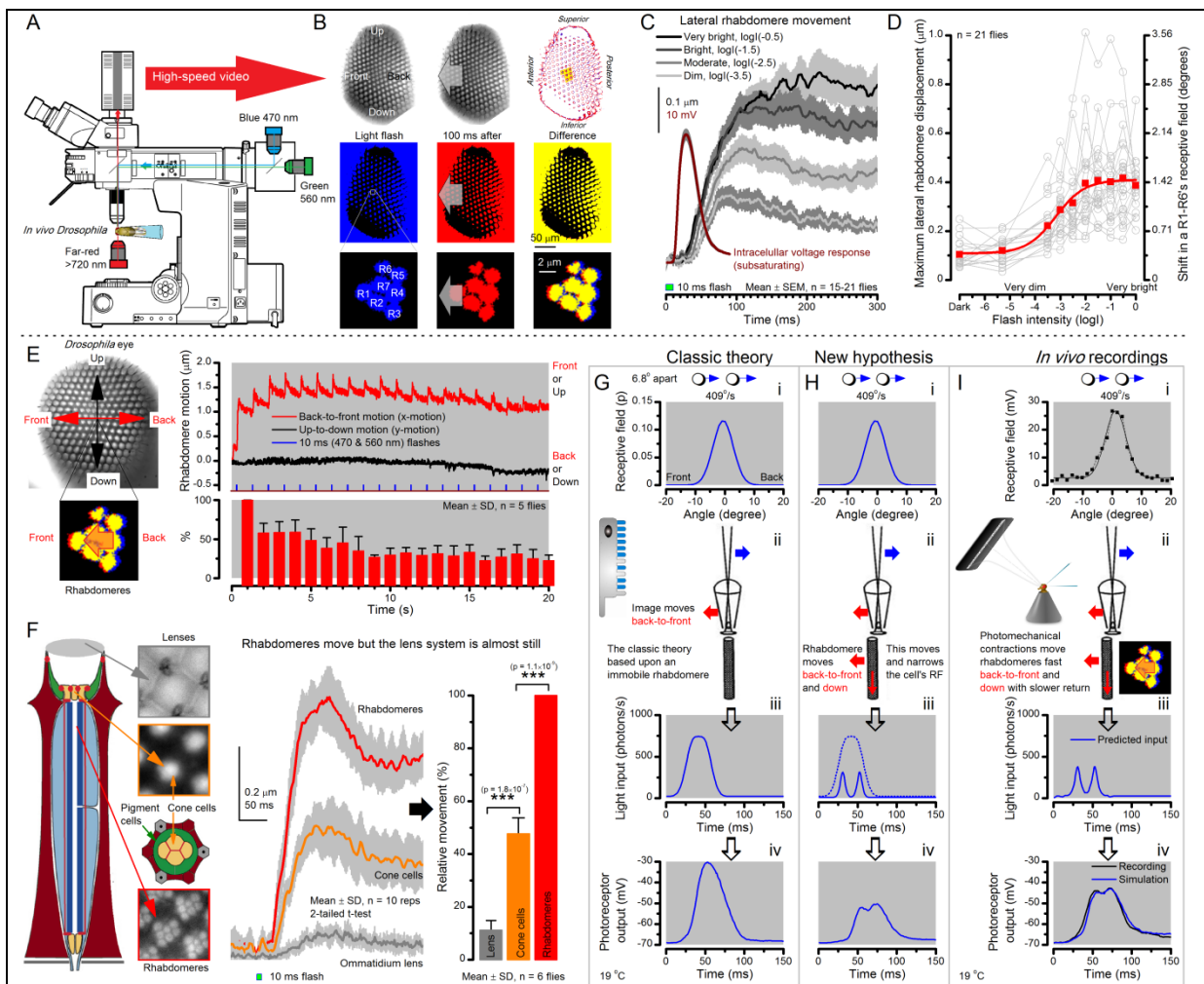


**Figure 8. Microsaccadic rhabdomere contractions and refractory photon sampling improve visual resolution of moving objects.** (A) High-speed videos showed fast lateral R1-R7 rhabdomere movements to blue/green flashes, recorded under far-red illumination that *Drosophila* barely saw (Wardill *et al.*, 2012). (B) Rhabdomeres moved inside those 7 ommatidia (up-right: their pseudopupil), which faced and absorbed the incident blue/green light, while the others reflected it. Rhabdomeres moved frontwards 8-20 ms after a flash onset, being maximally displaced 70-200 ms later, before returning. (C) Movements were larger and faster the brighter the flash, but slower than R1-R6s' voltage responses. (D) Movements followed R1-R6s' logarithmic light-sensitivity relationship. Concurrently, given the ommatidium optics (Stavenga, 2003b; Gonzalez-Bellido *et al.*, 2011), R1-R6s' receptive fields (RFs) shifted by 0.5-4.0°. (E) Rhabdomeres moved along the eye's horizontal (red) axis, with little vertical components (black), adapting to ~30% contractions in ~10 s during 1 s repetitive flashing. (F) Moving ommatidium structures. Cone and pigment cells, linking to the rhabdomeres by adherens-junctions (Tepass & Harris, 2007), formed an aperture smaller than the rhabdomeres' pseudopupil pattern. Rhabdomeres moved ~2-times more than this aperture, and ~10-times more than the lens. (G-H)

Simulated light inputs and photoreceptor outputs for the classic theory and new “microsaccadic sampling”-hypothesis when two dots cross a R1-R6’s RF (i) front-to-back at saccadic speeds. (G) In the classic model, because the rhabdomere (ii) and its broad RF (i) were immobile (ii), light input from the dots fused (iii), making them neurally unresolvable (iv). (H) In the new model, with rhabdomere photomechanics (ii) moving and narrowing its RF (here acceptance angle,  $\Delta\rho$ , narrows from  $8.1^\circ$  to  $4.0^\circ$ ), light input transformed into two intensity spikes (iii), which photoreceptor output resolved (iv). (I) New predictions matched recordings (**Figure 8-figure supplement 1**). Details in **Appendixes 7-8**.

1  
2 We found that 8-20 ms after a flash the rhabdomeres, which directly faced the light source at  
3 the image center, shifted rapidly towards the anterior side of their ommatidia (**Figures 8B**). These  
4 local movements were faster and larger the brighter the flash (**Figures 8C**), and reached their  
5 intensity-dependent maxima (0.2-1.2  $\mu\text{m}$ ; **Figure 8D**) in 70-200 ms, before returning more slowly to  
6 their original positions (**Appendix 7** analyses *hdc<sup>JK910</sup>*-rhabdomere responses). Because the mean R1-  
7 R6 rhabdomere tip diameter is  $\sim 1.7 \mu\text{m}$  (**Figure 5B**), a bright flash could shift it more than its half-  
8 width sideways. Consequently, the fast rhabdomere movements, whilst still  $\sim 3$ -times slower than their  
9 voltage responses (**Figure 8C**, wine), adapted photoreceptors photomechanically by shifting their  
10 receptive fields by  $0.5$ - $4.0^\circ$ , away from directly pointing to the light source.

11 Video footage at different eye locations indicated that light-activated rhabdomeres moved in  
12 back-to-front direction along the eye’s equatorial (anterior-posterior) plane (**Figure 8E**, red; **Video 3**),  
13 with little up-down components (black). Therefore, as each ommatidium lens inverts projected  
14 images, the photoreceptors’ receptive fields should follow front-to-back image motion. This global  
15 motion direction, which corresponds to a forward locomoting fly’s dominant horizontal optic flow  
16 field, most probably explains the phasic directional selectivity we found to opposing image motions  
17 (**Figure 7F**; **Appendix 8**). Thus, the responses to back-to-front moving dots were faster because the  
18 dots entered and exited each contracting photoreceptor’s front-to-back moving receptive field earlier;  
19 whereas the dots moving in the opposite direction stayed slightly longer inside each receptive field.

20 Video analyses further revealed that the first rhabdomere movement was the largest (**Figure**  
21 **8E**), but 1 s dark intervals, as used in **Figure 7**, could resensitize the photoreceptors for the next ( $\sim 0.5$   
22  $\mu\text{m}$ ) movements. Even  $< 100$  ms dark periods rescued noticeable motility (**Figure 2-figure**  
23 **supplement 2E**).

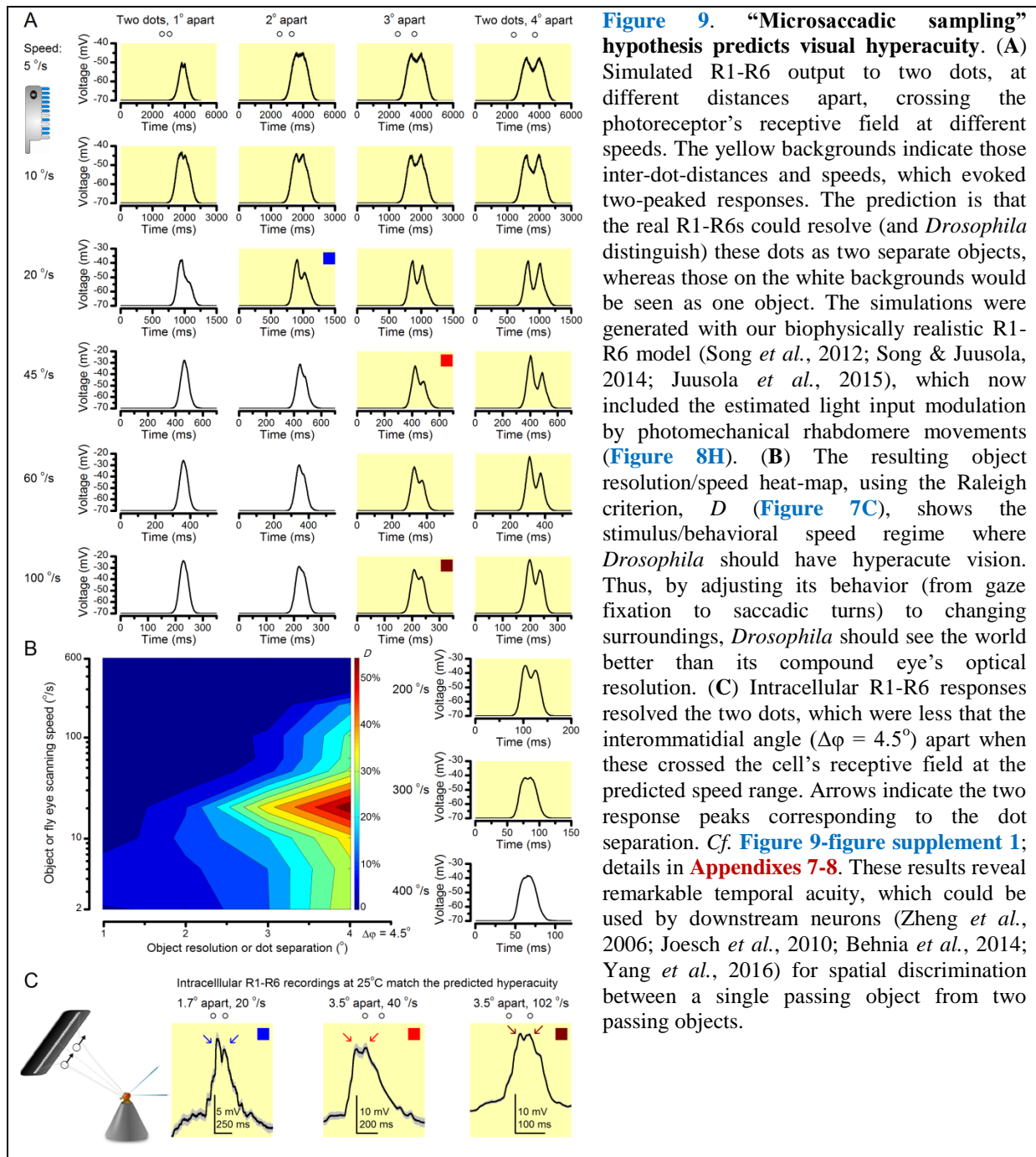
24 To inspect how rhabdomere contractions affected the cornea lens system’s image projection,  
25 we scanned ommatidia by z-axis piezo steps, with the imaged focal plane travelling down from the  
26 lens surface into rhabdomeres (**Figure 8F**; **Video 4**), delivering flashes at predetermined depths.  
27 Crucially, we found that the ommatidium lens stayed nearly still, while specific pigment and cone  
28 cells, which are connected to the rhabdomere tips by adherens junctions (Tepass & Harris, 2007),  
29 formed a narrow aperture that moved with the rhabdomeres but only half as much. Thus, as the lens  
30 system was immobile but the aperture and sensors (rhabdomeres) underneath swung differentially, the  
31 light input to the moving rhabdomeres was shaped dynamically. This implied that, during saccadic  
32 image motion, R1-R6s’ receptive fields might not only move but also narrow (**Appendixes 7-8**;  
33 **Video 2**).

34 Essentially, light input to a R1-R6 was modulated by the photoreceptor itself (**Figure 8F**). To  
35 estimate how these photomechanics influenced encoding, we implemented them in stochastic model  
36 simulations. We then compared how the predicted light inputs of the classic theory (**Figure 8G**) and  
37 the new ‘microsaccadic sampling’-hypothesis (**Figure 8H**) would drive R1-R6 output during the  
38 saccadic dot stimulation.

39 In the classic theory, the rhabdomere is immobile (ii). Therefore, light input of two moving  
40 dots was a convolution of two broad Gaussians (i) that fused together (iii), making them irresolvable  
41 to phototransduction (iv); this also flawed the Volterra-models (**Figure 7**).

42 In the new hypothesis, instead, as microvilli became light-activated (ii), the rhabdomere  
43 contracted away from the focal point, and then returned back more slowly, recovering from  
44 refractoriness. And because its receptive field moved and narrowed concurrently (its acceptance  
45 angle,  $\Delta\rho$ , halved to  $4.0^\circ$ ), the light input of two moving dots transformed into two intensity peaks  
46 (iii), in which time-separation was enhanced by the rhabdomere’s asymmetric motion. Crucially, with  
47 such input driving the refractory photon sampling model, its output (iv) closely predicted the  
48 responses to the two moving dots (**Figure 8I** and **Figure 8-figure supplement 1**). Interestingly, early

1 behavioral experiments in bright illumination (Götz, 1964) suggested similarly narrow R1-R6  
 2 acceptance angles ( $\sim 3.5^\circ$ ).  
 3



4  
 5 **From microsaccades to hyperacuity**

6 Because of the close correspondence between R1-R6 recordings and the new hypothesis (Appendixes  
 7 6-9), we used it further to predict whether *Drosophila* possessed hyperacute vision (Figure 9). We  
 8 asked whether ‘saccade-fixation-saccade’-like behaviors, when linked to refractory photon sampling  
 9 and photomechanical photoreceptor contractions, allowed encoding in time finer spatial details than  
 10 the compound eye’s optical limit ( $\Delta\phi \sim 4.5^\circ$ ). R1-R6 output was simulated to two bright dots 1-4°  
 11 apart, crossing its receptive field at different speeds at 25°C.

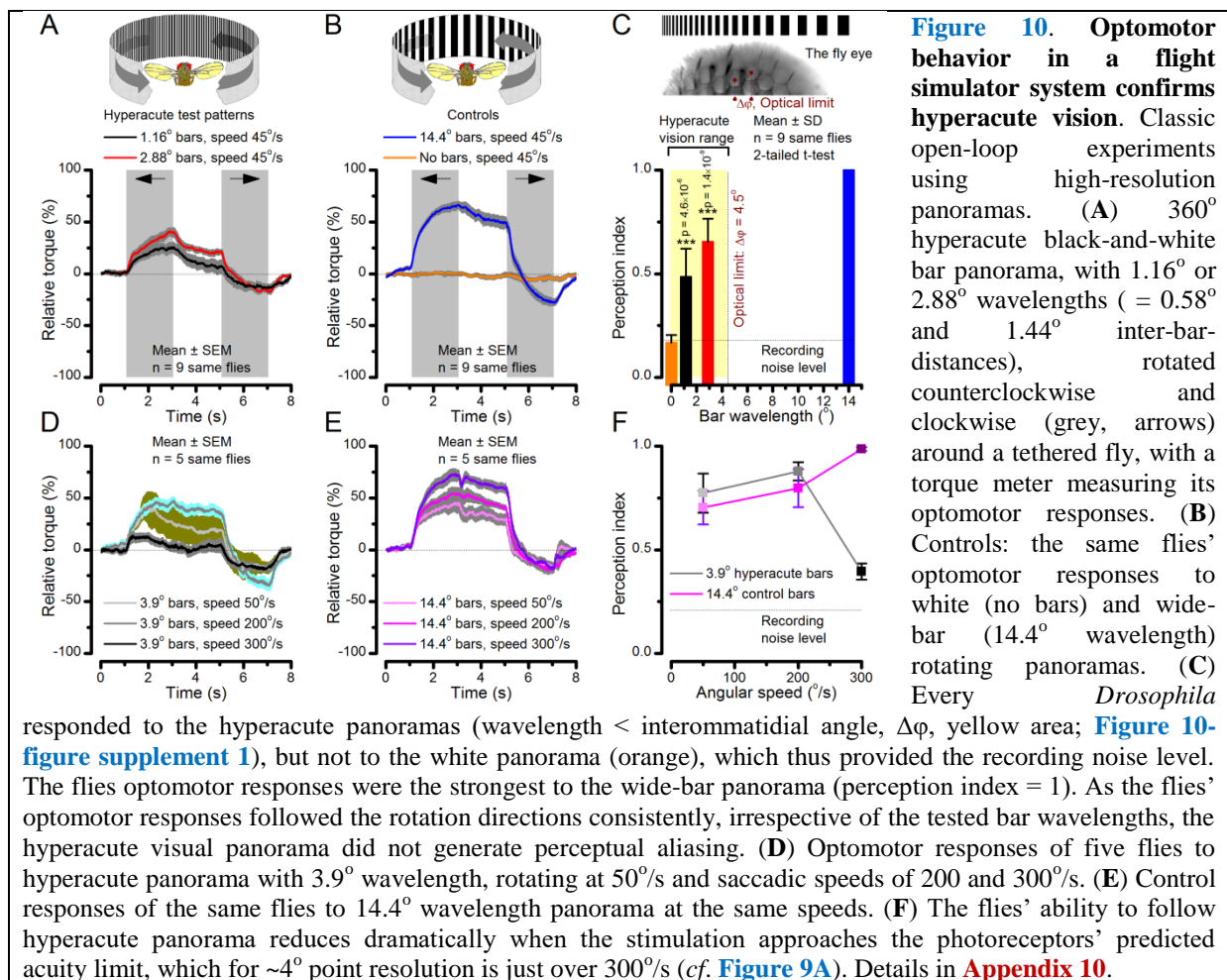
12 We found that if the dots, or a *Drosophila*, moved at suitable speed, a photoreceptor should  
 13 resolve them well (Figure 9A), with this performance depending upon the inter-dot-distance. When  
 14 the dots/eye moved at 10 %/s, a R1-R6 may capture image details at 1° resolution. But with slower

1 movement ( $\leq 2.5^\circ/s$ ), adaptation should fuse the dots together, making them neurally unresolvable.  
 2 Conversely,  $3^\circ$ -apart-dots should be seen at 5-100  $^\circ/s$  speeds and  $4^\circ$ -apart-dots even during fast  
 3 saccades (200-300  $^\circ/s$ ).

4 Thus, the ‘microsaccadic sampling’-hypothesis implied that *Drosophila* had hyperacute  
 5 vision over a broad speed range (Figure 9B), and through its own self-motion, could adjust the  
 6 resolution of its neural images. Further comparisons of model outputs with and without refractoriness  
 7 indicated that it extends the speed range of hyperacute vision (Appendix 8). Again, intracellular  
 8 recordings corroborated these predictions (Figure 9C and Figure 9-figure supplement 1),  
 9 demonstrating how acuity could be enhanced by encoding space in time.

10 These results meant that the unexpectedly fine temporal acuity of R1-R6s could be used by  
 11 downstream neurons (Zheng *et al.*, 2006; Joesch *et al.*, 2010; Rivera-Alba *et al.*, 2011; Wardill *et al.*,  
 12 2012; Behnia *et al.*, 2014), which can have even faster dynamics (Juusola *et al.*, 1995b; Uusitalo *et al.*,  
 13 1995; Zheng *et al.*, 2006), for spatial discrimination between a single passing object from two  
 14 passing objects, even if these objects were less than an interommatidial angle apart. The fly brain  
 15 could then integrate information from hyperacute moving objects and use it for directing behaviors.

16



17

## 18 Optomotor behavior confirms hyperacute vision

19 To test this prediction, we investigated the spatial resolution of *Drosophila* vision through their  
 20 optomotor behavior in a conventional flight simulator system, which used brightly-lit high-resolution  
 21 prints for panoramic scenes (Figure 10; Appendix 10). We asked whether tethered *Drosophila*  
 22 possessed motion vision hyperacuity by recording their yaw torque (optomotor response) to vertical  
 23 black-and-white bar panoramas with  $< 4.5^\circ$  wavelengths, which slowly rotated ( $45^\circ/s$ ) to clockwise  
 24 and counterclockwise.

25 We found that every tested fly responded down to  $\sim 1^\circ$  panoramic bar resolution (Figure 10A  
 26 and Figure 10-figure supplement 1) with their responses becoming smaller the finer its bars

1 (Figures 10A-C). Importantly, because these responses consistently followed the rotation direction  
2 changes, they were not caused by aliasing. Thus, optomotor behavior verified that *Drosophila* see the  
3 world at least in 4-fold finer detail than what was previously thought. Moreover, when a fine-grained  
4 (3.9°) panoramic image was rotated faster (Figure 10D), the response declined as predicted (*cf.* two  
5 dots 4° apart in Figure 9A). This result is consistent with photoreceptor output setting the perceptual  
6 limit for vision and demonstrates that *Drosophila* see hyperacute details even at saccadic speeds  
7 (Figures 10D-F).

## 8 9 DISCUSSION

10 We have provided deep new insight into spatiotemporal information processing in *Drosophila* R1-R6  
11 photoreceptors and animal perception in general. Our results indicate that the dynamic interplay  
12 between saccades and gaze fixation is important for both the maintenance and enhancement of vision  
13 already at the photoreceptor level. This interplay, which is commonly observed in locomoting  
14 *Drosophila* (Geurten *et al.*, 2014), makes light input to photoreceptors bursty.

15 We showed that high-contrast bursts, which resemble light input during a fly's saccadic  
16 behaviors, maximize photoreceptors' information capture in time, and provided evidence that such  
17 encoding involves four interlinked mechanisms. Light input is first regulated by two processes inside  
18 photoreceptors: slower screening pigment migration (intracellular pupil, 1-10 s) and much faster  
19 photomechanical rhabdomere contractions (0.01-1s). These modulations have low noise (Figure 2-  
20 figure supplement 2), enabling refractory photon sampling by microvilli to enhance information  
21 intake in phasic stimulus components. Finally, asymmetric synaptic inputs from the network  
22 differentiate individual R1-R6 outputs. Remarkably, over space, these mechanisms further sharpen  
23 neural resolvability by ~4-fold below the theoretical limit of the compound eye optics, providing  
24 hyperacute vision. Further analyses imply that these mechanisms with systematic rhabdomere size  
25 variations combat aliasing (Appendixes 2 and 5).

26 Thus, with microsaccadic sampling, a fly's behavioral decisions govern its visual  
27 information/acuity trade-off. To see the finest image details it should scan the world slowly, which  
28 probably happens during normal gaze fixation. But gaze fixation cannot be too slow; otherwise,  
29 adaptation would fade vision. Conversely, by locomoting faster, in a saccadic or bursty fashion, visual  
30 information capture in time is increased (see also: Juusola & de Polavieja, 2003), while surprisingly  
31 little spatial details about its surroundings would be lost.

32 This viewing strategy corresponds well with the recent human psychophysics results and  
33 modeling of ganglion cell firing (Rucci & Victor, 2015), which indicate that microsaccades and ocular  
34 drift in the foveal region of the retina actively enhance perception of spatial details (Rucci *et al.*, 2007;  
35 Poletti *et al.*, 2013; Rucci & Victor, 2015). Interestingly, here our findings further imply that, in  
36 *Drosophila*, the extraction of phasic stimulus features, which characterize object boundaries and line  
37 elements in visual scenes, already starts during sampling and integration of visual information in the  
38 microvilli, at the first processing stage (rather than later on in the retinal network or in the brain).

39 Our results make a general prediction about the optimal viewing strategy for maximizing  
40 information capture from the world. Animals should fixate gaze on darker features, as this resensitizes  
41 photoreceptors by relieving their refractory sampling units (*e.g.* microvilli). And then, rapidly move  
42 gaze across to brighter image areas, as saccadic crossings over high-contrast boundaries enhance  
43 information intake by increasing photoreceptors' sample (quantum bump) rate changes/time  
44 (Appendix 9).

45 Given the high occurrence of eye/head-saccades in animals with good vision (Land, 1999), it  
46 seems plausible that their photoreceptors could also have adapted encoding dynamics to quicken  
47 response modulation, reducing motion blur. Therefore, if information sampling biophysics in rods and  
48 cones were matched to microsaccadic eye movements, this could provide a mechanistic explanation to  
49 the old paradox: how saccadic gaze fixation provides stable perception of the world, while curtailing  
50 motion blur effects.

51

## 1 **Materials and Methods**

### 2 **Flies**

3 2-10 day old wild-type red-eyed (Canton-S and Berlin) fruit flies (*Drosophila melanogaster*) and  
4 *hdc<sup>JK910</sup>*-mutants were used in the experiments. Other transgenic and mutant *Drosophila* tests and  
5 controls are explained in specific **Appendixes**. *Drosophila* were raised at 18°C in a 12-hour/12-hour  
6 dark/light cycle and fed on standard medium in our laboratory culture.

### 8 **Electrophysiology**

9 Sharp microelectrode recordings from *Drosophila* R1-R6 photoreceptors were detailed before  
10 (Juusola & Hardie, 2001a; Juusola *et al.*, 2016), and we only list the key steps here. Flies were  
11 immobilized to a conical holder by beeswax (Juusola & Hardie, 2001a) (**Figure 1A**). A small hole,  
12 the size of a few ommatidia, was cut in the dorsal cornea for the recording electrode and sealed with  
13 Vaseline to prevent tissue from drying. R1-R6s' intracellular voltage responses were recorded to  
14 different spatiotemporal light patterns (see below) using sharp filamented quartz or borosilicate  
15 microelectrodes (120–220 MΩ), filled with 3 M KCl. A blunt reference electrode, filled with fly  
16 ringer, was inserted in the head capsule. The flies' temperature was kept either at  $19 \pm 1$  or  $25 \pm 1^\circ\text{C}$   
17 by a feedback-controlled Peltier device, as indicated in the figures. The recordings were performed  
18 after 1-2 minutes of dark adaptation, using the discontinuous clamp method with a switching  
19 frequency 20-40 kHz. The electrode capacitance was compensated using the head-stage output  
20 voltage. To minimize effects of damage and external noise on the analysis, only stable recordings of  
21 low-noise and high sensitivity were chosen for this study (sometimes lasting several hours). Such  
22 photoreceptors typically had resting potentials  $< -60$  mV in darkness and  $> 45$  mV responses to  
23 saturating test light pulses (Juusola & Hardie, 2001a).

24  
25 *Light stimulation.* We used a high power “white” LED (Seoul Z-Power P4 star, white, 100 Lumens) to  
26 test individual R1-R6 photoreceptors' encoding dynamics (**Figures 1** and **6F**). It was connected to a  
27 randomized quartz fiber optic bundle (transmission range: 180-1,200 nm), fitted with a lens  
28 (providing  $\sim 3^\circ$  homogeneous light disk as seen by the flies), and attached onto a Cardan arm system  
29 for accurate positioning at the center of each tested cell's receptive field. Its light output was driven  
30 by an OptoLED (Cairn Research Ltd, UK), which utilizes a feedback circuitry with a light-sensor.  
31 This LED has red component wavelengths, which minimizes prolonged depolarizing afterpotential  
32 (PDA) effects. Because long recordings can show sensitivity drifts, attributable to muscle activity  
33 (**Appendix 4**), the stimulus XY-position was regularly tested and, if needed, re-centered between long  
34 stimulus runs.

35 We used a bespoke 25 light-point array to measure individual R1-R6 photoreceptors'  
36 receptive fields and responses to moving point objects (bright dots, **Figure 7**; dark dots, **Appendix 9**).  
37 Again, a custom-made Cardan arm system was used to accurately position the array's center light-  
38 point (no. 13) at the center of each tested cell's receptive field. The dot size and the minimum inter-  
39 dot-distance, as seen by *Drosophila*, was  $1.7^\circ$ . Details of this device and the recording procedures are  
40 given in **Appendixes 4** and **6**.

41  
42 *Stimulus patterns.* Single photoreceptors' diurnal temporal encoding gamut was tested systematically  
43 over different bandwidth and contrast distributions; using 20 distinct light intensity time series  
44 stimuli, which were presented at the center of their receptive fields. The used test stimuli was based  
45 upon 5 different 2 s long Gaussian white-noise light intensity time series patterns, which had “flat”  
46 power spectrum up to 20, 50, 100, 200, or 500 Hz (**Figure 1B**), as low-pass filtered by MATLAB's  
47 filter toolbox, and the same peak-to-peak modulation (2 units). These were then superimposed on four  
48 backgrounds: BG0 (0 units, dark), BG0.5 (0.5 units), BG1 (1 unit) or BG1.5 (1.5 units, bright) on a  
49 linear intensity scale, giving altogether 20 unique stimulus patterns. As the two lowest backgrounds  
50 clipped downwards-modulation, prolonging dark intervals, the resulting stimuli ranged from high-  
51 contrast bursts ( $c = \Delta I/I \sim 1.46$  at BG0) to low-contrast Gaussian ( $c \sim 0.22$  at BG1.5).

52 As further controls, we tested how well R1-R6 photoreceptors responded to dark contrast  
53 bursts of different bandwidths (**Appendix 9**) and to their bright counterparts. In these experiments,  
54 R1-R6s were adapted for 10 s to BG0.5 and BG1 before repeated stimulation. In addition, we  
55 recorded the tested cells' responses to naturalistic light intensity time series (van Hateren, 1997a;

1 Song & Juusola, 2014) (NS), selected from van Hateren natural stimulus collection (van Hateren,  
2 1997a) (**Figure 2-figure supplement 3**). We also sampled light intensity time series from panoramic  
3 natural images, using three different velocity profiles of a published 10 s *Drosophila* walk (see **Video**  
4 **1**; details in **Appendix 3**). These stimuli were then played back to a R1-R6 photoreceptor by the  
5 “white” LED (see above).

6 In all these experiments,  $\geq 25$  consecutive responses to each repeated stimulus were recorded.

7  
8 *Data acquisition.* Both the stimuli and responses were filtered at 500 Hz (KEMO VBF/23 low-pass  
9 elliptic filter, UK), and sampled together at 1-10 kHz using a 12-bit A/D converter (National  
10 Instruments, USA), controlled by a custom-written software system, Biosyst in Matlab (Mathworks,  
11 USA) environment. For signal analyses, if need, the data was down-sampled to 1 kHz.

## 12 **Analyses**

13  
14 Because of short-term adaptive trends, we removed the first 3–10 responses to repeated stimulation  
15 from the analysis and used the most stable continuous segment of the recordings. Information  
16 theoretical methods for quantifying responses of approximately steady-state-adapted fly  
17 photoreceptors to different stimuli were described in detail before (Juusola & Hardie, 2001b; Juusola  
18 & de Polavieja, 2003; Song *et al.*, 2012; Song & Juusola, 2014). Below we list the key approaches  
19 used here.

20  
21 *Signal-to-noise ratio (SNR) and information transfer rate estimates.* In each recording, simulation or  
22 Poisson light stimulus series (see below), the signal was the mean, and the noise was the difference  
23 between individual traces and the signal (Juusola & Hardie, 2001a). Therefore, for a data chunk of 20  
24 responses ( $n = 20$  traces), there was one signal trace and 20 noise traces. The signal and noise traces  
25 were divided into 50% overlapping stretches and windowed with a Blackman–Harris 4-term window,  
26 each giving three 500-points-long samples. Because each trace was 2 s long, we obtained 60 spectral  
27 samples for the noise and 7 for the signal. These were averaged, respectively, to improve the  
28 estimates.

29  $SNR(f)$ , of the recording, simulation, or Poisson light stimulus series was calculated from their  
30 signal and noise power spectra,  $\langle |Sf|^2 \rangle$  and  $\langle |Nf|^2 \rangle$ , respectively, as their ratio, where  $||$  denotes the  
31 norm and  $\langle \rangle$  the average over the different stretches (Juusola & Hardie, 2001a). To eliminate data  
32 size and processing bias, the same number of traces ( $n = 20$ ) of equal length (2,000 points) and  
33 sampling rate (1 kHz; 1 ms bin size) were used for calculating the  $SNR(f)$  estimates for the  
34 corresponding real recordings, photoreceptor model simulations and the simulated Poisson stimuli.

35 Information transfer rates,  $R$ , for each recording, simulation, or Poisson light stimulus series  
36 were estimated by using the Shannon formula (Shannon, 1948), which has been shown to obtain  
37 robust estimates for these types of continuous signals (Juusola & de Polavieja, 2003; Song & Juusola,  
38 2014). We analyzed steady-state-adapted recordings and simulations, in which each response (or  
39 stimulus trace) is expected to be equally representative of the underlying encoding (or statistical)  
40 process. From  $SNR(f)$ , the information transfer rate estimates were calculated as follows:

$$41 \quad R = \int_0^{\infty} (\log_2[SNR(f) + 1])df \quad (1)$$

42  
43  
44 We used minimum = 2 Hz and maximum = 500 Hz (resulting from 1 kHz sampling rate and 500  
45 points window size). The underlying assumptions of this method and how the number and resolution  
46 of spectral signal and noise estimates and the finite size of the used data can affect the resulting  
47 Information transfer rate estimates have been analyzed before (van Hateren, 1992b; Juusola & Hardie,  
48 2001b; Juusola & de Polavieja, 2003; Song & Juusola, 2014) and are further discussed in **Appendix**  
49 **2**. All data analyses were performed with Matlab (MathWorks).

50  
51 *Measuring photoreceptors’ visual acuity.* We measured dark- and light-adapted wild-type R1-R6  
52 photoreceptors’ receptive fields by their acceptance angles,  $\Delta\rho$ , using intracellular voltage responses  
53 to random light-points in a stimulation array. These measurements were compared to those of  
54  $hdc^{JK910}$ -mutants (Burg *et al.*, 1993), in which first-order interneurons receive no neurotransmitter

1 (histamine) from photoreceptors and so are incapable of feedback-modulating the photoreceptor  
2 output. Both the wild-type and mutant R1-R6 photoreceptors' mean  $\Delta\rho$  was about twice the mean  
3 interommatidial angle,  $\Delta\phi$ . The stimulus apparatus, the method and result details and theoretical  
4 electron micrograph comparisons of their mean rhabdomere sizes are explained in **Appendixes 4-5**.

5  
6 *Spatiotemporal analyses using the classic conventional models.* Voltage responses of wild-type and  
7 *hdc<sup>JK910</sup>* R1-R6s to moving bright dots were evaluated against their respective classic model  
8 simulations, in which each recorded receptive field was convoluted by the same cell's impulse  
9 response (Srinivasan & Bernard, 1975; Juusola & French, 1997) (1st order Volterra kernels). The  
10 motion blur effects were quantified by comparing the real R1-R6 outputs to their deterministic model  
11 predictions. Details of the analysis are given in **Appendix 6**.

### 12 **Biophysical modeling**

13 *Time series analyses.* We used our recently published biophysically-realistic stochastic photon  
14 sampling model (Song *et al.*, 2012) of a *Drosophila* R1-R6 photoreceptor to simulate macroscopic  
15 voltage response to different repeated light intensity time series patterns from a point source (**Figures**  
16 **3-4**). The model has no free parameters. Its design and the general aims and details of these  
17 simulations are given in **Appendixes 1 and 2**. To eliminate data size bias, the signaling properties and  
18 performance of the simulations were quantified and compared to the corresponding recordings by  
19 using the same analytical routines on the same-sized data-chunks. The models were run using Matlab  
20 in the University of Sheffield computer cluster (Iceberg).

21  
22 For each stimulus, its mean was adjusted to maximize information of the simulated  
23 photoreceptor outputs, mimicking the action of the photomechanical adaptations (intracellular pupil  
24 mechanism and rhabdomere contractions; **Appendixes 2 and 7**). This optimization set the effective  
25 mean photon rates from  $8 \times 10^4$  at BG1.5 to  $8 \times 10^5$  photons/s at BG0 (**Figure 3**). Thus, each of these  
26 light levels was considered to represent the optimal daylight input (that survived the photomechanical  
27 adaptations and was absorbed by a rhabdomere), in which modulation enabled the largest sample  
28 (bump) rate changes. Otherwise, more of its sampling units (30,000 microvilli) would be either  
29 underutilized or refractory (saturation). The maximum information rates of the simulated  
30 photoreceptor outputs closely followed the corresponding mean information transfer rates of the real  
31 recordings over the whole tested encoding range (**Appendix 2**). This implies that the central function  
32 of the photoreceptors' combined photomechanical adaptations is to maximize their information  
33 transfer, and that the resulting estimates represent realistic maxima.

34  
35 *Encoding efficiency.* A photoreceptor's encoding efficiency,  $\eta$ , was the ratio between the information  
36 rates of its voltage output,  $R_{output}$ , and the corresponding effective light input,  $R_{input}$ :

$$37 \quad \eta = \frac{R_{output}}{R_{input}} \quad (2)$$

38  
39 with  $R_{output}$  and  $R_{input}$  estimated by the Shannon formula (Eq. 1). Details are in **Appendix 2**.

40  
41 *Modeling R1-R6 output to moving dots.* We developed a new "microsaccadic sampling"-model to  
42 predict how photomechanical rhabdomere contractions (microsaccades) move and narrow *Drosophila*  
43 R1-R6 photoreceptors' receptive fields to resolve fast-moving objects. **Appendix 8** gives the details  
44 of this modeling approach, which combines the stochastic photon sampling model (Song *et al.*, 2012)  
45 with additional fixed ommatidium optics and photomechanical rhabdomere contraction parameters.  
46 The same appendix shows examples of how refractory photon sampling and rhabdomere contractions  
47 jointly improve visual acuity.

### 48 **High-speed video of the light-induced rhabdomere movements**

49  
50 Cornea-neutralization method with antidromic far-red (>720 nm) illumination was used to observe  
51 deep pseudopupils (Franceschini & Kirschfeld, 1971b) (photoreceptor rhabdomeres) in the  
52 *Drosophila* eye at 21 °C. A high-speed camera (Andor Zyla, UK; 500 frames/s), connected to a  
53 purpose-built microscope system, recorded fast rhabdomere movements *in vivo* to blue-green light  
54

1 stimuli (470 + 535 nm peaks), which were delivered orthodromically into the eye. The method details,  
2 mutant and transgenic *Drosophila* used and the related image analyses are explained in **Appendix 7**.

### 3 4 **Flight simulator experiments**

5 *Open-loop configuration* was used to test hyperacute motion vision. Wild-type flies were tethered in a  
6 classic torque meter (Tang & Guo, 2001) with heads fixed, and lowered by a manipulator into the  
7 center of a black and white cylinder (spectral full-width: 380–900 nm). A flying fly saw a continuous  
8 panoramic scene (360°), which in the tests contained multiple vertical stripes (black and white bars of  
9 equal width). The control was a diffuse white background. After viewing the still scene for 1 s, it was  
10 spun counterclockwise by a linear stepping motor for 2 s, stopped for 2 s before rotating clockwise for  
11 2 s, and stopped again for 1 s. This 8 s stimulus was repeated 10 times and each trial, together with the  
12 fly's yaw torque responses, was sampled at 1 kHz (Wardill *et al.*, 2012). Flies followed the stripe  
13 scene rotations, generating yaw torque responses (optomotor responses to right and left), the strength  
14 of which reflected the strength of their motion perception. The flies did not follow the white control  
15 scene rotations. The panoramic scenes had  $\pm 360^\circ$  azimuth and  $\pm 45^\circ$  elevation, as seen by the fly. The  
16 stripe scenes had 1.0 contrast and their full-wavelength resolutions were either hyperacute (1.16° or  
17 2.88°) or coarse (14.40°), giving the inter-bar-distances of 0.58°, 1.44° and 7.20°, respectively. The  
18 white scene has zero contrast. The scene rotation velocity was 45 %/s.

### 19 20 **Transmission Electron Microscopy**

21 The fly eye dissection, fixation embedding, sectioning and imaging protocols for EM (**Figure 5A**) are  
22 described in **Appendix 5**.

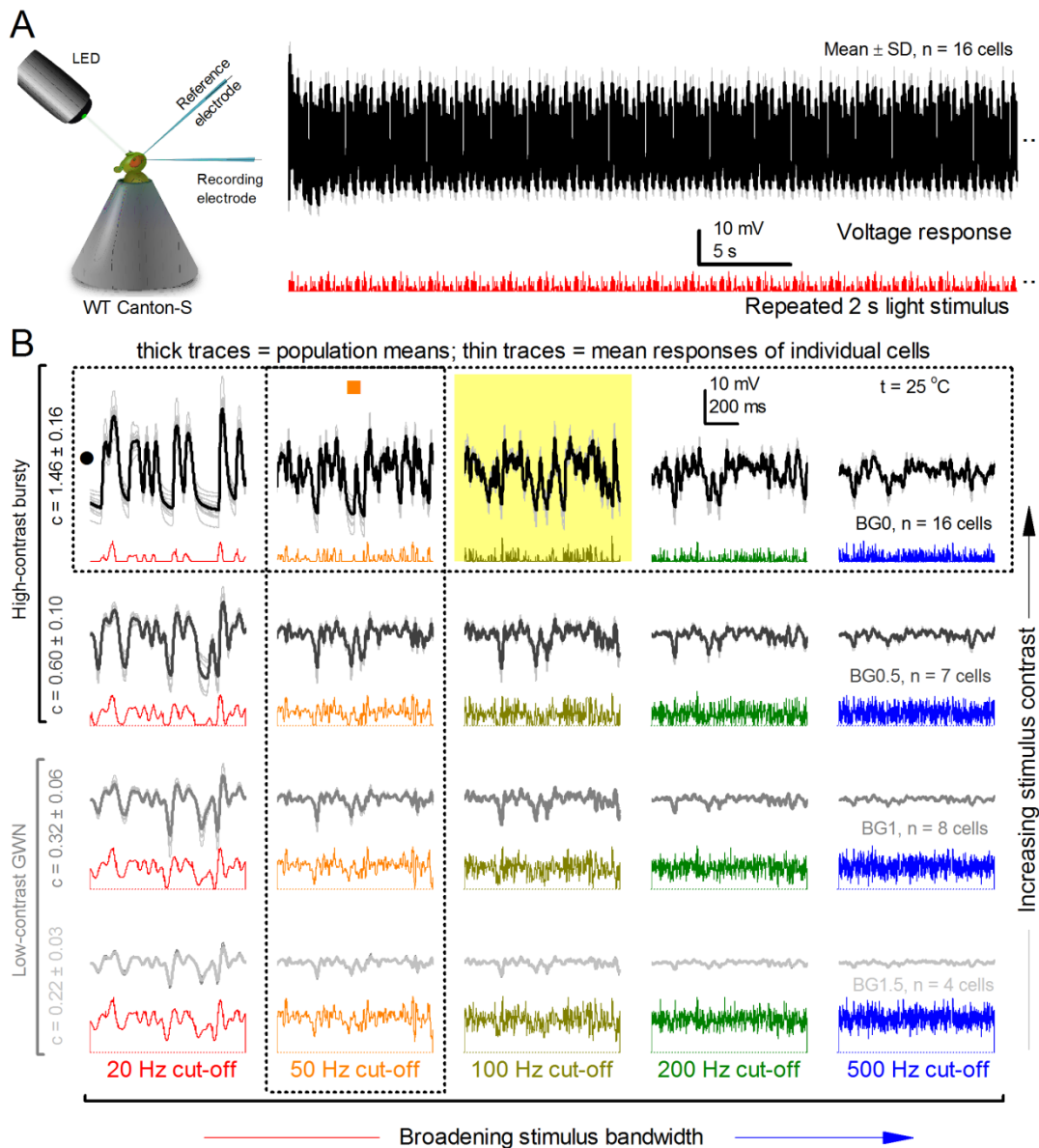
### 23 24 **Statistics**

25 Test responses were compared with their controls by performing two-tailed t-tests to evaluate the  
26 difference in the compared data. Welch's t-test was used to accommodate groups with different  
27 variances for the unpaired comparisons. In the figures, asterisks are used to mark the statistical  
28 significance: ns indicates  $p > 0.05$ , \* indicates  $p \leq 0.05$ , \*\* indicates  $p \leq 0.01$ , and \*\*\* indicates  $p \leq$   
29 0.001.

30  
31 **Acknowledgments:** We thank C-H. Lee, E. Chiappe, R. Strauss and E. Buchner for flies, S. Tang for  
32 help with the flight simulator, O. List for some illustrations, A. Nikolaev, A. Lin for discussions, and  
33 two anonymous referees for their suggestions. This work was supported by the Open Research Fund  
34 of the State Key Laboratory of Cognitive Neuroscience and Learning (M.J.), High-End Foreign  
35 Expert Grant by Chinese Government (GDT20151100004: M.J.), NSFC project (30810103906: M.J.),  
36 Jane and Aatos Erkkö Foundation Fellowships (M.J. and J.T.), The Leverhulme Trust grant (RPG-  
37 2012-567: M.J.) and the BBSRC grants (BB/F012071/1, BB/D001900/1 and BB/H013849/1: M.J.).  
38 The authors declare no competing financial interest.

1 **Figure supplements**

2



3

4 **Figure 1-figure supplement 1. R1-R6 output varies more cell-to-cell than trial-to-trial (cf. Figure**

5 **1) but show consistent stimulus-dependent dynamics over the whole encoding range. (A)** The

6 mean voltage response and SD of 15 R1-R6 cells to the same repeated 20 Hz bandwidth bursts.

7 Photoreceptor output adapts within ~2 s to the stimulation. (B) Population means (thick) and 4-16

8 mean voltage responses of individual photoreceptors (thin traces) to 20 different stimuli; each with

9 specific bandwidth (columns: from 20 Hz, red to 500 Hz, blue) and mean contrast (rows). Stimulation

10 changes from Gaussian white-noise (GWN; bottom) to bursts (top) with the light background: from

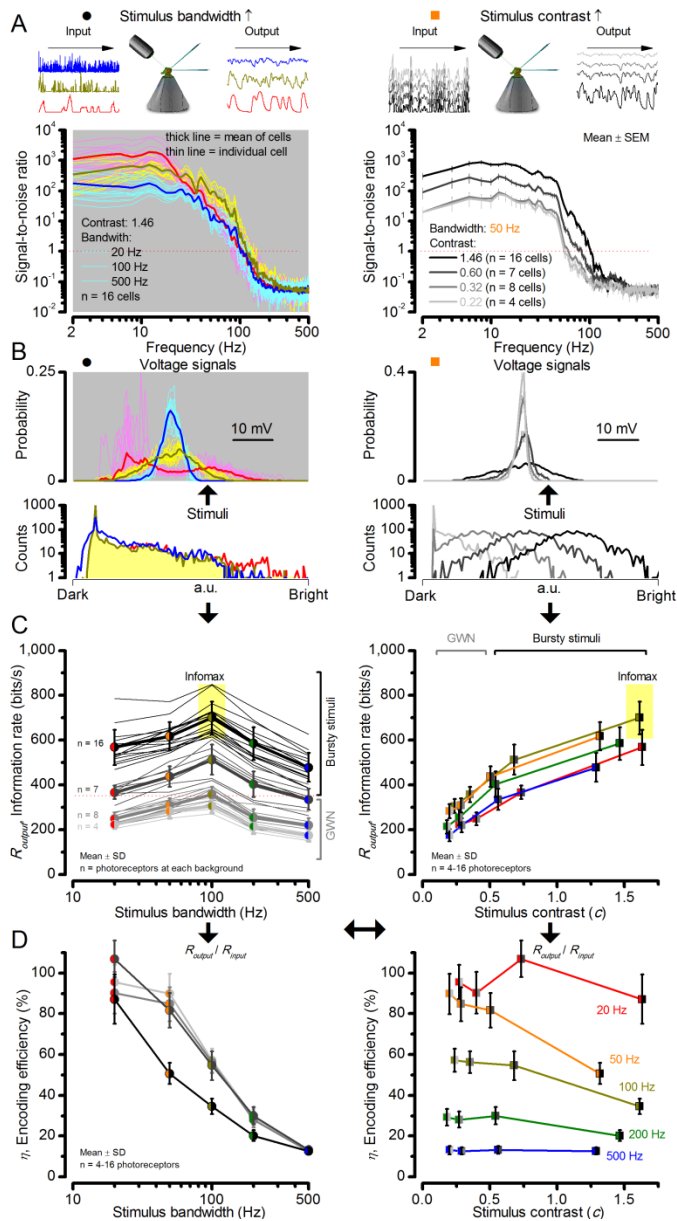
11 BG0 (dark) to BG1.5 (very bright). Left top: the traces from (A). The yellow box indicates the

12 responses with the highest entropy and information content. Vertical dotted rectangle (orange square)

13 and horizontal rectangle (black circle): responses for contrast and bandwidth analyses in **Figure 2-**

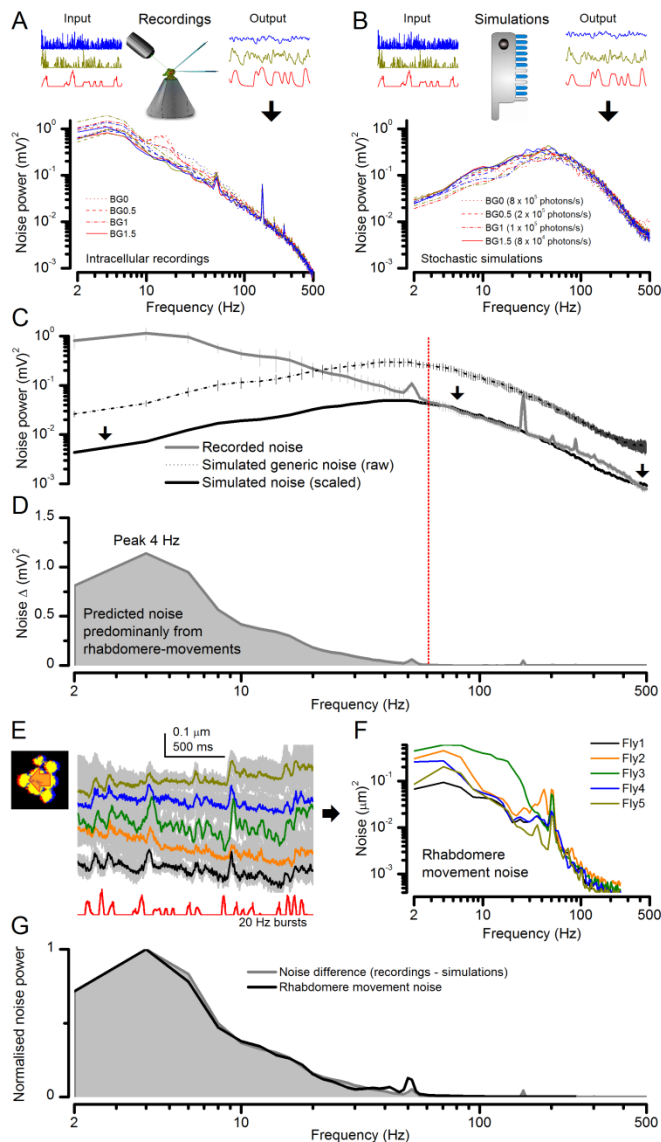
14 **figure supplement 1A**. All recordings were done at 25 °C. Compare this data to **Figure 1**.

15

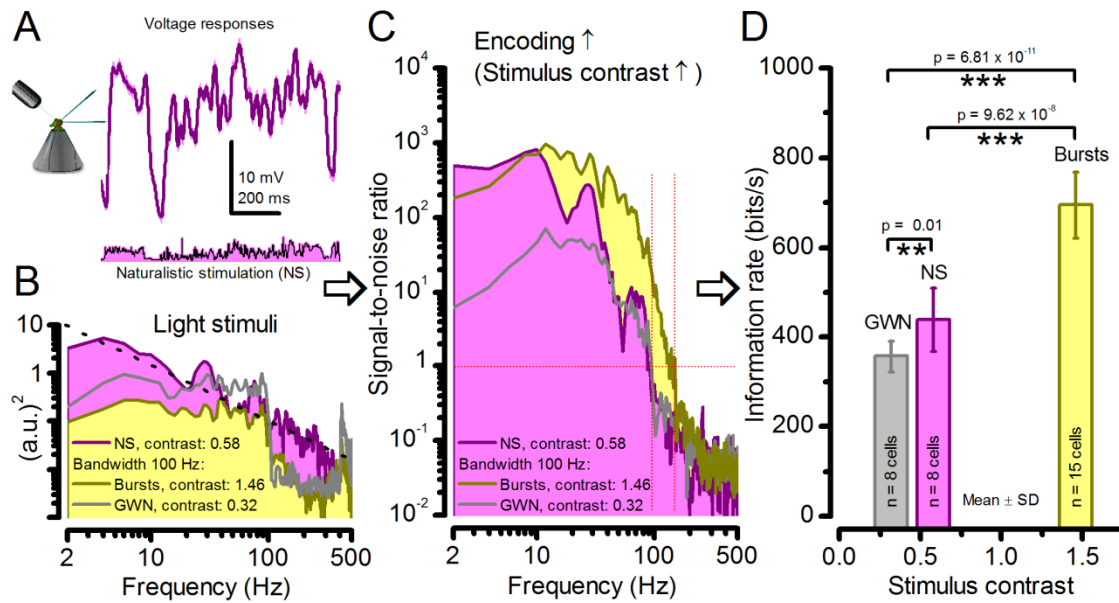


1  
2

3 **Figure 2-figure supplement 1. Signaling performance vary cell-to-cell but adapts similarly to**  
 4 **given stimulus statistics.** (A) Response signal-to-noise ratios (SNR) to 20 (red), 100 (yellow) and  
 5 500 Hz (blue) bandwidth (left) saccadic bursts, and to 50 Hz bandwidth stimuli of different contrasts  
 6 (right); color scheme as in **Figure 1**. SNR increases with contrast (right), reaching (in some cells)  
 7 ~6,000 maximum for 20 Hz bursts (left, red). All R1-R6s showed the broadest frequency range for  
 8 100 Hz bursts (yellow). (B) Highly skewed bursts drove mostly Gaussian responses (exception: 20  
 9 Hz, red), with 100 Hz bursts evoking the broadest amplitude range (yellow). (C) Information transfer  
 10 of all cells peaked for 100 Hz stimuli, irrespective of the tested contrast (or BG; left), having global  
 11 maxima (infomax) between 600-850 bits/s (yellow box). (D) Mean encoding efficiency ( $R_{\text{output}}/R_{\text{input}}$ )  
 12 reached >100% for 20 Hz bursts, with its extra information coming from the neighboring cells. For  
 13 determining  $R_{\text{input}}$  see **Figure 3**. Encoding efficiency fell with increasing stimulus bandwidth, but less  
 14 with contrast. Note: encoding efficiency for bursts ( $\eta^{\text{burst}}$ ; black trace, left) was lower than for GWNs  
 15 ( $\eta^{\text{GWN}}$ ; grey and light grey traces). Because photomechanical adaptations let optimally 8-times brighter  
 16 intensity modulation (photon absorption rate) through for high-contrast bursts ( $8 \times 10^5$  photons/s) than  
 17 for GWN ( $1 \times 10^5$  photons/s), their higher input information is higher;  $R_{\text{input}}^{\text{burst}} \gg R_{\text{input}}^{\text{GWN}}$ . Thus, whilst  
 18  $R_{\text{output}}^{\text{burst}} > R_{\text{output}}^{\text{GWN}}$ ,  $\eta^{\text{burst}} < \eta^{\text{GWN}}$  (**Appendix 2**).

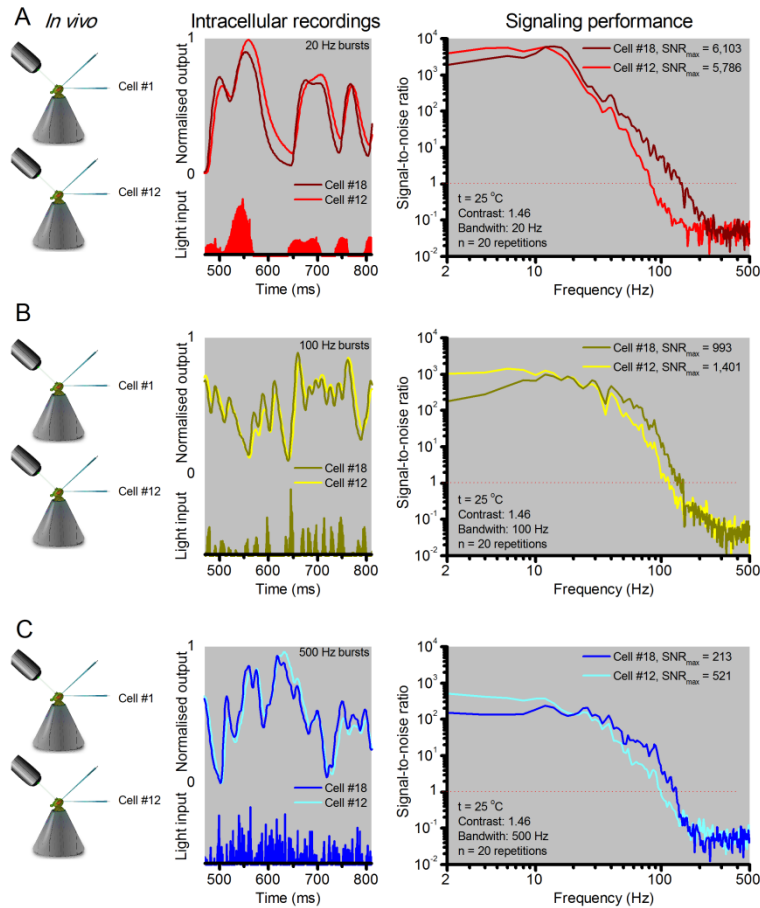


1  
2  
3 **Figure 2-figure supplement 2. Light-adapted R1-R6 noise is similar for all the test stimuli, with**  
4 **its high-frequencies reflecting the mean quantum bump shape and its low-frequencies the**  
5 **rhabdomere jitter. (A)** Photoreceptor noise (from **Figure 1**) remained largely constant for all the test  
6 stimuli; extracted from the responses (output) to stimulus repetition (input); see Methods. **(B)**  
7 Corresponding photoreceptor noise of the model (Song *et al.*, 2012; Song & Juusola, 2014)  
8 simulations was also broadly constant but lacked the recordings' low-frequency noise in **(A)**. **(C)** The  
9 mean simulated noise power ascends with membrane impedance, which here was larger than that in  
10 the recordings in **(A)**. Yet, the high-frequency parts of the real and simulated noise (>60 Hz),  
11 indicating the corresponding average light-adapted quantum bump waveform (Wong *et al.*, 1982;  
12 Juusola & Hardie, 2001b, a; Song *et al.*, 2012; Song & Juusola, 2014), sloped similarly. **(D)**  
13 Overlaying these exposed the low-frequency noise difference (<60 Hz). Our results (**Figure 8**)  
14 predicted that this difference was a by-product of photomechanical rhabdomere and eye muscle  
15 movements, which the simulations lacked. **(E)** Mean rhabdomere movement responses ( $\pm$  SD, grey)  
16 in five different flies to the same repeated 20 Hz high-contrast bursts. These were smaller than those  
17 to 1 s flashing (**Figure 8E**, **Appendix 7**). **(F)** Average variability of the recording series (mean –  
18 individual response) shown as rhabdomere movement noise power spectra. **(G)** Mean rhabdomere  
19 movement noise (black trace; from **F**) matched its prediction (grey; from **D**). Therefore, the  
20 recordings' extra noise resulted from variable rhabdomere contractions; jittering light input to R1-  
21 R6s. Crucially, this noise is minute; for 20 Hz saccadic bursts,  $\sim$ 1/6,000 of R1-R6 signal power  
22 (**Figure 2A**).



1  
2 **Figure 2-figure supplement 3. Strong responses to naturalistic stimulation (NS) carry only about**  
3 **half the information of the strongest responses to bursts.** (A) The mean (signal; purple) and  
4 voltage responses (pink) of a R1-R6 photoreceptor to naturalistic light intensity time series. (B) At the  
5 light source, NS (purple), which is dominated by low-frequency transitions between darker and  
6 brighter events, had higher power than GWN (grey) or bursty high-contrast stimuli (yellow), but its  
7 mean contrast (0.58) is between the other two. (C) Signal-to-noise ratio of responses to NS has a  
8 similar low-frequency maximum to responses to bursty 100 Hz stimuli, but lower values at high-  
9 frequencies, similar to GWN-driven responses (grey). Both of these signaling performance estimates  
10 are from the same R1-R6 in (A). (D) Information transfer rate in photoreceptor output directly  
11 depends upon the mean stimulus contrast. Photoreceptors encode more information during naturalistic  
12 stimulation than during GWN stimulation (see also: Song & Juusola, 2014). But encoding can further  
13 double during high-contrast bursts, which utilize better the refractory sampling dynamics of 30,000  
14 microvilli, generating the largest sampling rate changes. Significance by two-tailed t-test. For more  
15 explanation, see **Appendix 3**.

16

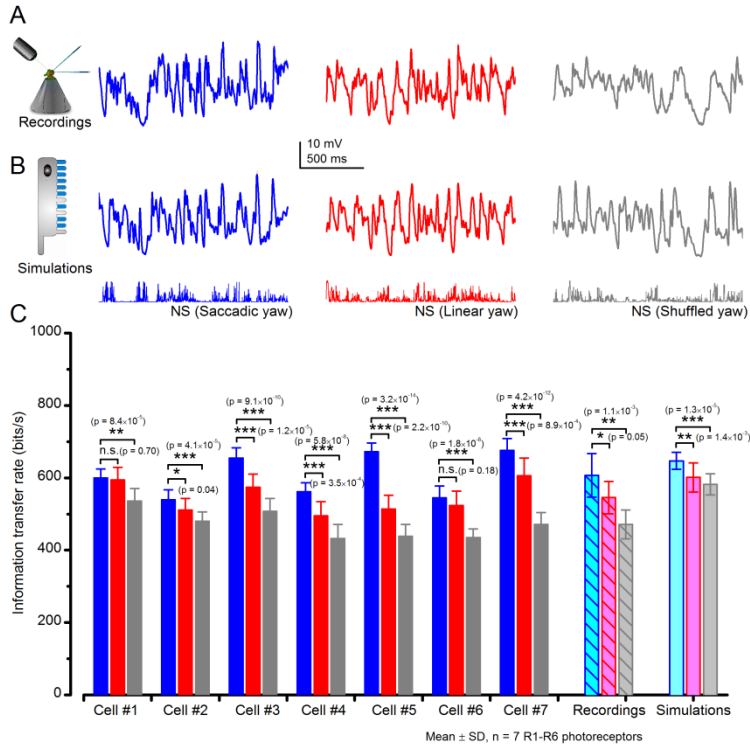


1  
2  
3  
4  
5  
6  
7  
8  
9  
10  
11  
12  
13

**Figure 5-figure supplement 1. R1-R6 photoreceptors' response waveforms and frequency range of reliable encoding vary cell-to-cell, and this variation does not reflect recording quality.**

Intracellular responses to the same repeated stimuli recorded *in vivo* from two different R1-R6 photoreceptors (Cell #18 and Cell #12) in two wild-type *Drosophila*. (A) 20 Hz light bursts drove both cells vigorously, but the output of Cell #18 rose and decayed faster. Both outputs had maximum signal-to-noise ratios (SNR<sub>max</sub>) > 5,000, but because of its faster response dynamics Cell #18 encoded better high stimulus frequencies (B-C) for 100 and 500 Hz light bursts, respectively, Cell #12's output had a higher SNR<sub>max</sub> but again lagged behind Cell #18's output. The corresponding information transfer rate estimates,  $R_{output}$ , for Cell #18 were 787 bits/s (20 Hz bursts), 850 bits/s (100 Hz) and 625 bits/s (500 Hz) and for Cell #12: 569 bits/s (20 Hz), 711 bits/s (100 Hz) and 503 bits/s (500 Hz).

1



2

3

4 **Figure 6-figure supplement 1. *Drosophila* R1-R6 photoreceptors generate responses with higher**

5 **information transfer rates to saccadic (bursty) naturalist light intensity time series (NS) than to**

6 **corresponding linear or shuffled stimulation. (A) Mean intracellular voltage responses of a R1-R6**

7 **photoreceptor to Naturalistic light intensities that have been modulated by saccadic (blue), linear (red)**

8 **and shuffled (gray) yaw signals. (B) Simulations of biophysically realistic *Drosophila* R1-R6**

9 **photoreceptor model (Appendix 1) to the same stimuli. (C) Mean information transfer rates of seven**

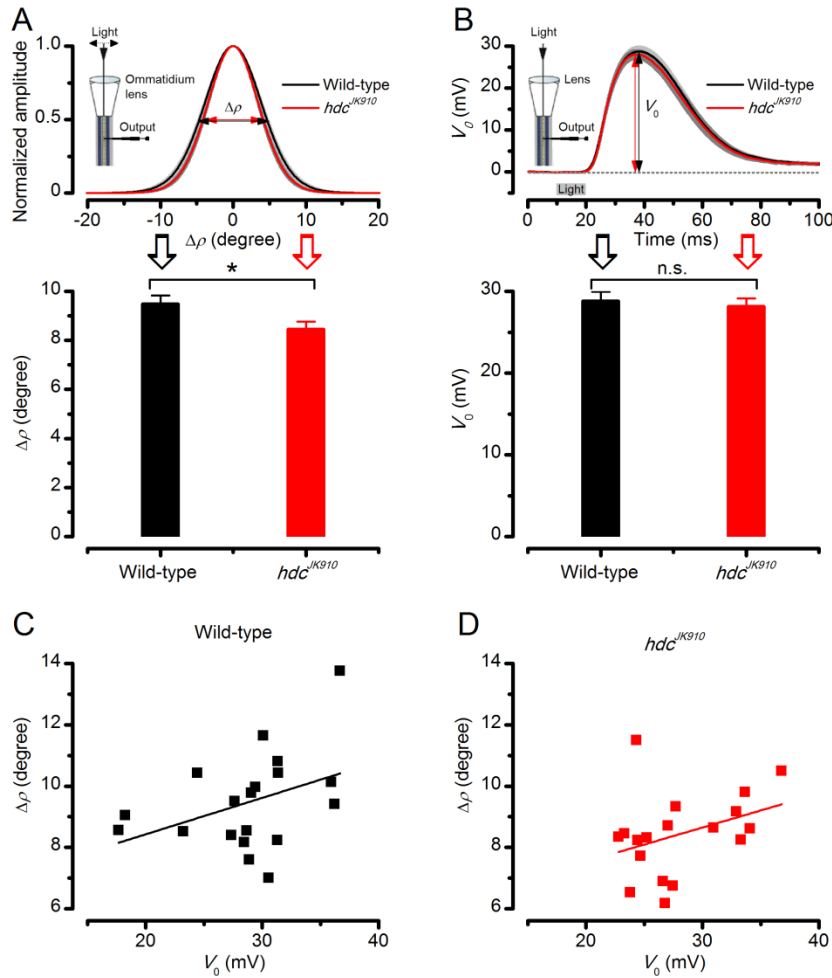
10 **R1-R6 photoreceptor outputs to the same stimuli and their population means. These information rates**

11 **are further compared to the corresponding model output rates. Note that every photoreceptor sampled**

12 **most information from the NS with saccadic modulation.**

13

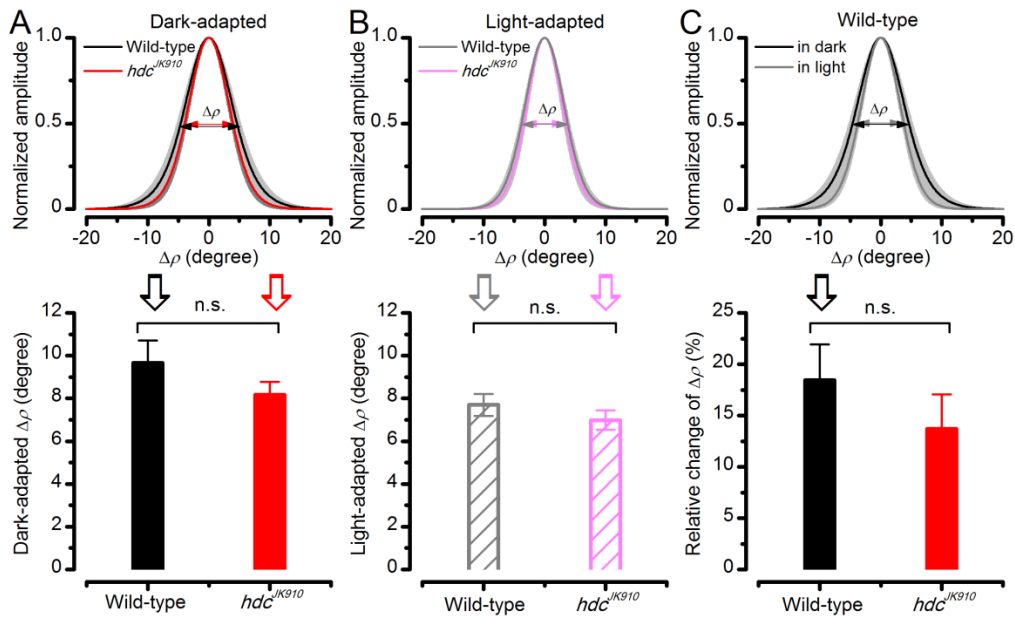
1



2

3

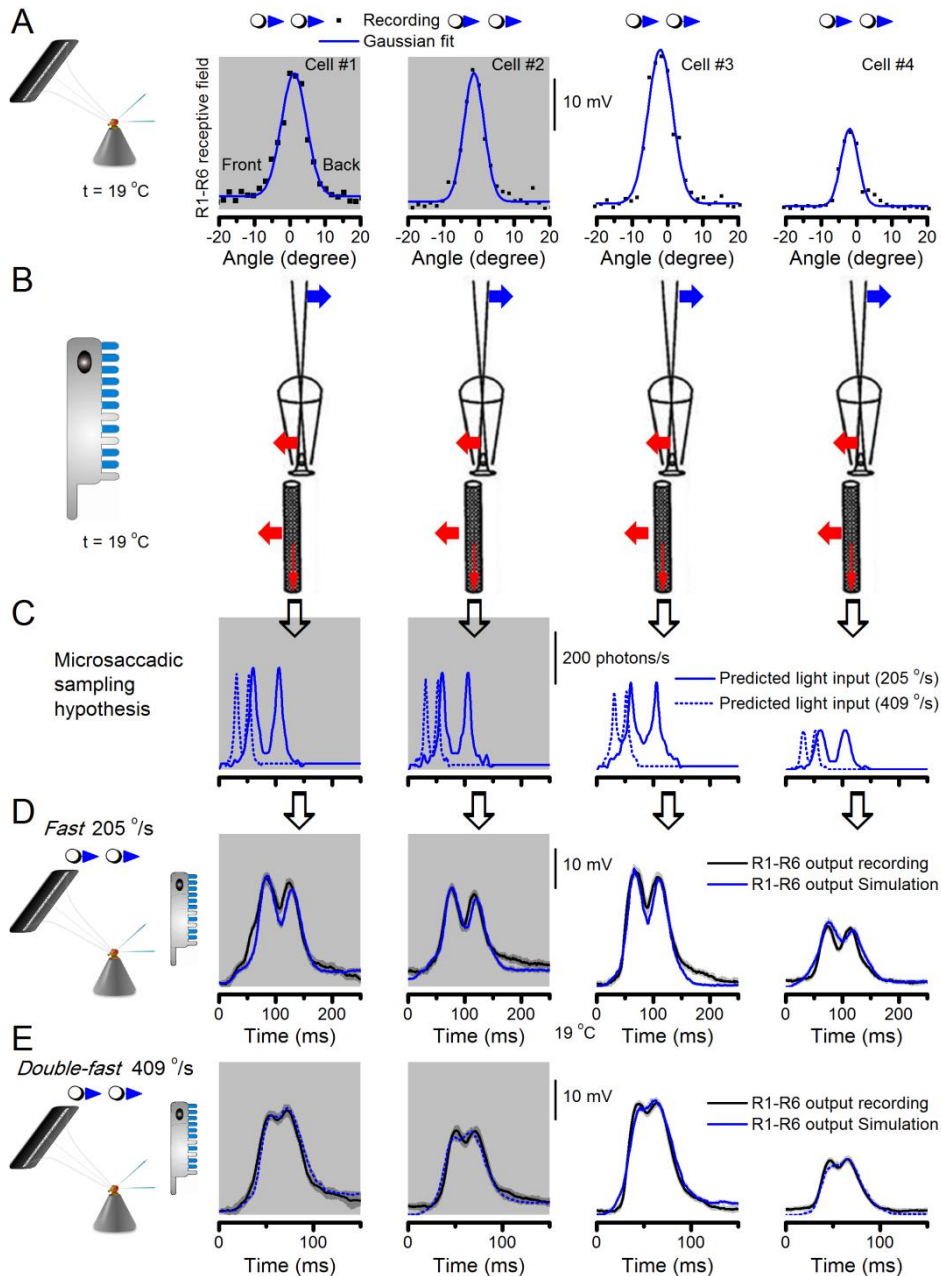
4 **Figure 7-figure supplement 1. Dark-adapted wild-type and *hdc*<sup>JK910</sup> R1-R6s' acceptance angles**  
5 **differ marginally.** The receptive field of each tested cell was estimated as in [Appendix 4](#), [Appendix](#)  
6 [figure 15](#). (A) Dark-adapted wild-type photoreceptors' receptive fields (above), shown as the mean of  
7 their Gaussian fits (black), were ~11% wider than those of *hdc*<sup>JK910</sup> photoreceptors (red). Their  
8 receptive field sizes (below) were quantified by the corresponding half-maximum widths, giving the  
9 mean acceptance angles:  $\Delta\rho_{\text{wild-type}} = 9.47 \pm 0.36^\circ$ ;  $\Delta\rho_{\text{hdc}} = 8.44 \pm 0.32^\circ$ ;  $p = 0.0397$ , two-tailed t-test.  
10 (B) Wild-type and mutant photoreceptors' peak responses (above), evoked by a sub-saturating 10 ms  
11 light flash (grey bar) at the center of the receptive field, showed similar dynamics and amplitudes,  $V_0$   
12 (below).  $V_{0\text{wild-type}} = 28.77 \pm 1.19$  mV;  $V_{0\text{hdc}} = 28.11 \pm 1.03$  mV;  $p = 0.67$ , two-tailed t-test. This  
13 indicates that *hdc*<sup>JK910</sup> phototransduction is functionally intact and wild-type-like. See also (Dau *et al.*,  
14 2016). (C) Linear correlation between  $\Delta\rho$  and  $V_0$  of dark-adapted wild-type photoreceptors. Adjusted  
15 R-squared = 0.1043. (D) Linear correlation between  $\Delta\rho$  and  $V_0$  of dark-adapted *hdc*<sup>JK910</sup>  
16 photoreceptors. Adjusted R-squared = 0.072. (A-D)  $n_{\text{wild-type}} = 19$ ;  $n_{\text{hdc}} = 18$ . (A, B) Mean  $\pm$  SEM; two-  
17 tailed t-test.  
18



1  
2  
3  
4  
5  
6  
7  
8  
9  
10  
11  
12

**Figure 7-figure supplement 2. Light-adaptation narrows wild-type and *hdc*<sup>JK910</sup> R1-R6s' receptive fields similarly.** Comparing wild-type and *hdc*<sup>JK910</sup> photoreceptors, of which receptive fields were assessed in both the dark- and light-adapted states. (A) Their dark-adapted and (B) and light-adapted  $\Delta\rho$  values were similar. Dark-adapted:  $\Delta\rho_{\text{wild-type}} = 9.65 \pm 1.06^\circ$ ;  $\Delta\rho_{\text{hdc}} = 8.16 \pm 0.62^\circ$ ;  $p = 0.258$ , two-tailed t-test. Light-adapted:  $\Delta\rho_{\text{wild-type}} = 7.7 \pm 0.52^\circ$ ;  $\Delta\rho_{\text{hdc}} = 6.98 \pm 0.46^\circ$ ;  $p = 0.323$ , two-tailed t-test. (C) Predictably, their receptive fields narrowed during light-adaptation (only wild-type shown). The relative changes between the two adaptation states between were statistically similar in wild-type and *hdc*<sup>JK910</sup> photoreceptors. Relative changes, calculated as  $C = \frac{\Delta\rho_{\text{Dark}} - \Delta\rho_{\text{Light}}}{\Delta\rho_{\text{Dark}}} \times 100\%$ .  $C_{\text{wild-type}} = 18.44 \pm 3.5\%$ ;  $C_{\text{hdc}} = 13.68 \pm 3.37\%$ ,  $p = 0.347$ , two-tailed t-test. A-C: Mean  $\pm$  SEM;  $n_{\text{wild-type}} = 6$ ;  $n_{\text{hdc}} = 8$  cells.

1



2

3

4

5

6

7

8

9

10

11

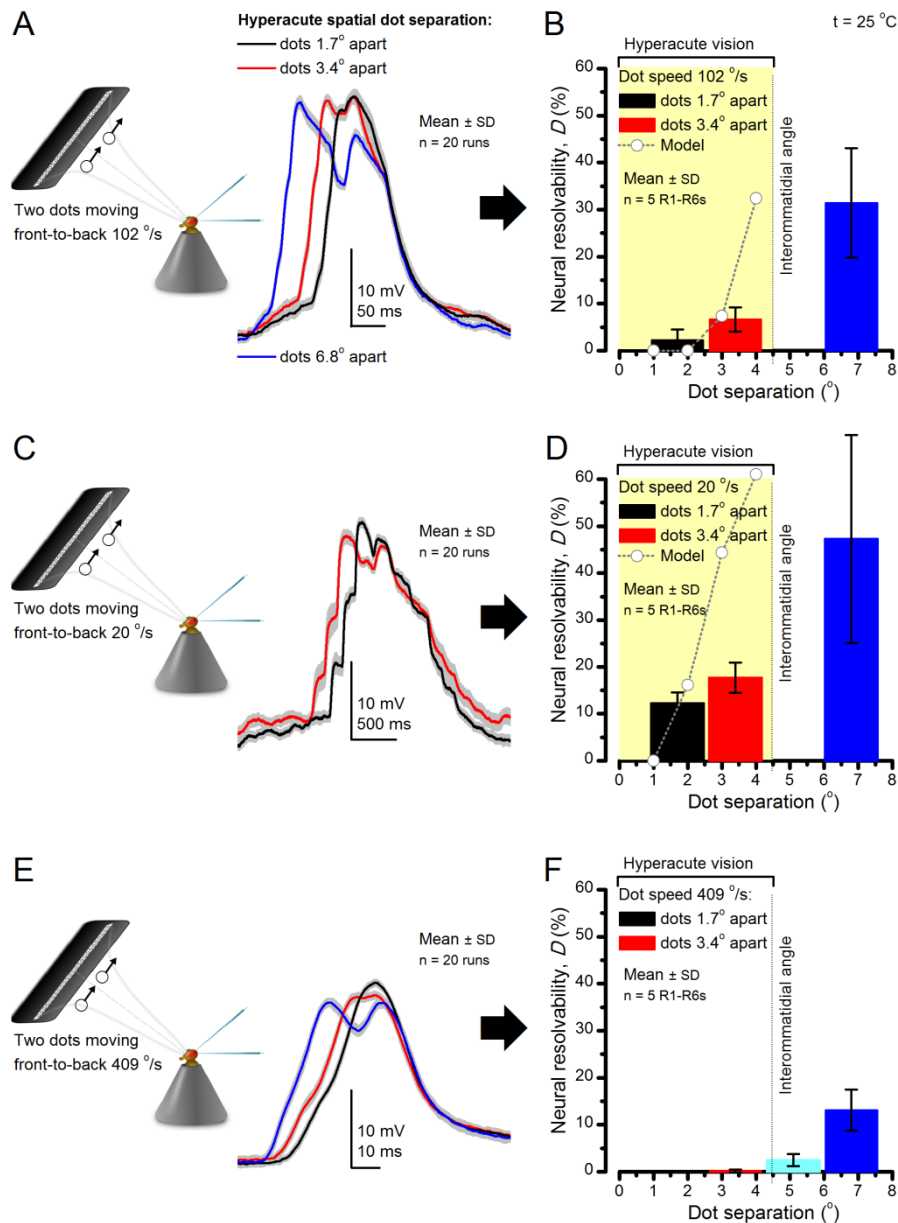
12

13

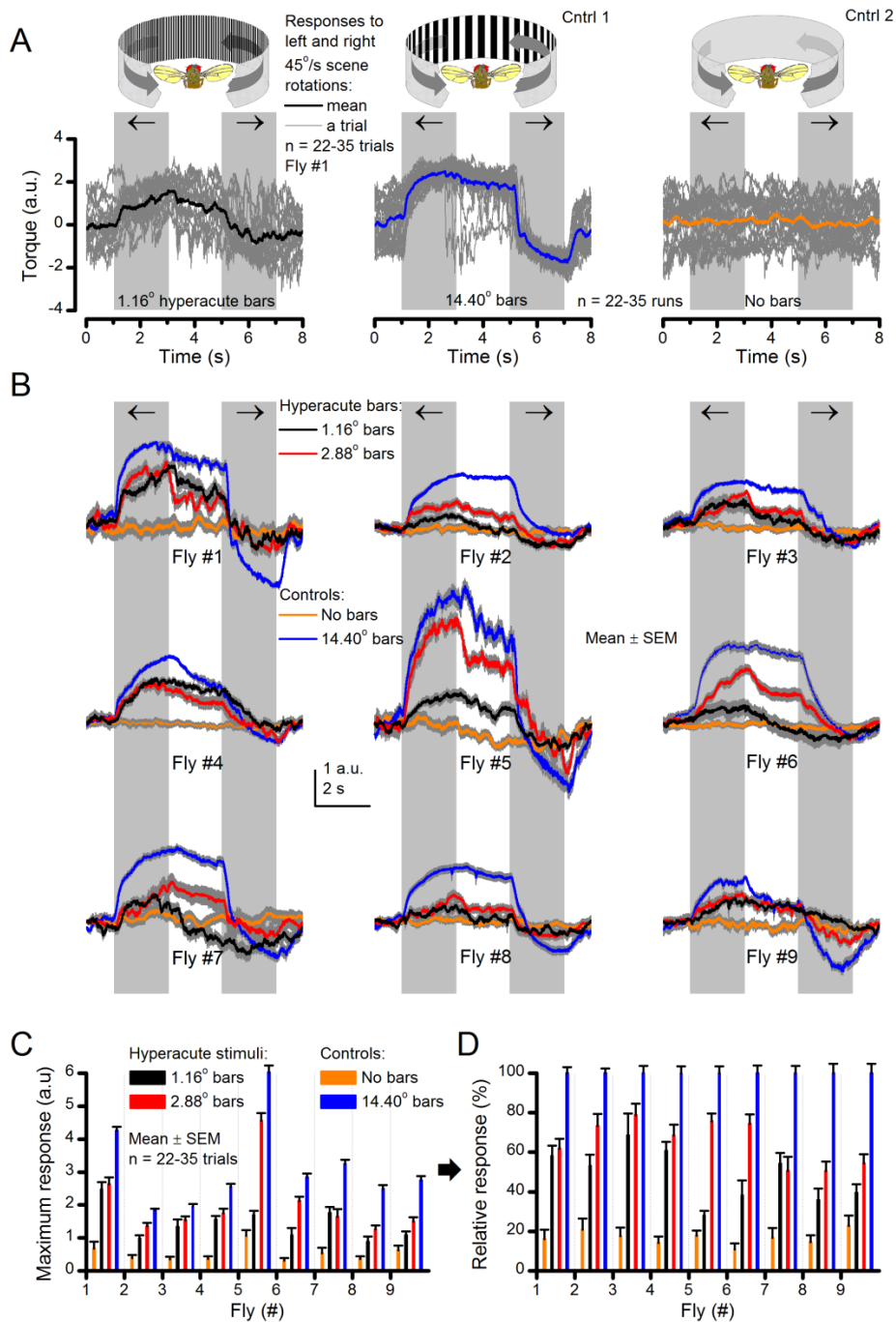
14

15

**Figure 8-figure supplement 1. Microsaccadic sampling hypothesis predicts realistic voltage output to two bright dots crossing a R1-R6's receptive field in saccadic speeds.** (A) Receptive fields of four R1-R6 photoreceptors, measured with 25 light point stimulator (Appendix 4). (B) Microsaccadic sampling hypothesis predicts that because the rhabdomeres move photomechanically, the photoreceptors' receptive fields move in the opposite direction and narrow transiently (acceptance angles,  $\Delta\rho$ , change from 8.2-9.5° to 3.5-4.5°). (C) The resulting light input for each tested photoreceptor was predicted from its measured receptive field in (A) by the microsaccadic sampling hypothesis. (D and E) These inputs then drove our biophysically realistic R1-R6 model, predicting the photoreceptor voltage output, which was compared to the corresponding real recordings. The simulated R1-R6 output closely resembled the recorded R1-R6 output of the same cells to saccadic two dot stimuli.



1  
 2 **Figure 9-figure supplement 1. Encoding space in time - intracellular R1-R6 recordings to two**  
 3 **bright dots crossing the receptive field show how their responses convey hyperacute spatial**  
 4 **information in time.** 25 light-point-array positioned at a R1-R6's receptive field center, generating  
 5 two bright front-to-back moving dots. (A) Characteristic responses of a R1-R6 at 25 °C to the dots,  
 6 1.7, 3.4 or 6.8° apart, travelling 102 °/s in front-to-back direction. (B) Individual outputs resolved the  
 7 dots, which were less than the interommatidial angle ( $\Delta\phi = 4.5^\circ$ ) apart (yellow box); resolvability  
 8 given by the Raleigh criterion (Figure 7C). Microsaccadic sampling model (Figure 9) predicted a  
 9 comparable resolvability threshold (dotted line). (C) At lower dot velocities (20-50 °/s),  
 10 corresponding to normal gaze fixation speeds in close-loop flight simulator experiments (Appendix  
 11 10), each R1-R6 responded to the tested hyperacute dot separations (1.7° and 3.4°) even stronger.  
 12 Notice the small staircase-like steps in voltage responses. These represent light from 25 individual  
 13 light-guide-ends being turned on/off in sequence to generate the moving dots, crossing the receptive  
 14 field slowly (see Appendix 6). (D) At 20 °/s velocity, neural resolvability to the tested hyperacute dot  
 15 separations was between 10-20%. (E) R1-R6 output to the two dots, having the same separations as  
 16 above, but now moving at fast saccadic velocity (409 °/s). (F) Although, at such a high speed, R1-R6  
 17 output could not resolve the hyperacute dot separations (1.7° and 3.4°) consistently, the dots were  
 18 nevertheless clearly detected when at 5.1° apart (cyan bar), which is about  $\Delta\phi$ .  
 19



1  
2  
3  
4  
5  
6  
7  
8  
9  
10  
11  
12

**Figure 10-figure supplement 1. Optomotor behavior in a flight simulator system demonstrates that *Drosophila* see hyperacute visual patterns.** (A) 22-35 individual optomotor responses (thin grey traces) and their mean (thick trace) of the same tethered fly to 45°/s clockwise and counterclockwise panoramic field rotations (light grey sections), having a full wavelength of 1.16° (left, black) or 14.40° (center, blue), or no-bar (right, orange) stimuli. (B) Every tested fly (n = 9) responded to hyperacute ( $\Delta\phi \sim 4.5^\circ$ ) bar stimuli (1.16° and 2.88°, red; having 0.58° and 1.44° inter-bar-distances, respectively) consistently. (C) Their maximum (peak-to-peak) responses to the hyperacute stimuli and the no-bar and coarse-bar controls. (D) The relative response strength to the hyperacute stimuli varied between 30-80% of the maximum responses to the coarse-bar stimulus.

1 **Video 1: Using a *Drosophila*'s saccadic walk to extrapolate light input to its photoreceptors from**  
2 **natural scenes**

3 A published recording of a fly's saccadic walk (Geurten *et al.*, 2014) was used to sample light  
4 intensity values from 360° panoramic images of natural scenes. We collected three types of light  
5 stimuli, resulting from: (a) saccadic, (b) median (linear) and (c) shuffled velocities of the walk.  
6

7 **Video 2: *Drosophila* R1-R8s in dissociated ommatidia contract photomechanically**

8 Wild-type and *trp/trpl*-mutant R1-R8 photoreceptors contract photomechanically to light flashes. The  
9 panels show: top, a sideview of *ex vivo* wild-type R1-R8 photoreceptors of a single dissociated  
10 ommatidium contracting to 1 ms bright light flash; bottom left, R1-R8 of a *trp/trpl* null-mutant, which  
11 express normal phototransduction reactants but lack completely their light-gated ion channels,  
12 contracting to a similar flash. Notably, *trp/trpl* photoreceptors cannot generate electrical responses to  
13 light, with their eyes showing no ERG signal (**Appendix 7**). Nonetheless, *trp/trpl*-mutant  
14 photoreceptors contract photomechanically (but require ~5 min dark-adaptation between flashes to  
15 restore their contractility). These observations are consistent with the hypothesis of the light-induced  
16 phosphatidylinositol 4,5-bisphosphate (PIP<sub>2</sub>) cleaving from the microvillar photoreceptor plasma  
17 membrane causing the rhabdomere contractions (Hardie & Franze, 2012). Video playback slowed  
18 down and down-sampled to reveal the contractions, which otherwise would be too fast to see with a  
19 naked eye. Each video clip is repeated three times with a running timer giving the time course of the  
20 contractions. Notice that the longitudinal contractions reduce the photoreceptor length. Thus, in an  
21 intact compound eye, the rhabdomeres would move inwards, away from the lens, likely narrowing  
22 their receptive fields (see **Appendix 7**, **Appendix figure 39** and **Appendix 8**, **Appendix figure 44**).  
23

24 **Video 3: *Drosophila* R1-R8 photoreceptors contract photomechanically *in vivo*, moving back-to-**  
25 **front inside each observed ommatidium**

26 We utilized the optical cornea-neutralization technique with antidromic deep-red (740 or 785 nm  
27 peak) illumination to observe deep pseudopupils (photoreceptor rhabdomeres that align with the  
28 observer's viewing axis) in the *Drosophila* eye. High-speed video captures fast rhabdomere  
29 movements to bright orthodromic blue-green flashes (470 + 535 nm peaks). The panels show: left,  
30 R1-R7 photoreceptor rhabdomere tips moving rapidly back-to-front and returning slower to each 10  
31 ms flash, delivered repeatedly every second; right, the cross-correlated horizontal (blue) and vertical  
32 (red) components as the time series of this movement. Grey vertical lines indicate each flash. The  
33 rhabdomere movement is caused by the photomechanical photoreceptor contractions (not by muscle  
34 activity). These *in vivo* movements are large, here 1.7 μm from dark-adapted rest-state; causing up to  
35 5 degree transient shift in the R1-R6 photoreceptors receptive fields (**Appendix 7**). Note average  
36 diameter of R1-R6 rhabdomeres is 1.7 μm (**Appendix 5**). The high-speed video rate was 500  
37 frames/s. Video playback slowed down and down-sampled to reveal the contractions, which otherwise  
38 would be too fast to see with a naked eye.  
39

40 **Video 4: While R1-R8s contract, the lens above is immobile but a cone-cell aperture, connected**  
41 **to the rhabdomere tips by adherens junctions, moves half as much as the rhabdomeres**

42 We used a z-axis micromanipulator to shift and reposition *Drosophila* in piezo-steps vertically  
43 underneath the microscope. This allowed the focused image, as projected on the camera, to scan  
44 through each studied ommatidium, providing exact depth readings in μm. We then recorded any  
45 structural movements inside the ommatidia to light flashes at different depths; from the corneal lens  
46 down to the narrow base, where the cone and pigment cells form an intersection between the  
47 crystalline cone and the rhabdomere. The left panels show: up, ommatidium lens; middle, basal  
48 cone/pigment cell layer; down, R1-R7 photoreceptor rhabdomeres tips during and after flash  
49 stimulation. The right panels show the cross-correlation time series of these high-speed videos: up, the  
50 corneal lens and the upper ommatidium structures were essentially immobile, and normally remained  
51 so throughout the recordings; Middle, cone cells that connect to the rhabdomere tips with adherens  
52 junctions (Tepass & Harris, 2007) showed clear light-induced movements; down, R1-R7 rhabdomeres  
53 moved half as much as the cone cells above. The high-speed video rate was 500 frames/s. Video  
54 playback slowed down and down-sampled to reveal the contractions, which otherwise would be too  
55 fast to see with a naked eye.

## Appendixes 1-10

1		
2		
3	<b>Table of Contents</b>	Pages: 34-36
4		
5	<b>Appendix 1: ‘Stochastic adaptive visual information sampling’-theory in brief</b>	(37-39)
6	<b>Overview</b>	37
7	<b>Stochastic adaptive sampling of information by R1-R6 photoreceptors</b>	37
8	<b>Main framework</b>	38
9	<b>Stochastic quantal models supersede empirical black-box approaches</b>	38
10	<i>Stochastic photon sampling fly photoreceptor model</i>	38
11	<i>Deterministic empirical fly photoreceptor models</i>	39
12		
13	<b>Appendix 2: Information maximization by photomechanical adaptations/connectivity</b>	(40-50)
14	<b>Overview</b>	40
15	<b>Fly photoreceptors’ pupil mechanism</b>	40
16	<b>Photomechanical light-screening hypothesis</b>	41
17	<b>Hypothesis testing and verification</b>	42
18	<b>New insight into maximal encoding of different stimulus statistics</b>	43
19	<i>Bursts</i>	43
20	<i>Gaussian white noise</i>	44
21	<b>Simulations’ maximal information transfer largely match those of recordings</b>	45
22	<b>Each R1-R6 receives different amounts of information from the network</b>	46
23	<b>Variable sampling matrix protects from aliasing, improving vision</b>	47
24	<b>Estimating a R1-R6’s encoding efficiency</b>	49
25		
26	<b>Appendix 3: Similarities and differences in encoding bursts and other stimuli</b>	(51-56)
27	<b>Overview</b>	51
28	<b>Why do bursty responses carry the most information?</b>	51
29	<b>Relevance of bursty responses for seeing better</b>	51
30	<b>Light intensity time series based on a <i>Drosophila</i>’s walk</b>	52
31	<b>Light intensity time series analyses – differential histograms</b>	53
32	<b>Selecting the stimulus patterns and their playback velocity</b>	54
33		
34	<b>Appendix 4: Spatial resolution (visual acuity) of the fly eye (conventional measure)</b>	(57-68)
35	<b>Overview</b>	57
36	<b>Optical limits of the fly compound eyes’ visual acuity</b>	57
37	<b>Rationale for investigating wild-type and <i>hdc</i> mutant R1-R6s’ receptive fields</b>	58
38	<b>Measurement and calculation of a photoreceptor’s receptive field</b>	59
39	<i>Method 1</i>	59
40	<i>Method 2</i>	60
41	<i>Method 3</i>	60
42	<i>25 LED light-point array and LED pads</i>	61
43	<i>Pseudo-random receptive field scans</i>	63
44	<i>Gaussian White-noise (GWN) stimuli</i>	64
45	<b>Receptive fields of dark-adapted photoreceptors</b>	64
46	<b>Receptive fields of light-adapted photoreceptors</b>	64
47	<b>R1-R6 acceptance angles are broader than the theoretical prediction</b>	65
48	<b>Slow <i>Drosophila</i> retina movements</b>	66
49	<b>Conclusions</b>	67
50		
51	<b>Appendix 5: R1-R6 rhabdomere sizes, neural superposition and hyperacuity schemes</b>	(69-74)
52	<b>Overview</b>	69
53	<b>Readjusting the current theoretical viewpoint</b>	69
54	<b>Electron micrographs</b>	69
55	<i>Fixation</i>	69

1	<i>Sectioning and staining</i>	70
2	<i>Rhabdomere measurements</i>	70
3	<b>R1-R6 rhabdomere sizes differ</b>	71
4	<b>Theoretical models for spatial hyperacuity</b>	72
5	<b>Possible dynamics arising from connectivity and variable rhabdomere sizes</b>	74
6		
7	<b>Appendix 6: Neural images of moving objects (recordings vs. classic predictions)</b>	(75-89)
8	<b>Overview</b>	75
9	<b>Retinal limitations and capacity to resolve moving objects</b>	75
10	<b>Moving visual stimuli</b>	76
11	<b>Gaussian white-noise (GWN) stimuli</b>	77
12	<b>Volterra series model of each tested <i>Drosophila</i> R1-R6</b>	77
13	<b>Conventional simulation of intracellular responses to object motion</b>	78
14	<b>Maximal responses to moving dots lag behind their actual positions</b>	79
15	<b>Response rise and decay to object motion show directional selectivity</b>	82
16	<b>Classic theory greatly overestimates motion blur in R1-R6 output</b>	84
17	<b>Modeling R1-R6 output by the Volterra series method</b>	86
18	<b>Classic theory underestimates how well R1-R6s resolve fast moving dots</b>	88
19	<b>Conclusions</b>	89
20		
21	<b>Appendix 7: Photomechanical microsaccades move photoreceptors' receptive fields</b>	(90-102)
22	<b>Overview</b>	90
23	<b>Rapid adaptation caused by light-induced R1-R8 contractions</b>	91
24	<b>High-speed video recordings of light-induced rhabdomere movements</b>	91
25	<b>Imaging setup for recording photomechanical rhabdomere contractions</b>	91
26	<b>Recording procedures</b>	93
27	<b>Key observations from unprocessed high-speed footage</b>	93
28	<b>Image analysis</b>	94
29	<b>Quantifying rhabdomere travels and their receptive field shifts</b>	94
30	<b><i>Trp/trpl</i>-mutants confirm the contractions' photomechanical origin</b>	95
31	<b>When rhabdomeres move, the ommatidium lens system above stays still</b>	96
32	<b>Light intensity-dependence of rhabdomere movements (<i>in vivo</i> dynamics)</b>	97
33	<b>Estimating light intensity falling upon the rhabdomeres</b>	99
34	<b><i>In vitro</i> rhabdomere movements</b>	99
35	<b>Photomechanical rhabdomere movements vs. R1-R6s' voltage responses</b>	99
36	<b>Light-adapted rhabdomere motion reflects rhodopsin/meta-rhodopsin balance</b>	101
37	<b>Rhabdomere contractions resensitise refractory sampling units</b>	102
38		
39	<b>Appendix 8: Microsaccadic sampling hypothesis for resolving fast-moving objects</b>	(103-114)
40	<b>Overview</b>	103
41	<b>Modeling a R1-R6's receptive field dynamics to moving dots</b>	103
42	<b>A. Stationary rhabdomere model (receptive field is fixed)</b>	103
43	<b>B. Photomechanical rhabdomere model (receptive field moves)</b>	105
44	<b>C. Photomechanical rhabdomere model (receptive field moves &amp; narrows)</b>	106
45	<b>What could cause the receptive field narrowing during moving light stimuli?</b>	108
46	<b>Specific predictions of our new hypothesis and their experimental validations</b>	108
47	<b>Photoreceptors resolve moving object up to high body-saccadic speeds</b>	110
48	<b>Prediction that R1-R6s encode hyperacute images in space-time</b>	111
49	<b>Refractory sampling improves hyperacute motion vision</b>	112
50	<b>Horizontal vs. vertical motion hyperacuity</b>	113
51	<b>Mirror symmetric contractions may improve rotatory motion detection</b>	113
52		
53	<b>Appendix 9: Microsaccadic rhabdomere movements &amp; R1-R6s' information capture</b>	(115-118)
54	<b>Overview</b>	115
55	<b>Microsaccades accentuate high-freq resolution but generate low-freq noise</b>	115

1	<b>Are saccades and fixations optimized to microsaccadic sampling?</b>	116
2	<b>Microsaccadic sampling of bright or dark moving point-objects</b>	117
3	<b>Microsaccadic sampling hypothesis and efficient coding</b>	118
4		
5	<b>Appendix 10: <i>Drosophila</i> behavior confirms hyperacute vision</b>	(119-121)
6	<b>Overview</b>	119
7	<b>Testing <i>Drosophila</i> visual behavior in flight simulator system</b>	119
8	<b>Open-loop experiments</b>	119
9	<i>Quantifying optomotor behavior</i>	120
10	<b>Why did the previous behavioral studies not find hyperacute vision?</b>	120
11		
12	<b>References</b>	(124-132)
13		

---

## Appendix 1: ‘Stochastic adaptive visual information sampling’-theory in brief

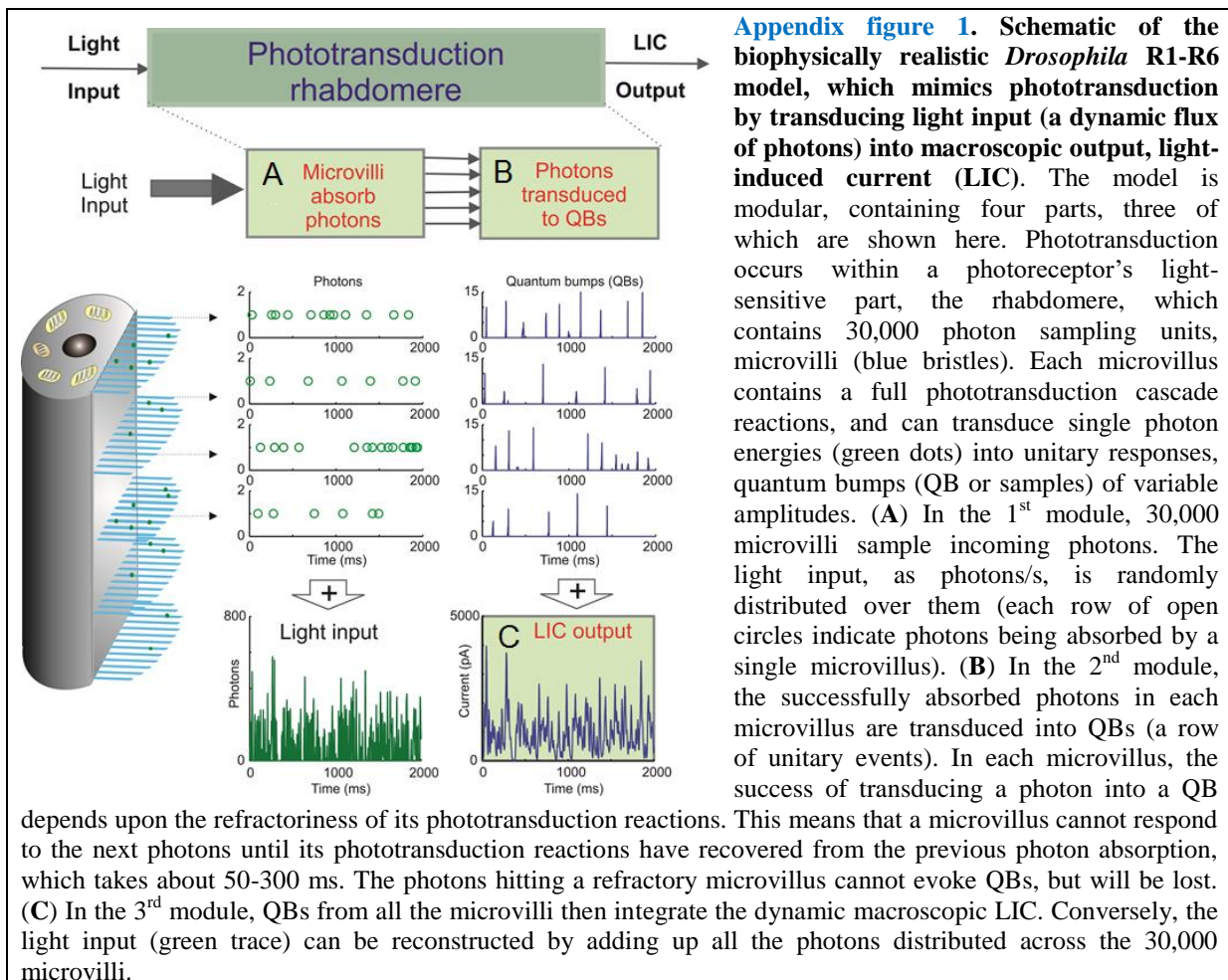
### Overview

This appendix describes the basic theoretical principles of how fly photoreceptors sample photons, providing central background information for the results presented in the main paper.

### Stochastic adaptive sampling of information by R1-R6 photoreceptors

Many lines of evidence imply that in a *Drosophila* R1-R6 photoreceptor 30,000 individual refractory sampling units (microvilli) integrate exponential photon flux changes ( $\sim 10^6$ -fold) from the environment into macroscopic voltage responses of biophysically limited amplitude range ( $\sim 60$  mV) and bandwidth ( $\sim 200$  Hz) (Juusola & Hardie, 2001a; Song *et al.*, 2012; Song & Juusola, 2014; Hardie & Juusola, 2015). In essence, a light-adapted R1-R6 counts photons imperfectly, which, nonetheless, adds up highly reproducible neural representations of light changes within its receptive field (Juusola *et al.*, 2015).

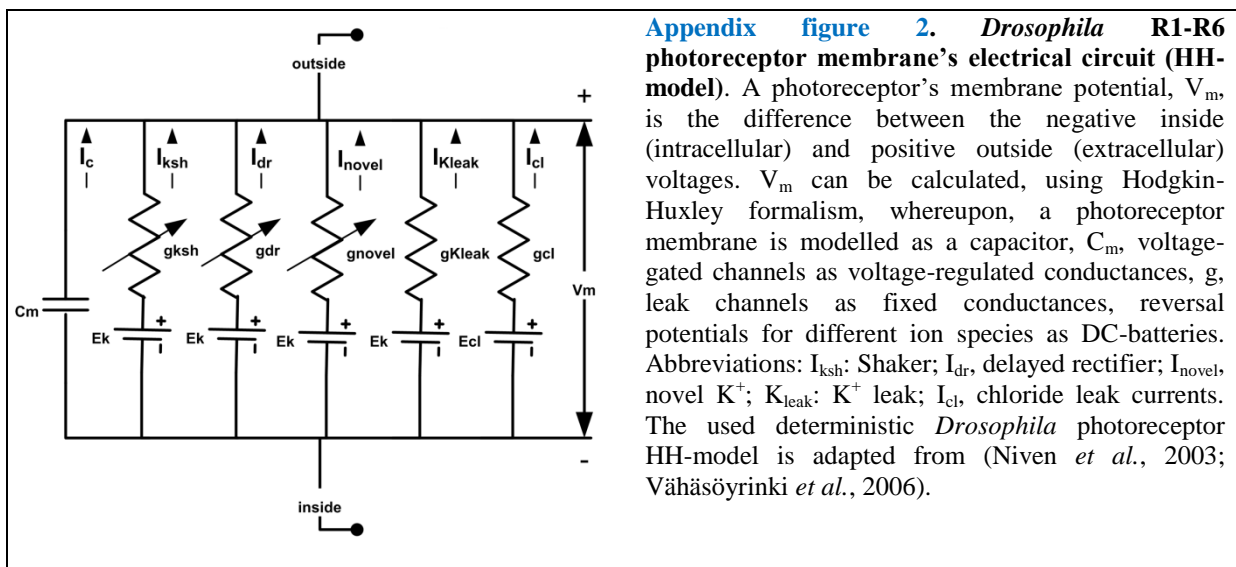
In this study, we quantify such quantal information processing through large-scale experimental and theoretical analyses. Our overriding aim is to analyze R1-R6s’ diurnal encoding range systematically; from light bursts to Gaussian white-noise stimulation to point-objects moving across their receptive fields at saccadic speeds. Because of the outstanding stability and signal-to-noise ratio of the intracellular recordings from *in vivo* R1-R6s (Juusola & Hardie, 2001a; Zheng *et al.*, 2006; Song & Juusola, 2014; Juusola *et al.*, 2016), providing apparent ergodicity, we can directly compare their voltage responses to those of biophysically realistic R1-R6 model simulations (Song *et al.*, 2012; Song & Juusola, 2014; Juusola *et al.*, 2015; Song *et al.*, 2016), in which stochastically operating microvilli sampled similar stimuli (Appendix figure 1). The mechanistic knowledge so obtained about the dynamics and limitations of quantal visual information processing provides us with deep new understanding of how well *Drosophila*, and other insect eyes, can see the world.



## 1 Main framework

2 We used our previously published biophysical *Drosophila* R1-R6 model (Song *et al.*, 2012; Song &  
3 Juusola, 2014; Juusola *et al.*, 2015; Song *et al.*, 2016) to simulate voltage responses to time series of  
4 light intensities. The model contains four modules (Song *et al.*, 2012; Song & Juusola, 2014; Juusola  
5 *et al.*, 2015; Song *et al.*, 2016):

- 6 • *Random Photon Absorption Model*: regulates photon hits (absorptions) in each microvillus,  
7 following Poisson statistics (Song *et al.*, 2016) (**Appendix figure 1A**).
- 8 • *Stochastic Bump Model*: stochastic biochemical reactions inside a microvillus capture and  
9 transduce the energy of photons to variable quantum bumps or failures (**Appendix figure**  
10 **1B**). Here, Gillespie algorithm provides discrete and stochastic phototransduction cascade  
11 simulations with few reactants as every reaction is explicitly simulated.
- 12 • *Summation Model*: bumps from 30,000 microvilli integrate to the macroscopic light-induced  
13 current (LIC) response (**Appendix figure 1C**).
- 14 • *Hodgkin-Huxley (HH) Model of the photoreceptor plasma membrane* (Niven *et al.*, 2003;  
15 Vähäsöyrinki *et al.*, 2006): transduces LIC into a voltage response (**Appendix figure 2**).



**Appendix figure 2. *Drosophila* R1-R6 photoreceptor membrane's electrical circuit (HH-model).** A photoreceptor's membrane potential,  $V_m$ , is the difference between the negative inside (intracellular) and positive outside (extracellular) voltages.  $V_m$  can be calculated, using Hodgkin-Huxley formalism, whereupon, a photoreceptor membrane is modelled as a capacitor,  $C_m$ , voltage-gated channels as voltage-regulated conductances,  $g$ , leak channels as fixed conductances, reversal potentials for different ion species as DC-batteries. Abbreviations:  $I_{ksh}$ : Shaker;  $I_{dr}$ , delayed rectifier;  $I_{novel}$ , novel  $K^+$ ;  $K_{leak}$ :  $K^+$  leak;  $I_{cl}$ , chloride leak currents. The used deterministic *Drosophila* photoreceptor HH-model is adapted from (Niven *et al.*, 2003; Vähäsöyrinki *et al.*, 2006).

17 The formalism, assumptions and many tests of the biophysical photoreceptor model, which  
18 has no free parameters, are given in our previous publications (Song *et al.*, 2012; Song & Juusola,  
19 2014; Juusola *et al.*, 2015). All its parameter values can be found and downloaded from:  
20 <http://www.sciencedirect.com/science/article/pii/S0960982212006343>  
21

## 23 Stochastic quantal models supersede empirical black-box approaches

### 24 *Stochastic photon sampling fly photoreceptor model:*

- 25 • Has no free parameters
- 26 • Is general - predicts realistic responses to any light stimulus pattern
- 27 • Is transferable - predicts realistic responses of different fly photoreceptors
- 28 • Provides deep mechanistic understanding to light information sampling

29 We have shown before that this quantal stochastic modeling approach is general and transferable, and  
30 therefore directly applicable to quantify photoreceptor functions in different light conditions and fly  
31 species (Song *et al.*, 2012; Song & Juusola, 2014; Juusola *et al.*, 2015). Importantly, it does not  
32 require full knowledge of all molecular players and dynamics in the phototransduction to generate  
33 realistic responses (Song *et al.*, 2012; Song & Juusola, 2014; Juusola *et al.*, 2015). From a  
34 computational viewpoint, the exactness of the simulated molecular interactions is not critical. As long  
35 as the photoreceptor model contains the right number of microvilli (*e.g.* 30,000 in a *Drosophila* and  
36 90,000 in a *Calliphora* R1-R6 photoreceptor), each of which is a semiautonomous photon sampling  
37 unit, and the dynamics of their photon-triggered unitary responses (quantum bumps [QB] or samples)

1 approximate those in the real recordings, it will sample and process information much like a real  
2 photoreceptor. Conversely, this further means that by knowing the number of microvilli and their  
3 average QB waveform, latency distribution, and refractory period distributions, we can closely predict  
4 a fly photoreceptor's macroscopic response to any given light intensity time series stimulus (*cf.*  
5 **Figures 3-4**). The same model can then be applied to estimate how well the real photoreceptor output  
6 resolves moving objects (see **Figures 8G-I** and **9**; **Appendix 8** gives the details of this approach).

7  
8 ***Deterministic empirical fly photoreceptor models:***

- 9 • Fit parameters to specific stimulus sets
- 10 • predict less accurately responses to new stimuli of different input statistics (to which the  
11 models have not been tuned to before)
- 12 • Cannot provide deep mechanistic understanding of how photoreceptors sample light  
13 information

14 In the conventional empirical “black-box” approaches, the photoreceptor models’ filters, such as  
15 linear and nonlinear kernels, and static nonlinearities are adjusted to minimize the difference between  
16 the recorded responses and the model output to a specific stimulus set (light condition) (French *et al.*,  
17 1993; Juusola *et al.*, 1995b; Juusola & French, 1997; Friederich *et al.*, 2009). However, because such  
18 *models are not built upon the real cells’ physical quantal information sampling constraints*, which  
19 change from one stimulus statistics to another (Song & Juusola, 2014), they struggle to respond  
20 accurately to new stimulus statistics. Explicitly, the models lack intrinsic structural information of  
21 how quantum bump dynamics and microvilli refractoriness must differ during different stimuli. For  
22 example, Volterra (French *et al.*, 1993) kernels estimated for Gaussian white-noise stimulation will  
23 predict less accurately responses to bursty light inputs. This is because during bursty light stimulation  
24 the fly photoreceptors’ quantal information sampling dynamics rapidly adapt to a different regime,  
25 where their microvilli (sampling units) are less refractory. Hence, the real photoreceptors now  
26 integrate macroscopic responses from larger sample (QB) rate changes of enhanced rise and decay  
27 dynamics. To appropriately approximate these new dynamics, the empirical models would need to  
28 generate new kernels of different temporal profiles, which is impossible without retuning the model  
29 parameters. Accordingly, without the biophysical knowledge being implemented in their  
30 mathematical structure, the classic dynamic photoreceptor models fail to predict how well the real  
31 photoreceptors resolve moving objects (see **Figure 7**, **Appendix 6** and **Appendix 8**).

## 1 **Appendix 2: Information maximization by photomechanical adaptations and connectivity**

### 3 **Overview**

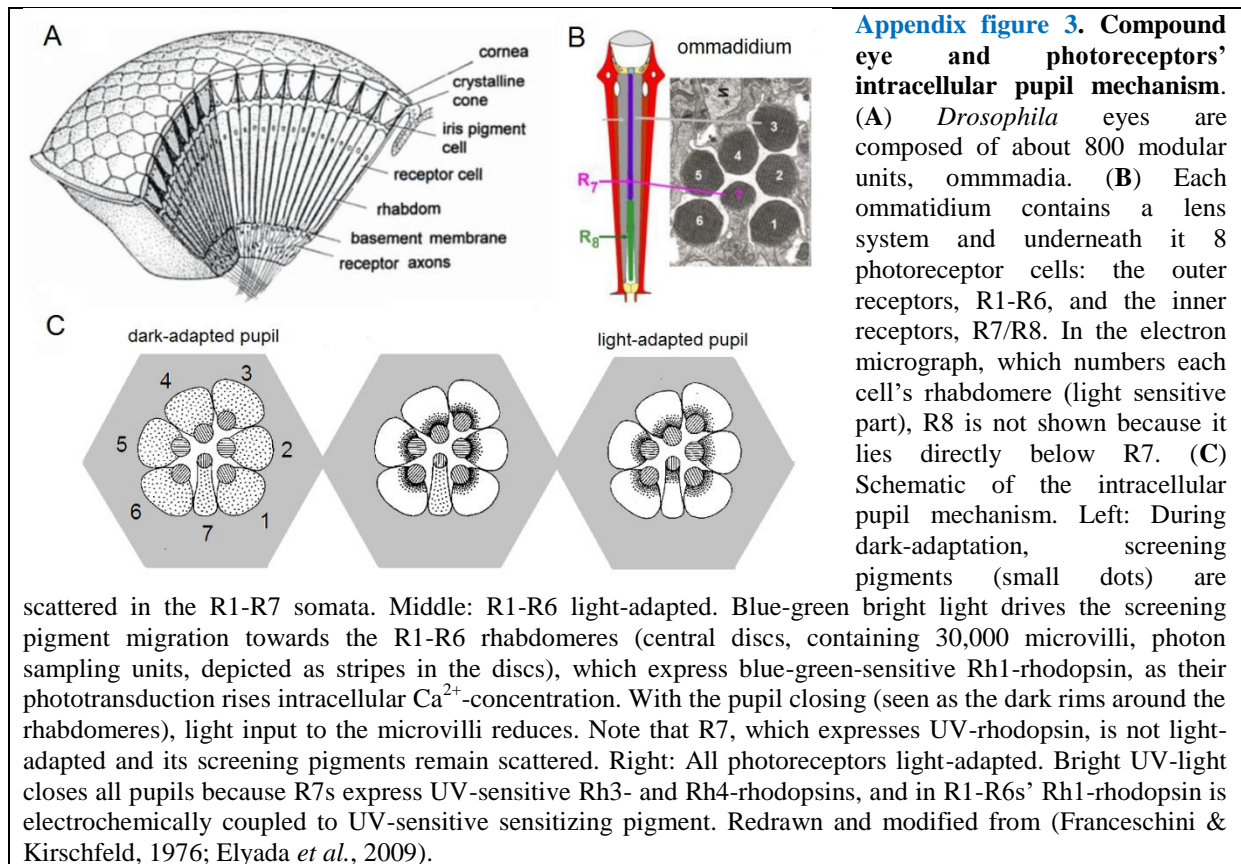
4 This appendix describes how the ‘stochastic adaptive visual information sampling’-theory (**Appendix**  
5 **1**) predicts and explains the roles of R1-R6 photoreceptors’ photomechanical adaptations and network  
6 connections in information maximization at different stimulus conditions, as shown in **Figures 1-4**.

7  
8 In this appendix:

- 9 • We test the hypotheses that photomechanical adaptations (intracellular pupil and rhabdomere  
10 contractions; see **Appendix 7**) and network connections in the *Drosophila* eye contribute  
11 importantly to optimizing the capture and representation of visual information.
- 12 • We first estimate through simulations how a R1-R6 photoreceptor’s intracellular pupil and  
13 rhabdomere contractions are jointly optimized for maximal information sampling by its  
14 30,000 microvilli. The simulations predict that these mechanisms’ optimal combined photon  
15 throughput in bright conditions (to be absorbed by an average R1-R6 photoreceptor) should  
16 be different for different stimuli.
- 17 • We then compare the model predictions to corresponding intracellular recordings and find a  
18 comprehensive agreement between the theory and mean experiments for all the tested stimuli.
- 19 • This striking correspondence enables us to further estimate how the lamina network shapes  
20 information transfer of individual R1-R6 photoreceptors.
- 21 • Remarkably, our data and analyses strongly suggest that voltage output is different in each  
22 R1-R6, which are brought together in neural superposition during development to sample  
23 light changes from a small local visual area.
- 24 • These results are consistent with the hypothesis that the variability in the retinal sampling  
25 matrix dynamics and topology minimizes aliasing and noise, enabling its parallel processing  
26 to generate reliable and maximally informative neural estimates of the variable world  
27 (Barlow, 1961; Yellott, 1982; Song & Juusola, 2014; Juusola *et al.*, 2015).
- 28 • Finally, we explain how to calculate a photoreceptor’s encoding efficiency for different light  
29 stimuli, highlighting the assumptions and limits of this method.

### 31 **Fly photoreceptors’ pupil mechanism**

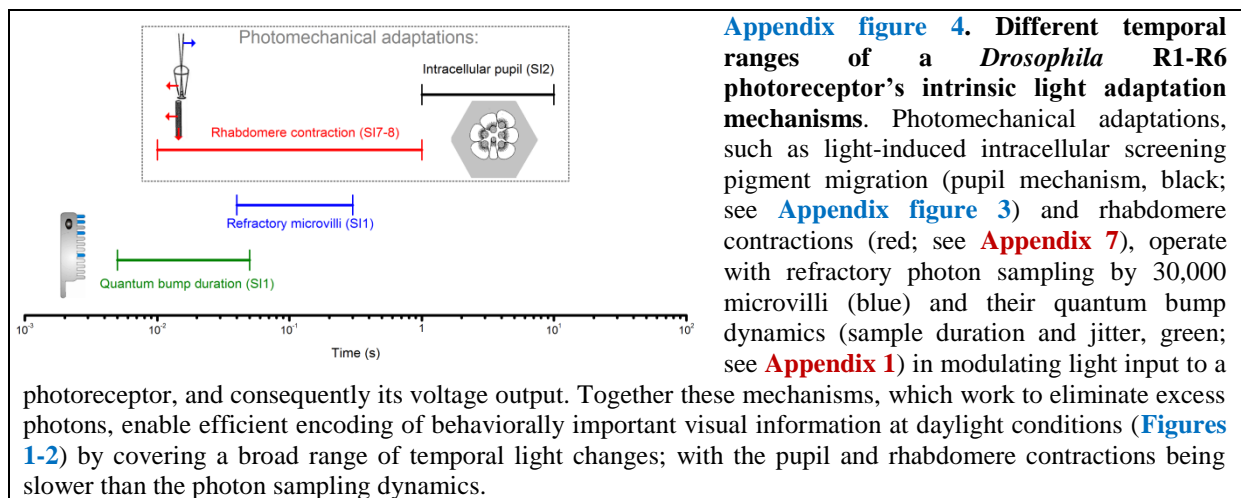
32 In a fly photoreceptor, intracellular screening pigments form its pupil mechanism (**Appendix figure**  
33 **3**). The pupil protects a photoreceptor’s sampling units (30,000 microvilli in a *Drosophila* R1-R6)  
34 from saturation (Howard *et al.*, 1987; Song & Juusola, 2014). At bright light exposure, screening  
35 pigments migrate to narrow the aperture they form collectively (Franceschini & Kirschfeld, 1971b),  
36 shielding off excess light from reaching the microvilli. This is important because midday sunshine on  
37 a photoreceptor may contain  $10^{6-8}$  photons/s, and without the pupil mechanism would deteriorate the  
38 encoding function of its finite microvillus population (Howard *et al.*, 1987; Song & Juusola, 2014).  
39 The pupil opening and closing seem modulated by light-driven intracellular  $Ca^{2+}$ -concentration  
40 changes (Hofstee & Stavenga, 1996), and show reasonably fast dynamics (from fully open to fully  
41 closed within 15 s) (Franceschini & Kirschfeld, 1976) for adapting its light throughput to ambient  
42 changes. Although our biophysical (stochastically operating) *Drosophila* photoreceptor model (Song  
43 *et al.*, 2012; Juusola *et al.*, 2015) lacks the pupil mechanism and any other photomechanical  
44 adaptations (*cf.* **Appendix 7**), their joint effects can be predicted through simulations; by assuming  
45 that their objective function is to maximize the photoreceptor’s information capture.



1  
2  
3  
4  
5  
6  
7  
8  
9  
10  
11

### Photomechanical light-screening hypothesis

We hypothesize that the intracellular pupil, besides affecting a photoreceptor's angular and spectral sensitivity (Stavenga, 2004a) (see **Appendix 4**), participates in maximizing a photoreceptor's information sampling by optimizing light input intensity to its microvilli in time. Specifically in this context, it works together with all other photomechanical adaptations within an ommatidium, including the much faster light-induced rhabdomere contractions (**Videos 2-4**), in protecting the microvilli from saturation. Thus, collectively, we consider the photomechanical adaptations (**Appendix figure 4**) as a biological manifestation of a mathematical information maximization function.



12  
13  
14  
15

To function optimally, the photomechanical adaptations need to regulate **input from** the ambient illumination so that the temporal light changes they let through would cause maximal sample (quantum bump) rate changes (Song & Juusola, 2014). The higher the photoreceptor's sample rate

1 changes, the higher its rate of information transfer (Song & Juusola, 2014). Too bright light would  
2 saturate microvilli because most of them would be rendered refractory, reducing their dynamic sample  
3 counts. Conversely, too dim light would not utilize microvilli population fully, producing low  
4 (suboptimal) sample counts. Therefore, the optimal light intensity throughput for maximum  
5 information capture is somewhere between. This value is expected to depend upon five factors:

- 6 • Light intensity time series structure (we consider all the 20 light patterns tested in **Figure 1B**)
- 7 • Number of microvilli (~30,000 in a R1-R6 *Drosophila* photoreceptor)
- 8 • Refractory period distribution of the microvilli (full range: 50-500 ms in a R1-R6 *Drosophila*  
9 photoreceptor)
- 10 • Quantum bump waveform (sample duration)
- 11 • Quantum bump latency distribution (“sample jitter”)

12 Detailed tests and descriptions of why and how these factors contribute to encoding in fly  
13 photoreceptors are given in our previous publications (Juusola *et al.*, 1994; Henderson *et al.*, 2000;  
14 Juusola & Hardie, 2001b, a; Juusola & de Polavieja, 2003; Song *et al.*, 2012; Song & Juusola, 2014;  
15 Juusola *et al.*, 2015).

### 16 **Hypothesis testing and verification**

17 To test the photomechanical light-screening hypothesis, we simulated voltage responses to 20  
18 different light patterns (**Figure 1B**) at 15 different light intensity (or brightness) levels, which ranged  
19 from  $5 \times 10^4$  to  $1 \times 10^6$  photons/s (5, 6, ...,  $9 \times 10^4$ ; 1, 2, ...,  $9 \times 10^5$ ;  $1 \times 10^6$ ). In each simulation, the  
20 stochastic photoreceptor model generated 20 independent responses to the given 2-seconds-long  
21 (2,000 points) light pattern of a given intensity, following the published procedures (Song & Juusola,  
22 2014). These 20 responses were used to estimate the model’s rate of information transfer for that  
23 specific stimulus pattern (1/20) at that specific light level (1/15). So all together, we could have  
24 simulated 20 repeated photoreceptor outputs to 300 (20 x 15) different 2,000-points-long stimulus  
25 patterns. But because the model’s maximum information transfer rate estimates turned out to be  
26 relatively straightforward to determine for many light patterns (*cf.* **Appendix figure 5**), the total  
27 number of simulations never reached this limit. Nevertheless, being computationally expensive, the  
28 stochastic simulations took months to complete.

29 Crucially, in all the simulations, the photoreceptor model was exactly the same. Its stochastic  
30 bump production dynamics (waveform, latency and refractory distributions) were governed by light-  
31 adapted values with every single parameter fixed, and these parameter values were unchanged in each  
32 simulation. The supplement of the reference (Song *et al.*, 2012) lists these parameter values, which  
33 were collected from intracellular experiments or logically extrapolated to be biophysically realistic for  
34 light-adapted *Drosophila* photoreceptors. This supplement is downloadable from:

35 <http://www.sciencedirect.com/science/article/pii/S0960982212006343>

36 **Figure 3B** shows the simulated voltage responses (traces above) that carried the maximum  
37 information transfer rates for the 20 tested light patterns (traces below) and the corresponding  
38 intensity levels (as effective photons/s) that evoked them. The simulations match the overall size,  
39 appearance and dynamics of the real recordings astonishingly well (**Figure 1B** and **Figure 1-figure**  
40 **supplement 1B**), indicating that the photoreceptor model, with its photomechanics optimizing light  
41 input intensity, samples and integrates light information much like its real-life counterparts. Notice  
42 that the optimal light intensity is the same for the different bandwidth (20, 50, 100, 200 and 500 Hz)  
43 stimuli within one BG. But for each BG (BG0, BG0.5, BG1 and BG1.5) this optimum is different. For  
44 example, for BG0, which results in bursty (high-contrast) stimulation, the optimal light intensity level  
45 is  $\sim 8 \times 10^5$  photons/s. Whereas for BG1.5 of low contrast Gaussian white-noise stimulation, this is 10-  
46 times lower ( $\sim 8 \times 10^4$  photons/s).

47 We express these intensity levels in units of *effective* photons/s. This is because, theoretically,  
48 we have deduced the mean photon throughput that effectively fluxes into microvilli for a *Drosophila*  
49 photoreceptor to sample the best estimates of the given light stimuli. In other words, if the  
50 photomechanical screening mechanisms set the light input intensity for maximal information capture,  
51 as is our hypothesis, then these light intensity values should also closely approximate the actual  
52 photon absorption changes that drive phototransduction in the real experiments (as recorded  
53 intracellularly from wild-type R1-R6 photoreceptors, which have the normal pupil mechanism and  
54

1 photomechanical rhabdomere contractility; **Figures 1** and **Figure 1-figure supplement 1B**). Note that  
2 as the preceding photomechanical light screening mechanisms eliminate photons, a photoreceptor's  
3 photon absorption rates will always be considerably lower than the photon emission rates from the  
4 light source.

5 Because of the remarkable dynamic correspondence between the experiments (**Figures 1-2**)  
6 and the theory (**Figures 3-4**) over the whole tested encoding space, we now judge that this hypothesis  
7 must be largely true. Importantly, this realization opens up new ways to analyze photoreceptor  
8 function. For example, by making the general assumption that the input - photon absorptions (and  
9 light emission from our LED light source) - follows Poisson statistics, we could further estimate the  
10 lower information transfer rate bound for each tested light intensity pattern (as absorbed by an average  
11 R1-R6 photoreceptor), and consequently the upper bound for the *Drosophila* photoreceptor's  
12 encoding efficiency (e.g. **Figure 2D**, **Figure 2-figure supplement 1D** and **Figure 4D**). More details  
13 about this assumption and the analysis are given at the end of this appendix (**Appendix 2**).  
14

### 15 **New insight into maximal visual encoding of different stimulus statistics**

16 The reasons why and how the optimal light intensity input (that drives a photoreceptor's information  
17 transfer maximally) is different for bursts and Gaussian white-noise stimulation are summarized in  
18 **Appendix figure 5**. Here we assess both cases using data from the stochastic *Drosophila* R1-R6  
19 photoreceptor model simulations, starting with light bursts.  
20

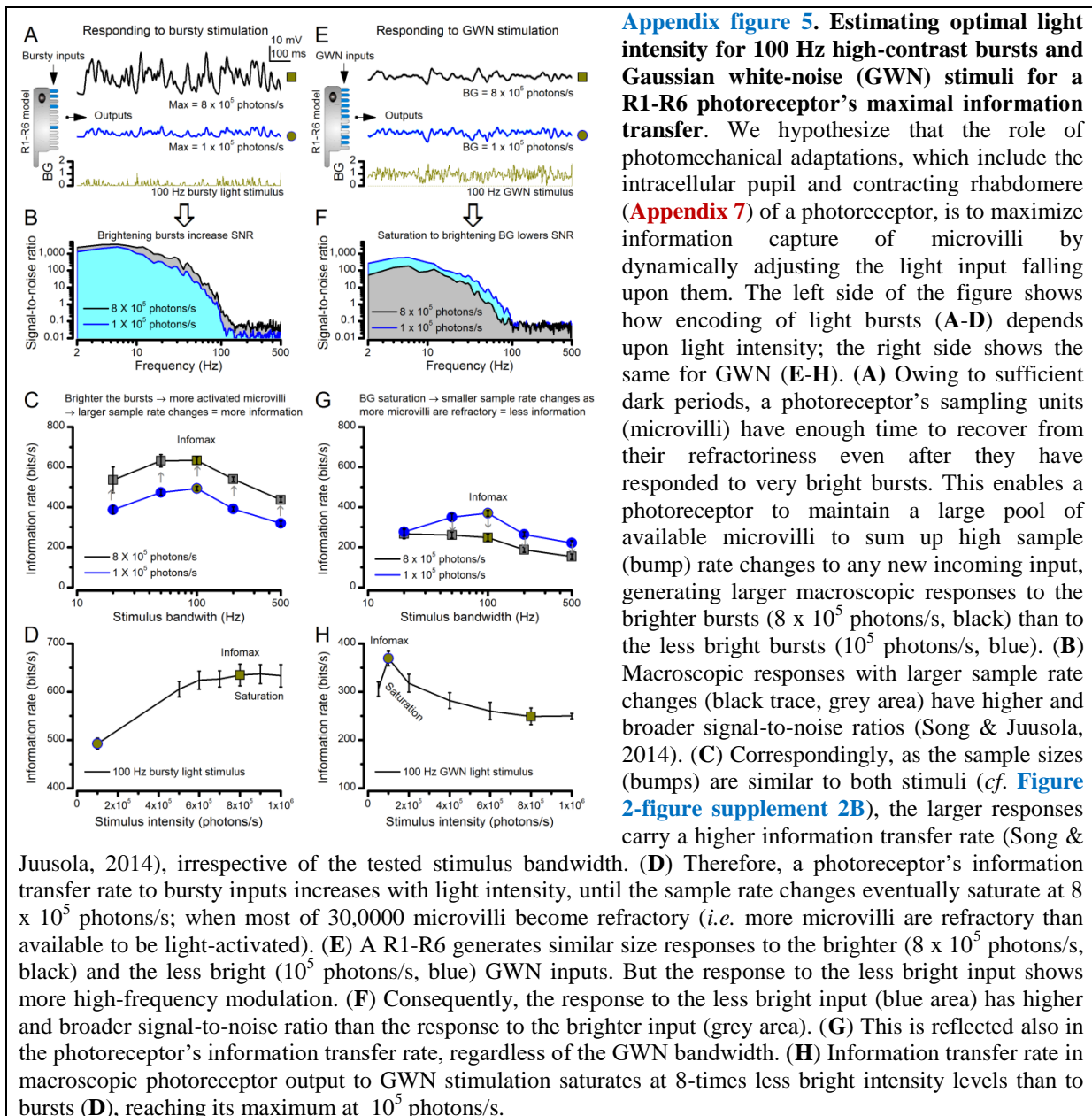
21 **Bursts** (**Appendix figure 5A-D**). These light intensity time series characteristically contain periods of  
22 longer dark contrasts, intertwined with brief and bright contrast events, as shown for 100 Hz  
23 bandwidth stimulation (**Appendix figure 5A**, dark-yellow trace). Based on our previous analyses  
24 (Song & Juusola, 2014), longer dark contrasts help to recover more refractory microvilli than equally-  
25 bright stimuli without these features, improving neural information capture. This makes it more  
26 difficult for bursty stimuli to saturate the photoreceptor output. By increasing the stimulus intensity 8-  
27 fold, here from  $1 \times 10^5$  to  $8 \times 10^5$  effective photons/s, simply evoked larger macroscopic responses.  
28 These, thus, integrated more samples (bumps); as indicated by the larger (black) and smaller (blue)  
29 trace, respectively.

30 Because noise changes little in light-adapted photoreceptor output (Juusola *et al.*, 1994;  
31 Juusola & Hardie, 2001b, a; Song *et al.*, 2012; Song & Juusola, 2014) (**Figure 2-figure supplement**  
32 **2**), the larger responses to brighter bursts have higher and broader signal-to-noise ratio,  $SNR_{output}(F)$ ,  
33 (**Appendix figure 5B**). This, in turn, results in higher information transfer rate estimates,  $R_{output}$   
34 (**Appendix figure 5C**), following Shannon's equation (Shannon, 1948):  
35

$$36 \quad R_{output} = \int_0^{\infty} (\log_2[SNR_{output}(f) + 1]) df \quad (A2.1)$$

37  
38 Note that with 1 kHz sampling rate used in every experiment, this estimation did not integrate  
39 information rate for frequencies from 0 to infinite, but from 2 to 500 Hz instead. However, the limited  
40 bandwidth would not considerably affect estimation results because: (i) high-frequency components  
41 have  $SNR \ll 1$  and therefore contain mostly noise. (ii) Whereas even a high  $SNR_{output}(F)$  contains  
42 little information in its low-frequency components, below 2 Hz. Note also that we have previously  
43 shown the generality of Shannon's information theory for estimating information transfer rates of  
44 continuous (analogue) repetitive responses, irrespective of their statistical structure (Juusola & de  
45 Polavieja, 2003; Song & Juusola, 2014). That is, for sufficient amount of data, Shannon's equation  
46 and triple extrapolation method, which is free of signal and noise additivity and Gaussian distribution  
47 assumptions, give comparable rate estimates. Thus, these estimates should evaluate the simulations'  
48 relative information rate differences truthfully; *i.e.* consistently with only small errors.

49 Markedly, a photoreceptor's performance is systematically better to the brighter bursts (black  
50 line) than to the less bright ones (blue line), irrespective of their bandwidth (**Appendix figure 5C**).  
51 Thus, for the brighter bursts, more microvilli are dynamically activated, generating larger sample rate  
52 changes. These bumps sum up larger (and more accentuated – see (Song & Juusola, 2014))  
53 macroscopic responses, packing in more information than the corresponding responses to the less  
54 bright bursts.



1  
2  
3  
4  
5  
6  
7  
8  
9  
10  
11  
12

However, because a *Drosophila* photoreceptor has a finite amount of microvilli, each of which - once activated by a photon's energy - stays briefly refractory, its sample rate changes and thus signaling performance first increases monotonically until about  $6 \times 10^5$  photons/s, before gradually saturating, and eventually decreasing, with increasing burst brightness (**Appendix figure 5D**). The photoreceptor model's maximum information transfer rate estimate ( $R_{max} = 631 \pm 31$  bits/s; marked by a square) for 100 Hz bright bursts is reached at the optimal stimulus intensity of  $8 \times 10^5$  effective photons/s. In other words, this is the amount light the photomechanical adaptations, including the intracellular pupil mechanism and rhabdomere contractions (see **Appendix 7**), should let through (to be absorbed) in bright daylight for the fly to see bursty real-world events best. The corresponding performance estimate with the less bright bursts ( $10^5$  effective photons/s) is  $493 \pm 12$  bits/s (circle).

13 **Gaussian white noise** (GWN, **Appendix figure 5E-H**). Because GWN lacks long dark contrasts, refractory microvilli have fewer chances to recover (Song & Juusola, 2014). Consequently, photoreceptor output to GWN begins to show signs of saturation at lower light intensity levels. **Appendix figure 5E** shows responses to 100 Hz bandwidth GWN with the mean intensity of  $1 \times 10^5$  (blue) or  $8 \times 10^5$  (black) effective photons/s, respectively. Both responses are about the same size, but

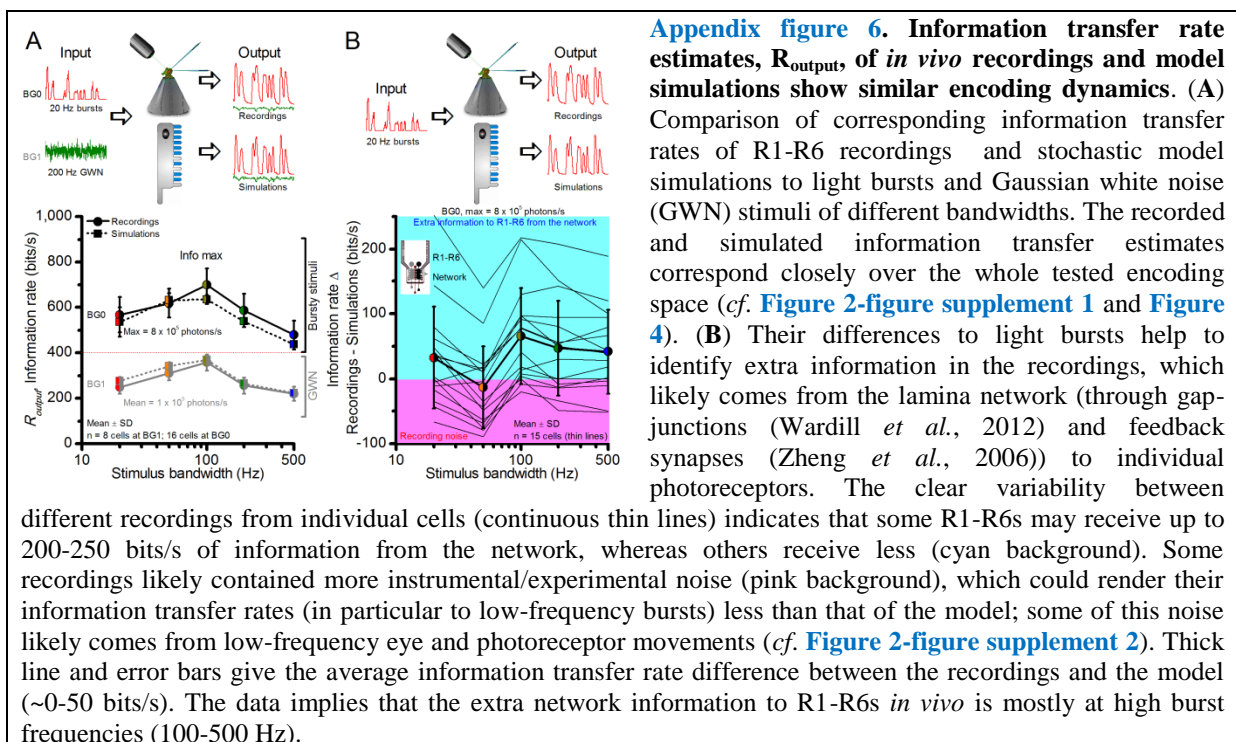
1 the one to the brighter stimulation carries less high-frequency modulation. As more microvilli become  
 2 refractory, smaller sample rate changes (modulation) map light changes into macroscopic responses.  
 3 (How refractoriness dynamically modulates bump counts and macroscopic response waveforms was  
 4 analyzed in detail recently (Song & Juusola, 2014), and thus is not repeated here). Hence, the  
 5 response to the brighter GWN (black/grey) has lower and narrower signal-to-noise ratio (**Appendix**  
 6 **figure 5F**) over the frequency range than the responses to the 8-times less bright GWN (blue).  
 7 Naturally, the same holds true for the photoreceptor's information transfer rate estimates (**Appendix**  
 8 **figure 5G**); the less bright GWN gives consistently a better performance (blue), irrespective of the  
 9 used stimulus bandwidth.

10 Again, the amount of microvilli and their refractoriness curb a photoreceptor's signaling  
 11 performance. But to minimize their impact on encoding GWN, the photomechanical screening needs  
 12 to be more restrictive, letting in less light. With brightening 100 Hz GWN (**Appendix figure 5H**), the  
 13 model's information transfer rate first steeply increases until its peak ( $R_{max} = 369 \pm 15$  bits/s; marked  
 14 by a circle) at  $10^5$  photons/s, and then swiftly declines as progressively more microvilli become  
 15 refractory and fewer samples are being produced. The corresponding transfer rate estimate for  $8 \times 10^5$   
 16 photons/s GWN is  $249 \pm 17$  bits/s (square). Notice, however, that although these results quantify the  
 17 optimal photon absorption rate for generating maximally informative responses to GWN, such  
 18 performance is far from the models' estimated information capacity of 631 bits/s (*cf.* **Appendix**  
 19 **figure 5D** and **Figure 4C**).

### 21 Simulations' maximal information transfer largely match those of recordings

22 We next compare the maximum information transfer rate estimates (squares) of the model simulations  
 23 to those of corresponding *in vivo* recordings (circles) for all BG0 (bursts) and BG1 (GWN) stimuli  
 24 (**Appendix figure 6A**). The simulated performance is very close to the measured mean performance  
 25 for all the tested stimuli, typically falling within the standard deviation of the recordings' information  
 26 transfer.

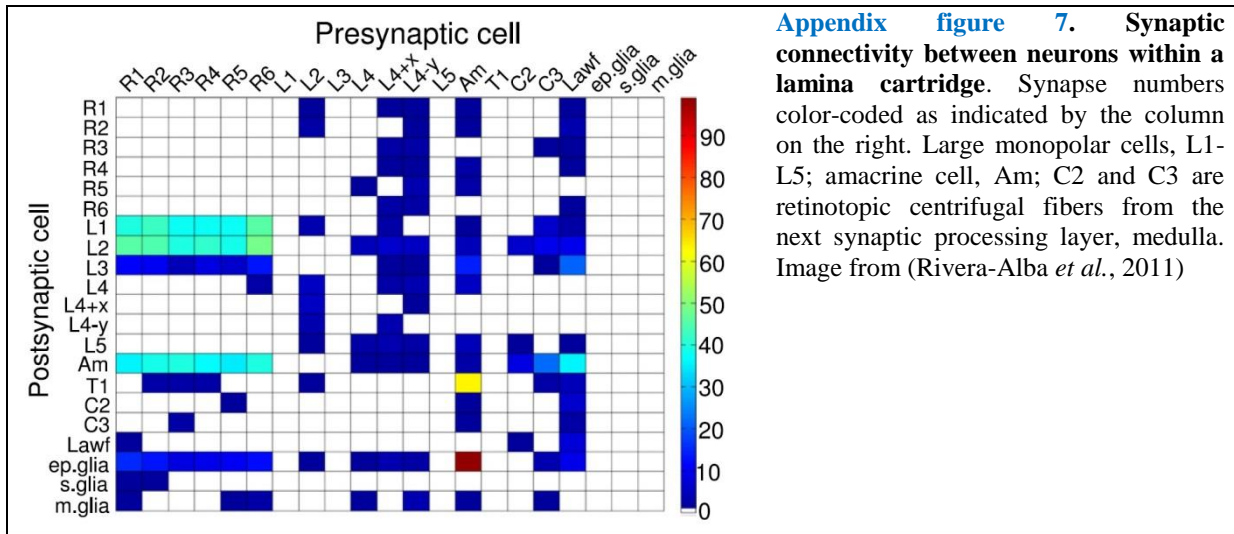
27 In further inspection, two interesting observations can be drawn from this data. First, for the  
 28 GWN stimuli, irrespective of their bandwidth, the maximum information transfer rate estimates of the  
 29 model (dotted line) are just a few bits/s (1-10%) higher than the corresponding mean estimates of the  
 30 real recordings (continuous line). These small differences are probably caused by recording noise.  
 31 Second, the simulations to bursty stimuli carry less information than the corresponding best  
 32 recordings, and the recordings show variations in their information transfer.



1  
2  
3  
4  
5  
6  
7  
8  
9  
10  
11  
12

## Each R1-R6 receives different amounts of information from the network

In [Appendix figure 6B](#), the difference in information rate estimates between the corresponding recordings and simulations to the bursty stimuli is plotted for each complete recording series (thin lines) of individual cells. The thick line gives the mean difference to all these cells' performance. Most noticeably, some photoreceptor cells carry ~100-200 bits/s more information from the bursty stimuli, but many other cells also show information rates that surpass the model's performance (see also [Figure 5](#)). Any information surplus (cyan background) presumably comes from the lamina network (Zheng *et al.*, 2006; Wardill *et al.*, 2012); through gap-junctions and feedback synapses from the cells that sample information from the same small visual area (due to neural superposition (Vigier, 1907b, a; Agi *et al.*, 2014)). The photoreceptor model lacks this network information.



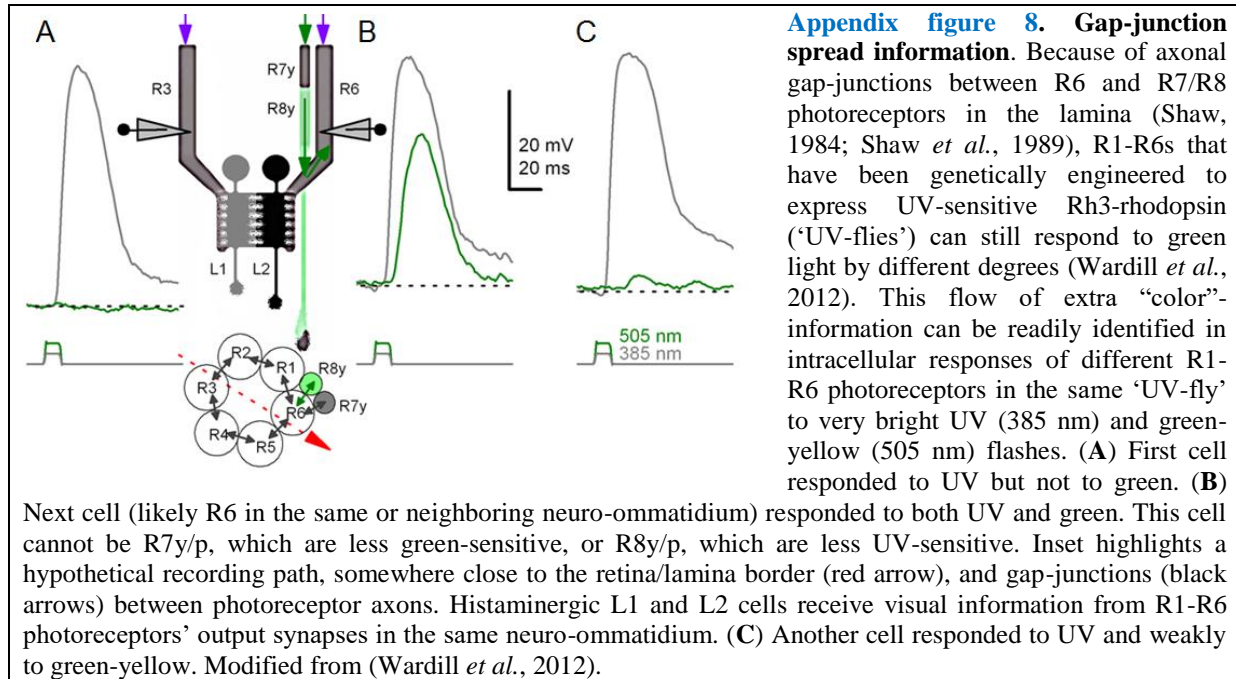
13  
14  
15  
16  
17  
18  
19  
20  
21  
22  
23  
24  
25  
26  
27  
28  
29  
30  
31  
32  
33  
34  
35  
36  
37  
38  
39

In fact, each of the six R1-R6s, which pool their inputs in the same lamina cartridge for feed-forward synaptic transmission, should show different information transfer rates. This is because the lamina connections are asymmetric ([Appendix figure 7](#)). Electron micrographs have shown that R1, R2, R3, R4, R5 and R6 make different amounts of feedback synapses with the lamina interneurons (Meinertzhagen & Oneil, 1991; Rivera-Alba *et al.*, 2011). Most feedbacks are provided by neurons belonging to the L2/L4 circuits (Meinertzhagen & Oneil, 1991; Rivera-Alba *et al.*, 2011). Whilst same-cartridge connections are selectively from L2 to R1 and R2 and from L4 to R5, all R1-R6s receive feedback signals from L4 of neighboring cartridges. There are further connections from Am to R1, R2, R4 and R5, and glia are also synaptically connected to the network (Meinertzhagen & Oneil, 1991; Rivera-Alba *et al.*, 2011), but only R6 makes direct gap-junctions (Shaw *et al.*, 1989) with R7 or R8. These asymmetric functional connections (Zheng *et al.*, 2006) may largely explain the variability in photoreceptor output ([Figure 1-figure supplement 1](#)) and information rates ([Figure 2-figure supplement 1C](#)).

Our recent work (Wardill *et al.*, 2012) further showed that during naturalistic stimulation R6 can receive up to ~200 bits/s of information from R8, as channeled through gap-junctions between these cells. Therefore, we infer here that the recordings with the highest information transfer rates (~850 bits/s) were probably of R6-type, which directly receive extra information from its R8y and R7y neighbors (Shaw, 1984; Shaw *et al.*, 1989; Wardill *et al.*, 2012) ([Appendix figure 8](#)). Conversely, the recordings, in which information rates were lower than those of the simulations ([Appendix figure 6B](#), pink background), carried presumably more recording/experimental noise, with one potential source being minute retinal movements (see [Appendixes 4, 6-9](#)).

Our intracellular recordings establish that during bright light stimulation, the voltage output of an individual photoreceptor is highly repeatable (*cf.* [Figure 1](#)). Consequently, our recording system could be used to study variability among individual R1-R6 photoreceptors of the fly eye. We discovered that for the same stimuli the characteristic output waveforms and frequency distributions of one particular cell are typically different to those of another photoreceptor ([Figure 5-figure](#)

1 **supplement 1**), even when recorded from the neighboring cells in the very same eye (by the same  
2 microelectrode). Because the signal-to-noise ratios of the recordings were very high (**Figure 2**),  
3 sometimes over 6,000, it was evident that the observed cell-to-cell variability had little to do with the  
4 quality of the recordings. Hence, in the *Drosophila* retina, R1-R6s show intercellular variability that is  
5 far greater than the observed small intracellular variability.  
6



7  
8 Collectively, these results strongly suggest that every R1-R6, which is pooled in one lamina  
9 cartridge under the developmental neural superposition principle (Agi *et al.*, 2014) to transmit  
10 information about light changes in a small area of visual space to visual interneurons (L1-L3 and Am)  
11 (Meinertzhagen & Oneil, 1991; Zheng *et al.*, 2006; Zheng *et al.*, 2009; Rivera-Alba *et al.*, 2011), has,  
12 in fact, its own unique output. Besides asymmetric connectivity within a neuro-ommatidium, some of  
13 the observed response variations may also reflect different recording locations. For example,  
14 *Drosophila* R1-R6s in the front of the eye might show different responsiveness to those at the back, as  
15 already shown for localized polarization-sensitivity differences (Wernet *et al.*, 2012). Compound eyes  
16 of many insects exhibit structural adaptations that alter their lens sizes and shapes locally, such as  
17 bright or acute zones for increasing sensitivity or resolution, respectively (Land, 1998). Furthermore,  
18 electrophysiological recordings in some fly species suggest that their photoreceptor output vary across  
19 the eyes and could be tuned to the spatial and temporal characteristics of the light environment  
20 (Hardie, 1985; Laughlin & Weckstrom, 1993; Burton *et al.*, 2001).

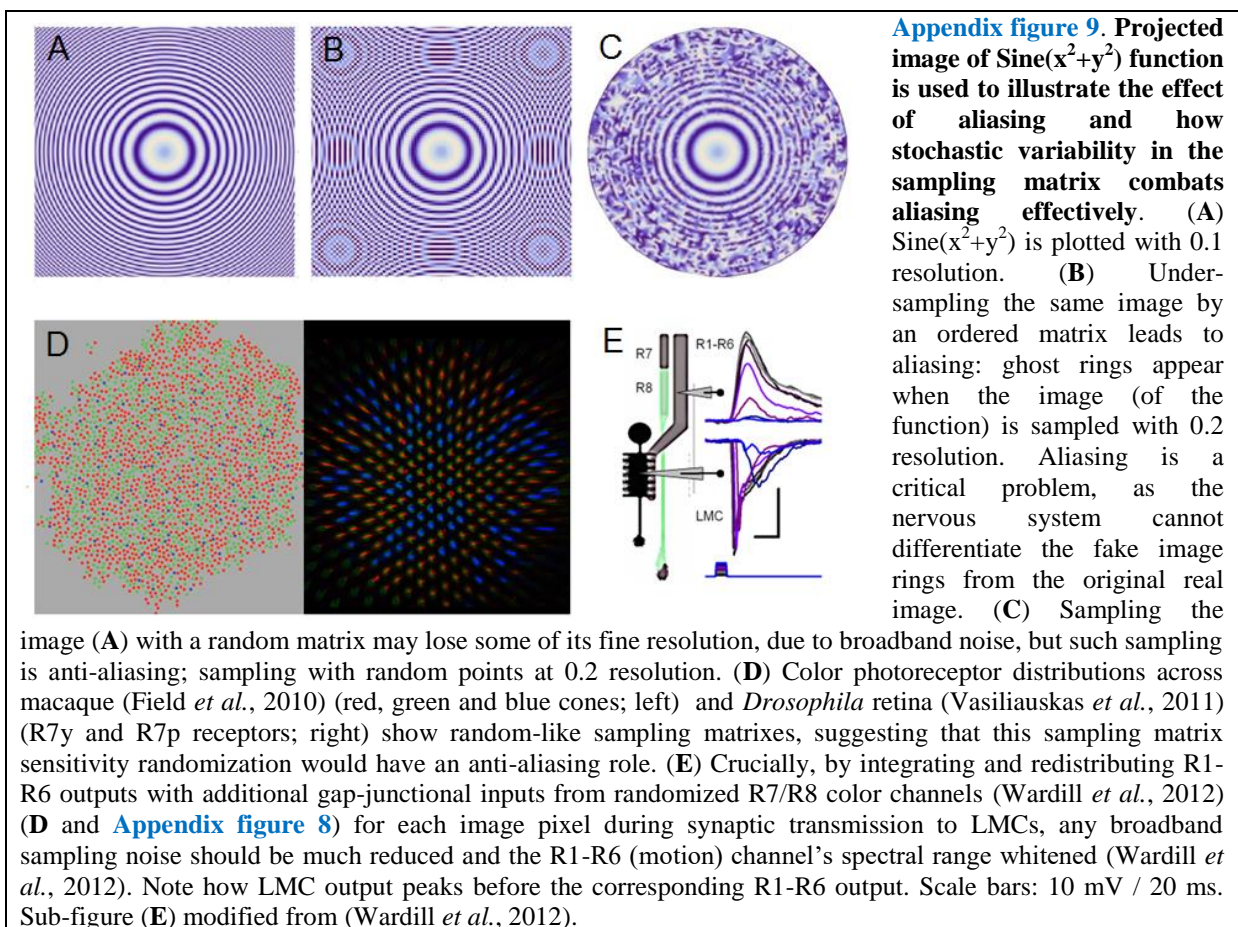
## 21 22 **Variable sampling matrix protects from aliasing, improving vision**

23 With each R1-R6 having variable "network-tuned" (and possibly "location-tuned") encoding  
24 properties and output, and with each image pixel being sampled through variable size rhabdomeres  
25 (see **Appendix 5, Appendix figure 20**) and ommatidial lenses (the photoreceptors' receptive fields  
26 vary; see **Appendix 4, Figure 7-figure supplement 1** and interommatidial angles change  
27 progressively from front to back (Gonzalez-Bellido *et al.*, 2011)), the *Drosophila* eye should generate  
28 reliable neural estimates of the variable world. This is because a sampling matrix made out of variable  
29 pixels (neurommatidia), in which size and sensitivity show random-like constituents:

- 30 • prevents aliasing of image information (**Appendix figure 9**); see also (Yellott, 1982; Dippe &  
31 Wold, 1985; Juusola *et al.*, 2015).
- 32 • mixes color information to the R1-R6 motion vision channel, whitening its spectral sensitivity  
33 (**Appendix figure 9E**) (Wardill *et al.*, 2012), which is a prerequisite for an optimal motion  
34 detector (Srinivasan, 1985).

1  
2  
3  
4  
5  
6  
7  
8  
9  
10  
11  
12  
13  
14  
15  
16

Aliasing effects are reduced by sampling faster and/or with finer spatial resolution, and eliminated by sampling more than twice over the highest stimulus frequency (Cover & Thomas, 1991). The Nyquist–Shannon sampling theorem establishes a sufficient condition for a sample rate that enables a discrete sequence of samples to capture all the information from a continuous-time signal of finite bandwidth. Specifically, it only applies to a class of mathematical functions having a Fourier transform that is zero outside of a finite region of frequencies. This condition, however, cannot be fully realized in sensory systems, which show finite spatiotemporal sampling resolution and evolved around  $1/f^n$ -stimulus (Field, 1987; van Hateren, 1997b) distributions of the real-world objects and events. Because any physical transformation affects signal and noise equally (data processing theorem (Shannon, 1948; Cover & Thomas, 1991)) and because real-world low-pass filters, such as a lens, cannot cut-off sharply at an exact point, but instead gradually eliminate frequency components and exhibit a fall-off or roll-off slope, aliasing effects would not be removed completely in an ordered sampling matrix. Therefore, to prevent phantom sensations of aliased signals fooling the brain and perception of physical reality, sampling matrixes of sensory systems must entail stochastic variations.



17  
18  
19  
20  
21  
22  
23  
24  
25  
26  
27

Whilst temporal and topological sampling matrix variations in retinae combat aliasing (Yellott, 1982; Juusola *et al.*, 2015), their trade-off is broad-band noise (Dippe & Wold, 1985) (Appendix figure 9C). This noise, however, is much reduced (or nearly eliminated) by parallel sampling of the same information (Song & Juusola, 2014; Juusola *et al.*, 2015). For example, noise reduction occurs naturally in the fly eye - both in time and in space. In every R1-R6 photoreceptor, 30,000 microvilli sample discrete information stochastically in time, generating virtually aliasing-free macroscopic responses of very high signal-to-noise (Figure 5-figure supplement 1). Whereas, across the lamina neuro-ommatidia of variable connectivity and spectral sensitivity, neural superposition integrates local R1-R8 signals of overlapping information from each pixel (a small largely aligned area in the visual space) to improve the signal-to-noise ratio of the sampled images (see Appendix 5).

1 Such images should provide the brain reliable and maximally informative estimates of the  
2 environment.

### 3 4 **Estimating a R1-R6's encoding efficiency**

5 A photoreceptor's encoding efficiency,  $\eta$ , is the ratio between the information rates of the voltage  
6 output,  $R_{output}$ , and the effective light input (photon absorptions),  $R_{input}$ , that drove it:

$$7 \quad \eta = \frac{R_{output}}{R_{input}} \quad (A2.2)$$

9  
10 As we already had determined the maximum photoreceptor output information rates,  $R_{output}$  (**Eq. A2.1**;  
11 **Figures 2C**, **Figure 2-figure supplement 1C** and **Figure 4C**), only the corresponding information  
12 rates of the effective light stimuli,  $R_{input}$ , needed to be worked out. Because the output simulations'  
13 maximum information rates matched well the corresponding mean rates of the real recordings  
14 (**Appendix figure 6A**), we had extrapolated successfully each effective light intensity (photon  
15 absorption) time series that drove the voltage response. Therefore, we could now estimate the rate of  
16 information transfer of the effective light input by making the following assumptions:

- 17 • Photon emission from the light source (LED) follows Poisson statistics; this may or may not  
18 be true (see the discussion below).
- 19 • But if true, the effective photons, which survived photomechanical adaptations (**Appendix**  
20 **figure 4**) and were absorbed by a photoreceptor and used for calculating  $R_{input}$ , should also  
21 follow Poisson statistics (Song *et al.*, 2012; Song & Juusola, 2014; Juusola *et al.*, 2015; Song  
22 *et al.*, 2016).

23  
24 Photons are thought to be emitted by the light source, such as the LEDs, at random, exhibiting  
25 detectable statistical fluctuations (shot noise). Such dynamics can be modelled by Poisson statistics  
26 (Song & Juusola, 2014). Therefore, as each light stimulus trace differs from any other, with their  
27 mean equaling their variance, we could estimate through simulations their average signals and noise,  
28 and signal-to-noise ratios,  $SNR_{input}(f)$ . The corresponding information transfer rates,  $R_{input}$ , could then  
29 be estimated by Shannon's equation (**Eq. A2.1**). For each tested stimulus pattern, this was done by  
30 using the same amount of simulated input data as with the output data (2,000 points x 20 repetitions)  
31 to control estimation bias. More details and examples about Poisson stimulus simulation procedures  
32 are given in (Song & Juusola, 2014).

- 33 • Notice that currently there are no manmade sensors more efficient than the biological  
34 photoreceptors themselves for measuring the photon emissions from the LED light source.  
35 Therefore, we had no good direct methods to measure the LED's photon rate changes at the  
36 same level of accuracy as the photoreceptor output that it evoked. Accordingly, calculating  
37 **mutual information** directly between the less accurate light input estimate and the more  
38 accurate photoreceptor output would be both impractical and erroneous.

39  
40 For the simulated inputs and outputs, the data processing theorem (Shannon, 1948) dictates that  $R_{input}$   
41  $\geq R_{output}$ ; thus  $\eta \leq 1$  ( $\leq 100\%$ ). If not, then one or both estimates are biased or incorrect; information  
42 cannot be created out of nothing. However, for the efficiency estimates based on the real recordings, it  
43 is quite possible that  $R_{output} > R_{input}$ , and thus  $\eta > 1$  ( $> 100\%$ ), because R1-R6s receive extra  
44 information from the network (**Appendix figure 7** and **Appendix figure 8**) that is missing from the  
45  $R_{input}$  estimates of an average R1-R6 photoreceptor's photon absorptions (*cf.* **Appendix figure 6B**).

46  
47 We recognize that there are methodological limitations and unknowns, which may affect the accuracy  
48 and consistency of these estimates:

- 49 • Experimental and theoretical evidence suggests that photon output of some light sources  
50 might be sub-Poisson (Teich *et al.*, 1984); meaning, not maximally random. If this were true  
51 for our LED, then our approach would slightly underestimate  $R_{input}$ , used in the experiments,  
52 and consequently overestimate *Drosophila* photoreceptors' encoding efficiency.
- 53 • Shannon's equation can bias information transfer rate estimates for any corresponding light  
54 input and photoreceptor output differently. This is because the signal and noise components

1 of the input and output may deviate from the expected Gaussian by different amounts. Even  
2 though we used systematically the same amount of data for both estimates (20 x 2,000 data  
3 points), in the cases where light distribution is skewed (bursty stimuli) but the photoreceptor  
4 output is more Gaussian, it is possible that Shannon's equation would underestimate input but  
5 not (or less so) output information, causing us to overestimate efficiency.

- 6 • Small data chunks limit analyses. In the past, we have compared information transfer rate  
7 estimates, as obtained by Shannon's equation to those estimated through the triple  
8 extrapolation method (Juusola & de Polavieja, 2003), which is directly derived from  
9 Shannon's information theory. For ergodic data of different distributions, and when  
10 appropriately applied, both methods provided similar estimates (Juusola & de Polavieja,  
11 2003; Song & Juusola, 2014). However, the triple extrapolation method works best with large  
12 sets of data; preferably containing >30 responses to the same stimulus (Juusola & de  
13 Polavieja, 2003). In the current study, because of the practical limitations (to map a  
14 photoreceptor's whole encoding space within a reasonable time), all the selected recordings  
15 and simulations consisted responses to 20 stimulus repetitions. This data size was deemed  
16 insufficient for an accurate estimate comparison between the two methods and was not done  
17 here. In the analyses, to provide fair comparison between simulations and recordings in all  
18 tested conditions, all the data chunks (for the recordings, simulations and stimuli) were  
19 exactly the same size (20 x 2,000 points) and they were processed systematically in the same  
20 way (apart from the two exceptions we discuss next). Therefore, the data-size bias should be  
21 under control and the results comparable within these limits.
- 22 • Implementation of Shannon's equation (**Eq. A2.1**) in digital computers typically requires  
23 windowing of the data chunks (for signal and noise) before calculating their power spectra  
24 though Fast Fourier Transfer (FFT). Windowing combats spectral leakage (smearing), but this  
25 affects especially low-frequency signals, in which information content is low. So this trade-  
26 off can be considered reasonable, and its effect on most performance estimates is marginal.  
27 But here as the input and output information transfer is calculated separately, windowing  
28 affects more 20 Hz GWN light input than its corresponding photoreceptor output. This is  
29 because windowing clips lower frequency power from 20 Hz GWN input, whereas in the  
30 simulated and real voltage responses much of this power is nonlinearly translated (through  
31 adaptation) to higher frequencies, including those over 20 Hz. The simulated light input, of  
32 course, carries no information on frequencies >20 Hz, but now it has also lost in windowing  
33 some of its low-frequency modulation, which the photoreceptors could translate into high-  
34 frequency voltage modulation (note, photomechanical phase enhancement can further  
35 contribute to this nonlinearity, see **Appendix 3**). For the two lowest intensity levels only, we  
36 judge that because of this methodological bias, the efficiency estimates for the 20 Hz GWN  
37 input-output data became unrealistic by a small margin of 10-40 bits/s, implying that  $R_{output} >$   
38  $R_{input}$ . Therefore, for data to these two stimuli only, we applied box-car windowing (instead of  
39 the normal Blackman-Harris type), to retain its low frequency information content, and so to  
40 reduce this bias.

41  
42 Because of all these possible error and bias sources, a *Drosophila* photoreceptor's encoding efficiency  
43 ( $\eta$ ) estimates given in this publication must be considered as upper bounds. Nonetheless, for real  
44 photoreceptors, it is realistic to expect their maxima to approach 100%, and in some cells (likely R6s)  
45 be beyond, for the tested low-frequency stimuli (20 Hz). This is because of the extra information from  
46 the network, which is missing from the simulated mean photon absorption estimates. (Note that in the  
47 *in vivo* experiments, the light source emits at each moment 100-10,000-times more photons than what  
48 can be absorbed by the tested photoreceptor. Thus, the light source's  $R_{input}^{emitted}$  always exceeds a  
49 photoreceptor's  $R_{input}^{absorbed}$ ).

50 Overall, the maximum  $\eta$  values are slightly higher but consistent with our previous  
51 (conservative) estimates of 90-95%, in which the light input intensity to microvilli was inferred by  
52 comparing the wild-type photoreceptor performance to that of white-eye mutants, lacking the  
53 intracellular pupil. Therefore, we conclude (again conservatively) that the error margin of these new  
54 encoding efficiency estimates may reach  $\pm 5\%$ .

## Appendix 3: Similarities and differences in encoding bursts and other stimuli

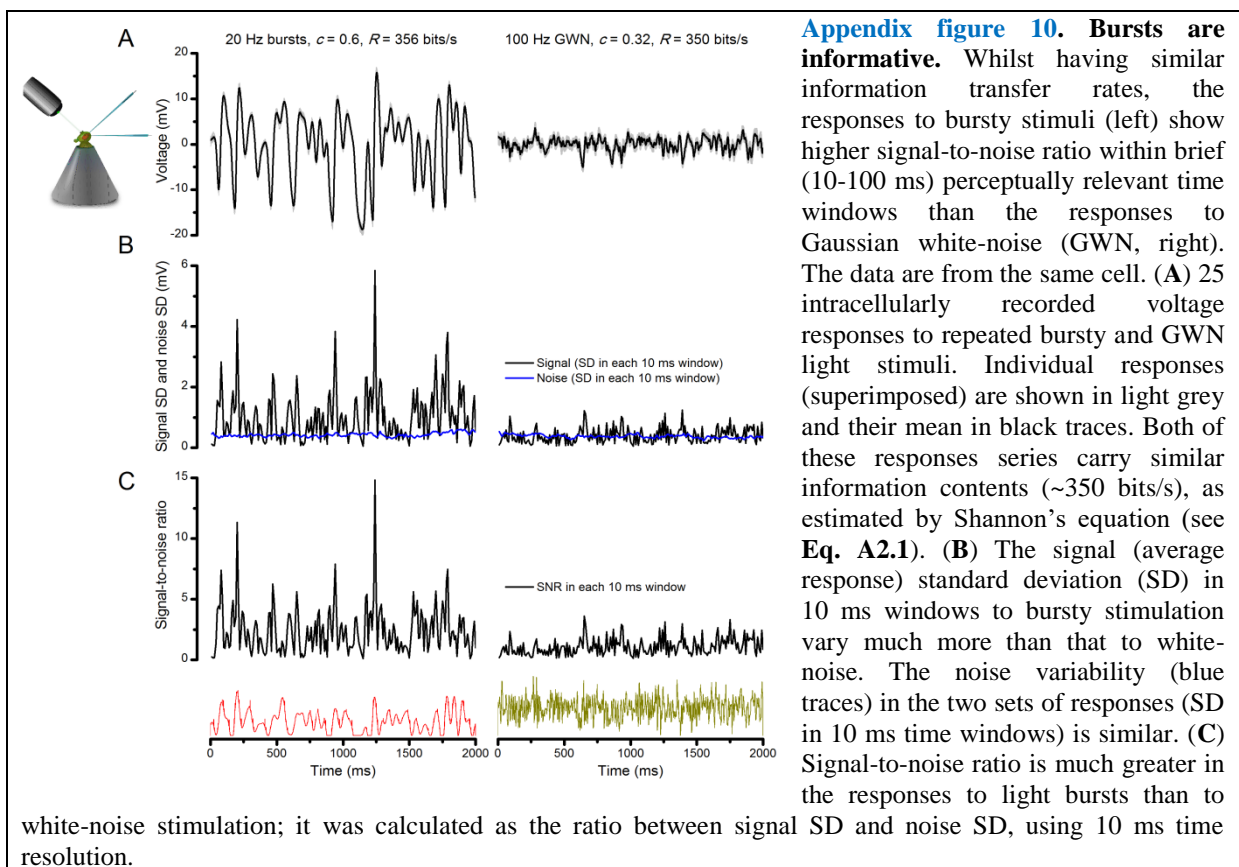
### Overview

This appendix explains why the encoding of high-contrast bursts is both highly informative and reliable, providing additional insight to the results presented in **Figures 1-6**. It also explains how we generated the different light intensity time series from panoramic images of natural scenes, following a *Drosophila*'s saccadic walking patterns (**Figure 6**), and how these stimuli were analyzed and used in the experiments.

### Why do bursty responses carry the most information?

**Figure 2-figure supplement 3** shows that R1-R6 photoreceptors can sample more information from high-contrast bursts than from naturalistic light intensity time series ( $1/f^{\alpha}$ -stimuli). We can explain this performance difference by the bursty stimuli' proportionally more, and more evenly distributed, long dark contrasts. Such events enable refractory microvilli to recover efficiently from their previous light-activation so that large numbers of them are continuously available to sample ongoing light changes; *i.e.* to transduce photons to quantum bumps. This leads to larger sample (quantum bump) rate changes and, thus, to a higher rate of information transfer (see also: Song & Juusola, 2014).

Moreover, fast high-contrast events survive the slower intracellular pupil mechanism (**Appendix 2**, *e.g.* **Appendix figure 4**) and photomechanical rhabdomere contractions (**Appendix 7**) well (**Figure 8C**). And consequently, fewer photons are being filtered out (lost) from high-contrast bursts than from naturalistic stimulation (**Figure 2-figure supplement 3B**, pink trace) or Gaussian white-noise (grey), which adapt the photoreceptors more continuously to the given light background. Therefore, at the level of the light source, bursty stimuli can have much lower power than the other two stimuli to drive photon-to-quantum bump sampling efficiently by 30,000 microvilli.



### Relevance of bursty responses for seeing germane visual patterns

From an information theoretic point of view, the amount of visual information that is encoded by a photoreceptor can be similar for bursty (phasic) and Gaussian (tonic) signals (**Figure 2C**; *cf.* 20 Hz

1 0.6-contrast bursts and 100 Hz 0.32-contrast GWN). However, when signal-detection-theoretic  
2 measures are applied, bursts outperform “tonic” GWN signals in indicating visual “things”; *i.e.* the  
3 occurrence of perceptually relevant changes in light input. Bursts appear somewhat like all-or-none  
4 events (**Appendix figure 10**), having much higher local signal-to-noise ratios in the rising or decaying  
5 phases of a photoreceptor’s voltage responses (Zheng *et al.*, 2006). They tower over the background  
6 noise, making their detection much easier than for the tiny blips of the GWN signals. Accordingly,  
7 photoreceptors’ voltage bursts support robust transmission of behaviorally relevant visual information  
8 and should further improve the reliability of synaptic transmission and perception (Zheng *et al.*, 2006;  
9 Zheng *et al.*, 2009).

### 11 **Light intensity time series based on a *Drosophila*’s walk**

12 By combining a fly’s movement during free walking (Geurten *et al.*, 2014) with natural image  
13 statistics, we estimated light intensity stimuli, which a *Drosophila* R1-R6 photoreceptor would face  
14 during locomotion through different natural scenes (**Figure 6** and **Video 1**).

15 To reproduce a fly’s saccadic movements and fixations during its 10 s walk (**Figure 6A**), we  
16 used the published angular velocity data (Geurten *et al.*, 2014) (**Figure 6B**; **Appendix figure 11C**).  
17 This was traced from Figure 1D in (Geurten *et al.*, 2014), using the unobscured section between 0.05-  
18 9.95 s, and re-sampled with 1 ms steps. The velocity was integrated over time to give the yaw signal  
19 (yaw(t)). Both the velocity and the yaw matched the original published data. Finally, the yaw was  
20 wrapped between 0° and 360°.

21 For generating the light intensity time series stimuli, which a walking fly would experience in  
22 different surroundings, we used six different 360° panoramic images (high-density digital photographs  
23 of natural scenes), taken from the internet (**Table 1**). These natural scenes were arbitrarily chosen  
24 from Google image search results, and we do not know how representative their image statistics are,  
25 for example, in respect to the van Hateren database (van Hateren, 1997a). Each image’s left (0°) and  
26 right (360°) side were stitched together to enable continuous viewing over a full rotation. The images  
27 were preprocessed in the following way:

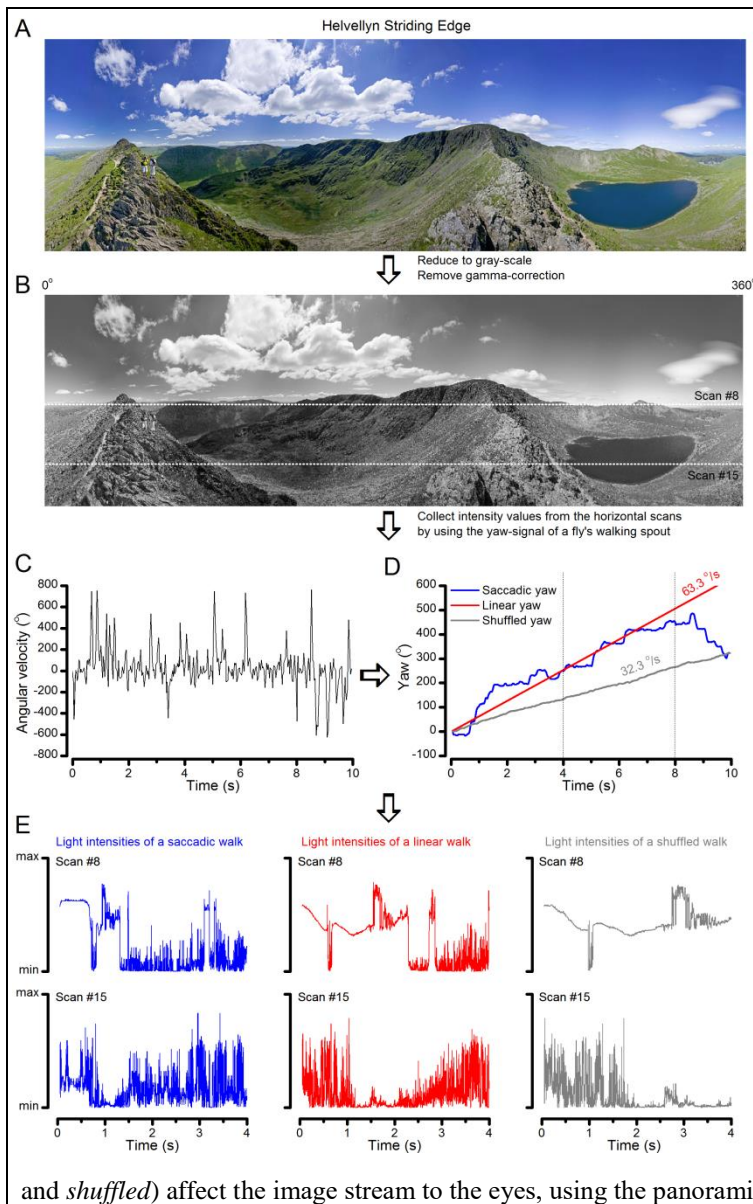
- 28 • Because stitching can cause errors (distortions), the lower and upper quarters of the images  
29 were discarded.
- 30 • The color images (**Appendix figure 11A**) were reduced to gray scale, and their gamma  
31 correction was removed, enabling us to use their raw intensity values (**Appendix figure 11B**).
- 32 • For each image, light intensity values were collected from 15 horizontal line scans taken in  
33 regular intervals (from top to bottom; **Appendix figure 11B**).

34 **Table 1.** The used six panoramic high-resolution digital images of natural scenes were downloaded from:  
[https://commons.wikimedia.org/wiki/File:Swampy\\_forest\\_panorama.jpg](https://commons.wikimedia.org/wiki/File:Swampy_forest_panorama.jpg)  
[https://commons.wikimedia.org/wiki/File:2014-08-29\\_11\\_51\\_08\\_Full\\_360\\_degree\\_panorama\\_from\\_the\\_fire\\_tower\\_on\\_Apple\\_Pie\\_Hill\\_in\\_Wharton\\_State\\_Forest\\_Tabernacle\\_Township,\\_New\\_Jersey.jpg](https://commons.wikimedia.org/wiki/File:2014-08-29_11_51_08_Full_360_degree_panorama_from_the_fire_tower_on_Apple_Pie_Hill_in_Wharton_State_Forest_Tabernacle_Township,_New_Jersey.jpg)  
[https://en.wikipedia.org/wiki/File:Helvellyn\\_Striding\\_Edge\\_360\\_Panorama,\\_Lake\\_District\\_-\\_June\\_09.jpg](https://en.wikipedia.org/wiki/File:Helvellyn_Striding_Edge_360_Panorama,_Lake_District_-_June_09.jpg)  
[https://commons.wikimedia.org/wiki/File:Schleien%C3%B6cher\\_Hard\\_360%C2%B0\\_Panorama.jpg](https://commons.wikimedia.org/wiki/File:Schleien%C3%B6cher_Hard_360%C2%B0_Panorama.jpg)  
[https://farm3.staticflickr.com/2820/9296652749\\_7c502de9e7\\_o.jpg](https://farm3.staticflickr.com/2820/9296652749_7c502de9e7_o.jpg)  
<http://www.bodenstab.org/panorama/images/Green%20Valley/panorama.jpg>

35 As each image spanned 360° horizontally, we could calculate the degree-value between 0° and  
36 360° for each pixel (intensity) in the horizontal line scans (Intensity(angle)). The pixel intensity values  
37 (within the chosen horizontal line) were then sampled at the corresponding yaw positions (**Appendix**  
38 **figure 11D**; in degrees) of the fly’s walk for each 1 ms time-bin (Intensity(yaw(t))). This generated  
39 unique light intensity time series (**Appendix figure 11E**), which mimicked walk-induced  
40 photoreceptor stimulation from the given scene. In the sampling, each yaw value was automatically  
41 rounded to the closest pixels angle value (**Appendix figure 11C**, blue traces). Note: this process  
42 assumes that, during a free walk, the fly head would not rotate or move vertically.

43 We also generated two sets of control light intensity time series data from the same images.  
44 1<sup>st</sup> control: to compare saccadic movements to linear movements (named *linear*), we used the same  
45 walk’s median yaw velocity of 63.3 °/s (median(abs(angularvel(t)))) (**Appendix figure 11D**, red  
46

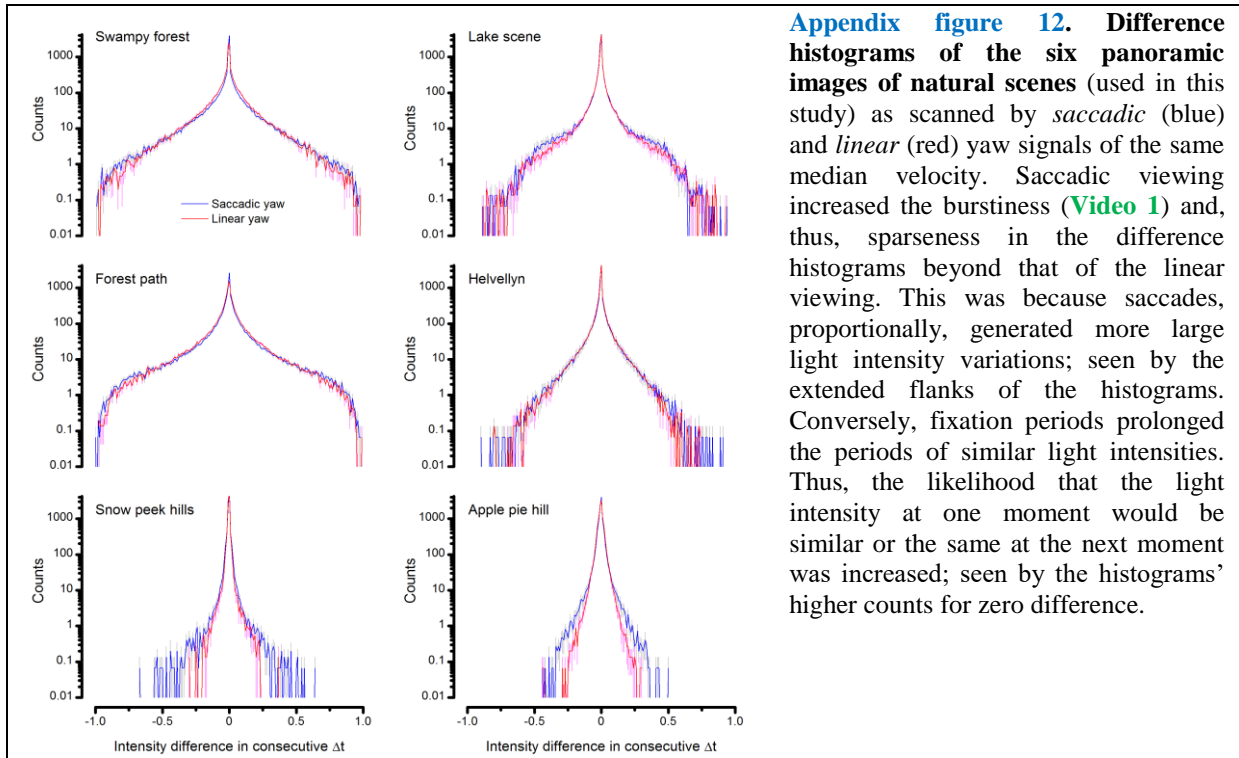
1 traces). 2<sup>nd</sup> control: we shuffled the angular velocity trace values (named *shuffled*; gray traces); this  
 2 removed all time correlations in the velocity trace without affecting its histogram. **Appendix figure**  
 3 **11E** shows two examples of the saccadic (test) and the two control light intensity time series, taken  
 4 from two different horizontal scan lines (scans 8 and 15 in **Appendix figure 11B**).  
 5



6  
 7 **Light intensity time series analysis – differential histograms**  
 8 Intensity changes for *saccadic*, *linear* and *shuffled* locomotion dynamics were calculated by  
 9 subtracting 2 neighboring points in each intensity series (using Matlab “*diff*”-function). The  
 10 corresponding ‘intensity change’-histograms were calculated from all 15 traces per each image.  
 11 Differential histogram was calculated as the mean of the ‘intensity change’-histograms.

12 We found (predictably) that the differential histograms of the saccadic light intensity time  
 13 series were sparser than those of the corresponding linear light intensity time series stimuli (of the  
 14 same median velocity; **Figure 6D**). This was true for all the tested panoramic images (**Appendix**  
 15 **figure 12**). Saccadic sampling (blue traces) “burstified” light input. This was because it increased the  
 16 proportion of rare large intensity differences between two consecutive moments in comparison to  
 17 linear sampling (red); *i.e.* saccades made the histogram flanks to reach out further. Furthermore, the  
 18 fixation periods made it more likely that light intensity over the neighboring moments remained  
 19 similar or the same (higher proportion of zero values). These features are obvious in **Video 1**.

1



2

### 3 **Selecting the stimulus patters and their playback velocity**

4 There are important factors to consider when selecting the stimulus series and their playback velocity  
5 for testing how self-motion affects R1-R6 photoreceptors ability to encode naturalistic stimulation.

6 A fly photoreceptor's information transfer rate is limited by (i) the number of its photon  
7 sampling units (Howard *et al.*, 1987; Song *et al.*, 2012; Song & Juusola, 2014; Juusola *et al.*, 2015)  
8 (30,000 and 90,000 microvilli in a typical *Drosophila* and *Calliphora* R1-R6, respectively) and (ii) the  
9 speed, (iii) reliability (jitter) and (iv) recoverability (refractoriness) of their phototransduction  
10 reactions (Juusola & Hardie, 2001b, a; Song *et al.*, 2012; Song & Juusola, 2014; Juusola *et al.*, 2015).  
11 In general, the more efficiently the light stimulus utilizes the available microvilli population in  
12 generating the larger sample (quantum bump) rate changes, the higher the photoreceptor's information  
13 transfer rate (Song & Juusola, 2014) (see **Appendix 2**). Consequently, the efficiency of photon  
14 sampling depends upon the stimulus speed and statistics (Juusola & de Polavieja, 2003; Zheng *et al.*,  
15 2009; Song *et al.*, 2012; Song & Juusola, 2014) (**Appendix figure 13**). For naturalistic light intensity  
16 time series stimulation (NS), we have previously shown that:

- 17 • A R1-R6 photoreceptor's information transfer increases with stimulus playback velocity until  
18 saturation, when most of its microvilli likely become refractory for most of the time (Juusola  
19 & de Polavieja, 2003; Song *et al.*, 2012; Song & Juusola, 2014; Juusola *et al.*, 2015)  
20 (**Appendix figure 13A-C**). This information increase results from the increased entropy rate  
21 in photoreceptor output (**Appendix figure 13B**), as it reliably packs in more sample rate  
22 changes in a given time unit. The corresponding noise entropy rate (Juusola & de Polavieja,  
23 2003), similar to noise power (**Figure 2-figure supplement 2A**), remains practically  
24 invariable.
- 25 • Sample rate changes in R1-R6 output further depend upon the stimulus structure (Juusola &  
26 de Polavieja, 2003; Song *et al.*, 2012; Song & Juusola, 2014; Juusola *et al.*, 2015) (the  
27 distribution of its dark and bright contrasts). For example, R1-R6 output information peaks at  
28 lower playback velocity (10 kHz) for NS<sub>1</sub>, which had fewer long dark-contrast periods (to  
29 recover refractory microvilli) than for NS<sub>2</sub> (>20 kHz), which had more and more evenly  
30 spaced dark-contrasts (**Appendix figure 13C**).

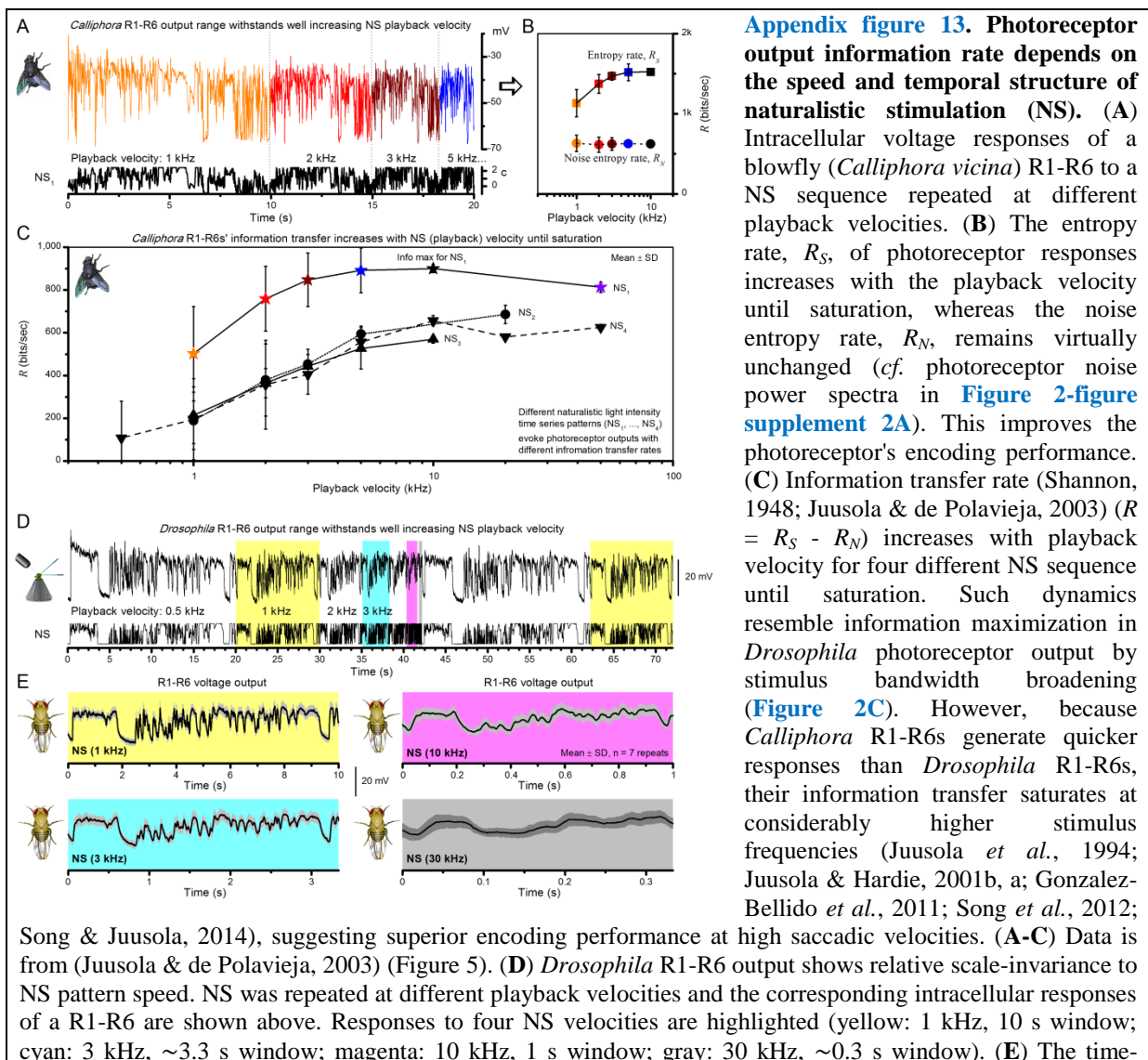
31

1 For testing how naturalistic *saccadic*, *linear* and *shuffled* locomotion patterns affect *Drosophila* R1-  
 2 R6s' encoding performance (**Figure 6F**), we used the three corresponding light intensity time series  
 3 stimuli (first 8,000-points) from "swampy forest" panorama (line scan #8). These stimulus sequences  
 4 were selected because each of them carried high-contrast modulation. In the intracellular experiments  
 5 and model simulations, these stimuli were repeatedly presented one after another to each tested  
 6 photoreceptor with 4 kHz playback velocity. This stimulus speed was chosen because:

- 7 • It would cover well the broad velocity range of natural visual inputs to photoreceptors,  
 8 including both the slower walking and the faster saccadic flight behaviors.
- 9 • Each stimulus could be presented in 2 s, enabling us to collect 30 responses in 1 min and the  
 10 three different sets of data in 3 min, keeping the recordings conditions under control.
- 11 • It evokes high R1-R6 information transfer, which for many high-contrast NS sequences  
 12 approaches their maxima (Juusola & de Polavieja, 2003; Zheng *et al.*, 2009) (*cf.* **Appendix**  
 13 **figure 13D-E**). Theoretically, *Drosophila* R1-R6 output information rate cannot exceed ~850  
 14 bits/s (**Figure 2C**), which was evoked by 100 Hz bursts. Such stimulus entailed the right mix  
 15 of bright and dark contrasts to optimally utilize a R1-R6's frequency and amplitude ranges.

16 These stimuli evoked comparable responses (of high information rates) both from R1-R6  
 17 photoreceptors *in vivo* and the biophysically realistic R1-R6 model (**Appendix 1**). The recordings and  
 18 the simulations showed consistently that the voltage responses to saccadic (*i.e.* the most bursty) light  
 19 intensity time series had the highest information transfer rate (**Figure 6F**; **Figure 6-figure**  
 20 **supplement 1**).

21



normalized shapes of R1-R6 output emphasize similar aspects in NS, regardless of the used playback velocity (here from 0.5 to 30 kHz). R1-R6s integrate voltage responses of a similar size for the same NS pattern, much irrespective of its speed. Mean  $\pm$  SD shown, n=7 traces. (D-E) Data is from (Zheng *et al.*, 2009) (Figure 4).

1

2 Finally, we note that it is possible that in scenes with different spatial structure (particularly lower  
3 spatial frequency structure), flies would use different turn velocities to bring contrast features into  
4 ideal sampling range (irrespective of saccades making sampling shorter). Future studies need to  
5 explore whether such a match with saccade statistics exists.

## Appendix 4: Spatial resolution (visual acuity) of the *Drosophila* eye (conventional measure)

### Overview

This appendix describes in detail a new method to measure a *Drosophila* photoreceptor's receptive field, and provides important background information about the experimental and theoretical results presented in [Figures 7-9](#).

In this appendix:

- We test the hypothesis that in the *Drosophila* eye visual information is integrated laterally in dim conditions, and fed back synaptically to its photoreceptors, contributing to their spatial responsiveness.
- We measure dark- and moderately light-adapted wild-type R1-R6 photoreceptors' receptive fields by their acceptance angles,  $\Delta\rho$ , using intracellularly recorded voltage responses to light flashes, delivered from randomized positions of an orthogonal stimulation array.
- We compare these measurements to those of histamine-mutants (Burg *et al.*, 1993; Melzig *et al.*, 1996; Melzig *et al.*, 1998) (*hdc*<sup>*JK910*</sup>), in which first-order interneurons are blind (receiving no neurotransmitter from photoreceptors) and so incapable of feedback-modulating photoreceptor output.
- We show that the average acceptance angles of dark-adapted wild-type photoreceptors are 10.9% broader than those of the mutant, while light-adapted cells show no such difference.
- We characterize slow spontaneous retinal movements in the *Drosophila* eye and show how this activity can influence intracellular photoreceptor recordings.
- Our results suggest that in dim conditions spatial information is pooled in the lamina and fed-back to wild-type photoreceptors. Such excitatory lateral synaptic modulation, which is missing in the mutant, increases spatial sensitivity, broadening the photoreceptors' receptive fields.

### Optical limits of the fly compound eyes' visual acuity

Visual acuity is defined as the minimum angle that the eye can resolve. In the fly compound eye, if each ommatidium constitutes a sampling point in space, then the eye's maximal spatial resolution is set by the density of its ommatidial array (Snyder *et al.*, 1977). Suppose a regular pattern of black and white stripes is presented to a fly. The maximum spatial frequency that the fly can resolve,  $\nu_s$ , is achieved when one ommatidium points to a black stripe and its adjacent ommatidium points to the next white stripe ([Appendix figure 14A](#)). Thus, the interommatidial angle (Snyder & Miller, 1977), angle,  $\Delta\phi$ , is the key parameter in determining  $\nu_s$ . For the compound eyes with hexagonal layout, as is the case of most flies, the effective interommatidial angle,  $\Delta\phi_e$  ([Appendix figure 14B](#)), can be calculated as:

$$\Delta\phi_e = \cos(30^\circ) \Delta\phi = \frac{\sqrt{3}}{2} \Delta\phi \quad (\text{A4.1})$$

Thus, the upper limit of the fly eye's visual acuity is given by:

$$\nu_s = \frac{1}{2(\Delta\phi_e)} = \frac{1}{\sqrt{3}(\Delta\phi)} \quad (\text{A4.2})$$

Whether this limit is achieved or not depends upon the spatial performance of a photoreceptor (Snyder, 1977). However, when estimating a photoreceptor's receptive field, which is quantified by its width at half-maximum, or acceptance angle (Warrant & McIntyre, 1993),  $\Delta\rho$ , we need to consider several contributing factors.

Firstly, since the ommatidium lens and a photoreceptor's rhabdomere are very small, optical quality is strongly affected by light diffraction, of which airy pattern (the point-spread function) depends upon light wavelength,  $\lambda$ , lens diameter,  $D$ , rhabdomere diameter,  $d$ , and focal distance,  $f$  ([Appendix figure 14C](#)). Theoretically, the blurring functions at the ommatidium lens and rhabdomere tip are both Gaussian and therefore can be combined (Snyder, 1977) to yield a simple approximation of  $\Delta\rho$ :

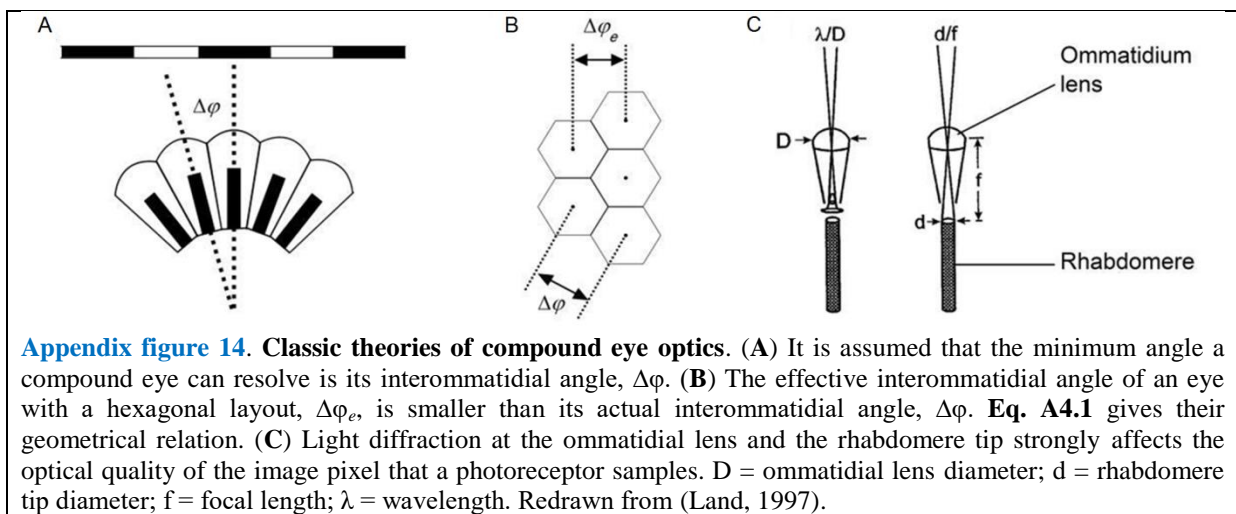
1  
2  
3  
4  
5  
6  
7  
8  
9  
10  
11  
12  
13  
14  
15  
16  
17  
18  
19  
20  
21  
22  
23

$$\Delta\rho = \sqrt{\left(\frac{\lambda}{D}\right)^2 + \left(\frac{d}{f}\right)^2} \quad (\text{A4.3})$$

However, owing to the rather complex waveguide properties of small-diameter rhabdomeres, this formula is somewhat inaccurate. Van Hateren (van Hateren, 1984) and Stavenga (Stavenga, 2003b, a) found that along a fly photoreceptor’s rhabdomere only a limited number of light patterns (modes) could be formed and that this number depends upon the incident angle of light, leading to a smaller actual  $\Delta\rho$  than what **Eq. A4.3** implies.

Another contributing factor is the spatial cross talk, in which a photon escapes the rhabdomere it first travels in and enters an adjacent rhabdomere (Horridge *et al.*, 1976). Such an effect is likely to happen when the cross-talk index of the ommatidia/rhabdomere structure is less than three (Wijngaard & Stavenga, 1975). This was indeed reported for *Drosophila* (Gonzalez-Bellido *et al.*, 2011), suggesting that its neural images might have lower resolution than theoretically calculated from the optics.

Lastly, the intracellular pupil mechanism further affects  $\Delta\rho$  estimation. Inside each photoreceptor cell, there are tiny pigment granules that migrate toward its rhabdomere boundary upon light adaptation (see **Appendix 2, Appendix figure 3**). These pigments absorb and scatter light that travels inside the rhabdomere, reducing the light influx absorbable by its rhodopsin molecules (Kirschfeld & Franceschini, 1969; Boschek, 1971; Roebroek & Stavenga, 1990). Consequently, the pupil mechanism shapes a photoreceptor’s angular and spectral sensitivity (Stavenga, 2004a). Moreover, in **Appendix 2**, we show by experiments and theory that it further helps to maximize a photoreceptor’s information transfer; by optimizing the light intensity passing into the rhabdomere.



24  
25  
26  
27  
28  
29  
30  
31  
32  
33  
34  
35  
36  
37  
38  
39

### Rationale for investigating wild-type and *hdc* R1-R6s’ receptive fields

The fly compound eyes are small and size-constrained, presumably to save energy and improve survival (Land, 1998; Laughlin *et al.*, 1998; Niven *et al.*, 2007). This puts their sensitivity/acuity trade-off under intense evolutionary pressure (Snyder *et al.*, 1977; Laughlin, 1989; Nilsson, 1989; Warrant & McIntyre, 1992). While an increase in ommatidium size would improve photon capture, it would also result in fewer sampling points (image pixels) in the eye, lowering the resolution of its neural responses (neural images of the world). In dim conditions, where photon noise is relatively large compared to available information (signal), the task to enhance visual reliability and sensitivity becomes challenging. Optical mechanisms, including the widening of photoreceptor receptive fields by pupil opening (Williams, 1982; Laughlin, 1992; Nilsson & Ro, 1994; Stavenga, 2004a), can increase the amount of light collected in each ommatidium only to some extent. Yet under dim illumination, insect visual behaviors appear remarkably robust (Pick & Buchner, 1979; Warrant *et al.*, 1996; Honkanen *et al.*, 2014), suggesting that their eyes’ neural mechanisms could successfully overcome the apparent shortfall in photon supply (Warrant, 1999).

Sensitivity can be increased neurally at the cost of decreasing acuity by (i) increasing

1 photoreceptors' voltage/light intensity gain (Laughlin & Hardie, 1978; Matic & Laughlin, 1981; Song  
2 *et al.*, 2012), (ii) increasing their integration time (temporal summation) (Skorupski & Chittka, 2010;  
3 Song *et al.*, 2012) and (iii) spatially summing information, or reducing lateral inhibition from neural  
4 neighbors (Srinivasan *et al.*, 1982; van Hateren, 1992c, 1993b). Experimentally, spatial summation  
5 has been shown to occur in the directionally-selective motion-detecting (DSMD) neurons of the fly  
6 lobula plate (Srinivasan & Dvorak, 1980), but it is possible that such signals might also reflect  
7 upstream processing in the earlier optic neuropiles (the lamina, medulla and lobula).

8 Although the fly photoreceptor biophysics for adapting temporal summation are well  
9 characterized (Juusola *et al.*, 1994; Juusola & Hardie, 2001b, a; Song *et al.*, 2012; Song & Juusola,  
10 2014; Hardie & Juusola, 2015; Juusola *et al.*, 2015) (see **Appendixes 1-3**), the neural substrate for  
11 spatial summation is less well understood. In the lamina, electrical couplings by gap-junctions were  
12 found only between the photoreceptor axons that share the same optical axis (Ribi, 1978; Shaw, 1984;  
13 van Hateren, 1986; Shaw *et al.*, 1989) in neural superposition. Hence, these presynaptic connections  
14 probably cannot distribute spatial information. Nonetheless, postsynaptically, the evidence is more  
15 suggestive. Intracellular responses of the histaminergic interneurons (large monopolar cells, LMCs) to  
16 narrow (point source) and wide-field light stimuli match well the theoretical predictions of  
17 spatiotemporal summation (Dubs *et al.*, 1981; van Hateren, 1992a, b). This notion was further  
18 advocated by the structural study in the nocturnal bee *Megalopta genalis* (Greiner *et al.*, 2005)  
19 lamina, which revealed extensive synaptic connections between adjacent cartridges. Finally, early  
20 functional studies of the housefly (*Musca domestica*) photoreceptors (Dubs *et al.*, 1981) indicated that  
21 quantum bumps, recorded to dim light at the behavioral threshold, contain additional small-amplitude  
22 events. These were judged not to be generated by the impaled cells but by single photon captures in  
23 their neighbors; with the receptive fields being wider than what were expected from the optics alone  
24 (Dubs, 1982).

25 In this appendix, we test whether or how spatial information is integrated laterally and fed  
26 back synaptically to photoreceptors, contributing to their acceptance angles,  $\Delta\mu$ . The tight coupling  
27 between feed-forward and feedback pathways in the photoreceptor-lamina circuit is known to have  
28 crucial roles in maintaining robust adaptation and temporal coding efficiency (Zheng *et al.*, 2006;  
29 Nikolaev *et al.*, 2009; Zheng *et al.*, 2009). Theoretically, similar spatial information regulation should  
30 further improve fly vision. Specifically here, we take advantage of *Drosophila* genetics and compare  
31 R1-R6 photoreceptor outputs of wild-type and *hdc*<sup>JK910</sup> mutant. Synaptic transmission from *hdc*<sup>JK910</sup>  
32 photoreceptors is blocked, making their interneurons effectively blind (Dau *et al.*, 2016). Therefore,  
33 feedback from the mutant LMCs (and possibly from amacrine cells (Zheng *et al.*, 2006; Hu *et al.*,  
34 2015), Am, which also receive histaminergic input from photoreceptors) to R1-R6s cannot contain  
35 any lateral modulation, neither inhibitory nor excitatory.

36 We show that the dark-adapted wild-type R1-R6 photoreceptors' mean acceptance angles are  
37 10.9% broader than in the mutant, while no significant differences are found between the light-  
38 adapted cells. We further show how stimulus history and retinal movements affect the receptive fields  
39 in the *Drosophila* eye. Our results suggest that in dim conditions spatial information is pooled in the  
40 lamina and channeled back to R1-R6 photoreceptors in the form of excitatory synaptic modulation,  
41 which increases spatial responsiveness by broadening the cells' receptive fields.

### 42 43 **Measurement and calculation of a R1-R6's receptive field**

44 A photoreceptor's receptive field can be estimated electrophysiologically by measuring its  
45 intracellular response amplitudes,  $V_n$ , to a light flash intensity,  $I_n$ , at varying angular positions,  $\alpha_n$ .  
46 From all these  $V_n$ ,  $I_n$ , and  $\alpha_n$  values generated by a complete scan, the receptive field width can be  
47 computed by three different methods as comparatively reviewed below.

48  
49 **Method 1.**  $V_n$  is clamped to a constant value in a closed-loop system, which accordingly vary  $I_n$  for  
50 each tested light source positions (Smakman *et al.*, 1984; Smakman & Stavenga, 1987). Sensitivity at  
51 each position,  $S_n$ , is then defined by:

$$52 \quad 53 \quad 54 \quad S_n = \frac{I_o}{I_n} \quad (\text{A4.4})$$

1 where  $I_0$  is the intensity required from a point source at the center of the receptive field. The  
2 definition of sensitivity can be equivalently expressed as the light source at an off-axis position. The  
3 off-axis light intensity needs to be  $\frac{1}{S_n}$ -fold brighter than the axial one to stimulate responses of the  
4 same amplitude.

5 After corresponding  $S_n$  was computed for every  $S_n$ , the sensitivity-angle relation is fitted by a  
6 Gaussian function. The width at the half-maximum of this Gaussian curve is called the *acceptance*  
7 *angle*. This is the conventional parameter,  $\Delta\rho$ , for quantifying the receptive field width.

8  
9 **Method 2**, in which the same light flash intensity  $I_n$  is tested at many different angular positions, is  
10 the most widely used (Wilson, 1975; Horridge *et al.*, 1976; Hardie, 1979; Mimura, 1981; Gonzalez-  
11 Bellido *et al.*, 2011). Initially, the  $V/\log(I)$  relation of the impaled photoreceptor is determined at the  
12 center of its receptive field by presenting logarithmically intensified flashes from a point-like light  
13 source (through scaled neutral density filters).  $V_n$  elicited by the light at each off-axis angle,  $V_n$ , is  
14 then substituted into the  $V/\log(I)$  function to estimate,  $I_a$ , the light intensity that was effectively  
15 absorbed by the cell's photopigments. Angular sensitivity,  $S_n$ , is given by **Eq. A4.5**:

$$S_n = \frac{I_a}{I_n} \quad (\text{A4.5})$$

16  
17  
18  
19 Gaussian fitting and the acceptance angle calculation are performed as in Method 1.

20 Method 2 is based upon the same principle as Method 1, which is to assess the light intensity  
21 necessary to elicit a criterion response (Warrant & Nilsson, 2006). When the light-point with  
22 intensity  $I_0$  is exactly at the optical axis of the cell, sensitivity is the highest with the response  
23 amplitude  $V_0$ . To evoke  $V_n = V_0$  by a light source located at an angular position,  $\alpha_n$ , it is required that  
24 the effective intensity  $I_a$  equals to  $I_0$ . Given the angular sensitivity formula:

$$S_n = \frac{I_a}{I_n} = \frac{I_0}{I_n} \quad (\text{A4.6})$$

25  
26  
27 the necessary intensity  $I_n$  would be  $\frac{1}{S_n}$ -fold brighter than  $I_0$ .

28 Though Method 2 does not require a closed-loop system and is, therefore, less  
29 experimentally challenging, its effective intensity,  $I_a$ , estimation has drawbacks. Fitting  $V/\log(I)$   
30 function to a small number of maximum amplitude values, which are adaptation-dependent, can  
31 introduce scaling errors. Whilst its underlying assumptions, that the voltage/(effective intensity)  
32 relation is static and independent of light source position, neglect possible dynamic and lateral  
33 interactions between neighboring cells.

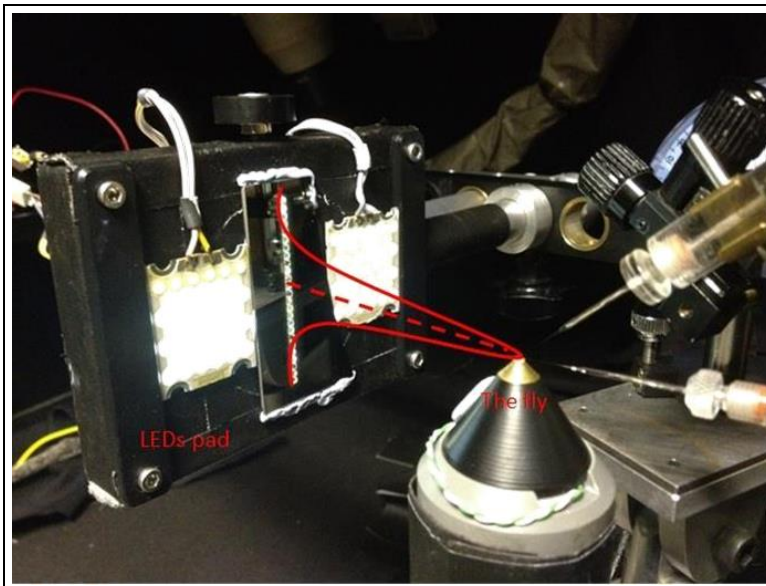
34 Nonetheless, the outcomes of both methods are theoretically independent of photoreceptor  
35 biophysics and the test flash intensity. Hence, they enable electrophysiological receptive field  
36 measurements to be compared with those derived from optical, morphological and waveguide  
37 theories.

38  
39 **Method 3**. Similar to Method 2, each tested photoreceptor is stimulated by the same light intensity  
40 flashes at different angular positions around its optical axes. Response amplitude  $V_n$  to a light flash  
41 coming from an angle  $\alpha_n$  is then normalized to the maximum response evoked by the on-axis light  
42 source,  $V_0$ . The receptive field is determined by the Gaussian fitting of the relation between ratios  
43  $V_n/V_0$  and incident angle  $\alpha_n$ . This may yield wider half-maximum widths ( $\Delta\rho$  values) than the  
44 acceptance angles (Washizu *et al.*, 1964; Burkhardt, 1977) estimated by using Method 1 and Method  
45 2.

46 We used Method 3 to estimate R1-R6 photoreceptors' receptive fields from intracellular  
47 recordings, despite its disadvantages; the results would depend on the flash intensity and would not be  
48 fully comparable to other approaches and the previous studies in *Drosophila*. Our main rationale was  
49 that this method characterizes "how well the flies see" most directly and reliably, without making any  
50 assumptions about lateral interactions between photoreceptors and LMC feedbacks. Moreover, the  
51 method's limitations should not compromise our objectives to compare the receptive fields in  
52 different genotypes and to report how these are affected by different light conditions and stimulation

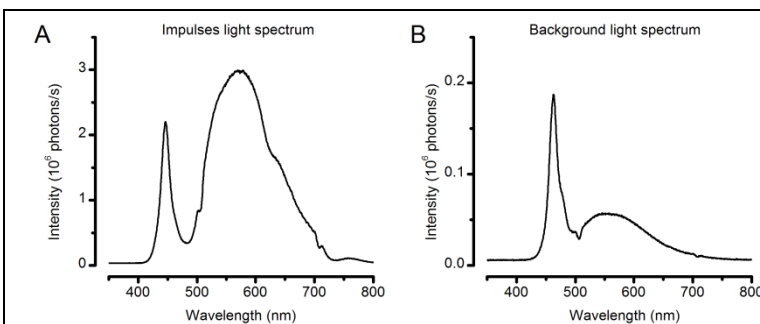
1 history. And importantly, these receptive field estimates could be directly used in further calculations  
2 to assess the same photoreceptors' theoretical acuity to detect moving objects, as shown in  
3 **Appendixes 6-8**. Experimentally, it was also unfeasible to expand our recording set-up either with a  
4 closed-loop system (as in Method 1) or with easily exchangeable neutral density filter sets for  
5 characterizing  $V/\log(I)$  function (as in Method 2).

6  
7 **25 LED light-point array and LED pads.** A R1-R6 photoreceptor's receptive field was scanned by  
8 using an array of 25 light-points, mounted on a Cardan arm (**Appendix figure 15**). Each light-point  
9 (small light guide end) subtended an angle of  $1.7^\circ$  as seen by the fly, transmitting its light output from  
10 its specific LED (1/25). The system was controlled by 2 channels, both with voltage inputs ranging  
11 from 0 V to 10 V. Channel 0 was used to select the light-point while Channel 1 was used to linearly  
12 set its intensity.  
13



**Appendix figure 15. 25 light-point stimulus array.** Each tested dark-adapted photoreceptor's receptive field (red Gaussian) was assessed by measuring its intracellular responses to successive flashes from 25 light-points. In light-adaptation experiments, two 39-LED pads, (on both sides of the vertical stimulus array) provided background illumination. The intact fly was fixed inside the conical holder, which was placed upon a close-looped Peltier-element system, providing accurate temperature control (at  $19^\circ\text{C}$ ). The rig was attached on a black anti-vibration table, inside a black-painted Faraday cage, to reduce noise and light scatter.

14  
15 **Appendix figure 16A** shows a typical light-point's spectral density measured at the light-guide end.  
16 Each light-point had a narrow spectral **Peak1** at  $\sim 450$  nm and a broader **Peak2** at  $\sim 570$  nm, in which  
17 intensities and wavelengths are listed in **Table 2**. Based on their relatively small variations, all 25  
18 light-points provided reasonably uniform light input, except the 4-times brighter No.22 (see below).  
19 This is because a fly photoreceptor's response amplitudes differ only marginally until light intensity  
20 changes several-fold, as defined by the sigmoidal  $V/\log(I)$  relationship (Matic & Laughlin, 1981).  
21 Standard light flashes, containing  $\sim 2 \times 10^6$  photons/s at **Peak1** and  $\sim 3 \times 10^6$  photons/s at **Peak2**, were  
22 produced by setting Channel 1 to an input value of 2 V. Here, the estimated photon counts are given at  
23 the light source, not at the level of photoreceptor sampling. Moreover, in the experiments, to evoke  
24 subsaturating responses, we used a neutral density filter plate to cut the light-point intensity by 100-  
25 fold.  
26



**Appendix figure 16. Spectral properties of the light stimuli.** (A) Typical spectral density of the light impulses delivered by the 25-point array. Note the spectra has two prominent peaks, named **Peak1** ( $\sim 450$  nm) and **Peak2** ( $\sim 570$  nm). (B) Spectral density of a single LED on the two Lamina pads, which were used to provide ambient background illumination during light-adaptation

experiments. These spectral intensities (photon counts) were measured by a spectrometer (Hamamatsu Mini C10082CAH, Japan).

1

Light-point	Peak1 wavelength (nm)	Peak1 intensity (10 <sup>6</sup> photons/s)	Peak2 wavelength (nm)	Peak2 intensity (10 <sup>6</sup> photons/s)
No.1	448	2.720	571	2.805
No.2	452	1.790	570	2.818
No.3	448	2.618	565	2.900
No.4	451	1.840	576	3.020
No.5	451	2.570	575	3.710
No.6	451	2.214	572	3.640
No.7	452	1.430	575	2.020
No.8	446	2.203	570	2.990
No.9	453	1.465	571	2.350
No.10	451	3.300	578	5.100
No.11	453	1.877	575	3.080
No.12	455	1.763	575	3.020
No.13	451	2.334	575	3.440
No.14	451	2.009	576	2.634
No.15	454	2.400	568	4.480
No.16	452	2.390	572	4.165
No.17	455	3.190	566	3.010
No.18	452	1.990	578	3.320
No.19	455	1.958	578	3.336
No.20	454	1.745	569	2.670
No.21	450	2.642	573	2.314
No.22	452	9.520	572	13.300
No.23	452	2.420	575	3.380
No.24	452	2.658	573	3.284
No.25	452	1.670	570	2.750

**Table 2. Light flash peak wavelengths and intensities delivered by each of the 25 light-points in the stimulus array.** The given light intensities were measured at the light source by Hamamatsu Mini C10082CAH spectrometer, before 100-fold neutral density filtering. Thus, these values are estimated to be 10<sup>-3</sup>-times higher than the corresponding effective photon rates at the level of R1-R6 sampling (see [Appendix 2](#), [Appendix figure 5](#)). Accordingly at the optical axis, the center LED (No.13), with the neutral density filter on it, evoked subsaturating (~20-35 mV) responses from *Drosophila* R1-R6 photoreceptors ([Appendix figure 17](#)).

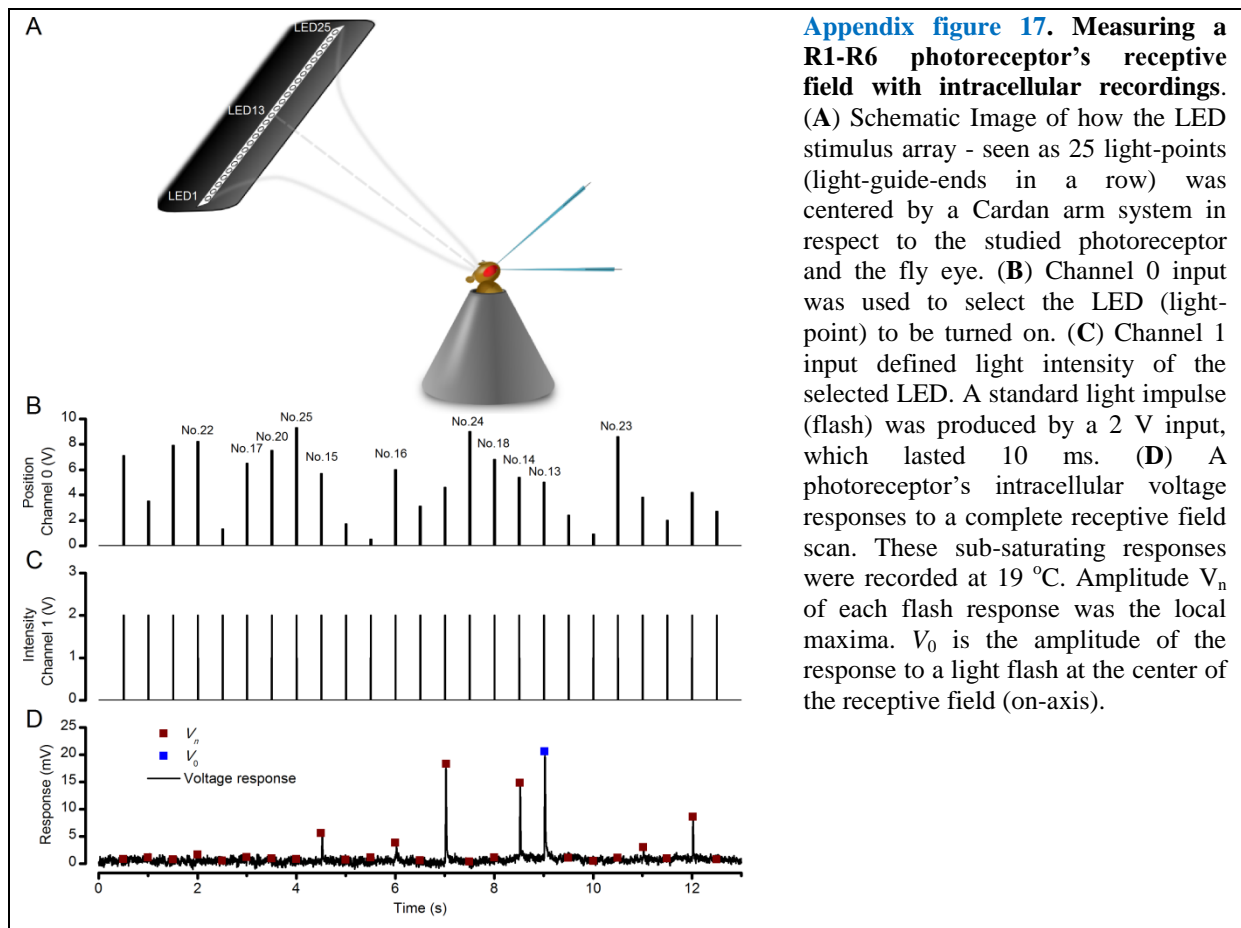
2

3 Light-point No.22 was 4-fold brighter than the others. However, no attempt was made to correct its  
4 intensity for three reasons. Firstly, it was located at the tested receptive fields' periphery, and thus had  
5 limited influence on the measurements. Secondly, because this "error" occurred stereotypically in  
6 every experiment, the brighter No.22 would not bias the comparative studies (see below). Lastly,  
7 having one brighter light-point was beneficial for other experiments, as will be shown in [Appendix 6](#).

1 Two Lamina LED pads, each with 39 similar LEDs, provided ambient illumination to  
2 moderately light-adapt the tested photoreceptors. The pads were located at the outer half and outside  
3 each tested cell's receptive field (**Appendix figure 15**). Thus, a large portion of their light projected  
4 onto the neighboring photoreceptors. But the pads also illuminated the whole recording chamber,  
5 revealing its spatial structure and possibly inducing spatial processing in the lamina network. Light  
6 from each of the pad's LEDs peaked at 460 nm (**Appendix figure 16B**), delivering estimated  $\sim 2 \times$   
7  $10^5$  photons/s.

8  
9 **Pseudo-random receptive field scans.** Before recording intracellular voltage responses from a R1-R6  
10 photoreceptor, we located its receptive field center. This was done by flashing the light-point No.13  
11 (at the center of the array) and moving the array (with the Cardan arm along its XY-axes) until the  
12 maximum response amplitude was elicited. The array was then locked at this position.

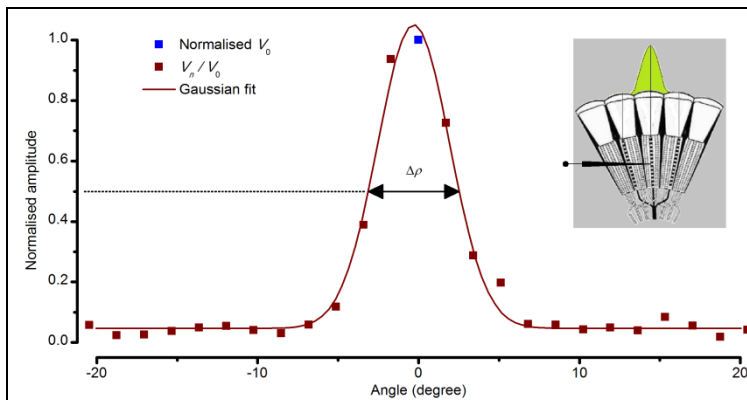
13 In the dark-adaptation experiments, the photoreceptor faced darkness (**Appendix figure 17A**)  
14 for 30-60 s before its receptive field was measured. In the light-adaptation experiments, preselected  
15 background illumination (using the LED pads: **Appendix figure 15**) was turned on 30-60 s before the  
16 corresponding receptive field measurement.  
17



18 A complete scan of a photoreceptor's receptive field comprised 25 subsaturating flashes from  
19 all the light-points, one after another in a pseudo-random order (**Appendix figure 17B**). Each flash  
20 lasted 10 ms, and was 490 ms apart from the next one (**Appendix figure 17C**). Although this inter-  
21 flash-interval largely rescued the photoreceptor sensitivity, spatiotemporal adaptation might have still  
22 affected their responses. For instance, a flash near the center of the receptive field would light-adapt  
23 the cell more than one at the periphery, possibly causing the response to the next flash to be  
24 artificially smaller. Therefore, by randomizing the order of flash positions - with the Matlab command  
25 `randperm(25)` - we could reduce this kind of potential adaptation effects.

26  
27 Channel 0 input was turned on only when Channel 1 was set to zero V; that is, in the resting

1 period when all the light-points were off. Otherwise, the transitions of Channel 0 input values would  
 2 generate running dot images. Each tested photoreceptor's responses to 2-5 repetitions of  
 3 pseudorandom scans were averaged (**Appendix figure 17D**) before the acceptance angle (or half-  
 4 maximum width),  $\Delta\rho$ , of its receptive field was determined (**Appendix figure 18**).  
 5



**Appendix figure 18. Estimating a dark-adapted *Drosophila* R1-R6 photoreceptor's receptive field and its half-width.** Flash response amplitudes  $V_n$  were initially normalized to  $V_0$ , the maximum response elicited by an on-axis light-point. A Gaussian curve was then fitted to these normalized values, yielding an estimate of the receptive field. Half-maximum width of this Gaussian function,  $\Delta\rho$ , defined the tested photoreceptor's acceptance angle. The

schematic fly eye inset clarifies how a single photoreceptor integrates light from the world spatially through its receptive field (green area), whilst being bounded by the ommatidial lens system. For a standard measurement, each tested photoreceptor's intracellular responses to 2-5 repetitions of pseudorandom scans (as shown in **Appendix figure 17**) were averaged.

6  
 7 **Gaussian white-noise (GWN) stimuli.** Light-point No.13 intensity was controlled by setting Channel  
 8 0 input to 5 V and modulating Channel 1 input with a white-noise time series, which had a mean  
 9 value of 2.5 V and cut-off frequency of 200 Hz. With these settings, light-point No.13 emitted  $2.5 \times$   
 10  $10^6$  photons/s at **Peak1** (451 nm) and  $3.75 \times 10^6$  photons/s at **Peak2** (575 nm) on average (**Table 2**).  
 11 But, as in other experiments, these intensities were reduced 100-fold by neutral density filtering  
 12

### 13 Receptive fields of dark-adapted photoreceptors

14 In every experiment, we first assessed the recorded photoreceptor's receptive field after dark-  
 15 adaptation (**Figure 7-figure supplement 1A**). Wild-type R1-R6s' mean acceptance angle, measured  
 16 as their receptive fields' half-maximum width,  $\Delta\rho$ , was  $9.47 \pm 0.36^\circ$  ( $\pm$  SEM,  $n = 19$  cells), ranging  
 17 from  $7.00^\circ$  to  $11.65^\circ$ . Interestingly, *hdc*<sup>JK910</sup> R1-R6's receptive fields were 10.9% narrower ( $p =$   
 18  $0.0397$ , two-tailed t-test). Their mean, minimum and maximum acceptance angles were  $8.44 \pm 0.32^\circ$   
 19 ( $n = 18$  cells),  $6.18^\circ$  and  $11.50^\circ$ , respectively.

20 Because each photoreceptor's flash response amplitudes,  $V_n$ , were directly used to estimate its  
 21 receptive field (**Figure 7-figure supplement 1B**), rather than being converted to angular sensitivities  
 22 (see above), the obtained  $\Delta\rho$  metric depended upon the cell's output/input characteristics and the test  
 23 flash intensity. To ensure that wild-type and *hdc*<sup>JK910</sup> photoreceptors'  $\Delta\rho$  comparison was unbiased by  
 24 variable on-axis light sensitivities, we also compared their maximum response amplitudes,  $V_0$ , and  
 25  $V_0/\Delta\rho$  relations.

26 The corresponding  $V_0$  values were very similar (**Figure 7-figure supplement 1B**) and mostly  
 27 within 20-35 mV sub-saturated linear range of the photoreceptors'  $V/\log(I)$  curves (Dau *et al.*, 2016).  
 28 Moreover, in both wild-type and the *hdc* mutant, the linear correlations between  $V_0$  and  $\Delta\rho$  reflected  
 29 only a weak trend of more sensitive photoreceptors (larger  $V_0$ ) having wider receptive fields (larger  
 30  $\Delta\rho$ ) (**Figure 7-figure supplement 1C, D**).

31 Together, these findings indicate that the narrower  $\Delta\rho$  of dark-adapted *hdc*<sup>JK910</sup> photoreceptors  
 32 neither resulted from altered phototransduction nor was an artefact of this measurement method.  
 33

### 34 Receptive fields of light-adapted photoreceptors

35 A photoreceptor's  $\Delta\rho$  measured under light-adaptation (at specific ambient illumination; **Appendix**  
 36 **figure 15**) should be smaller than during dark-adaptation. There are four reasons for this difference:

- 37 • Light-adaptation steepens a photoreceptor's  $V/\log(I)$  function (Laughlin & Hardie, 1978;  
 38 Matic & Laughlin, 1981; Eguchi & Horikoshi, 1984). This reduces the difference between  $I_0$   
 39 and  $I_{a50}$  (or the effective intensity that could evoke response amplitude  $V_2^0$ ), which in turn

1 leads to a smaller  $\alpha_{50}$  (or the corresponding angular position of  $I_{a50}$ ) and thus to a smaller  $\Delta\rho$ ,  
2 as reported by the chosen method.

- 3 • Because the test flash intensity was kept unchanged, their contrast would be lower during  
4 light-adaptation than in the dark-adaption experiments, further reducing the  $I_o/I_{a50}$  ratio,  $\alpha_{50}$   
5 and  $\Delta\rho$ .
- 6 • Light adaptation activates screening pigment migration, narrowing the intracellular pupil (*cf.*  
7 **Appendix 2, Appendix figure 3**). The narrower pupil effectively reduces the amount of light  
8 from off-axis angles that can be absorbed by rhodopsin-molecules in the rhabdomere (Hardie,  
9 1979; Smakman *et al.*, 1984; Stavenga, 2004a, b), reducing  $\Delta\rho$ .
- 10 • Theoretical studies and some experimental data suggest that in dim conditions neural signal  
11 summation from neighboring cells may enhance sensitivity. But in bright conditions, lack of  
12 summation, increased lateral inhibition or both improve image resolution (Srinivasan *et al.*,  
13 1982; van Hateren, 1992c, 1993a; Warrant, 1999; Klaus & Warrant, 2009).

14  
15 To quantify how moderate ambient light affects the fly eye's spatial responsiveness, we analyzed the  
16 receptive fields of six wild-type ( $n = 6$ ) and eight  $hdc^{JK910}$  ( $n = 8$ ) photoreceptors both at their dark-  
17 and light-adapted states.

18  
19 At the dark-adapted state, the acceptance angles of wild-type and  $hdc^{JK910}$  R1-R6s' receptive fields,  
20  $\Delta\rho$ , were  $9.65 \pm 1.06^\circ$  and  $8.16 \pm 0.62^\circ$  (mean  $\pm$  SEM), respectively (**Box 4.8A**). However, owing to  
21 the smaller test and control group sizes than in **Figure 7-figure supplement 1A**, this average  
22 difference (15.44%), though similar, was now statistically insignificant ( $p = 0.258$ , two-tailed t-test).

23  
24 At the light-adapted state, under the given ambient illumination (**Figure 7-figure supplement 2B**),  
25 the corresponding  $\Delta\rho$  values were  $7.70 \pm 0.52^\circ$  for wild-type photoreceptors and  $6.98 \pm 0.46^\circ$  for their  
26  $hdc^{JK910}$  counterparts. Thus, light-adaptation significantly reduced  $\Delta\rho$  values from dark-adaptation ( $p$   
27  $= 3.49 \times 10^{-4}$ , paired two-tailed t-test). Switching from the dark- to light-adapted states, wild-type  
28 photoreceptors' receptive fields narrowed down by  $18.44 \pm 3.5\%$  (**Figure 7-figure supplement 2C**),  
29 slightly more than those of mutants, which changed by  $13.68 \pm 3.37\%$ . Yet, none of these parameters  
30 differed significantly between the wild-type and mutant photoreceptors.

### 31 32 **R1-R6 acceptance angles are much broader than the theoretical prediction**

33 Based on the ommatidium dimensions, as extracted from histological images of fixed/non-living  
34 retinæ, and the waveguide optic theory, Stavenga (Stavenga, 2003b) calculated that the acceptance  
35 angles of dark-adapted *Drosophila* R1-R6 photoreceptors should be from  $3.8$  to  $5.0^\circ$  (as amended for  
36  $16.5 \mu\text{m}$  diameter ommatidium lens). Yet, our current ( $\Delta\rho = 9.47^\circ$ ; **Figure 7-figure supplement 1** and  
37 **2**) and earlier (Gonzalez-Bellido *et al.*, 2011) measurements ( $\Delta\rho = 8.23^\circ$ ; using **Method 2** above)  
38 clearly showed that their acceptance angles *in vivo* are in fact about twice as large. What kind of  
39 physical mechanism(s) could explain this discrepancy between the theory and measurements?

40 We briefly introduce here some key points of the new 'microsaccadic sampling hypothesis',  
41 which is examined in detail in **Appendixes 7-8**.

- 42 • Living R1-R6 photoreceptors are not still but transiently contract to light (Hardie & Franze,  
43 2012) (**Video 3**). We show in **Figure 8** (see also **Appendixes 7-8**) that this causes  
44 considerable horizontal rhabdomere movements (up to  $1.4 \mu\text{m}$ , peaking  $\sim 60$ - $150$  ms after a  
45 flash onset and returning back slower). As the lens system stays practically put, the  
46 rhabdomere tips shift away from the central axis, skewing the light input and narrowing the  
47 photoreceptors' receptive fields dynamically.
- 48 • Rhabdomere contractions also move their tips axially; transiently down the focal plane  
49 (**Video 2**).
  - 50 ○ In a dark-adapted state, rhabdomere tips are elongated upwards (closer to the ommatidium  
51 lens), and possibly out of focus, collecting light through the lens system over a wider  
52 space. Thus, R1-R6s' acceptance angles would be broader for light flashes spaced by  
53 normal (500 ms) intervals, which recover refractory microvilli, returning rhabdomeres to  
54 their old positions. But during a bright passing light stimulus, which progressively

1 contracts R1-R6s, their acceptance angles dynamically narrow as the rhabdomeres draw a  
2 bit deeper in the retina.

- 3 ○ At a moderate light-adaptation state (**Figure 7-figure supplement 2**), the intracellular  
4 pupil mechanism has reduced light input and the rhabdomere lengths should occupy a  
5 position (or set-point), which allows further contractions to light increments (*cf.* hair cells  
6 in the inner ear (Howard *et al.*, 1988)). However, here, R1-R6s' acceptance angles would  
7 still be broader for flashes with 500 ms intervals. Thus, the rhabdomeres would return to  
8 their pre-flash positions, which are closer to the lens than during a bright passing light  
9 stimulus.
- 10 ● Photomechanical R1-R6 contractions are partially levered by the adherence junctions (Tepass  
11 & Harris, 2007) from their rhabdomeres to the above cone cells and epithelial pigment cells,  
12 which form the inner wall of the ommatidium underneath the lens (**Figure 8F**). Thus, as the  
13 photoreceptors contract to light, their adherence junctions appear to pull the pigment cells,  
14 moving and narrowing the aperture (and the light beam) in the front of their rhabdomere tips  
15 (**Video 4**).

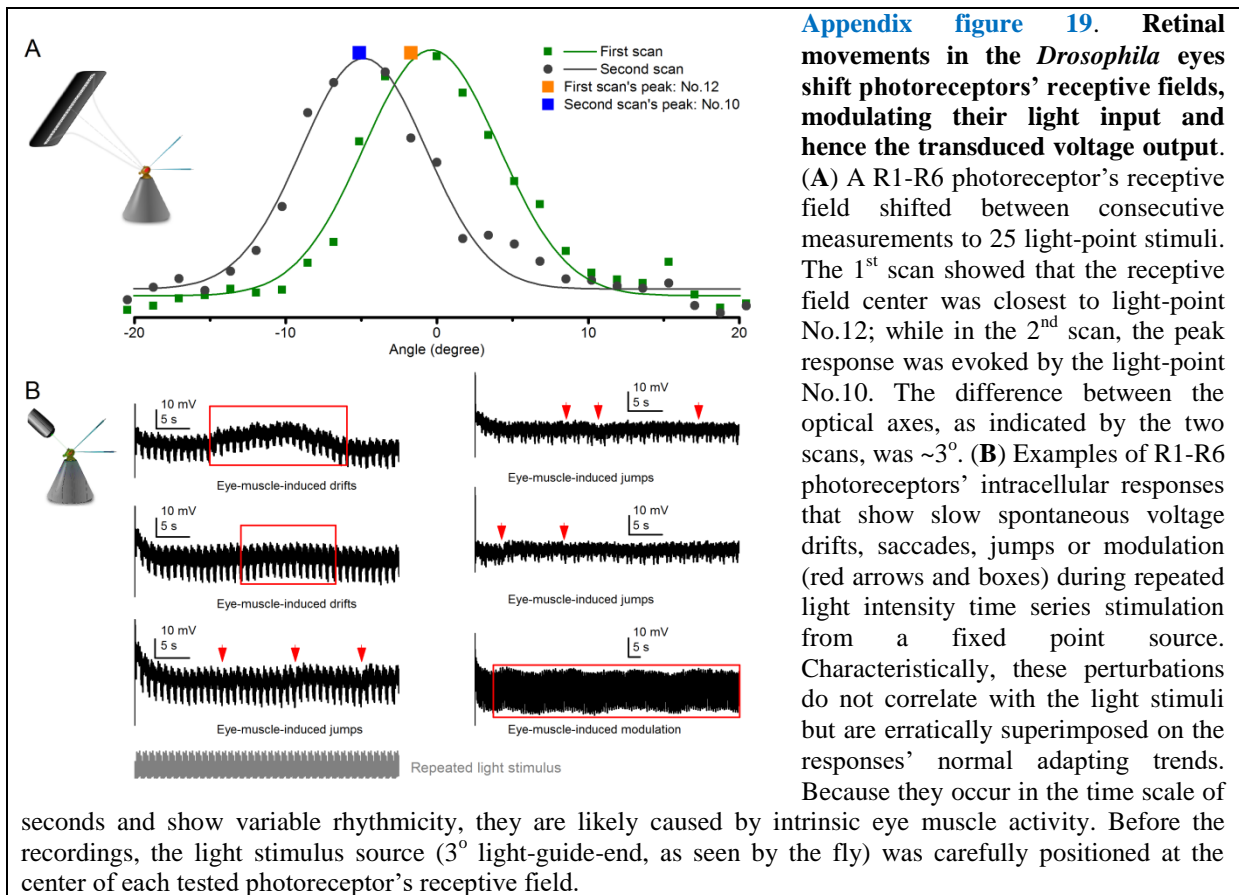
### 16 17 **Slow *Drosophila* retina movements**

18 Despite a *Drosophila*'s head and thorax being immobilized to the conical holder (**Appendix figure**  
19 **17A**), its eyes could still move affecting the electrophysiological recordings (Kirschfeld &  
20 Franceschini, 1969). Retinal movements, caused by spontaneous intraocular muscle activity, have  
21 been described in larger flies (Franceschini *et al.*, 1991; Franceschini & Chagneux, 1994;  
22 Franceschini *et al.*, 1995; Franceschini & Chagneux, 1997; Franceschini, 1998) and treated by  
23 different methods, including cooling, anesthesia and fixing their slightly pulled-out antennae  
24 (Smakman *et al.*, 1984).

25 Here we report possibly related but slower retinal movements in fixed *Drosophila*  
26 preparations *in vivo*. **Appendix figure 19A** shows an example, in which the optical axis of a R1-R6  
27 photoreceptor moved between two consecutive receptive field scans. In the 1<sup>st</sup> scan, the receptive field  
28 center, which was localized by the largest flash response, corresponded to the light-point No.12.  
29 However, the 2<sup>nd</sup> receptive field scan indicated that the cell's optical axis pointed toward the light-  
30 point No.10. This displacement corresponds to an angular movement of  $\sim 3^\circ$ . We found that about  
31 50% of photoreceptors, in which receptive fields were scanned more than once (8/18 wild-type and  
32 8/16 mutant cells), displayed similar retinal movements in the range of 1-3.5°. Moreover, these  
33 movements occurred in both front-to-back and back-to-front directions, validating that they were not  
34 equipment related artefacts; for example, not caused by gravitational drift in the 25 light-point  
35 stimulus array (**Appendix figure 15**).

36 It has been suggested that recordings from damaged fly photoreceptors may result in (i)  
37 extraordinarily wide acceptance angles, (ii) diminishing sensitivity (Wilson, 1975), or (iii) markedly  
38 asymmetrical receptive fields, attributed to artificial electrical coupling between neighboring cells  
39 (Smakman & Stavenga, 1987). To ensure that high-quality  $\Delta\rho$  measurements were presented in this  
40 study, we only considered data from photoreceptors in which intracellular responses were stable and  
41 repeatable, and their receptive fields reasonably symmetrical. However, we acknowledge that  
42 *Drosophila* eye movements can inadvertently affect the receptive field assessment accuracy.

43 The *slow* retinal movements and drifts that shift R1-R6 photoreceptors' receptive fields are  
44 likely driven by eye muscle (Hengstenberg, 1971) activity. These movements can modulate light input  
45 to photoreceptors, causing spontaneous dips and peaks in their output during continuous repetitive  
46 stimulation, as is sometimes seen during long-lasting intracellular recordings (**Appendix figure 19B**).  
47 Because this additional input modulation seems largely occur in the timescale of seconds, it should  
48 reduce mostly the low-frequency signal-to-noise ratio in the R1-R6 output. In this study, to obtain as  
49 good estimates as possible of the *Drosophila* photoreceptors' encoding capacity, we only used data  
50 from the very best (most stable) recording series. These recordings (**Figures 1-2; Figure 1-figure**  
51 **supplement 1; Figure 2-figure supplement 1**) showed very little or no clear signs of such  
52 perturbations.



1  
2  
3  
4  
5  
6  
7  
8  
9

Furthermore, in **Appendixes 7-8**, we quantify how all *Drosophila* photoreceptors exhibit *fast* light-triggered photomechanical micro-saccades, peaking  $\sim 100$  ms after the stimulus onset and lasting 0.2-3 s, depending upon the stimulus intensity. These microsaccades directly modulate light input from the moving objects and consequently photoreceptor output, and we show through simulations and recordings how they can improve the spatiotemporal resolution of neural images (**Figures 8 and 9; Figure 8-figure supplement 1 and Figure 9-figure supplement 1**).

## Conclusions

In this appendix, we described how receptive fields (spatial responsiveness) and acceptance angles ( $\Delta\rho$ ) of wild-type and synaptically-blind *hdc<sup>JK910</sup>* R1-R6 photoreceptors were estimated, using intracellular voltage responses to new light-point array stimulation. Their characteristics in the dark- and moderately light-adapted states, and after prolonged light stimulation, were compared to test the hypothesis that spatial information summation in the lamina contributes to *Drosophila* photoreceptor function. We found that the dark-adapted wild-type R1-R6s show wider receptive fields. But in steady illumination, the two photoreceptor groups'  $\Delta\rho$ -estimates adapted similarly.

Could the difference between the dark-adapted wild-type and *hdc<sup>JK910</sup>* receptive field widths result from recording artefacts? It is well known that LMCs' hyperpolarizing intracellular responses to light pulses depolarize the surrounding extracellular space (Shaw, 1975), seen as the on-transient in the electroretinogram (ERG) recordings (Heisenberg, 1971). Theoretically, these signals could be picked up by recording microelectrodes, adding artificial components to the intracellularly measured  $V_n$ , and so making wild-type photoreceptors' receptive fields appear wider (Hardie *et al.*, 1981). However, we can essentially rule out this notion because the Gaussian functions, which quantified the actual recordings, were fitted to their real flank amplitudes rather than to zero (**Appendix figure 18**). Consequently, any extra DC component would not affect the resulting  $\Delta\rho$ -estimates. Furthermore, our past comparative study, which included different synaptic mutant flies, failed to find clear signs for ERG contamination in high-quality intracellular wild-type photoreceptor recordings (Zheng *et al.*, 2006). Whereas by lacking neurotransmitter histamine, *hdc<sup>JK910</sup>* LMCs cannot respond to light (Burg

28

1 *et al.*, 1993; Melzig *et al.*, 1996; Melzig *et al.*, 1998), and thus *hdc*<sup>JK910</sup> photoreceptor recordings  
2 cannot be ERG contaminated. Hence, we conclude that ERG signals could only have marginal  
3 contribution to our results at most.

4 In fact, the dark-adapted photoreceptors'  $\Delta\rho$ -estimates constituted the most reliable data in  
5 this appendix, with the largest number of samples ( $n_{\text{wild-type}} = 19$ ,  $n_{\text{hdc}} = 18$  cells) obtained through  
6 consistent recording protocols. In every experiment, the receptive field assessment in the dark-adapted  
7 state was strictly the first examination, following the standard stimulus centering procedure. This  
8 minimized any potential downgrade in the recording quality or variation in the stimulation history.  
9 Notably, our estimate of WT *Drosophila* R1-R6 photoreceptors' average receptive field half-width in  
10 the dark-adapted state,  $\Delta\rho = 9.47 \pm 0.36^\circ$  ( $n = 19$  cells; see **Method 3**, above), is reasonably similar to  
11 the previous estimate of  $8.23 \pm 0.54^\circ$  ( $n = 11$  cells) (Gonzalez-Bellido *et al.*, 2011), which was  
12 obtained through a less stationary recording apparatus/method with more assumptions (see **Method 2**,  
13 above).

14 The dominant factors determining a fly photoreceptor's receptive field are optical, waveguide  
15 properties and, particularly for the chosen measurement method, the phototransduction characteristics  
16 (Snyder, 1977; Land, 1997; Stavenga, 2003b, a). For blowflies, it has been shown that the receptive  
17 field shape can be largely derived from the optical structure dimensions with the waveguide theory  
18 (Smakman *et al.*, 1984). Given the *hdc*<sup>JK910</sup> mutants' seemingly normal ommatidial and rhabdomere  
19 optics, as seen *in vivo* (**Appendix 7**) and under electron microscopy (**Appendix 5**; R1-R6 rhabdomere  
20 diameters,  $d$ , were ~96% of the wild-type), and their wild-type like photoreceptor voltage/intensity  
21 relations to brief light pulses (Dau *et al.*, 2016), it is reasonable to expect that their  $\Delta\rho$ -estimates  
22 would be close to wild-type. This should especially be true in light-adaptation, which is predicted to  
23 make photoreceptor output more independent of its neighbors (Atick, 1992; van Hateren, 1992c, b).  
24 And indeed, we found  $\Delta\rho$ -estimates of the light-adapted wild-type and *hdc*<sup>JK910</sup> photoreceptors alike.  
25 But because of this conformity, the 10.9% difference between their dark-adapted acceptance angles  
26 requires an additional explanation. Although at the flanks this difference increases (**Figure 7-figure**  
27 **supplement 1A**), it still may seem rather small when compared to the measured cell-to-cell variation  
28 within each genotype, with the respective maxima being 66% and 88% wider than the minima, and its  
29 statistical significance becomes less with fewer samples (**Figure 7-figure supplement 2A**).  
30 Nevertheless, the finding is conceptually important as it supports an expansion in the classic spatial  
31 vision paradigm; from the optical constraints to spatial information summation in the network (Stockl  
32 *et al.*, 2016).

33 The dark-adapted wild-type photoreceptors' wider receptive fields are consistent with what  
34 we know about how synaptic inputs are channeled from lamina interneurons to R1-R6 axons  
35 (Meinertzhagen & Oneil, 1991; Sinakevitch & Strausfeld, 2004; Zheng *et al.*, 2006; Zheng *et al.*,  
36 2009; Abou Tayoun *et al.*, 2011; Rivera-Alba *et al.*, 2011; Hu *et al.*, 2015). Thus, the corresponding  
37 narrower receptive fields of mutant photoreceptors seem most sensibly attributed to the missing  
38 excitatory feedback modulation from their interneurons (Zheng *et al.*, 2006; Nikolaev *et al.*, 2009;  
39 Zheng *et al.*, 2009; Dau *et al.*, 2016). As shown by intracellular recordings (Zheng *et al.*, 2006; Dau *et*  
40 *al.*, 2016), feedforward and feedback signals dynamically contribute to photoreceptor and interneuron  
41 outputs *in vivo*. When the probability of light saturation is low, the stronger synaptic transmission in  
42 both pathways helps to amplify their response amplitudes.

43 Therefore, taken together with the findings of Dubs *et al.* (1981) and Dubs (1982), these  
44 results suggest that under dim illumination, lateral excitation spreads synaptically within the lamina of  
45 the fly visual system. Spatial information summation is likely implemented by the first-order  
46 interneurons and fed back to photoreceptors through connections (Meinertzhagen & Oneil, 1991;  
47 Rivera-Alba *et al.*, 2011) that utilize excitatory neurotransmitters (Zheng *et al.*, 2006; Hu *et al.*, 2015).  
48 This model is further supported by our anatomical observations (**Appendix 5** and **Appendix 7**), which  
49 imply that there are no major developmental defects in *hdc*<sup>JK910</sup> retina and that their lens systems and  
50 rhabdomere sizes are broadly wild-type-like.

## Appendix 5: R1-R6 rhabdomere sizes, neural superposition and hyperacuity schemes

### Overview

This appendix shows how R1-R6 rhabdomere diameters vary systematically and consistently in *Drosophila* ommatidia and provides supporting background information for the results presented in [Figures 7-9](#) and [Appendix 4](#).

In this appendix:

- We measure wild-type and *hdc<sup>JK910</sup>* histamine-mutant (Burg *et al.*, 1993; Melzig *et al.*, 1996; Melzig *et al.*, 1998) R1-R6 photoreceptors' rhabdomere sizes from the electron micrographs of their retinæ.
- We compare these measurements to their electrophysiologically measured receptive field estimates ([Appendix 4](#)).
- We show that the mean wild-type R1-R6 rhabdomere diameter,  $d_{R1-R6}$ , is only ~4.1% wider than in *hdc<sup>JK910</sup>* mutant eyes. This difference may contribute in part to their 10.9% wider average acceptance angle ( $\Delta\rho$ ) in a dark-adapted state ([Appendix 4](#)), but cannot fully explain it (see also [Appendix 7](#)).
- We further show that in both phenotypes R1, R3 and R6 rhabdomeres are systematically larger than R2 and R4 rhabdomeres. As for the maximum difference, the mean R1 rhabdomere diameter ( $d_{R1} = 1.8433 \pm 0.1294 \mu\text{m}$ , mean  $\pm$  SD) is about 18% wider than that of R4 ( $d_{R4} = 1.5691 \pm 0.0915 \mu\text{m}$ ,  $n = 25$ ,  $p = 2.3419 \times 10^{-11}$ , 2-tailed t-test).
- These findings imply that each R1-R6 photoreceptor should have a different receptive field size (coinciding with their considerable  $\Delta\rho$  variation seen in [Appendix 4](#), [Figure 7-figure supplement 1C](#)).
- Our results further suggest an asymmetric information integration model, in which the neural superposition of different-sized overlapping receptive fields (of the neighboring R1-R6s) has a potential to contribute in enhancing *Drosophila*'s visual acuity beyond the presumed optical limits of its compound eyes (as revealed by behavioral experiments in [Appendix 9](#)).

### Readjusting the current theoretical viewpoint

Neural superposition eyes provide more samples from local light intensity changes for each image pixel, represented by large monopolar cell (L1 and L2) outputs. In the conventional viewpoint, each pixel's signal-to-noise improves by  $\sqrt{6}$  because its L1 and L2 receive similar inputs from six "physiologically identical" R1-R6 photoreceptors, which sample information from the same small area in the visual space. Thus, the conventional assumptions and limits for neural superposition performance are:

- Each R1-R6 functions virtually identically, generating similar outputs to the same light input
- Each R1-R6 in superposition has an identical receptive field size and shape
- The receptive fields in superposition overlap perfectly
- Each image pixel represents sampling and processing within its inter-ommatidial angle
- Inter-ommatidial angle sets the visual resolution of the *Drosophila* eye

This appendix presents anatomical and theoretical evidence that these assumptions and limits are overly simplistic and suggests ways the real neural images could be sharpened beyond them to improve *Drosophila* vision.

### Electron micrographs

**Fixation.** Flies were cold anaesthetized on ice and transferred to a drop of pre-fixative (modified Karnovsky's fixative (Shaw *et al.*, 1989): 2.5% glutaraldehyde, 2.5% paraformaldehyde in 0.1 M sodium cacodylate buffered to pH 7.3) on a transparent agar dissection dish. Dissection was performed using a shard of a razor blade (Feather S). Flies were restrained on their backs with insect pins through their lower abdomen and distal proboscis. Their heads were severed, probosces excised, and halved. The left half-heads were collected in fresh pre-fixative and kept for 2 h at room temperature under normal lighting conditions.

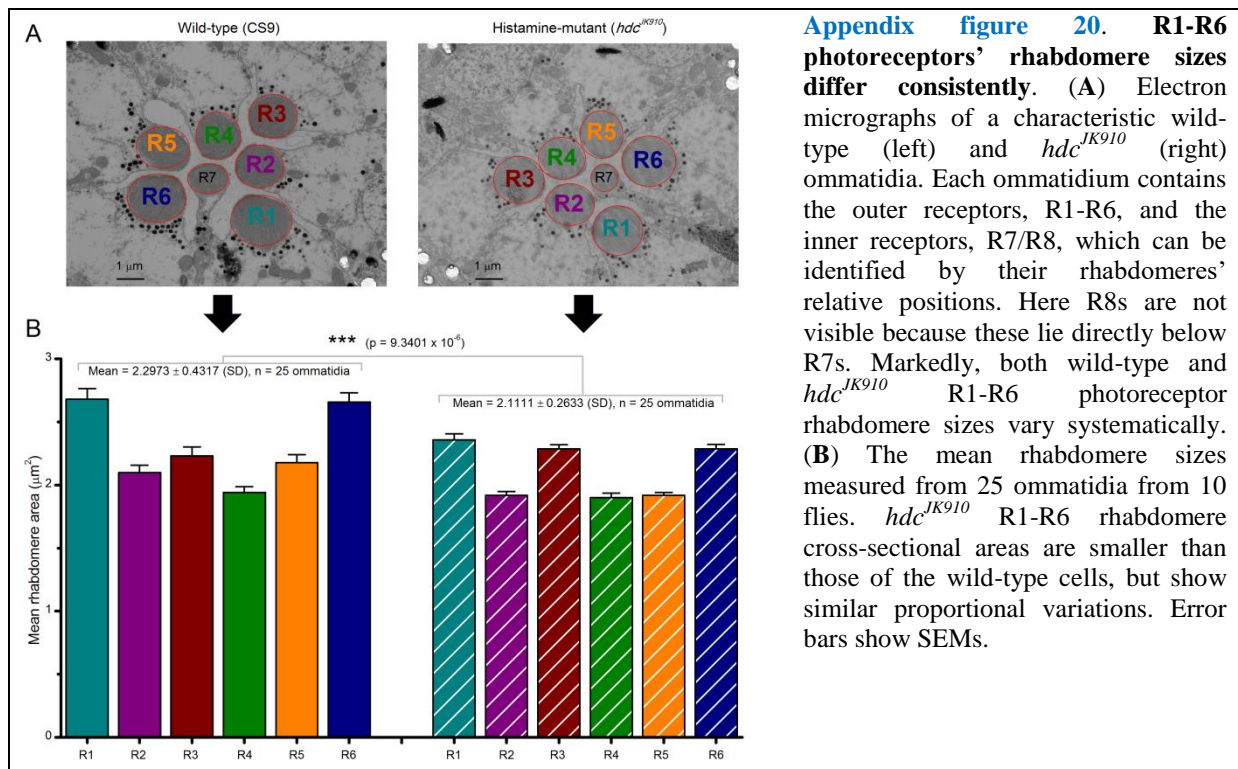
After pre-fixation, the half-heads were washed (2 x 15 min) in 0.1 M Cacodylate buffer, and

1 then transferred to a 1 h post-fixative step, comprising Veronal Acetate buffer and 2% Osmium  
2 Tetroxide in the fridge (4 °C). They were moved back to room temperature for a 9 min wash (1:1  
3 Veronal Acetate and double-distilled H<sub>2</sub>O mixture), and serially dehydrated in multi-well plates with  
4 subsequent 9 min washes in 50%, 70%, 80%, 90%, 95% and 2 x 100% ethanol.

5 Post-dehydration, the half-heads were transferred to small glass vials for infiltration. They  
6 were covered in Propylene Oxide (PPO) for 2 x 9 min, transferred into a 1:1 PPO:Epoxy resin mixture  
7 (Poly/Bed® 812) and left overnight. The following morning, the half-heads were placed in freshly  
8 made pure resin for 4 h, and placed in fresh resin for a further 72 h at 60 °C in the oven. Fixation  
9 protocol was kindly provided by Professor Ian Meinertzhagen at Dalhousie University, Canada.

10  
11 **Sectioning and staining.** Embedded half-heads were first sectioned (at 0.5 μm thickness) using a  
12 glass knife, mounted in an ultramicrotome (Reichert-Jung Ultracut E, Germany). Samples were  
13 collected on glass slides, stained using Toluidine Blue and observed under a light microscope. This  
14 process was repeated and the cutting angle was continuously optimized until the correct orientation  
15 and sample depth was achieved; stopping when approximately 40 ommatidia were discernible. The  
16 block was then trimmed and shaped for ultra-thin sectioning. The trimming was necessary to reduce  
17 cutting pressure on the sample-block and resulting sections, thus helping to prevent “chattering” and  
18 compression artefacts. Ultra-thin sections (85 nm thickness) were cut using a diamond cutting knife  
19 (DiATOME Ultra 45°, USA), mounted and controlled using the ultramicrotome. The knife edge was  
20 first cleaned using a polystyrol rod to ensure integrity of the sample-blocks. The cutting angles were  
21 aligned and the automatic approach- and return-speeds set on the microtome. Sectioning was  
22 automatic and samples were collected in the knife water boat.

23 Sections were transferred to Formvar-coated mesh-grids and stained for imaging: 25 min in  
24 Uranyl Acetate; a double-distilled H<sub>2</sub>O wash; 5 min in Reynolds’ Lead Citrate (Reynolds, 1963); and  
25 a final double-distilled H<sub>2</sub>O wash.  
26



27

28 **Rhabdomere measurements.** Transmission EM images for R1-R6 rhabdomere size comparisons were  
29 taken below the rhabdomere tips, as sectioned 25 μm down from the corneal surface of the  
30 ommatidium lens. 25 wild-type and *hdc<sup>JK910</sup>* ommatidia (n = 25) from 10 flies of each phenotype were  
31 used to estimate R1-R6 rhabdomere sizes. The images were processed with ImageJ software. Because  
32 the rhabdomere cross-sectional area is often better approximated by an ellipse than a circle

1 (**Appendix figure 20A**), for greater accuracy, its circumference was fitted with an ellipse.

2 For an EM rhabdomere area,  $A$ , its mean diameter was then taken:  $d = 2 \times \sqrt{\frac{A}{\pi}}$ . Note that the  
 3 obtained mean rhabdomere diameter estimates are somewhat smaller than the previous estimates,  
 4 which measured the minimum and maximum rhabdomere diameters from edge-to-edge (Gonzalez-  
 5 Bellido, 2009; Gonzalez-Bellido *et al.*, 2011). Here, instead, we standardized the measurement  
 6 protocol to reduce  $d$ -estimation bias between the wild-type and  $hdc^{JK910}$  electron micrographs to  
 7 obtain straightforward statistical comparisons of their means. Nevertheless, both these and the  
 8 previous (Gonzalez-Bellido, 2009)  $d$ -estimates indicated systematic rhabdomere size differences.

9  
 10 **R1-R6 rhabdomere sizes differ**

11 *Drosophila* R1-R6 photoreceptors' rhabdomere sizes vary systematically and consistently in each  
 12 ommatidium (**Appendix figure 20B**). R1 and R6 rhabdomere cross-sectional areas are always the  
 13 largest and R4 rhabdomeres the smallest (**Table 3**).

14 Theoretically, a fly photoreceptor's receptive field size depends upon its rhabdomere  
 15 diameter,  $d$  (**Eq. A4.3**). This relationship was recently supported experimentally by comparing the  
 16 rhabdomere diameters and acceptance angle estimates,  $\Delta\rho$ , of *Drosophila* R1-R6 photoreceptors to  
 17 those of killer fly (*Coenosia attenuata*), both of which eyes have rather similar ommatidial lens sizes  
 18 (16–17 vs 14–20  $\mu\text{m}$ ) and focal lengths (21.36 vs 24.70  $\mu\text{m}$ ) (Gonzalez-Bellido *et al.*, 2011), *cf.* **Eq.**  
 19 **A4.3**. In ♀ *Drosophila*, maximum  $d$  was  $\sim 2 \mu\text{m}$  and in ♀ *Coenosia*  $\sim 1 \mu\text{m}$ , while *Drosophila*'s mean  
 20  $\Delta\rho$ -estimate was  $8.23 \pm 0.54^\circ$  and *Coenosia*'s  $2.88 \pm 0.07^\circ$  (Gonzalez-Bellido *et al.*, 2011). Thus, the  
 21 wider rhabdomere tip correlates strongly with the wider receptive field.

22 Accordingly, with each *Drosophila* ommatidium hosting R1-R6 rhabdomeres of distinct size  
 23 differences (**Appendix figure 20B**, left; **Table 3**), the receptive fields of the neighboring R1-R6,  
 24 which are pooled together in neural superposition, should differ in size and overlap broadly. These  
 25 observations and analysis concur with the broad variability of the intracellularly measured wild-type  
 26 R1-R6s' receptive field widths (**Appendix 4: Figure 7-figure supplement 1A, C**).

27 However, although collectively the mean wild-type R1-R6 rhabdomere cross-sectional areas  
 28 (**Tables 4-5**) are larger than their  $hdc^{JK910}$  counterparts (**Appendix figure 20B**), their corresponding  
 29 diameter differences are small. The average wild-type R1-R6 rhabdomere diameter, (WT  $d_{R1-R6} = 1.70$   
 30  $\pm 0.15 \mu\text{m}$ ; mean  $\pm$  SD,  $n = 150$  rhabdomeres; **Figure 5**) is only  $\sim 4.1\%$  wider than in  $hdc^{JK910}$  mutant  
 31 eyes ( $hdc^{JK910} d_{R1-R6} = 1.64 \pm 0.10 \mu\text{m}$ ;  $n = 150$  rhabdomeres), as extrapolated from the ellipsoid  
 32 rhabdomere area fits. Thus,  $hdc^{JK910}$  photoreceptors' smaller average rhabdomere diameters can  
 33 contribute to their  $\sim 10.9\%$  narrower  $\Delta\rho$  (**Appendix 4: Figure 7-figure supplement 1A, D**), but  
 34 cannot fully explain it (**Appendix figure 20B**, right).

35

Significance t-test 2-tail	wild-type R1	wild-type R2	wild-type R3	wild-type R4	wild-type R5	wild-type R6
wild-type R1	N/A	5.3626 x $10^{-7}$	1.3033 x $10^{-4}$	3.6882 x $10^{-10}$	1.5564 x $10^{-5}$	0.8282
wild-type R2	5.3626 x $10^{-7}$	N/A	0.1531	0.0371	0.3760	3.4906 x $10^{-7}$
wild-type R3	1.3033 x $10^{-4}$	0.1531	N/A	0.0011	0.5736	1.3187 x $10^{-4}$
wild-type R4	3.6882 x $10^{-10}$	0.0371	0.0011	N/A	0.0047	1.2193 x $10^{-10}$
wild-type R5	1.5564 x $10^{-5}$	0.3760	0.5736	0.0047	N/A	1.3479 x $10^{-5}$
wild-type R6	0.8282	3.4906 x $10^{-7}$	1.3187 x $10^{-4}$	1.2193 x $10^{-10}$	1.3479 x $10^{-5}$	N/A

**Table 3. Statistical comparison of wild-type Canton-S R1-R6 rhabdomere cross-sectional areas.** The table gives the differences as p-values, calculated for 25 ommatidia of 10 flies at the same retinal depth. Red indicates statistically significant difference. R4 rhabdomeres are smaller than the other rhabdomeres, whereas R1 and R6 are always the largest.

1

Significance t-test 2-tail	<i>hdc<sup>JK910</sup></i> R1	<i>hdc<sup>JK910</sup></i> R2	<i>hdc<sup>JK910</sup></i> R3	<i>hdc<sup>JK910</sup></i> R4	<i>hdc<sup>JK910</sup></i> R5	<i>hdc<sup>JK910</sup></i> R6
<i>hdc<sup>JK910</sup></i> R1	N/A	4.7387 x 10 <sup>-10</sup>	0.2281	6.3122 x 10 <sup>-10</sup>	1.0125 x 10 <sup>-10</sup>	0.2335
<i>hdc<sup>JK910</sup></i> R2	4.7387 x 10 <sup>-10</sup>	N/A	7.9300 x 10 <sup>-11</sup>	0.7006	0.9897	2.0471 x 10 <sup>-10</sup>
<i>hdc<sup>JK910</sup></i> R3	0.2281	7.9300 x 10 <sup>-11</sup>	N/A	1.9466 x 10 <sup>-10</sup>	5.0272 x 10 <sup>-12</sup>	0.9921
<i>hdc<sup>JK910</sup></i> R4	6.3122 x 10 <sup>-10</sup>	0.7006	1.9466 x 10 <sup>-10</sup>	N/A	0.6830	4.3275 x 10 <sup>-10</sup>
<i>hdc<sup>JK910</sup></i> R5	1.0125 x 10 <sup>-10</sup>	0.9897	5.0272 x 10 <sup>-12</sup>	0.6830	N/A	1.6775 x 10 <sup>-11</sup>
<i>hdc<sup>JK910</sup></i> R6	0.2335	2.0471 x 10 <sup>-10</sup>	0.9921	4.3275 x 10 <sup>-10</sup>	1.6775 x 10 <sup>-11</sup>	N/A

**Table 4. Statistical comparison of *hdc<sup>JK910</sup>* R1-R6 rhabdomere cross-sectional areas.** The table gives the differences as p-values, calculated for 25 ommatidia of 10 flies at the same retinal depth. Red indicates statistically significant difference. R2, R4 and R5 rhabdomeres are smaller than R1, R3 and R6 rhabdomeres.

2

Significance t-test 2-tail	wild-type R1	wild-type R2	wild-type R3	wild-type R4	wild-type R5	wild-type R6
<i>hdc<sup>JK910</sup></i> R1	0.0014	0.0012	0.1434	1.0091 x 10 <sup>-7</sup>	0.0302	0.0015
<i>hdc<sup>JK910</sup></i> R2	1.8211 x 10 <sup>-11</sup>	0.0078	1.5520 x 10 <sup>-4</sup>	0.6952	7.1690 x 10 <sup>-4</sup>	3.5405 x 10 <sup>-12</sup>
<i>hdc<sup>JK910</sup></i> R3	5.1489 x 10 <sup>-5</sup>	0.0073	0.4818	1.8478 x 10 <sup>-7</sup>	0.1415	3.8432 x 10 <sup>-5</sup>
<i>hdc<sup>JK910</sup></i> R4	1.7483 x 10 <sup>-11</sup>	0.0051	1.0904 x 10 <sup>-4</sup>	0.5015	4.9066 x 10 <sup>-4</sup>	3.7421 x 10 <sup>-12</sup>
<i>hdc<sup>JK910</sup></i> R5	9.2505 x 10 <sup>-12</sup>	0.0056	1.0272 x 10 <sup>-4</sup>	0.6710	4.8280 x 10 <sup>-4</sup>	1.5313 x 10 <sup>-12</sup>
<i>hdc<sup>JK910</sup></i> R6	5.6987 x 10 <sup>-5</sup>	0.0083	0.4903	2.8960 x 10 <sup>-7</sup>	0.1480	4.3539 x 10 <sup>-5</sup>

**Table 5. Statistical comparison of wild-type and *hdc<sup>JK910</sup>* R1-R6 rhabdomere cross-sectional areas.** The table gives the differences as p-values, calculated for 25 ommatidia of 10 flies at the same retinal depth. Red indicates statistically significant difference. The wild-type and mutant R3 and R4 rhabdomeres are the same size (highlighted in bold); the other wild-type rhabdomeres are larger than their respective counterparts.

3

4

### Theoretical models for spatial hyperacuity

5

6

7

8

9

10

11

12

13

14

15

16

17

18

19

20

21

22

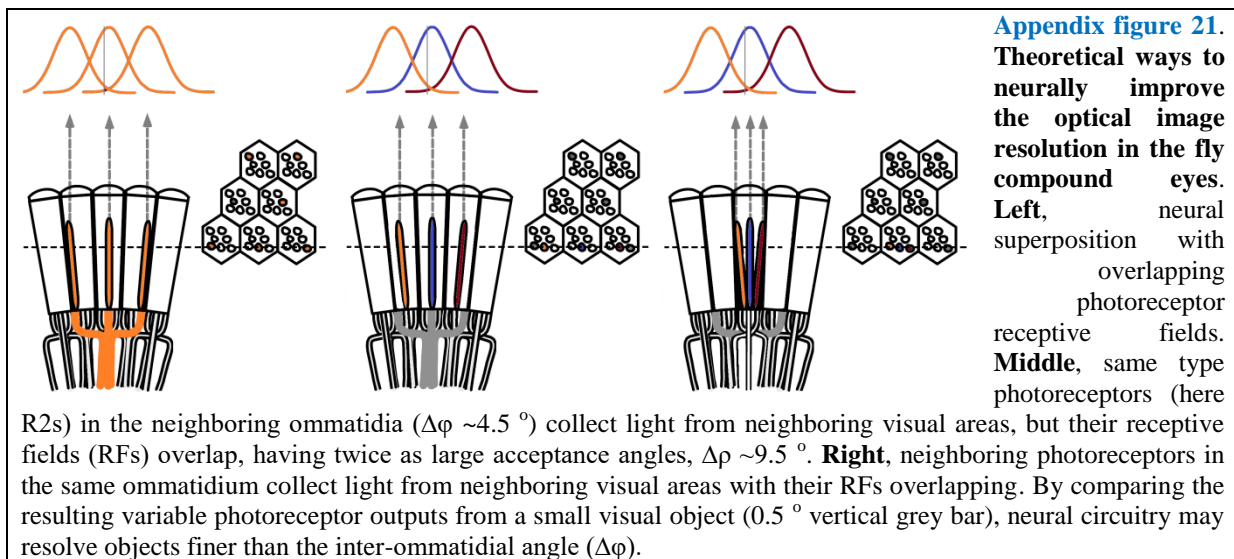
In the *Drosophila* compound eye, R1-R6 photoreceptors' mean acceptance angle ( $\Delta\rho \sim 9.5^\circ$ ) is on average about twice as wide (see **Appendix 4**) as its mean inter-ommatidial angle ( $\Delta\phi \sim 4.5^\circ$ ) (Gonzalez-Bellido *et al.*, 2011). Such an eye design could potentially facilitate spatial hyperacuity through neural image processing. In the vein of previous suggestions for manmade optoelectrical systems (Luke *et al.*, 2012) and retinae of other species (Zurek & Nelson, 2012), we consider three alternative hypothetical scenarios based upon neighboring R1-R6s' overlapping receptive fields (RFs).

The first case (**Appendix figure 21**, left) considers RF variations of the photoreceptors in neural superposition. An image of an object (here, a thin  $1^\circ$  vertical bar, grey) stimulates simultaneously eight photoreceptors (R1-R8), which gather light information about the same area in the visual space by their overlapping RFs (for clarity only R1-R3' RFs are shown; orange Gaussians). However, because the rhabdomere diameters,  $d$ , vary considerably and consistently between them (e.g. R1 and R6 rhabdomere diameters areas are  $\sim 18\%$  wider than those of R4s; **Appendix figure 20**), so could also be their RF sizes (see **Appendix 4**, Eq. A4.3), causing overlaps. Six of these inputs (R1-R6) are pooled in the lamina. Consequently, even a small ( $1^\circ$ ) displacement of the vertical bar stimulus (grey) could lead to variable but specific light intensity modulations in each of the six converging input channels. Their signals to LMCs (L1-L3), which in high signal-to-noise conditions transforms input modulations into phasic responses (Zettler & Järvilehto, 1972; Järvilehto & Zettler,

1 1973; Zheng *et al.*, 2006; Zheng *et al.*, 2009; Wardill *et al.*, 2012), could therefore be different before  
2 and after the bar displacement and possibly neurally detectable.

3 In the second case (**Appendix figure 21**, middle), six photoreceptor cells of the same type  
4 (say R2s) in the neighboring ommatidia gather light information from the neighboring small visual  
5 areas ( $\sim 4.5^\circ$  apart, as separated by the interommatidial angle), but their receptive fields ( $\sim 9.5^\circ$  half-  
6 widths) overlap; for clarity only three R2s are shown: orange, blue and red. Lateral connections (L4,  
7 Lawf and Am cells) between lamina neuro-ommatidia could then be used by LMCs to compare their  
8 outputs, enhancing the spatial resolution of each neural channel (see **Appendix 2**, **Appendix figure**  
9 **7**).

10 In the third case (**Appendix figure 21**, right), R1-R6 photoreceptor cells in the same  
11 ommatidium gather light information from the neighboring small visual areas, but their receptive  
12 fields overlap; again for clarity only three: orange (R1), blue (R2) and red (R3) are shown. Lateral  
13 connections (L4, Lawf and Am cells) between adjacent lamina neuro-ommatidia may enable LMCs to  
14 compare their outputs, enhancing the spatial resolution of each neural channel.  
15



16 All these circuit models could theoretically contribute to motion vision hyperacuity, which  
17 occurs when a stationary *Drosophila* eye resolves object motion finer than its  $\sim 4.5^\circ$  inter-ommatidial  
18 angle (the average sampling point or photoreceptor spacing). And crucially, in **Appendix 10**, we use a  
19 flight simulator system to demonstrate and quantify *Drosophila* hyperacute optomotor behavior to  
20 sub-interommatidial stimuli ( $1-4^\circ$ ). However in **Appendix 7-8**, we further provide decisive evidence  
21 that the spatiotemporal resolution of the early neural images is improved by synchronized and  
22 coherent photomechanical rhabdomere contractions (Hardie & Franze, 2012), which move and  
23 narrow R1-R6s' receptive fields. Together with refractory information sampling, this enables  
24 photoreceptors to encode space in time. Therefore, as the RFs narrow with moving stimuli, this  
25 reduces the overlap between the neighboring RFs and, consequently, affects the potential resolving  
26 power of the circuit models in **Appendix figure 21**.  
27

28 We conclude that **at the photoreceptor level** the overlapping RFs provide neither necessary  
29 nor sufficient mechanistic explanations for the *Drosophila* spatiotemporal hyperacuity. However, **at**  
30 **the lamina interneuron level**, such connectivity arrangements may further enhance hyperacute vision.  
31 It is also possible that any kind of retinal image enhancement would be further coordinated centrally  
32 to match the visual needs of a locomoting fly. In walking blowflies, intraocular muscles in both the  
33 left and right eye seem to contract synchronously with increasing rates, causing vergence eye  
34 movements (Franceschini *et al.*, 1991; Franceschini & Chagneux, 1994; Franceschini *et al.*, 1995;  
35 Franceschini & Chagneux, 1997; Franceschini, 1998). **Finally, we note that** in lobula plate motion  
36 sensitive cells, responses to moving visual stimuli increase with locomotion (Chiappe *et al.*, 2010;  
37 Haag *et al.*, 2010; Maimon *et al.*, 2010; Tang & Juusola, 2010), **although there is currently no**  
38 **evidence to relate this phenomenon to hyperacuity, as characterized here.**

1  
2  
3  
4  
5  
6  
7  
8  
9  
10  
11  
12  
13  
14  
15

**Possible dynamics arising from connectivity and variable rhabdomere sizes**

Temporal output modulation through gap-junctions between R1-R6 and R7-R8 photoreceptor axons could further contribute, as a possible network mechanism, to the acuity improvements that we report in this publication (Figures 7-8; see Appendix 6). *Drosophila* R1-R6s have larger rhabdomeres, each with ~30,000 microvilli, whereas those of R7s and R8s contain only ~15,000. Owing to superposition in each neuro-ommatidium, both of these photoreceptor classes integrate photons from the same small area in space, but for given light changes, the macroscopic R1-R6 output rises and decays faster than those of R7s and R8s. This is because R1-R6 rhabdomeres integrate twice as many samples (quantum bumps) from the same stimulus and their membranes have likely smaller time constant (Anderson & Laughlin, 2000). Therefore, at each moment in time, R1-R6 and R7-R8 outputs carry a dynamic phase difference. If their responses were to antagonize each other through the gap-junctions between R6 and R7/R8 axons (Shaw, 1984; Shaw *et al.*, 1989; Wardill *et al.*, 2012), similar to the crosstalk between *Calliphora* R7 and R8 outputs (Hardie, 1984), phasic R1-R6 output components could be enhanced even further.

## 1 **Appendix 6: Neural images of moving point-objects (R1-R6 recordings vs. classic predictions)**

### 3 **Overview**

4 This appendix describes a new method to measure *Drosophila* photoreceptor output to moving dots,  
5 and shows how these responses provide much higher visual resolution and motion blur resistance than  
6 what is predicted by the classic theories, supporting the results in [Figures 7-9](#).

8 In this appendix:

- 9 • We measure how well dark- and moderately light-adapted wild-type *Drosophila* R1-R6  
10 photoreceptors resolve bright dots (point-objects), which cross their receptive fields at  
11 different speeds.
- 12 • We compare these intracellular recordings to those of histamine-mutants, *hdc<sup>JK910</sup>* (Burg *et al.*,  
13 1993; Melzig *et al.*, 1996; Melzig *et al.*, 1998), in which first-order interneurons are blind  
14 (receive no neurotransmitter from photoreceptors) and thus incapable of feedback-modulating  
15 the photoreceptor output.
- 16 • We further record voltage responses of blowfly (*Calliphora vicina*) R1-R6 photoreceptors to  
17 moving point-objects, as an additional test of our experimental setup, stimulus paradigm and  
18 mathematical analyses, validating this method.
- 19 • We evaluate the wild-type and mutant recordings against their respective classic model  
20 simulations, in which each recorded receptive field is convolved by the same cell's impulse  
21 response.
- 22 • Our results indicate that both wild-type and *hdc<sup>JK910</sup>* R1-R6s resolve moving dots about  
23 equally well, and significantly better than the corresponding classic model simulations.
- 24 • These findings demonstrate that the classic deterministic photoreceptor models (Srinivasan &  
25 Bernard, 1975; Juusola & French, 1997; Land, 1997) for resolving moving objects grossly  
26 underestimate the visual resolving power of real photoreceptors.
- 27 • Consequently, the classic theory overestimates the effects of motion blur on *Drosophila*  
28 vision during saccadic behaviors.

### 30 **Retinal limitations and capacity to resolve moving objects**

31 A single photoreceptor's voltage responses can give important insight into neural image processing  
32 behind a fly's ability to detect small objects, whether in high-speed chasing flights or against a  
33 cluttered background (Burton & Laughlin, 2003; Brinkworth *et al.*, 2008). Theoretically, when a  
34 point-object moves uniformly across an array of photoreceptors, each cell would produce a similar  
35 response. But these responses would be displaced in time,  $t$ , which it takes for the object to travel  
36 between two adjacent cells' receptive field centers (Srinivasan & Bernard, 1975). Thus, the response  
37 of the whole array, as a collective neural representation of the moving point-object, would be a  
38 travelling pattern with a mirrored waveform. Mathematically, this can be extrapolated from a single  
39 photoreceptor's response. We now apply this classic approach to simplify the questions about neural  
40 images of moving point-objects and compare its predictions to R1-R6s' spatiotemporal responses.

41 First, we consider the problem of neural latency compensation in motion perception. This is  
42 related to the flash-lag effects observed in humans (Krekelberg & Lappe, 2001; Nijhawan, 2002). Due  
43 to the inevitable phototransduction delays, every sighted animal should encounter this problem and  
44 *Drosophila* is not an exception. At 19 °C, its photoreceptors' voltage responses rise ~10 ms from the  
45 light flash and peak 15-30 ms later (Juusola & Hardie, 2001b). Given that a fly's saccadic turning  
46 speed (Fry *et al.*, 2003) in flight can exceed 1,000 °/s, such delays need compensating by network  
47 computations. Otherwise, neural images of its surroundings could lag behind their actual positions by  
48 more than 25°, making fast and accurate visual behaviors seemingly infeasible.

49 Such compensations have been shown to occur early on in vertebrate eyes. In the tiger  
50 salamander and rabbit retina, ganglion cells' firing rates lag behind flashing but not moving bars  
51 (Berry *et al.*, 1999). Whether similar processing happens in insect eyes is unknown. By analyzing  
52 *Calliphora*, wild-type *Drosophila* and *hdc<sup>JK910</sup>* R1-R6 output to a point-object crossing their receptive  
53 fields, we find their time-to-peak values broadly similar to those evoked by light flashes. Therefore,  
54 these lag times are not, or at most weakly, compensated by the signal spread between photoreceptors.

1 Second, we examine whether R1-R6 output to point-object motion displays directional  
2 preference, as suggested by the asymmetric synaptic feedback to them (Meinertzhagen & Oneil, 1991;  
3 Rivera-Alba *et al.*, 2011). While both L1 and L2 monopolar cells mediate a major neural pathway in  
4 the lamina, L2s show richer connectivity. Only L2 projects feedback to R1-R6 and have reciprocal  
5 connections with L4, which in turn connects to L4s of the neighboring neural cartridges (Braitenberg  
6 & Debbage, 1974), providing further feedback to photoreceptors (Meinertzhagen & Oneil, 1991;  
7 Rivera-Alba *et al.*, 2011). We find that whilst the photoreceptors' peak responses show no clear  
8 directional preference, their rise and delay time courses to front-to-back and back-to-front moving  
9 point-objects often differ significantly. Although **it is still possible that** these differences may in part  
10 be augmented by the asymmetric network feedback, we show in **Appendixes 7-8** that they actually  
11 originate from photomechanical R1-R8 contractions (Hardie & Franze, 2012).

12 Third, we investigate whether network regulation affects R1-R6 cell's spatiotemporal acuity.  
13 By using the classic approaches (Srinivasan & Bernard, 1975; Juusola & French, 1997; Land, 1997),  
14 we estimate the theoretical blur effects and the eye's ability to resolve bright dots moving at certain  
15 speeds. Furthermore, we apply the Volterra series, a widely used "black-box" modeling method  
16 (Marmarelis & McCann, 1973; Eckert & Bishop, 1975; Gemperlein & McCann, 1975; Juusola *et al.*,  
17 1995b; Korenberg *et al.*, 1998), to simulate wild-type and *hdc<sup>JK910</sup>* R1-R6 output to these point-objects  
18 (Juusola *et al.*, 2003; Niven *et al.*, 2004). Remarkably, the simulations make it clear that these models  
19 cannot predict the recordings accurately (see **Appendix 1** and **Figures 7** and **8G-I**).

20 Spatiotemporal resolution of the eye is thought to be determined by two components with  
21 special characteristics: the static spatial resolution of light input, as channeled through the optics  
22 (Srinivasan & Bernard, 1975; Hornstein *et al.*, 2000), and the temporal response dynamics of  
23 photoreceptors. These characteristics are further influenced by the photoreceptors' adaptation state  
24 and synaptic feedback. The classic approaches suggest that because wild-type R1-R6s' acceptance  
25 angles ( $\Delta\rho$ ) are 10.9% wider than those of *hdc<sup>JK910</sup>* but their response dynamics are similar (see  
26 **Appendix 4**), they should produce blurrier images (of wider spatial half-width,  $S$ ). Moreover, as  
27 *hdc<sup>JK910</sup>* R1-R6s lack synaptic feedback modulation (Dau *et al.*, 2016), their predicted higher acuity  
28 should reflect differences in spatiotemporal photon sampling dynamics. Our recordings show,  
29 however, that both wild-type and *hdc<sup>JK910</sup>* R1-R6s resolve moving dots at least twice as well what the  
30 classic theory predicts, and that any resolvability difference between these cells largely disappears  
31 against a lit background. Thus, in dim conditions, lateral summation within the network may sensitize  
32 R1-R6 output by trading-off acuity, whereas in bright conditions more independent photoreceptor  
33 output sharpens neural images. Nonetheless, the classic theory cannot account for these dynamics, as  
34 it greatly overestimates the effect of motion blur on photoreceptor output.

35 We later demonstrate in **Appendixes 7-8** how and why the model simulations (of this  
36 appendix) differ from the corresponding recordings. Essentially, this is because the classic theoretical  
37 approaches do not incorporate two interlinked biophysical mechanisms that are critical for high  
38 acuity. (i) Rapid photomechanical photoreceptor contractions (Hardie & Franze, 2012) accentuate  
39 light input dynamically by shifting (front-to-back) and narrowing the cell's receptive field as moving  
40 bright point-objects enter in its view. While (ii) stochastic refractory photon sampling by microvilli  
41 accentuates the temporal dynamics in R1-R6 output. These mechanisms work together to improve the  
42 acuity and resolvability of moving objects far beyond the predictions of the classic models.

### 43 44 **Moving visual stimuli**

45 The 25 light-point array and LEDs pads, which we used for creating images of moving objects and  
46 providing ambient illumination, respectively, are described in **Appendix 4**. In the *Drosophila*  
47 experiments, the 25 light-point array was placed 6.7 cm away from the fly, subtending an angle of  
48  $40.92^\circ$ . This gave each light-point (dot)  $1.7^\circ$  size and minimum inter-dot-distance. In the *Calliphora*  
49 experiments, these parameters were 17 cm (distance) and  $16.73^\circ$  (viewing angle).

50 Images of one moving point-object (dot) were produced by briefly turning each light-point on  
51 and off, one after another in an incremental (for front-to-back direction) or decremental order (for  
52 back-to-front direction). Accordingly, Channel 0 input was driven with increasing or decreasing  
53 "ramp" (**Appendix figure 24A**), while Channel 1 input was set to 2 V. The travelling time of an  
54 object, or duration of the "ramp", was between 50 ms and 2 s, resulting in object speeds within  
55 naturalistic range (Schilstra & Van Hateren, 1999; van Hateren & Schilstra, 1999; Fry *et al.*, 2003):

1 from 20 to 818 °/s for *Drosophila* and 8 to 334 °/s for *Calliphora*.

2 The ability to resolve two moving point-objects of *Drosophila* photoreceptors were tested in  
3 dark-and light-adaptation conditions. In light-adaptation experiments, two 39-LED pads, on both sides  
4 of the 25 light-point array, provided background illumination (see **Appendix 4, Appendix figure 15**).  
5 The two dots in the 25 light-point array were separated by 6.8° (four dark points in between) and  
6 moved together at different speeds; typically, 205, 409 or 818 °/s. Each stimulus was presented 8-10  
7 times to the fly and the resulting photoreceptor responses were averaged before being analyzed.

### 9 **Gaussian white-noise (GWN) stimuli**

10 To evaluate how well the classic theory of fly compound eye optics/function (Srinivasan & Bernard,  
11 1975; Juusola & French, 1997; Land, 1998) explains single *Drosophila* R1-R6 photoreceptors ability  
12 to resolve moving dots, we needed to estimate each photoreceptor's linear impulse response (the 1<sup>st</sup>  
13 Volterra kernel) separately. The cell's voltage response to moving dots could then be predicted by  
14 convolving each recorded receptive field by the same cell's impulse response

15 Light-point No.13 intensity was controlled by setting Channel 0 input to 5 V and modulating  
16 Channel 1 input with a Gaussian white-noise (GWN) time series, which had the mean value of 2.5 V  
17 and cut-off frequency of 200 Hz. With these settings, light-point No.13 delivered  $2.5 \times 10^6$  photons/s  
18 at **Peak1** (451 nm) and  $3.75 \times 10^6$  photons/s at **Peak2** (575 nm) on average (cf. **Appendix 4: Table**  
19 **2**). Finally, these intensities were reduced 100-fold by neutral density filtering

### 21 **Volterra series model of each tested *Drosophila* R1-R6**

22 The principal assumptions of the Volterra series method are that the system has finite memory and is  
23 time-invariant (Schetzen, 1980). That is, (i) the relationship between output (photoreceptor voltage  
24 response)  $y(t)$  and input (light stimuli)  $u(t)$  is characterized by an unchanging impulse response and  
25 (ii)  $y(t)$  depends only on current and past values of  $u(t - \tau) \rightarrow u(t)$  with limited regression time,  $\tau$ . The  
26 continuous form of this input/output relationship is described by the following equation:

$$27 \quad y(t) = k_0 + \int_0^T k_1(\tau)u(t - \tau)d\tau + \int_0^T \int_0^T k_2u(t - \tau_1)u(t - \tau_2)d\tau_1d\tau_2 \quad (\text{A6.1})$$

28 where  $k_0$ ,  $k_1$  and  $k_2$  are the zero-, first- and second-order time-invariant kernels, which define the  
29 system's impulse response.  $T$  is the finite system memory limit.

30 Note that the model order is not limited, as expressed only up to 2<sup>nd</sup>-order in **Eq. A6.1**, but  
31 instead could be extended arbitrarily further. However, it has been shown that a light-adapted fly  
32 photoreceptor's response to GWN light intensity time series stimulation, as used in these experiments,  
33 can be approximated well by the linear terms (Juusola *et al.*, 1994; Juusola *et al.*, 1995a).

34 Therefore, the estimation of system output was simplified to a linear convolution of input  
35 with zero- and first-order kernels. Each measurement of photoreceptor voltage response and light  
36 stimuli could be fitted into the discrete and simplified form of **Eq. A6.1** as:

$$37 \quad \begin{aligned} 38 \quad y(n) &= k_0 + k_1(0)u(n) + k_1(1)u(n-1) + \dots + k_1(T)u(n-T) \\ 39 \quad y(n-1) &= k_0 + k_1(0)u(n-1) + k_1(1)u(n-2) + \dots + k_1(T)u(n-1-T) \\ &\vdots \\ 40 \quad y(n-N) &= k_0 + k_1(0)u(n-N) + k_1(1)u(n-N-1) + \dots + k_1(T)u(n-n-T) \end{aligned} \quad (\text{A6.2})$$

41 The group of **Eq. A6.2**, which approximates  $N$  values of photoreceptor output, was then re-arranged  
42 into matrix form:

$$43 \quad \begin{pmatrix} y(n) \\ y(n-1) \\ \vdots \\ y(n-N) \end{pmatrix} = \begin{pmatrix} 1 & u(n) & u(n-1) & \dots & u(n-T) \\ 1 & u(n-1) & u(n-2) & \dots & u(n-1-T) \\ & & \vdots & & \\ 1 & u(n-N) & u(n-N-1) & \dots & u(n-N-T) \end{pmatrix} \times \begin{pmatrix} k_0 \\ k_1(0) \\ k_1(1) \\ \vdots \\ k_1(T) \end{pmatrix} \quad (\text{A6.3})$$

44 Equivalently, **Eq. A6.3** could be symbolized as:

$$Y = P\theta \quad (\text{A6.4})$$

where vector  $Y$  contained a sequence of  $N$  output values,  $P$  was the regression matrix constructed from the lagged input values, and the column  $\theta$  elements were the kernel values. The problem of determining a photoreceptor's Volterra series model was hence broken down to designing input stimuli  $u(t)$  and measuring output values  $y(t)$  to construct matrices  $P$  and  $Y$  of **Eq. A6.4**, and estimating  $\theta$ .

$u(t)$  was a GWN series with 200 Hz bandwidth, which thus tested the whole frequency range of photoreceptor output. Initially, each tested photoreceptor was steady-state-adapted to the chosen light background (the average brightness of the GWN stimuli) for 30-60 s (see also **Appendix 4**). Input was then delivered from the light-point No.13, by setting Channel 0 to 5 V and modulating Channel 1 input by the GWN series around the mean value of 2.5 V. Each time series was 3-second-long and was repeated 8-10 times before the responses were averaged. The first 1.5 s of the recorded data was used to estimate the kernel values.

Photoreceptor output  $y(t)$  was sampled at 10 kHz. It was then preprocessed by removing the mean value and trends, and down-sampled.

Once the matrices  $Y$  and  $P$  of **Eq. A6.4** are constructed, there are several approaches to estimate  $\theta$  with minimal error, such as the least squares regression by using Gram-Schmidt orthogonalisation (Korenberg *et al.*, 1988; Korenberg & Paarmann, 1989) or Meixner functions (Asyali & Juusola, 2005). Here,  $\theta$  was approximated by the single value decomposition method (Golub & Reinsch, 1970; Lawson & Hanson, 1974), in which the factorization of matrix  $P$  and the calculation of its Moore-Penrose pseudoinverse matrix,  $P^+$ , were carried out by the command `pinv(P)` in MATLAB. The linear least-squares estimation of  $\theta$ ,  $\hat{\theta}$ , was given by:

$$\hat{\theta} = P^+Y \quad (\text{A6.5})$$

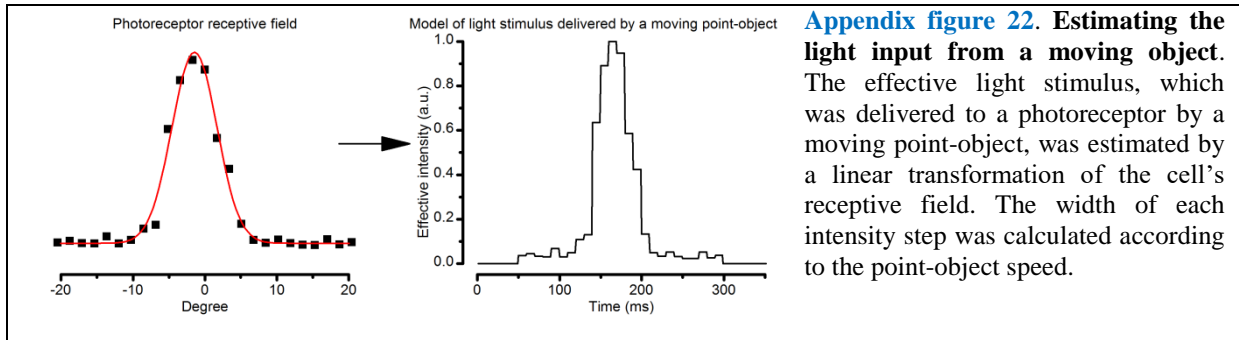
The computed kernels and the second half of GWN stimuli were then substituted to **Eq. A6.2** to yield the model prediction of the photoreceptor response. The accuracy, or fitness,  $F$ , of the prediction was quantified by the complement of its mean squared error:

$$F = 1 - MSE = 1 - \frac{\overline{(y' - y)^2}}{\overline{(y - \bar{y})^2}} \quad (\text{A6.6})$$

where  $y$  were the actual data measured from the photoreceptor voltage response and  $y'$  were the values simulated by the mathematical model.

### Conventional simulation of intracellular responses to object motion

After determining and testing the Volterra model, we next approximated the light stimuli (input) delivered by the point-objects crossing a photoreceptor's receptive field. Since a photoreceptor's voltage response was assumed to be linearly correlated to light input, the response amplitudes to the subsaturating light flashes during the receptive field scans (see **Appendix 4**) were also considered linear measurements of the effective intensity from each light-point. Therefore,  $u_m(t)$ , created by one moving point-object, was modelled as 25 intensity steps, in which amplitudes were proportional to their corresponding flash responses (**Appendix figure 22**). The temporal width of each step was calculated according to the object speed. Similarly,  $u'_m(t)$  of two moving point-objects was constructed from the superimposition of  $u_m(t)$  and  $u_m(t + \Delta)$ , where  $\Delta$  was calculated according to the point-objects' speed and their separation angle.

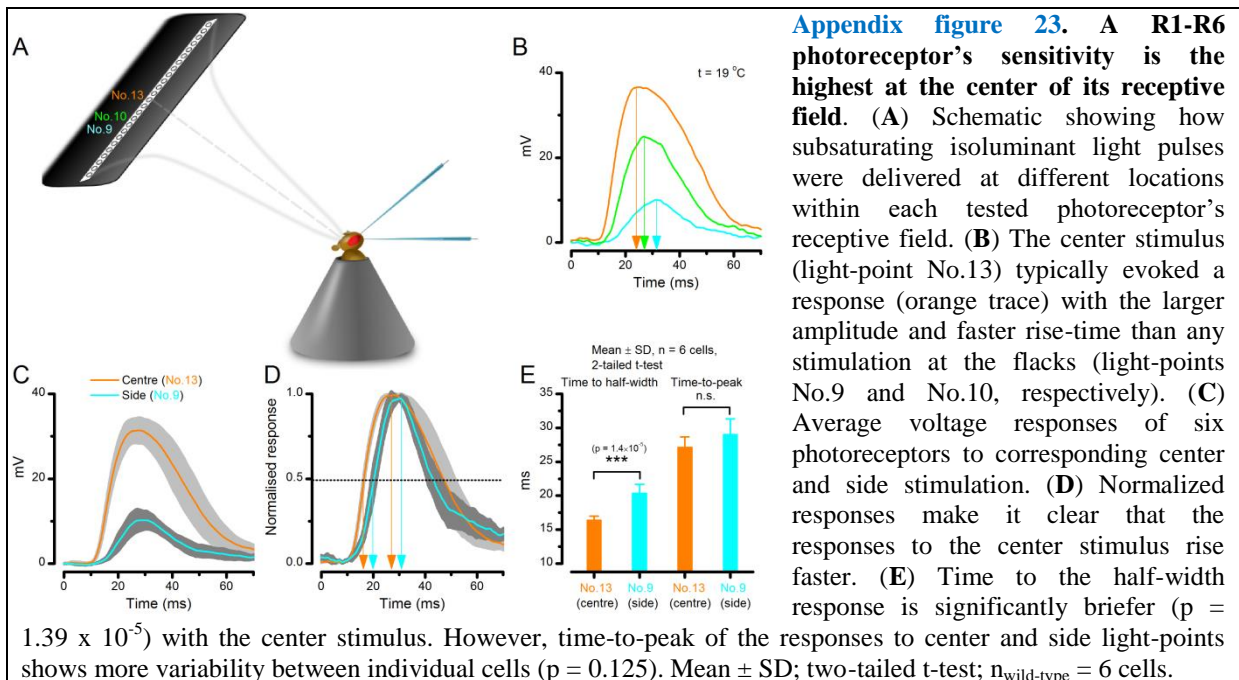


**Appendix figure 22. Estimating the light input from a moving object.** The effective light stimulus, which was delivered to a photoreceptor by a moving point-object, was estimated by a linear transformation of the cell's receptive field. The width of each intensity step was calculated according to the point-object speed.

1  
2 Lastly, a photoreceptor's voltage response to point-object motion was simulated by substituting input  
3  $u_m(t)$  or  $u'_m(t)$  and the kernels values to the zero- and first-order terms of Eq. A6.2.

### 4 Maximal responses to moving dots lag behind their actual positions

5  
6 Neural images in the fly retina, lamina and medulla are generated by retinotopically mapping the  
7 surrounding light intensity distribution. This means that light coming from each point in space is  
8 sampled and processed by one neural cartridge (or neuro-ommatidia) (Meinertzhagen & Oneil, 1991).  
9 While a stationary object might be seen by several photoreceptors belonging to neighboring  
10 ommatidia due to their large acceptance angles (Appendix 4) and overlapping receptive fields  
11 (Appendix 5), the object position is almost certainly perceived on the photoreceptor's optical axis.  
12 This position, along its corresponding lamina/medulla cartridge below, produces the largest/fastest  
13 intracellular responses (Appendix figure 23; see also Appendix 4) as it channels the maximum light  
14 influx into the rhabdomere (see Appendix 2).  
15

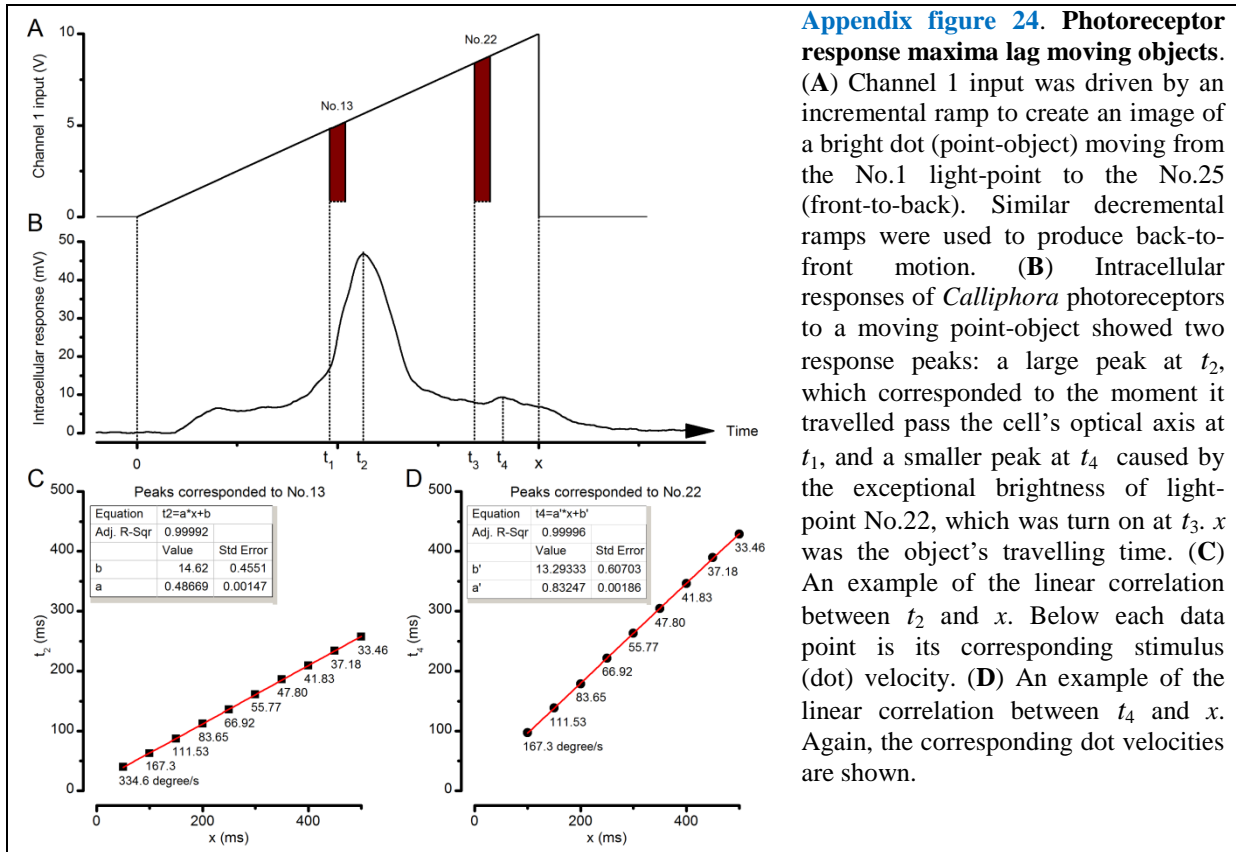


16  
17 Furthermore, it is customarily assumed that a moving point-object's position would be  
18 associated with the peak of its neural image. However, this does not necessarily mean that a R1-R6's  
19 response maximum would indicate the object position. Rather, it is more plausible - especially during  
20 high signal-to-noise ratio conditions (bright stimulation) - that the lamina circuitry (cf. Appendix 2,  
21 Appendix figure 9E) would be amplifying more the photoreceptor signal derivative. This is because  
22 the large monopolar cells (LMCs) are then more tuned to responding to the rate of light changes  
23 (Zettler & Järvillehto, 1972; van Hateren, 1992b; Juusola *et al.*, 1995a; Zheng *et al.*, 2006).  
24

In fact, neural latency might be compensated at the subsequent processing stages in the visual

1 system, so that the peak of the travelling network response wave would closely follow the object's  
 2 actual position, as is the case of the vertebrate ganglion cells (Berry *et al.*, 1999). Theoretically, if  
 3 such “correction” occurred maximally at the single neuron level, it would mark the coincidence of  
 4 two events. (i) The neuron’s response would peak as (ii) the object passes its receptive field center.

5 To examine whether, or to what degree, neural images of moving objects are compensated for  
 6 latency at the first processing stage in the fly R1-R6 photoreceptors, we measured their intracellular  
 7 voltage responses while presenting the fly with a bright dot moving at different speeds.  
 8



9  
 10 **Appendix figure 24B** depicts a typical response waveform of a blowfly (*Calliphora vicina*)  
 11 R1-R6 to a bright moving dot (the point-object in **Appendix figure 24A**). Let  $x$  be the time needed for  
 12 it to travel through the 25 light-point array,  $t_1$  be the moment when the dot pass the cell’s optical axis,  
 13 *i.e.* the corresponding light-point is turned on, and  $t_2$  be when the intracellular response peaks. With  
 14 varying  $x$ , and thus the dot speed,  $t_1$ , can be computed as:

$$t_1 = a \times x \tag{A6.7}$$

16 where the coefficient  $a$  is a constant. The aim was to align the 25 light-point array so that the point  
 17 No.13 lies at the tested photoreceptor’s receptive field center. Therefore in theory,  $a$  is approximately  
 18 0.48. However, the light-point No.13 might, in fact, be off-axis. For example, the cell’s receptive field  
 19 center could lie in between No.13 and No.12, causing inaccuracy in the calculation of  $a$ ,  $t_1$  and lag  
 20 time  $b$ , which is given by:

$$b = t_2 - t_1 \tag{A6.8}$$

22 To overcome this ambiguity, we plotted  $t_2$  against  $x$ , given that:

$$t_2 = t_1 + b = a \times x + b \tag{A6.9}$$

24 **Appendix figure 24C** illustrates an example of the relationship between  $t_2$  and  $x$  obtained from a  
 25 *Calliphora* R1-R6. The two parameters fitted exceedingly well to a linear relationship (adjusted R-  
 26 squared > 0.9999), in which coefficient  $a$  and lag time  $b$  were found as 0.486 and 14.62 ms,  
 27 respectively. These data show that in this particular case, indeed light-point No.13 was close to the  
 28 center of the cell’s receptive field and that lag time  $b$  was virtually unchanged for different object

1 speeds. The on-axial position of the light-point No.13 was later confirmed by 11 receptive field scans,  
 2 all of which indicated that response elicited by a light flash from No.13 was the largest (data not  
 3 shown).

4 The same photoreceptor was also stimulated by repeating a light flash, to which its voltage  
 5 response peaked 15 ms later. The small difference between the lag time of motion response and the  
 6 response time-to-peak to a flash does not readily imply neural network latency compensation. In case  
 7 of the moving stimuli, photoreceptor was stimulated when the dot entered its receptive field, causing  
 8 its intracellular voltage to start depolarizing before the dot reached the cell's optical axis. Conversely,  
 9 the photoreceptor's response to light impulse was only elicited after the stimulus onset, making its  
 10 time-to-peak slightly longer than the lag time.

11 In the classic flash-lag psychological experiment, where a flashing bar and another uniformly  
 12 illuminated one travelled together, the former was perceived to be trailing (Nijhawan, 1994; Brenner  
 13 & Smeets, 2000). Thus, it is probable that at some stage in the visual system, the voltage response  
 14 peak (maximum) caused by moving object would display shorter delay than those elicited by  
 15 increasing light intensity. In the present study, the light-point No.22 was 4-fold brighter than the  
 16 others, as discussed in **Appendix 4**, and indirectly played the role of the flashing bar, causing a "local  
 17 peak" in a photoreceptor's voltage response (**Appendix figure 24B**). Hence, to further examine neural  
 18 latency of R1-R6 output, we next assessed the lag time,  $b'$ , corresponding to this peak in the response.  
 19 Given  $t_3$  is the moment when No.22 was turned on, which can be calculated as:

$$20 \quad t_3 = a' \times x \quad (\text{A6.10})$$

21 and  $t_4$  is the time of the local response peak (**Appendix figure 24B**), lag time is defined as their  
 22 difference:

$$23 \quad b' = t_4 - t_3 \quad (\text{A6.11})$$

24 The relationship between  $t_4$  and  $x$  could also be described by linear fitting with almost zero residue  
 25 (**Appendix figure 24D**), yielding  $a'$  and  $b'$  values of 0.83 and 13.29 ms, respectively.

26 These data exemplify that a photoreceptor's response maxima, no matter whether caused by a  
 27 point-object moving across its receptive field or by an unexpected increase in light intensity, show  
 28 similar lag time characteristics. Both  $b$  and  $b'$  were independent of the object speed and comparable to  
 29 the response time-to-peak, as induced by a comparable flash. These features were reproducible and  
 30 general; observed in all 7 tested *Calliphora* photoreceptors, without exception (**Table 6**).

Animal	Flash response time-to-peak (ms)	Peaks corresponding to the receptive field center		Peaks corresponding to the light-point No.22	
		Lag-time $b$ (ms)	Adj. R-Sqr	Lag-time $b'$ (ms)	Adj. R-Sqr
<i>Calliphora</i>	14.85 ± 0.78	14.6 ± 0.64	0.99985 ± 0.00012	13.9 ± 3.59	0.99985 ± 0.00017
		n = 7		n = 5	

**Table 6. Response latency to dot motion analyses in *Calliphora* R1-R6s** (Mean ± SD). Intracellular recordings were performed at 19 °C. The tested moving dot (point-object) velocities were: 334.6, 167.3, 111.53, 83.65, 66.92, 55.77, 47.8, 41.83, 37.18 and 33.46 °/sec.

Animal	Flash response time-to-peak (ms)	Front-to-back		Back-to-front	
		Lag-time $b$ (ms)	Adj. R-Sqr	Lag-time $b$ (ms)	Adj. R-Sqr
Wild-type <i>Drosophila</i>	23.81 ± 1.41	21.41 ± 4.5	0.99649 ± 0.0065	22.54 ± 4.15	0.99378 ± 0.007
		n = 12		n = 5	
<i>hdc<sup>JK910</sup></i>	24.4 ± 1.08	21.82 ± 1.36	0.9992 ± 0.0008	23.79 ± 5.72	0.9978 ± 0.003
		n = 3			

**Table 7. Response latency to dot motion analyses in *Drosophila* wild-type and *hdc*<sup>JK910</sup> R1-R6s (Mean ± SD).** Intracellular recordings were performed at 19 °C. The tested point-object velocities were: 818.4, 409.2, 272.8, 204.6, 163.68, 136.4, 116.91, 102.3, 90.93 and 81.84 %/s. Note, these statistics are collected from individual recordings, not from paired data.

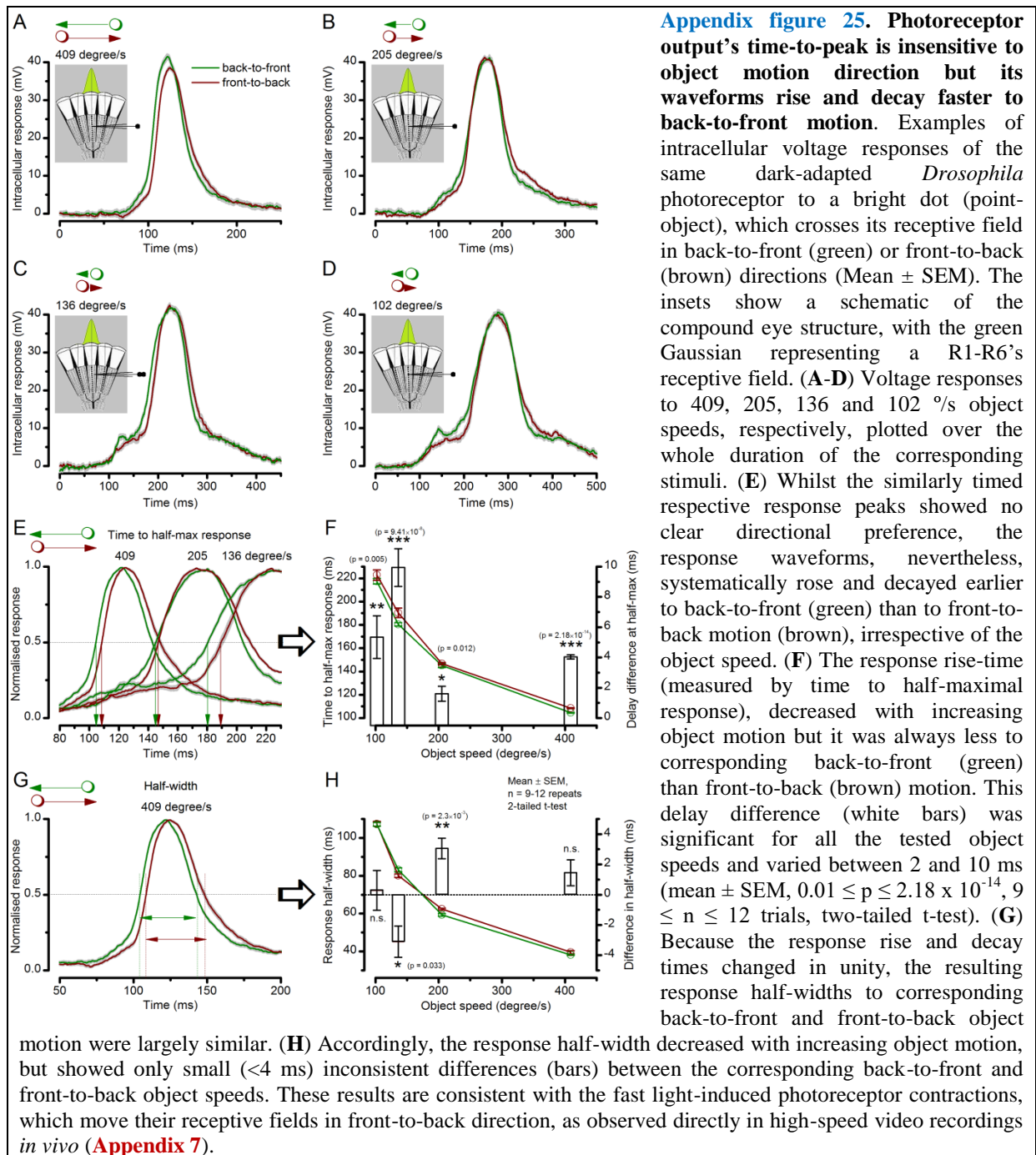
1  
2 *Drosophila* photoreceptors' voltage responses did not clearly exhibit the “local peak” to the  
3 light-point No.22; possibly owing to their slower temporal dynamics. Nevertheless, the temporal  
4 position of the “global peak”, measured by  $t_2$  of wild-type ( $n = 12$ ) and *hdc*<sup>JK910</sup> ( $n = 3$ ) photoreceptor  
5 outputs, consistently showed linear correlation to  $x$  and comparable lag-time/time-to-peak values  
6 (Table 7). Their corresponding maxima showed slightly larger lag time variations, and thus the linear  
7 fits were not as error-free as with the *Calliphora* data. Nonetheless, overall, the mathematical relation  
8 between their peak response lag time and the object speed appeared similar. The comparable wild-  
9 type and *hdc*<sup>JK910</sup> R1-R6 output maxima to the tested point-object velocities, as recorded from their  
10 somata, suggests that their response dynamics mostly reflect similar phototransduction processing,  
11 with possibly only marginal influence from the lamina network.

12 Altogether, these data imply that fly phototransduction machinery (see Appendixes 1-2)  
13 samples intensity changes and object motion much the same way. Because its peak responses lag  
14 behind the actual positions of the moving objects, the neural latency of moving objects is most likely  
15 compensated downstream by image processing within the interneuron networks, starting with the  
16 LMCs (cf. Appendix 2, Appendix figure 9E).

#### 17 **Response rise and decay to object motion show directional selectivity**

18 As summarized in Table 7, *Drosophila* photoreceptors' maximum responses to a front-to-back or  
19 back-to-front moving bright dot did not exhibit clear signs of *latency compensation*, as indicated by  
20 their similar time-to-peak durations (estimated from the population means of individual unpaired  
21 recordings). Interestingly, in the paired recordings, however, the response rise and decay time-courses  
22 often showed considerable *latency modulation*.

23 Appendix figure 25 depicts intracellular responses to a moving dot, passing a  
24 photoreceptor's receptive field front-to-back and back-to-front at (A) 409, (B) 205, (C) 136 and (D)  
25 102 %/s. Although their time-to-peak values appeared similar, the response rise and decay dynamics  
26 showed clear differences (Appendix figure 25E-H), which correlated with the dot speed and motion  
27 direction. We shall later show in Appendix 7, using high-speed video recordings of photoreceptor  
28 rhabdomeres, that their photomechanical contractions (Hardie & Franze, 2012) occur in back-to-front  
29 direction. Light input modulation by these directional microsaccades can much explain the phasic  
30 differences in photoreceptor output to different directional point-object motions.  
31  
32



1  
2  
3  
4  
5  
6  
7  
8  
9  
10  
11  
12  
13  
14

When a R1-R6 contracts to light input, its receptive field moves front-to-back (Appendixes 7-8). Thus, with the ommatidium lens inverting images, its responses to the back-to-front dot motion raise systematically slightly earlier (Appendix figure 25E, F). This rise-time lag reduces because the dot moves against the receptive field motion, whilst the rise-time lag increases during comparable front-to-back motion when the dot moves along the receptive field motion. In other words, a dot stayed a bit longer within a R1-R6's receptive field during front-to-back motion than back-to-front motion. Such phasic differences were consistently observed in most recordings over the tested speed range. For example, 205 %s back-to-front movement evoked narrower temporal response half-widths in 8/10 R1-R6s than the opposite movement. Similarly, 409 %s back-to-front movement evoked narrower temporal response half-widths in 6/10 R1-R6s (in 2 cells, these were identical; and wider in 2).

In summary, a prominent feature of R1-R6s' voltage responses to opposing object motion directions is their similar time-to-peak values. This was found in all somatic recordings of *Calliphora*

1 and *Drosophila* photoreceptors. Intriguingly, though, we further identified small (2-10 ms) but  
 2 significant differences in the response rise and decay to front-to-back and back-to-front object motion.  
 3 These phasic differences in photoreceptor output can be largely explained by each cell's directional  
 4 photomechanical contractions, and we later show how these contribute to improving the fly's visual  
 5 acuity (**Appendixes 7-8**). It is plausible that these directional preferences would be further enhanced  
 6 downstream at the level of network processing. During bright stimulation, LMCs respond most  
 7 strongly to the rate of change in photoreceptor output (Juusola *et al.*, 1995a; Zheng *et al.*, 2006;  
 8 Zheng *et al.*, 2009; Wardill *et al.*, 2012), with the rich connectivity of the optic lobes proving further  
 9 possibilities for the required phase coding (Meinertzhagen & Oneil, 1991; Rivera-Alba *et al.*, 2011;  
 10 Wardill *et al.*, 2012; Behnia *et al.*, 2014).

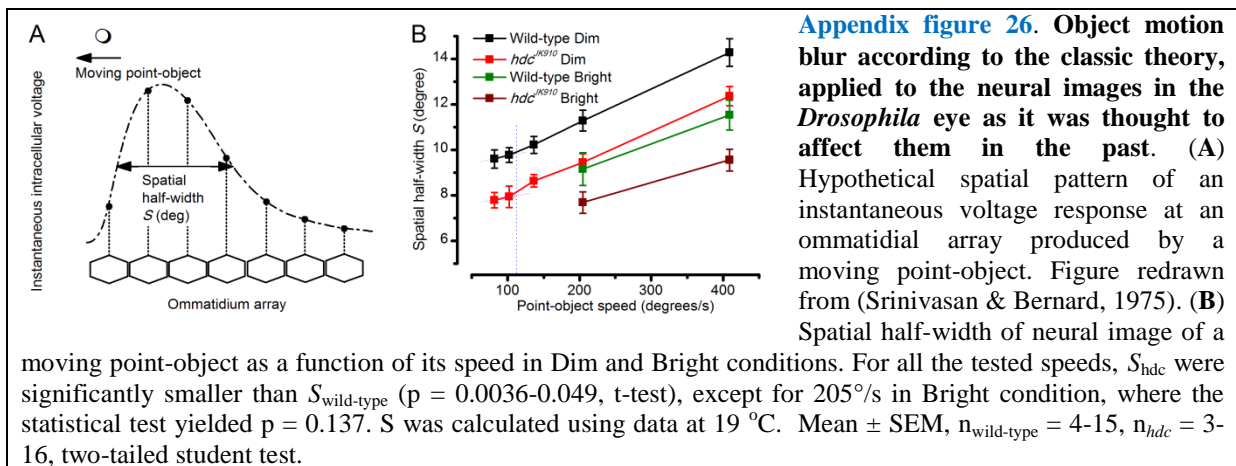
11  
 12 **Classic theory greatly overestimates motion blur in R1-R6 output**

13 We showed in **Appendix 4** that dark-adapted *hdc<sup>JK910</sup>* photoreceptors have narrower receptive fields  
 14 (acceptance angles) than their wild-type counterparts but broadly similar response dynamics (**Figure**  
 15 **7-figure supplement 1**). Thus, the prediction is that *hdc<sup>JK910</sup>* R1-R6s should produce slightly sharper  
 16 neural images than their wild-type counterparts after dark-adaptation. Classic theoretical approaches  
 17 have been used to predict how the spatial and temporal factors might jointly affect visual acuity  
 18 (Srinivasan & Bernard, 1975; Juusola & French, 1997). Accordingly here, we first predict with them  
 19 the motion blur effects on wild-type and *hdc<sup>JK910</sup>* R1-R6 outputs. Later on, we test the ability of these  
 20 cells to distinguish two dots moving together, separated by less than the cell's acceptance angles.

21 Since a fast moving bright dot can stimulate several photoreceptors virtually at the same time  
 22 (**Appendix figure 26A**), theoretically, it should not be perceived as a single point but a streak, of  
 23 which length is a function of object speed. This motion blur effect is classically quantified by the  
 24 spatial half-width  $S$  of object's neural image. Because the spatial response in the retina has a similar  
 25 waveform with the temporal response of a single photoreceptor (Srinivasan & Bernard, 1975; Juusola  
 26 & French, 1997),  $S$  can be calculated as:

27 
$$S = w \times T_h \tag{A6.12}$$

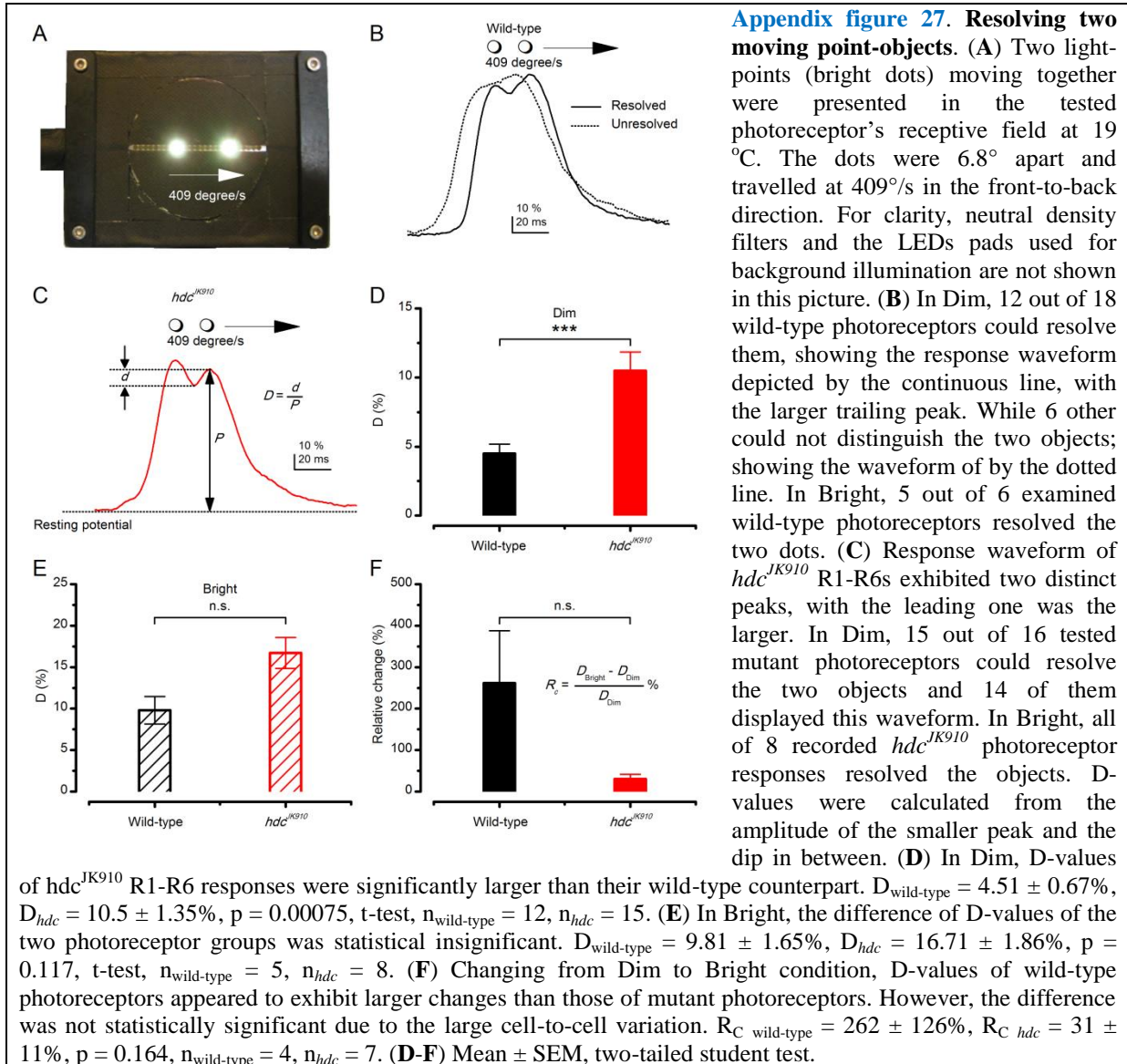
28 where  $w$  is the object speed and  $T_h$  (cf. **Appendix figure 25G**) is the temporal half-width of a single  
 29 photoreceptor response.  
 30



31  
 32 **Appendix figure 26B** illustrates the predicted relationship between the object speed and neural image  
 33 resolution in wild-type and *hdc<sup>JK910</sup>* *Drosophila*. These estimates imply that the spatial half-width of  
 34 wild-type neural images should be 1-2° wider than that of the *hdc<sup>JK910</sup>* during both the dim and bright  
 35 conditions, reflecting wild-type R1-R6s' wider acceptance angles ( $\Delta\rho$ ) (see **Appendix 4, Figure 7-**  
 36 **figure supplements 1A** and **2B**). This prediction agrees with the previous theoretical works  
 37 (Srinivasan & Bernard, 1975; Juusola & French, 1997), which used similar methods to indicate two  
 38 distinct regions of image resolution. Thus, theoretically, at low object speeds, visual acuity should be  
 39 mostly determined by a photoreceptor's spatial receptive field, but at high speeds, the motion-blur  
 40 effect should increase rapidly, becoming the dominating factor. The corresponding trend differences

1 (as separated by a thin dotted line) suggest that the point-object speed threshold dividing the two  
 2 regions would be about 100-120 °/s.

3 Remarkably, however, we next demonstrate how these theoretical predictions greatly  
 4 overestimate motion blur effects in R1-R6 output, and that these cells can, in fact, resolve image  
 5 details finer than the half-width of their receptive fields, even at very high saccadic speeds.  
 6



7  
 8 In the second type of experiment, two bright dots, which were less than the half-width of a  
 9 R1-R6's receptive field (6.8°) apart, crossed its receptive field at 409 °/s (Appendix figure 27A).  
 10 Each tested photoreceptor's ability to distinguish the dots was assessed whether its response showed  
 11 two clear peaks (Appendix figure 27B, solid line) or only one (dotted line). Quite unexpectedly, even  
 12 at the low room-temperature of 19 °C, where phototransduction is slower than at the flies' preferred  
 13 temperature of 25 °C (Sayeed & Benzer, 1996; Juusola & Hardie, 2001b), 12/18 of wild-type R1-R6  
 14 photoreceptors and 15/16 *hdc<sup>JK910</sup>* R1-R6s could clearly resolve the two dots. (Note that at 25 °C,  
 15 every tested R1-R6 resolved them well; Figure 9-figure supplement 1E-F). Amongst the wild-type  
 16 responses, the trailing peak was often larger than the leading one (Appendix figure 27B, solid line),  
 17 whereas all but one *hdc<sup>JK910</sup>* R1-R6 had the larger leading peak (Appendix figure 27C). This  
 18 observation suggests that excitatory synaptic feedback modulation, which *hdc<sup>JK910</sup>* photoreceptors  
 19 lack, may enhance the second peak in the wild-type responses. Resolvability was further quantified by  
 20 D-values:

$$D = \frac{d}{P} \% \quad (\text{A6.13})$$

Where  $P$  is the amplitude of the smaller peak and  $d$  is the depth of the response dip between the two peaks (**Appendix figure 27C**). In darkness,  $D$ -values measured from the mutant photoreceptors were, on average, more than double those of wild-type ( $D_{\text{wild-type}} = 4.51 \pm 2.33\%$ ,  $D_{\text{hdc}} = 10.5 \pm 5.23\%$ ), indicating that  $\text{hdc}^{\text{JK910}}$  R1-R6s resolve the two points more clearly than their wild-type counterpart (**Appendix figure 27D**). Under light-adaptation (ambient illumination), while R1-R6s of both genotypes exhibited significant improvements in their image resolution ( $D_{\text{wild-type}} = 9.81 \pm 3.7\%$ ,  $D_{\text{hdc}} = 14.85 \pm 6.95\%$ ), the difference between the two groups decreased and was at the margin of statistical significance (**Appendix figure 27E**;  $p = 0.058$ , t-test). Taking into account only the cells in which  $D$ -values were measured in both dim and bright conditions, the enhancement of  $D$ -values to the ambient light change was quantified by their relative change:

$$R_c = \frac{D_{\text{Bright}} - D_{\text{Dim}}}{D_{\text{Dim}}} \% \quad (\text{A6.14})$$

On average, wild-type  $D$ -values improved by 262%, ranging from 43% to 604%. These changes appeared to be markedly larger than those observed in  $\text{hdc}^{\text{JK910}}$  photoreceptors, which varied from 4% to 89% and averaged as 31%. Yet, the difference between the two groups was not statistically significant because of the large individual variations (**Appendix figure 27F**).

In **Figure 7**, we further analyze the resolvability of those high-quality wild-type and  $\text{hdc}^{\text{JK910}}$  R1-R6s, from which we recorded the impulse response and receptive field measurements at the two adapting backgrounds - dim and bright at 25°C, as well as responses to both 205 and 409 °/s moving dots. Such data allowed us to compare the classic theory to the real recordings even more thoroughly.

Together, these results show that the theoretical spatial half-width,  $S$ , grossly underestimates R1-R6 photoreceptors' image resolution. Recordings clarify that two bright dots that travel 409 °/s can, in fact, be resolved by a single photoreceptor, even when the dots (6.8° separation) are less than the photoreceptor's acceptance angle ( $\Delta\rho = 9.5^\circ$ ) apart. Therefore, a R1-R6 photoreceptor's real spatial half-width for the same high (saccadic) speed must be less than half of the theoretical estimate (~15°; **Appendix figure 26B**). In other words, the classic theory overestimates the role of motion blur on *Drosophila* vision, as its R1-R6 photoreceptors resolve fast-moving dots beyond the predicted motion blur limit.

The recordings further indicate, consistent with  $\text{hdc}^{\text{JK910}}$  R1-R6s' marginally narrower acceptance angles (**Appendix 4, Figure 7-figure supplements 1-2**), that their spatiotemporal resolution is somewhat better than that of wild-type photoreceptors, both in dim and moderately bright conditions. However, when ambient light intensity was changed, the spatiotemporal resolutions of wild-type R1-R6s improved more. Here, possible contributing factors include:

- Slight (~4%) differences in the photoreceptors' rhabdomere diameters (see **Appendix 5**)
- Dynamic and homeostatic regulation of  $[\text{Ca}^{2+}]_i$ , membrane properties and synaptic feedback (Dau *et al.*, 2016)
- Intracellular pupil (see **Appendix 2** and **Appendix 4**)
- Differences in photomechanical rhabdomere contractions (see **Appendixes 7-8**)
- Electrical coupling between the cells

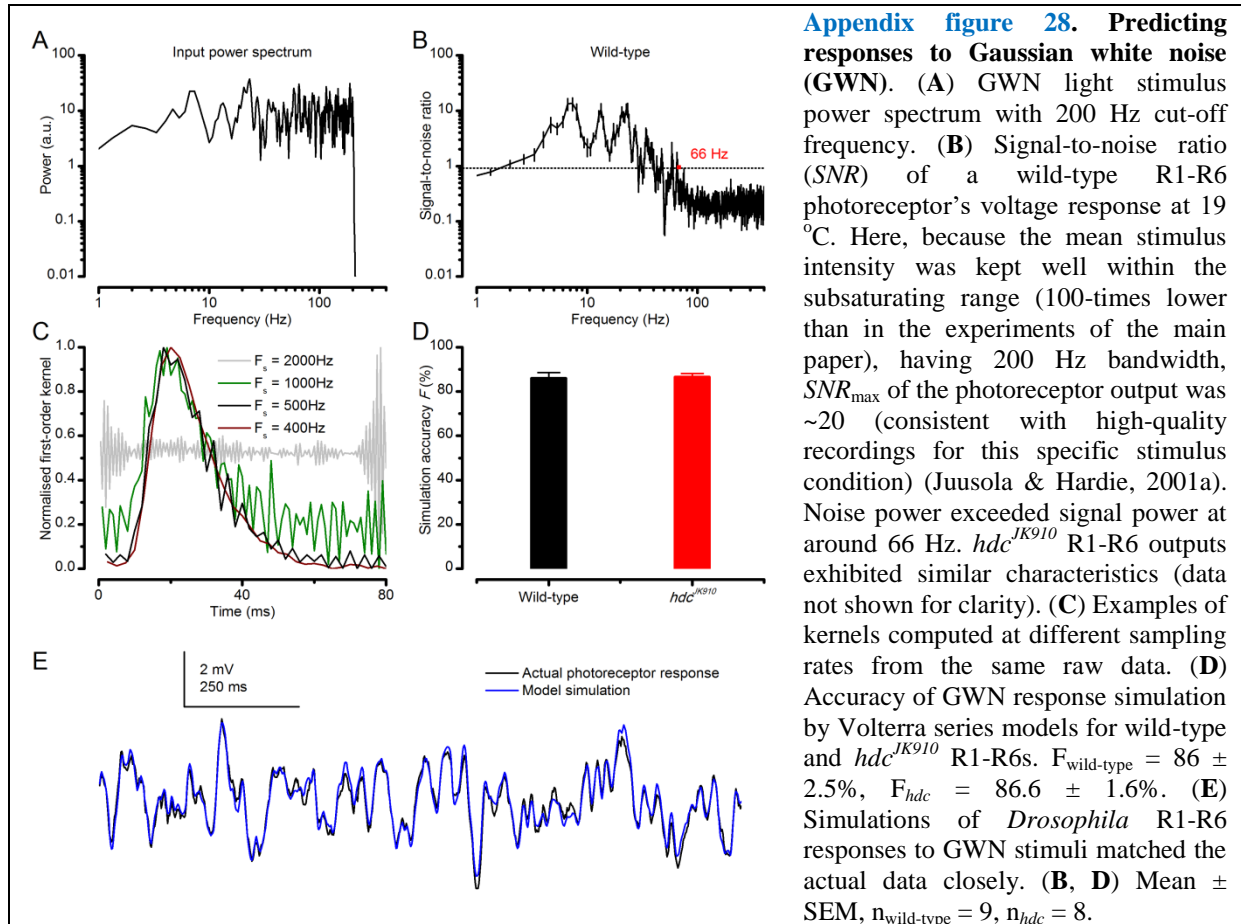
Their potential roles are further discussed in **Appendixes 7-8**

### Modeling R1-R6 output by the Volterra series method

Volterra kernels of each photoreceptor model were computed from the first half (1.5 s) of GWN data, before the other half of recorded light stimuli and voltage responses were used to validate the model. Because the output simulation accuracy depends upon input statistics and the model computation specifications, the system identification process was optimized by selecting suitable parameters.

Firstly, to test whether the selected 200 Hz input bandwidth was appropriate (**Appendix figure 28A**), we analyzed the resulting signal-to-noise (SNR) ratio of photoreceptor output (**Appendix figure 28B**). SNR decayed below 1 at around 66 Hz; at which point photoreceptor response contained more noise than signal. Thus, the GWN stimuli predictably activated a R1-R6 photoreceptor's whole frequency range.

1 Secondly, we assessed different sampling rates. According to the Nyquist-Shannon sampling  
 2 theorem, a signal without frequencies higher than  $B$  Hz can be perfectly sampled and reconstructed  
 3 (Shannon, 1948) by sampling rate  $F_s$  of  $2B$  Hz. Because the bandwidth of interest was 0-66 Hz, the  
 4 data could be processed, in theory, at any sampling rate from 132 Hz to the recorded rate of 10 kHz,  
 5 without compromising its information content.  
 6



**Appendix figure 28. Predicting responses to Gaussian white noise (GWN).** (A) GWN light stimulus power spectrum with 200 Hz cut-off frequency. (B) Signal-to-noise ratio (SNR) of a wild-type R1-R6 photoreceptor's voltage response at 19 °C. Here, because the mean stimulus intensity was kept well within the subsaturating range (100-times lower than in the experiments of the main paper), having 200 Hz bandwidth,  $SNR_{max}$  of the photoreceptor output was  $\sim 20$  (consistent with high-quality recordings for this specific stimulus condition) (Juusola & Hardie, 2001a). Noise power exceeded signal power at around 66 Hz.  $hdc^{JK910}$  R1-R6 outputs exhibited similar characteristics (data not shown for clarity). (C) Examples of kernels computed at different sampling rates from the same raw data. (D) Accuracy of GWN response simulation by Volterra series models for wild-type and  $hdc^{JK910}$  R1-R6s.  $F_{wild-type} = 86 \pm 2.5\%$ ,  $F_{hdc} = 86.6 \pm 1.6\%$ . (E) Simulations of *Drosophila* R1-R6 responses to GWN stimuli matched the actual data closely. (B, D) Mean  $\pm$  SEM,  $n_{wild-type} = 9$ ,  $n_{hdc} = 8$ .

7  
 8 We found that higher sampling rates yielded models, which predicted R1-R6 output with  
 9 slightly higher accuracy. However, their kernels also exhibited larger fluctuations, and the kernels did  
 10 not decay to zero over time, most likely due to high-frequency noise. For  $F_s = 1,000$  Hz and higher,  
 11 such fluctuations undermined the physiological meaning of the Volterra 1<sup>st</sup>-order kernel (**Appendix**  
 12 **figure 28C**), which is the photoreceptor's impulse response (Victor, 1992). Thus, the kernels  
 13 computed from too richly-sampled data would be useful only for response prediction to this particular  
 14 GWN stimulus.

15 On the other hand, while computations performed with lower  $F_s$  data would produce  
 16 smoother kernels, a low sampling rate would also limit the model's other applications. For example,  
 17 Volterra series models were used to simulate photoreceptor response to the image of moving objects  
 18 created by the 25 light-point array. For an object moving at 409 °/s, its travelling time across the array  
 19 was 100 ms, or 4 ms per light-point. As the simulation required at least 2 data-points per light-point,  
 20  $F_s$  was chosen to be 500 Hz, at which rate reasonably smooth kernels could still be produced  
 21 (**Appendix figure 28C**). Moreover, because the 1<sup>st</sup>-order kernel values decayed to zero at 50-60 ms, it  
 22 was deemed that a 80 ms kernel length was sufficient for the computations.

23 Volterra series models, computed from data sampled at 500 Hz, could consistently predict  
 24 response of *Drosophila* photoreceptors to GWN stimuli (for example, see **Appendix figure 28E**). On  
 25 average, the model simulation accuracy, given by **Eq. A6.6**, was  $\sim 86\%$  for both wild-type and  $hdc^{JK910}$   
 26 photoreceptors (**Appendix figure 28D**). These high  $F$  values confirmed that a linear Volterra series  
 27 model could approximate light-adapted *Drosophila* photoreceptor output to the test stimulation

1 appropriately.

2

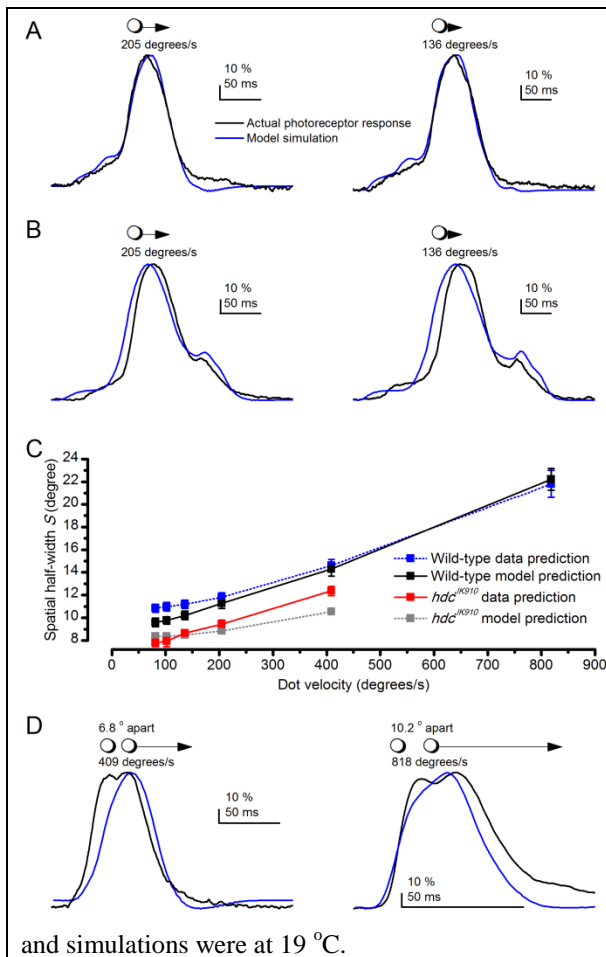
### 3 **Classic theory underestimates how well R1-R6s resolve fast moving dots**

4 By approximating the light input directly from the receptive field measurements (**Appendix figure**  
 5 **22**) and the corresponding R1-R6 output by Volterra series (**Appendix figure 28C**), we could  
 6 estimate each tested *Drosophila* photoreceptor's responses to moving bright dots. This was done by  
 7 convolving the extrapolated light stimuli with the corresponding impulse responses.

8 The model predictions for a single moving stimulus were far less consistent than those for  
 9 GWN stimuli. **Appendix figures 29A-B** show representative simulations with broadly acceptable and  
 10 clearly unacceptable accuracies, respectively, together with the corresponding intracellular recordings.

11 From both the recordings and simulations, we further calculated the theoretical dot motion  
 12 effects on the neural image resolution, or spatial half-width,  $S$  (**Appendix figures 29C**). As explained  
 13 above (*cf.* **Appendix figure 26B**), the classic theory can only broadly suggest the relative differences  
 14 between wild-type and mutant performances. Here, its application to the simulations further  
 15 underestimated the spatial half-width predictions of wild-type recordings and over-estimated those of  
 16 the *hdc* mutant.

17



**Appendix figure 29. Prediction accuracy of the Volterra series photoreceptor models to moving point-objects varies considerably.** (A) Two examples of model simulations, which were reasonably close to the actual intracellular recordings to the tested dot motion. (B) Two examples of simulations that clearly differed from the recordings. (C) Theoretical predictions of photoreceptor output spatial half-width, calculated from the recordings and simulations as a function of the point-object speed. Mean  $\pm$  SEM,  $n_{\text{wild-type}} = 9$ ,  $n_{\text{hdc}} = 8$ . The theoretical spatial half-widths of the simulations differ from those of the recordings. *E.g.* the wild-type recordings (black) predicted consistently narrower  $S$  than the corresponding simulations (blue). The predicted resolvability of the resulting neural image, or spatial half-width ( $S$ ), was consistently lower for the simulations than for the recordings. (D) Crucially, Volterra series models failed to predict how well the actual photoreceptor output resolves two close objects moving together very fast (shown for 409 and 818  $^{\circ}$ /s). For the 818  $^{\circ}$ /s prediction, we used here the fastest impulse response, recorded from another cell, but even so, the model still could not resolve the two dots. Thus, the actual spatial half-width of R1-R6s, limiting *Drosophila*'s resolving power at high image velocities, is about half of that estimated in (C). (Note, the dynamic biophysical mechanisms causing this difference – both in light input and photoreceptor output – are explained in **Appendix 8**. Recordings and simulations were at 19  $^{\circ}$ C.

18

19 Most critically, however, Volterra series models consistently failed to predict the fast phasic  
 20 components of the recorded voltage responses, and thus their real resolvability, to two fast moving  
 21 dots (**Appendix figures 29D**; see also **Figure 7**). The model simulations, and hence its underlying  
 22 classic theory, always predicted lower resolvability than what we saw in the actual recordings. Further  
 23 investigations (**Appendixes 7-8**) revealed that this discrepancy reflected the missing biophysical  
 24 mechanisms of the empirical black-box models (see **Appendix 1**). Specifically, the used  
 25 photoreceptor models lacked: (i) the photomechanical rhabdomere movements, which shift and  
 26 narrow a R1-R6's receptive fields, and (ii) the refractory sampling, which allows many microvilli

1 (after the 1<sup>st</sup> dot) to recover from refractoriness (Song *et al.*, 2012; Song & Juusola, 2014; Juusola *et*  
2 *al.*, 2015) to respond to the 2<sup>nd</sup> dot. Moreover, by tuning and validating the Volterra kernels to GWN  
3 stimuli at relative steady-state, we inadvertently limited its exposure to (iii) excitatory dynamic  
4 synaptic feedback modulation (Zheng *et al.*, 2006; Dau *et al.*, 2016), which accentuates sudden  
5 changes in photoreceptor output. For these reasons, the responses of real R1-R6s, which naturally  
6 utilize the given mechanisms, showed systematically larger widths and 2<sup>nd</sup>-peaks, providing higher  
7 resolvability.

8 We show in **Figures 8G-I**, **Figure 8-figure supplement 1** and **Appendixes 7-8** that a new  
9 biophysically realistic microsaccadic sampling model, which allows for realistic refractory quantal  
10 phototransduction (Song & Juusola, 2014) and photomechanical rhabdomere contractions (Hardie &  
11 Franze, 2012), yields (significantly better) theoretical predictions that closely approximate the real  
12 R1-R6 output. Importantly, in **Appendix 9**, we further show that R1-R6 output to two **dark** dots,  
13 moving at saccadic speeds, has the same relative resolution as their output to the corresponding two  
14 **bright** dots. Collectively, our results demonstrate that *Drosophila* photoreceptors resolve fast moving  
15 objects far better than what was believed previously.

## 16 17 **Conclusions**

18 In this appendix, we used intracellular recordings and classic theoretical approaches to study how fly  
19 photoreceptors encode moving bright dots. Model simulations about each tested R1-R6s'  
20 spatiotemporal responses were compared to the actual recordings to the same stimuli. We found that  
21 both wild-type and *hdc<sup>JK910</sup>* photoreceptors resolved moving dots nearly equally well, and  
22 significantly better than the corresponding deterministic simulations. These findings demonstrate that  
23 the classic dynamic photoreceptor models (Srinivasan & Bernard, 1975; Juusola & French, 1997;  
24 Land, 1997), which lack knowledge about the underlying phototransduction biophysics and  
25 photomechanics, grossly underestimate the spatiotemporal resolution of the real cells.

26 Animals counter self-motion blur effects by moving their eyes. This compensates for head  
27 and body movements by keeping the neural image position near stationary as long as possible (Land,  
28 1999). Interestingly here, a fly photoreceptor's response to two moving point-objects represents an  
29 opposite case where image motion, in fact, improves acuity. In the classic theory, to resolve two  
30 stationary objects, at least three photoreceptors are required so that the intensity difference in between  
31 can be detected. Because *Drosophila* photoreceptors' interommatidial angles (Land, 1997; Gonzalez-  
32 Bellido *et al.*, 2011) vary from 3.4° to 9.0° and their average acceptance angle is ~9.5° (**Appendix 4**),  
33 its eye should not resolve two point-objects 6.8° apart. Nevertheless, responses of single  
34 photoreceptors, during even very fast (saccadic-speed) (Geurten *et al.*, 2014) movements, show large  
35 enough dips (in their temporal dynamics) to indicate that the objects are resolved neurally. In the  
36 classic theory instead, the outputs of several adjacent photoreceptors had to be processed together to  
37 distinguish two moving point-objects from one stationary object, in which brightness changes over  
38 time. This example highlights the inseparability of spatiotemporal information processing and visual  
39 acuity.

40 The unique advantages of the present study were the bespoke equipment and stimulus  
41 paradigm. These allowed high-quality photoreceptor recordings with precisely controlled moving  
42 point-objects stimulation. Therefore, we could directly test and compare the theoretically predicted  
43 relationship between the neural image resolution and the object speed (Srinivasan & Bernard, 1975;  
44 Juusola & French, 1997) to the experimental data. However, the equipment also had limitations to be  
45 improved in future research. Wider object speed range is necessary, especially for testing insect eyes  
46 with fast responses. Owing to the long transient time, each light-point now required 2 ms switching  
47 period. Consequently, the minimum travelling time was 50 ms and the object speed limit in  
48 *Calliphora* experiments was 334 °/s, which is far slower than observed during the flies' saccadic flight  
49 behaviors (Schilstra & Van Hateren, 1999; van Hateren & Schilstra, 1999) (2,000-4,000 °/s). Whilst  
50 positioning the light-point array closer to the fly eye would increase object angular speed, it would  
51 compromise resolution as fewer light-points would then lie within a tested cell's receptive field.

52 In **Appendixes 7-9**, we show how both the enhanced resolvability of moving point-objects  
53 and the phasic modulation of their rising and decaying phases, as was shown here, emerge from the  
54 joint contributions of photomechanical rhabdomere contraction and its refractory information  
55 sampling.

## Appendix 7: Photomechanical microsaccades move photoreceptors' receptive fields

### Overview

This appendix describes a new powerful high-speed video recording method to measure photomechanical rhabdomere movements *in situ*, and provides important experimental and theoretical background information for the results presented in **Figures 8-9**.

In this appendix:

- We utilize the optical cornea-neutralization technique (Franceschini & Kirschfeld, 1971b, a) with antidromic deep-red (740 or 785 nm peak) illumination to observe deep pseudopupils (photoreceptor rhabdomeres that align with the observer's viewing axis) in the *Drosophila* eye. We use an ultra-sensitive high-speed camera with a purpose-built microscope system to record fast rhabdomere movements across the compound eyes, while delivering blue-green stimuli (470 + 535 nm peaks) orthodromically into the eye.
- We show that light-activation moves rhabdomeres (**Video 3**) side-ways (horizontally) both in dark- and light-adapted eyes. This movement starts after a 8-20 ms delay from the light stimulus onset, and reaches its peak in about 70-150 ms. Because these movements have fast onset and light intensity-dependency, which are similar to those of the R1-R6 photoreceptors' intracellular voltage responses to comparable stimuli, they must result from individual photoreceptors' photomechanical contractions; see (Hardie & Franze, 2012).
- We show that *trp/trpl*-mutant photoreceptors, which have normal phototransduction reactions but lack the light-gated ion channels, also contract to light. Since these photoreceptors cannot produce electrical responses and thus communicate electrically or synaptically with other cells, including eye muscles, their contractility cannot be caused by eye muscle activity but must be intrinsic, supporting the earlier hypothesis (of phototransduction reactants interacting locally with the plasma membrane) (Hardie & Franze, 2012).
- We show that light moves rhabdomeres fast in the back-to-front direction, while darkness returns them back to their original positions slower. Because the ommatidium lens inverts images, R1-R8 photoreceptors' receptive fields move in the opposite direction - front-to-back after light and back-to-front after darkness. Therefore, when front-to-back moving bright dots cross the eyes, the photoreceptors' receptive fields move along. But when bright dots cross the eyes in the back-to-front direction, the photoreceptors' receptive fields move against them (*cf.* **Appendix 6**).
- At the level of rhabdomere tips, the horizontal movements can be up to 1.4  $\mu\text{m}$ , as measured occasionally in light-adapted eyes. Therefore, given the known optical dimensions, these photomechanical microsaccades can rapidly shift R1-R6 photoreceptors' receptive fields by  $\sim 5^\circ$ . Remarkably, such a large image pixel displacement reaches the average interommatidial angle,  $\Delta\phi \sim 4.5\text{-}5^\circ$ , in the *Drosophila* eye (*cf.* **Appendix 4**; **Appendix figure 14**).
- We show that the light stimulus also contracts rhabdomeres axially (**Video 2**; inwardly: 0.5-1.7  $\mu\text{m}$ ), down away from the lens. This transient increase in focal length should contribute in narrowing R1-R6's receptive fields dynamically. We further show that specific cone- and pigment-cells inside each ommatidium form an aperture, which is connected to the rhabdomere tips. During light stimulation, this aperture moves laterally with the rhabdomeres but only half as much (**Video 4**). And since the ommatidium lens remains practically immobile, the light beam falling upon the rhabdomeres is shaped dynamically. These observations mean that a R1-R6's receptive field must both move and narrow during dynamic light stimulation.
- We show that rhabdomeres of *hdc<sup>JK910</sup>* histamine-mutant (Burg *et al.*, 1993; Melzig *et al.*, 1996; Melzig *et al.*, 1998) R1-R6 photoreceptors, in which visual interneurons are blind (receive no neurotransmitter from photoreceptors), have broadly wild-type-like contraction dynamics, again refuting the role of eye muscle activity in the data. But interestingly, their light-sensitivity is about 10-fold reduced, similar to their voltage responses (Dau *et al.*, 2016). In part, this may reflect *hdc<sup>JK910</sup>* photoreceptors' smaller size. Given that *hdc<sup>JK910</sup>* rhabdomere diameters are  $\sim 4\%$  smaller than in wild-type (**Appendix 5**), their length should also be

1 reduced in the same proportion. As the average wild-type R1-R6 is  $\sim 100 \mu\text{m}$ , *hdc*<sup>JK910</sup> R1-R6s  
2 should be  $\sim 4 \mu\text{m}$  shorter. And indeed we find *in situ* that *hdc*<sup>JK910</sup> rhabdomere tips are  $\sim 4 \mu\text{m}$   
3 further away from the lens than the wild-type tips. In addition, the higher  $[\text{Ca}^{2+}]_i$ , caused by  
4 tonic excitatory synaptic feedback overload (Dau *et al.*, 2016), may further affect their  
5 mobility, possibly retaining them in a slightly more contracted state.  
6

### 7 **Rapid adaptation caused by light-induced R1-R8 contractions**

8 Atomic force microscopy (AFM) at the dissected *Drosophila* eyes' corneal surface (Hardie & Franze,  
9 2012) has shown up to 275 nm radial movements to brief light pulses, caused by transient  
10 *photomechanical* R1-R8 photoreceptor contractions. Such movements are too small and fast to see  
11 with the naked eye, and were initially considered: (i) only to participate in gating photoreceptor's  
12 transduction-channels, and (ii) possibly too small to affect fly vision in general. In this appendix, we  
13 use high-speed video microscopy to show that *in vivo* the underlying photomechanical rhabdomere  
14 (light sensor) movements are larger both laterally (horizontally: 0.3-1.4  $\mu\text{m}$ ) and axially (inwardly:  
15 0.5-1.7  $\mu\text{m}$ ). Because these movements are also synchronous, ubiquitous, robust and reproducible,  
16 they influence how the fly eyes sample visual information about the world.  
17

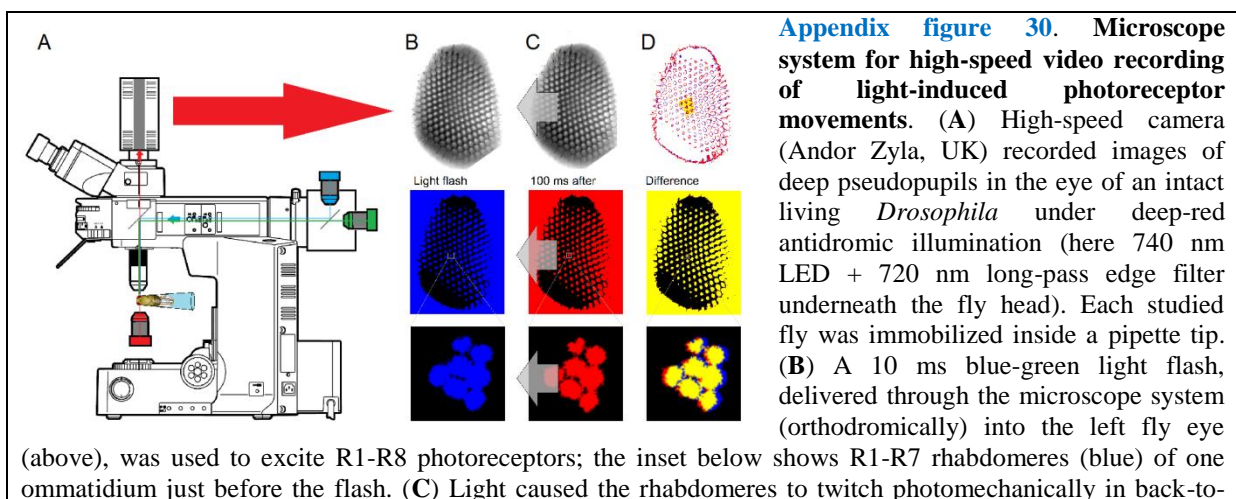
### 18 **High-speed video recordings of light-induced rhabdomere movements**

19 Dark-adapted dissociated photoreceptors rapidly contract to light (Hardie & Franze, 2012) (**Video 2**).  
20 It has been suggested that this contraction results from light-induced phosphatidylinositol 4,5-  
21 bisphosphate (PIP<sub>2</sub>) cleaving, which modulates their rhabdomere membrane volume and so  
22 participates in gating the phototransduction-channels (*trp* and *trpl*) (Hardie & Juusola, 2015).

23 Here, we directly test the hypotheses that (i) the photomechanical photoreceptor contractions  
24 occur also in intact flies in normal stimulus conditions, and (ii) these movements serve the purpose of  
25 modulating light input to photoreceptors and thus photoreceptor output. We do this by recording high-  
26 speed video of how *Drosophila* photoreceptor rhabdomeres move to different light stimuli *in vivo*, and  
27 by analyzing and characterizing how these movements affect R1-R6s' receptive fields. Later on, in  
28 **Appendix 8**, we include their light input parameter changes in biophysically-realistic mathematical  
29 models to predict R1-R6 voltage output to moving visual stimuli.  
30

### 31 **Imaging setup for recording photomechanical rhabdomere contractions**

32 We used the optical cornea-neutralization method to monitor how light stimuli evoke *Drosophila*  
33 photoreceptor rhabdomere movements. The imaging system was constructed upon an upright  
34 microscope (Olympus BX51), secured to a XY-micrometer stage on an anti-vibration table  
35 (MellesGriot, UK) (**Appendix figure 30**). To minimize light pollution in the recordings, the system  
36 was light-shielded inside a black Faraday cage with black lightproof curtains in the front, and the  
37 experiments were performed in a dark room. For collecting and recording deep pseudopupil images,  
38 the system was equipped with a 40x water immersion objective (Zeiss C Achromplan NIR 40x/0.8 w,  
39  $\infty/0.17$ , Germany) and an ultra-sensitive high-speed camera (Andor Zyla, UK), respectively.  
40

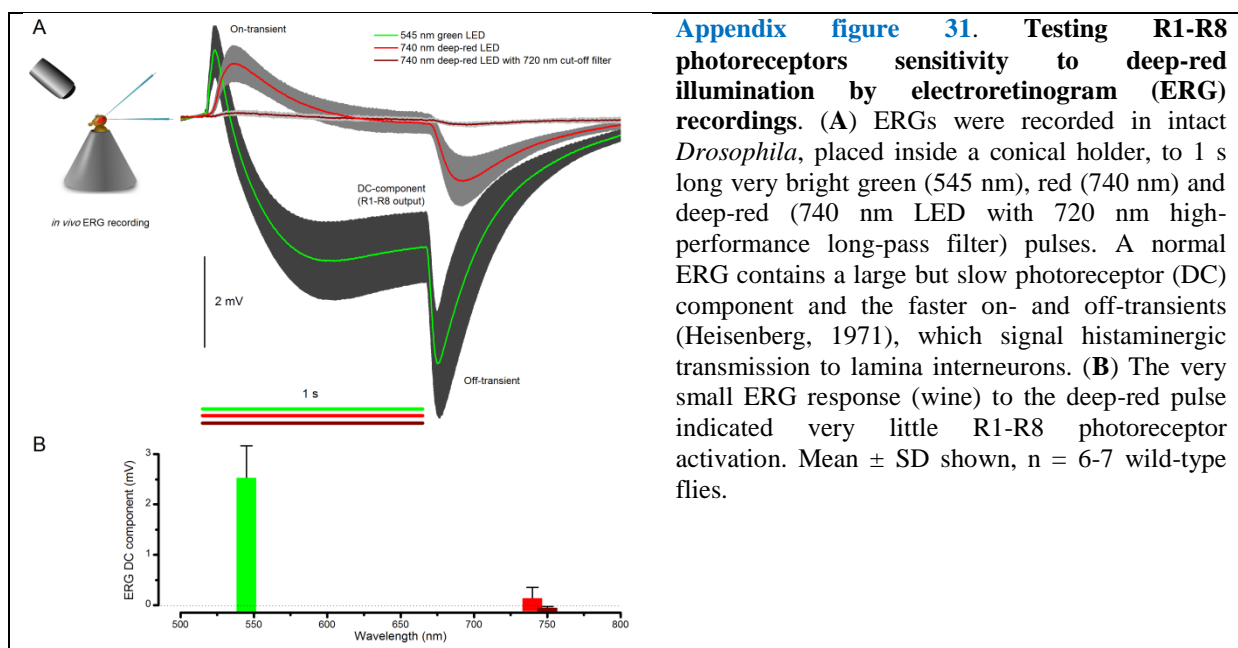


front direction (arrows) after 8-16 ms delay, with the photoreceptors being maximally displaced in ~100 ms from the stimulus onset. Invariably, this was seen as a sudden jump in the recorded rhabdomere position (red). (D) The difference in the rhabdomere position (displacement) before and after the flash, depended upon the light intensity, ranging between 0.3-1.4  $\mu\text{m}$ ; note a typical R1-R6 rhabdomere diameter is about 1.7  $\mu\text{m}$  (Appendix 5). The frame subtraction (before and after the light flash) indicates that only the rhabdomeres that aligned directly with the blue/green light source moved (within the 7 central ommatidia; yellow area), while the rest of the eye remained immobile. Accordingly, the difference image shows little ommatidial walls, as these and other immobile eye structures became mostly subtracted away. In contrast, eye muscle activity, which is every so often seen with this preparation (Appendix 4, Appendix figure 19) occurs more gradually and moves all the eye structures together.

1  
2 A *Drosophila* was gently fastened to an enlarged fine-end of a 1 ml pipette tip by puffing air  
3 from a 100 ml syringe at the large end until the fly head and ~1/5 of the thorax emerged outside  
4 (Appendix figure 30A). The head and thorax were carefully fixed (from the proboscis and cuticle) to  
5 the pipette wall in a preferred orientation by melted beeswax, without touching the eyes. The fly was  
6 then positioned with a remote-controlled XYZ-fine resolution micromanipulator (Sensapex, Finland)  
7 underneath the water immersion objective, using both visual inspection and live video stream on a  
8 computer monitor.

9 Antidromic illumination (through the fly head) revealed the deep pseudopupils of the fly eyes.  
10 It was provided with a high-power deep-red light source (740 nm LED with 720 nm high-pass edge-  
11 filter; or 785 nm LED with  $\pm 10$  nm bandpass filter), driven by a linear current LED driver (Cairn  
12 OptoLED, UK). Note that very bright deep-red illumination, which is a prerequisite for good signal-  
13 to-noise ratio high-speed video imaging, activates R1-R8 photoreceptors only marginally. This is  
14 because their different rhodopsins' absorbance maxima are at much lower wavelengths (Britt *et al.*,  
15 1993; Wardill *et al.*, 2012). The photoreceptors' near insensitivity to  $>720$  nm red light was confirmed  
16 *in vivo* by ERG recordings (Appendix figure 31).

17 Orthodromic light stimulation (through the 40x objective into the eye), which evoked the  
18 photoreceptor contractions, was delivered by two high-power LEDs: 470 nm (blue) and 545 nm  
19 (green), each separately controlled by its own driver (Cairn OptoLED, UK). These peak wavelengths  
20 were selected to activate R1-R6s' rhodopsin (Rh1) and its meta-form near maximally, and so through  
21 joint stimulation to minimize desensitization by prolonged depolarizing after-potentials (PDA)  
22 (Minke, 2012). Simultaneous stimuli from the two LEDs were merged into one focused beam by a  
23 495 nm dichroic mirror and low-pass-filtered at 590 nm. Pseudopupil signals of the observed fly eye  
24 (left or right) were split spectrally by another dichroic mirror (600 nm), and essentially only red image  
25 intensity information ( $\geq 600$  nm) was picked up by the high-speed camera.



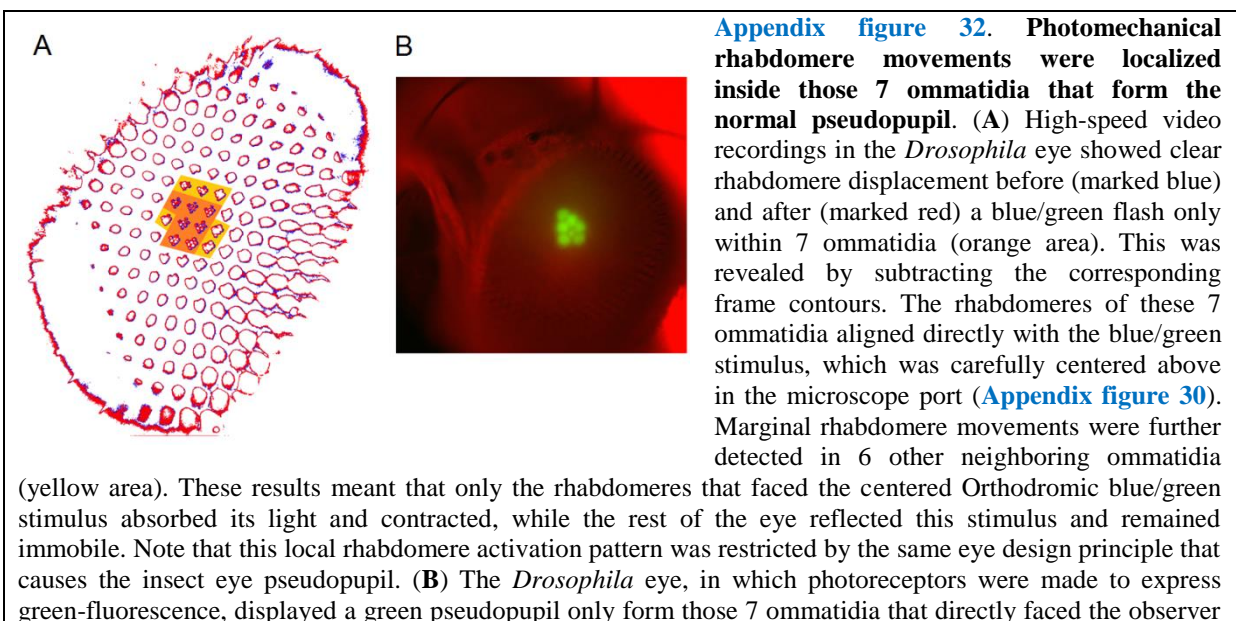
## 1 **Recording procedures**

2 Light stimulus generation was performed by a custom-written Matlab (MathWorks, USA) program  
3 (Biosyst; M. Juusola, 1997-2015) (Juusola & Hardie, 2001a; Juusola & de Polavieja, 2003) with an  
4 interface package for National Instruments (USA) boards (MATDAQ; H. P. C. Robinson, 1997–  
5 2008). The length of the light stimuli (including the continuous deep-red background and the  
6 blue/green stimulus patterns) was made to match the number of frames to be acquired by the Andor  
7 camera, and the stimuli were externally triggered by the camera software (Solis). During the  
8 recordings, the frames were first buffered in the RAM in high-speed and then transferred on the  
9 computer's hard drive. Light stimulus intensity could be attenuated by a neutral density filter set  
10 (Thorn Labs, USA), covering a 5.3 log intensity unit range.

## 11 **Key observations from unprocessed high-speed footage**

12 High-speed video microscopy ([Appendix figure 30A](#); e.g. [Video 3](#)) from intact wild-type *Drosophila*  
13 eyes ( $n \gg 100$  flies) showed repeatedly and unequivocally that:

- 14 • Full-field light flashes evoked rapid local R1-R7 rhabdomere movements within those 7  
15 ommatidia, which at the center of the imaged view, faced the blue/green stimulus source  
16 directly ([Appendix figure 32A](#), orange area). Rhabdomeres in few other neighboring  
17 ommatidia also moved marginally (yellow area), but not obviously in other ommatidia. This  
18 meant that only the ommatidia that aligned with the blue/green stimulation absorbed the  
19 incident light, while those to one side reflected it. This local area, which showed  
20 photomechanical rhabdomere movements, closely matched *Drosophila*' normal pseudopupil  
21 ([Appendix figure 32B](#)).
- 22 • The rhabdomere movement was in the back-to-front direction ([Appendix figure 30B-D](#)),  
23 whilst in darkness, the rhabdomeres returned in front-to-back to their original positions more  
24 slowly. These dynamics and their directions were similar in both the left and right eye.
- 25 • Because light always moved the rhabdomeres back-to-front, the corresponding neural images  
26 of the left and the right eye comprise left-right mirror symmetry; i.e. against the vertical  
27 (sagittal) plane, the rhabdomeres in the left and right eye display mirror symmetric motion.  
28 We show later in [Appendix 8](#) how this symmetry may allow *Drosophila* photoreceptors to  
29 encode orientation information during saccades or image rotation.
- 30 • The rhabdomere movement directions seemed homogeneous (at least in the 1<sup>st</sup>  
31 approximation) across each tested eye, appearing similar in its different regions: whether  
32 measured at its up, down, front or back ommatidia. Such “pixel interlocking” across the  
33 whole eye's visual field may help to preserve, or enhance, the neural images' spatial  
34 resolution of the world.
- 35
- 36

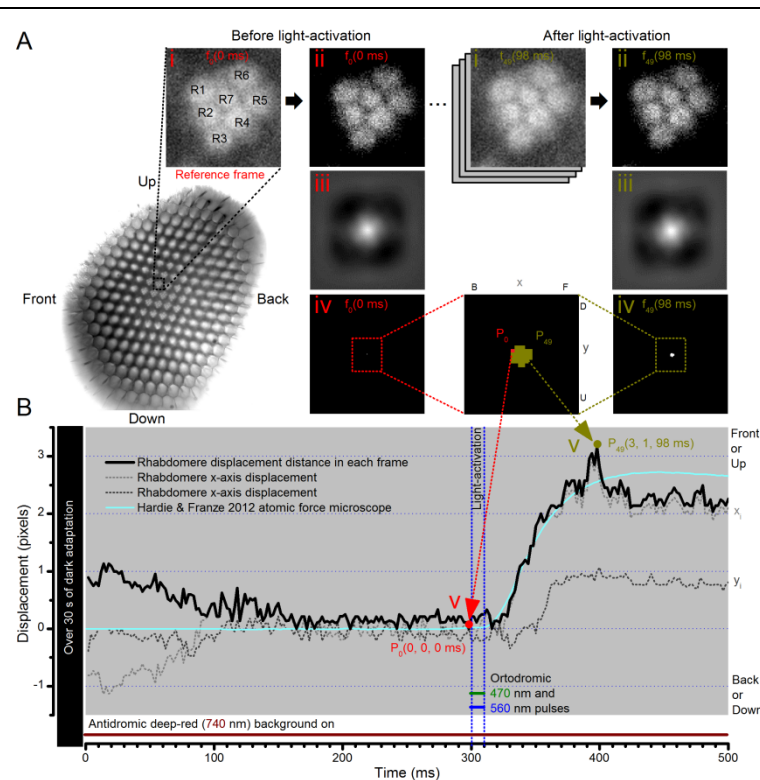


(and the blue light source through the microscope lenses). This happened because these ommatidia (their rhabdomeres) both absorbed the incident blue light and their GFP-molecules released green light back to the observer's eye/camera, while the other ommatidia around reflected the blue light.

## Image analysis

To accurately quantify the size and direction of the observed rhabdomere movements in time we devised specific image-analysis procedures. First, the stored images (raw data frames of each recording) in the hard drive were exported as a tiff stack, in which pixel intensity range was set by the frames' minimum and maximum values, using the camera software (Andor SOLIS). ImageJ software was then used to convert the tiff-stack into a single tiff-file. Finally, custom-written Matlab programs (scripts) were used to process and analyze the images (**Appendix figure 33A**). These methods included:

- i. Loading the image stack.
- ii. Subtracting the median and mean from each frame and setting its negative values to (0, 0) to remove the dark noise background. This process was repeated for every frame.
- iii. Calculating 2D cross-correlation between each frame and the reference frame.
- iv. Selecting the cross-correlation values, which were  $\geq 95\%$  of the maximum (peak) value. This was repeated for every frame.
- v. Calculating the weighted average position of the peak by using all the positions of the previous selection and using the cross correlation values as weights both in x- and y-direction. This was repeated for every frame.
- vi. Subtracting the reference frame position from every frame.



## Appendix figure 33. Cross-correlation image analysis to estimate photomechanical R1-R7 rhabdomere movements.

(A) Analytical steps are shown for the reference frame at time zero ( $f_0$ ), 2 ms before the 10 blue/green light stimulus pulse (red), and for the frame at the maximum rhabdomere displacement ( $f_{49}$ ), 98 ms after (dark yellow). High-speed camera images of rhabdomeres were recorded using 750 nm red light. (i) Image stacks were uploaded, and (ii) the median of each frame was subtracted to remove its noise background. (iii) 2D cross-correlation was calculated for each frame, and (iv) the values within 5% of their peak value were selected. (v) The weighted mean peak positions gave each frame's x- and y-positions at its specific time point, and their distance,  $\sqrt{x^2+y^2}$ , the total rhabdomere displacement (in pixels) against the reference frame position. Notice that the 2D cross-correlation images have flipped x- and

y-axis directions (up, U, appears down, D; front, F, appears back, B). (B) The resulting rhabdomere displacement distance and the corresponding x- and y-positions are plotted for each frame in time at 2 ms resolution (500 frames/s), against the reference frame position,  $P_0(0, 0, 0)$ . A comparable (inverted) atomic force microscopy data (cyan) closely matches the rise-time dynamic of the cross-correlation rhabdomere displacement estimate, validating our analytical approach. The analysis also implies that well dark-adapted photoreceptors may respond weakly to deep-red (740 nm) light onset (black trace 0-100 ms). Note R8 rhabdomere, which lies directly below R7, likely contracts too.

## Quantifying rhabdomere travels and their receptive field shifts

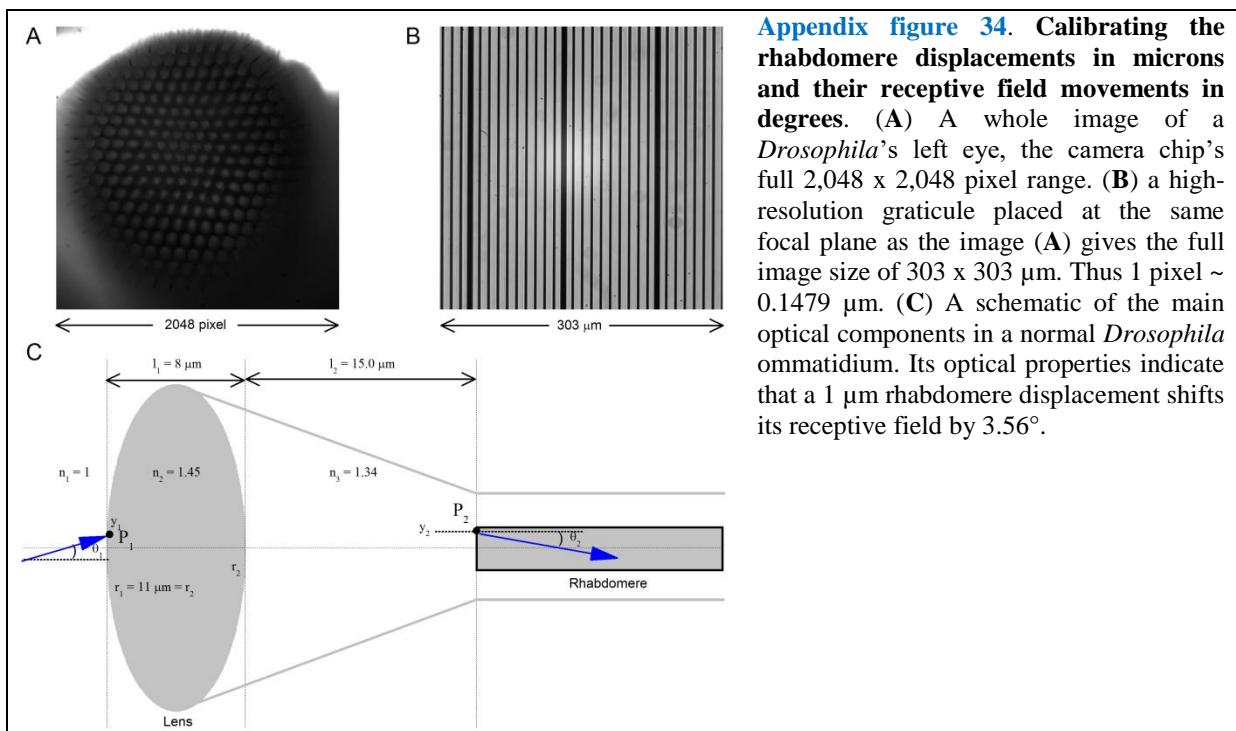
1 In this study, the rhabdomere displacement measurements are given in microns ( $\mu\text{m}$ ) and the resulting  
 2 receptive field movements in degrees ( $^\circ$ ). **Appendix figure 34A** shows a whole image of a  
 3 *Drosophila*'s left eye, as focused upon its rhabdomeres in the center and magnified by the microscope  
 4 system to use the camera's full 2,048 x 2,048 pixel range. By placing a high-resolution  $\mu\text{m}$ -graticule  
 5 on the same focal plane (**Appendix figure 34B**), we calibrated that the whole image is 303 x 303  $\mu\text{m}$ .  
 6 After converting the recorded rhabdomere displacements from pixels (**Appendix figure 33**) into  
 7 microns, we then used the published parameters (Stavenga, 2003b) about the *Drosophila* ommatidium  
 8 optics (**Appendix figure 34C**) to translate these measurements into corresponding receptive field  
 9 movements in degrees.

10 *Drosophila* ommatidium optical parameters were described by (Stavenga, 2003b) and  
 11 (Gonzalez-Bellido *et al.*, 2011). Its biconvex facet lens focuses light to a rhabdomere (grey rectangle)  
 12 tip. The outer and inner lens curvatures,  $r_1 = -r_2$ , are 11  $\mu\text{m}$ , and its thickness,  $l_1$ , is 8  $\mu\text{m}$ . Distance  
 13 from lens to the rhabdomere,  $l_2$ , is 15  $\mu\text{m}$ . Reflective indices,  $n$ , for the object space, lens and image  
 14 space, respectively, are:  $n_1 = 1$ ,  $n_2 = 1.45$  and  $n_3 = 1.34$ .

15 We used standard ray transfer matrix analysis (Laufer, 1996) to determine optical properties  
 16 between the lens surface,  $P_1$ , and the rhabdomere tip,  $P_2$ . Both of these are represented as vectors of  
 17 their positions,  $y$ , and angles,  $\theta$ :  $P_1 = \begin{bmatrix} y_1 \\ \theta_1 \end{bmatrix}$  and  $P_2 = \begin{bmatrix} y_2 \\ \theta_2 \end{bmatrix}$ . Then, the optical system of the facet lens  
 18 follows equation  $P_2 = M P_1$ , where

19  $M = \begin{bmatrix} 0.23 & 1.61 * 10^{-5} \\ -3.63 * 10^4 & 0.71 \end{bmatrix}$ , obtained from the ray transfer matrix analysis.

20 The transform matrix clarifies that the distance,  $y_2$  (at  $P_2$ ), mostly depends upon the angle  $\theta_1$   
 21 (of  $P_1$ ). Thus, 1  $\mu\text{m}$  movement gives  $1 \times 10^{-6} / 1.61 \times 10^{-5} = 0.0621$  (rad) angular change, which is 3.56  
 22  $^\circ / \mu\text{m}$ . This movement is an inverse of the visual field movement. Note that by using the comparable  
 23 optical parameter values of (Gonzalez-Bellido *et al.*, 2011) (and considering the normal lens f-value  
 24 variation across the *Drosophila* ommatidia), gives practically the same movement ratio ( $\pm 5\%$  error).  
 25

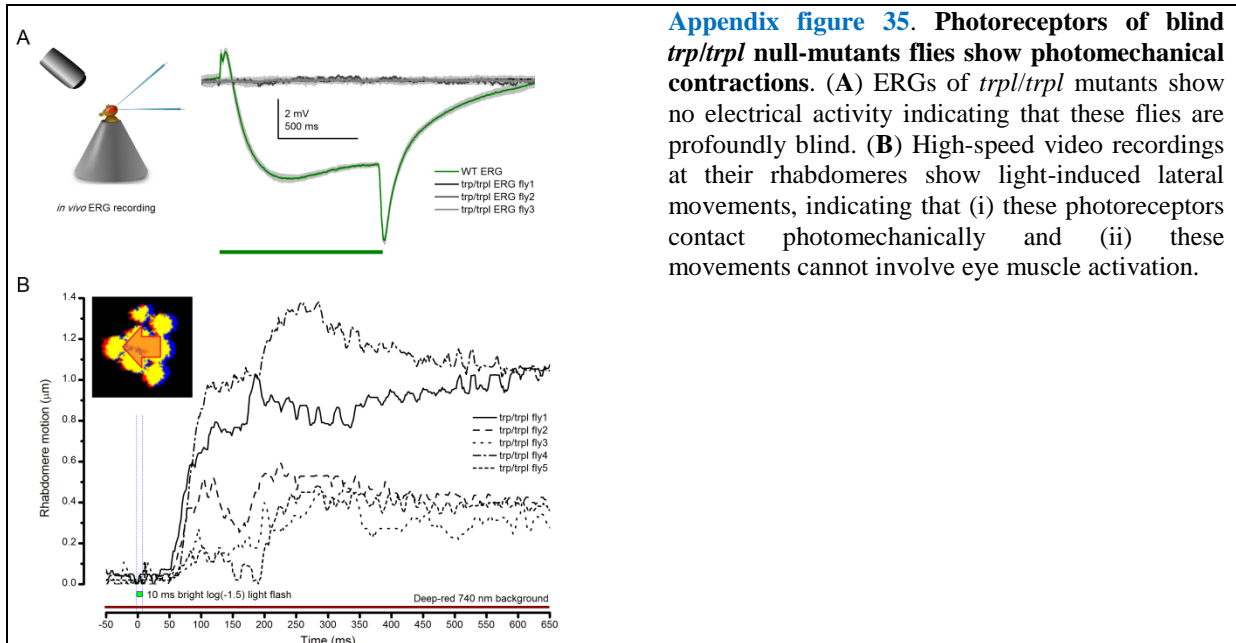


26

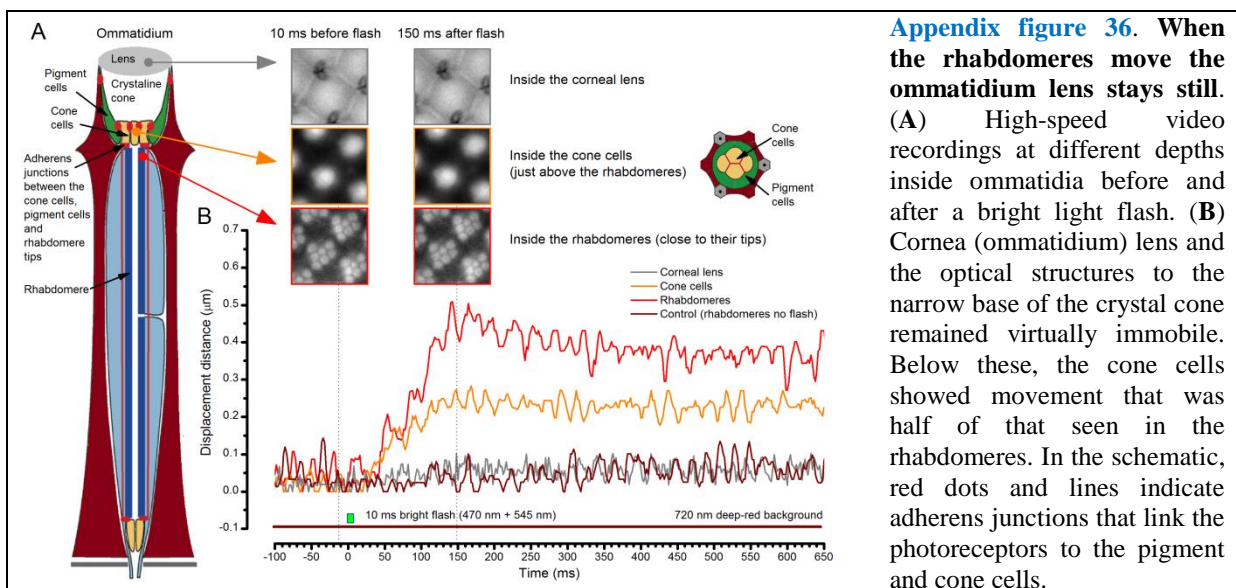
### 27 *Trp/trpl*-mutants confirm the contractions' photomechanical origin

28 We then tested whether the rhabdomere contractions were generated by the photoreceptors themselves  
 29 (photomechanically) or by eye muscle activity. This was done by recording in *trp/trpl* null-mutants,  
 30 which express normal phototransduction reactants but lack completely their light-gated ion channels.  
 31 Consequently, these photoreceptors did not generate electrical responses to light, and their eyes

1 showed no ERG signal (**Appendix figure 35A**). Nonetheless, high-speed video recordings revealed  
 2 that *trp/trpl*-mutant photoreceptors contracted photomechanically (**Appendix figure 35B**; see also  
 3 **Video 2**). These observations are consistent with the hypothesis of the light-induced  
 4 phosphatidylinositol 4,5-bisphosphate (PIP<sub>2</sub>) cleaving from the microvillar photoreceptor plasma  
 5 membrane causing the rhabdomere contractions (Hardie & Franze, 2012).  
 6



7  
 8 **When rhabdomeres move, the ommatidium lens system above stays still**  
 9 Using the high-speed video microscopy, we next tested whether the *Drosophila* lens system or any  
 10 other ommatidium structures moved during the rhabdomere movements (**Appendix figure 36**). In the  
 11 experiments, a z-axis micromanipulator (Sensapex, Finland) was used to shift and reposition  
 12 *Drosophila* in piezo-steps vertically. This allowed the focused image, as projected on the camera, to  
 13 scan through each studied ommatidium, providing exact depth readings in  $\mu\text{m}$ . We then recorded any  
 14 structural movements inside the ommatidia at different depths; from their corneal lens down to the  
 15 narrow base, where the cone and pigment cells form an intersection between the crystalline cone and  
 16 the rhabdomere tips (Tepass & Harris, 2007).  
 17



18

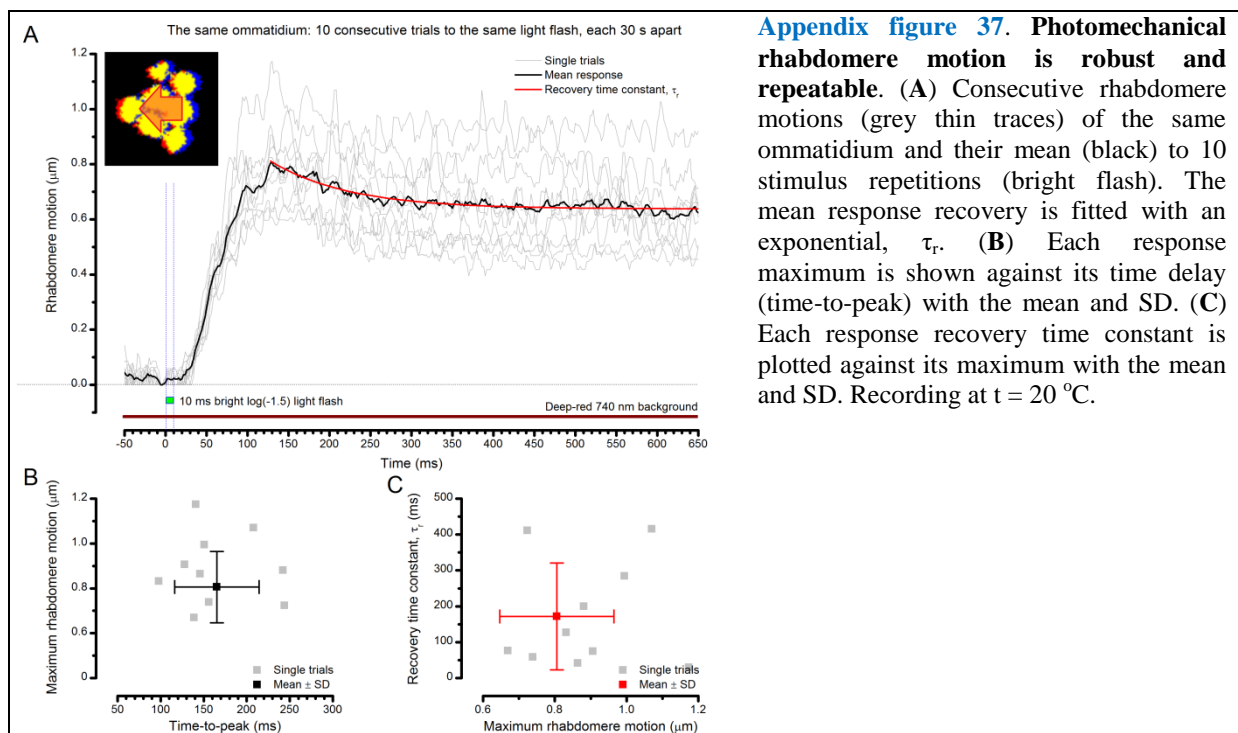
1 We found that when the rhabdomeres moved photomechanically (**Appendix figure 36B**, red  
2 trace; **Video 4**) the corneal lens and the upper ommatidium structures were essentially immobile  
3 (grey), and normally remained so throughout the recordings. However, clear stimulus-induced  
4 movements were detected at the basal cone/pigment cell layer (orange; also inset) that connects to the  
5 rhabdomere tips with adherens junctions (Tepass & Harris, 2007). Although it is less clear how much  
6 these structures reflected the rhabdomere motion underneath or were pulled by it, it is quite certain  
7 that they formed an aperture in the light path, which moved less than the light-sensors (rhabdomeres)  
8 below (orange vs. red). In **Appendix 8**, we analyze how such an interaction might dynamically  
9 narrow the R1-R6s' receptive fields to visual motion.

10 Overall, these results further verified that in normal stable recordings the used blue/green  
11 light flash was not evoking eye muscle activity, which would otherwise move the whole eye.  
12

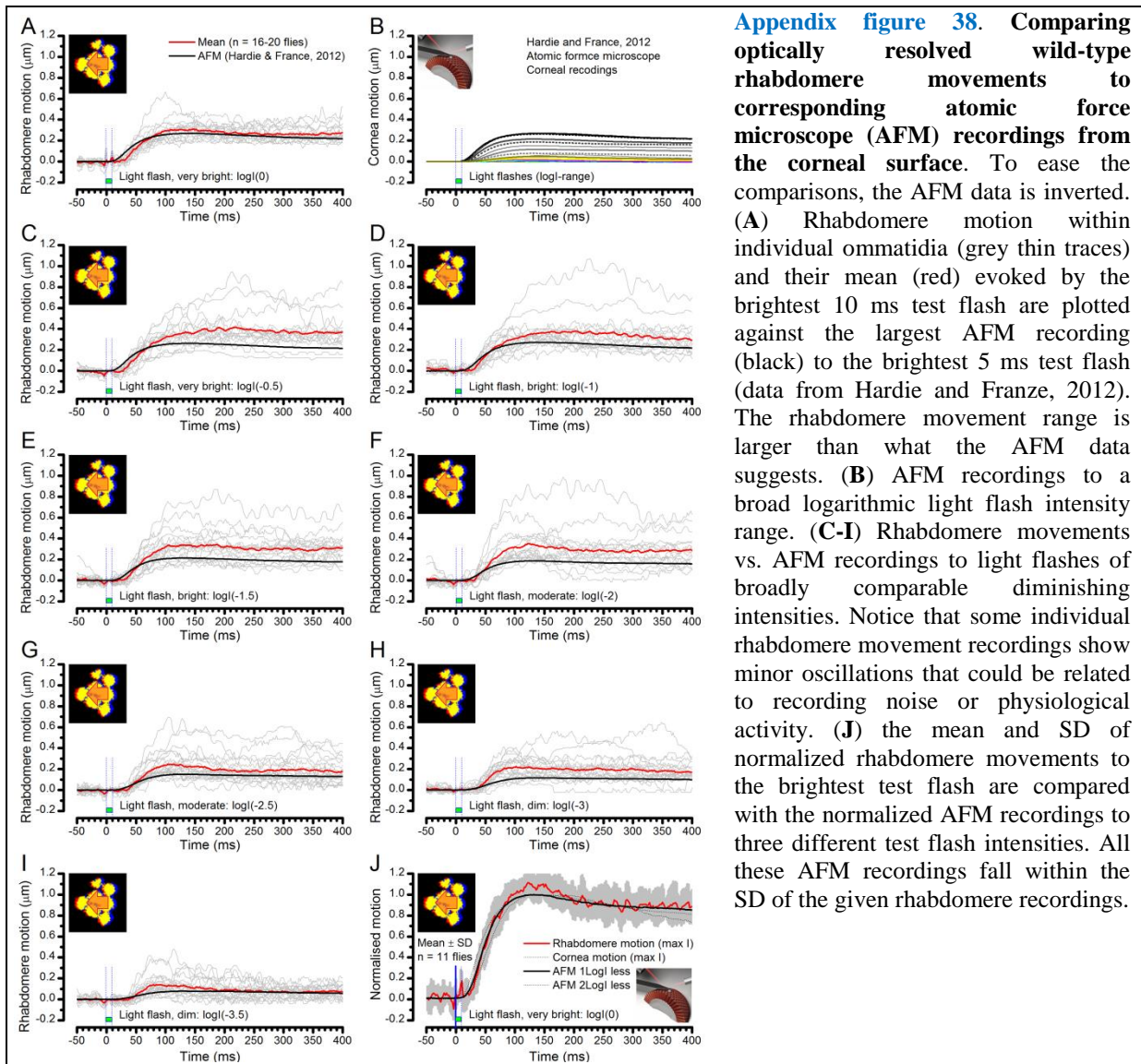
### 13 Light intensity-dependence of rhabdomere movements (*in vivo* dynamics)

14 Through a wide-ranging testing regime, we further discovered (**Appendix figure 37** and **Appendix**  
15 **figure 38**) that:

- 16 • Light-induced R1-R7 rhabdomere movements were robust and repeatable. **Appendix figure**  
17 **37A** shows 10 trials (thin grey traces) and their mean (black) to a 10 ms bright flash measured  
18 from the same ommatidium. Between each flash, the eye was dark-adapted for 30 s. Characteristically,  
19 the rhabdomeres contracted to every light flash without a failure. Whilst these movements showed  
20 amplitude variations, their dynamic behavior was similar. Here, they reached their peak (mean = 0.806  $\mu\text{m}$ , **Appendix figure 37B**)  
21 in about 140 ms and then decayed back to the baseline slower, mean  $\tau_r \sim 190$  ms (**Appendix figure 37C**).  
22
- 23 • Dark-adapted R1-R7 rhabdomeres' maximum movement range (**Appendix figure 38A-I**) was  
24 considerably larger (0.3-1.2  $\mu\text{m}$ ) than the displacement range measured *ex vivo* by atomic  
25 force microscope (**Appendix figure 38B**,  $\text{AFM}_{\text{max}} \leq 0.275 \mu\text{m}$ ) (Hardie & Franze, 2012) on  
26 the corneal surface. This difference is hardly surprising. AFM measures axial (inward) cornea  
27 displacements, presumably resulting from a large number of simultaneous photoreceptor  
28 contractions underneath, whereas our high-speed video microscopy method measures  
29 orthogonal (horizontal) rhabdomere movements locally at their source. Owing to the slight  
30 excitation caused by the bright 740 nm red-light background needed for *in vivo* imaging  
31 (**Appendix figure 33B**), the actual rhabdomere movements in full dark-adapted conditions  
32 could be even larger.  
33



- 1       • The rhabdomere movement recordings (thin grey traces) from single ommatidia of individual  
 2 flies vary more than the corneal AFM data (black traces). The sizable variations in their  
 3 movement range and fine dynamics (such as minor oscillations) imply both considerable trial-  
 4 to-trial (**Appendix figure 37**) and fly-to-fly variability (**Appendix figure 38**). Much of this is  
 5 clearly physiological, as rhabdomere movement sizes and waveforms to specific stimuli were  
 6 similar in one fly but often slightly different to those seen in another fly. However, because of  
 7 the extreme sensitivity of our method (**Appendix figure 33B**, providing subpixel movement  
 8 resolution), some of the variations clearly reflected experimental noise. Such noise included  
 9 microscopic mechanical vibrations in the recording system, minute spontaneous eye muscle  
 10 activity (see **Appendix 4**, **Appendix figure 19**), and Poisson-noise, in which the image  
 11 signal-to-noise ratio - as captured by the camera's CMOS sensor - reduced the more the faster  
 12 the sampling. Appropriately, the average responses (red) to different intensity flashes were  
 13 smoother, yet still remained much larger than in the AFM data.  
 14



- 15       • The average rise and decay time courses of the normalized rhabdomere movement recordings  
 16 followed closely those of the normalized AMF recordings (**Appendix figure 38J**). Such  
 17 dynamic conformity strongly suggests that both the methods capture accurately  
 18 photomechanical R1-R8 photoreceptor contractions in their fast natural time resolution. But  
 19 these observations also provided further evidence that *ex vivo* AFM data underestimate the  
 20 actual magnitude of rhabdomere movements within ommatidia. In fact, it seems possible that  
 21

1 to maximize neural images' spatial resolution, the eye's architectural design dampens the lens  
2 system movement, while its sensors (rhabdomeres) contract. This would inadvertently impede  
3 the AFM signal (axial movement), and any horizontal lens shift (**Appendix figure 36**),  
4 measured on the corneal surface.

### 6 **Estimating light intensity falling upon the rhabdomeres**

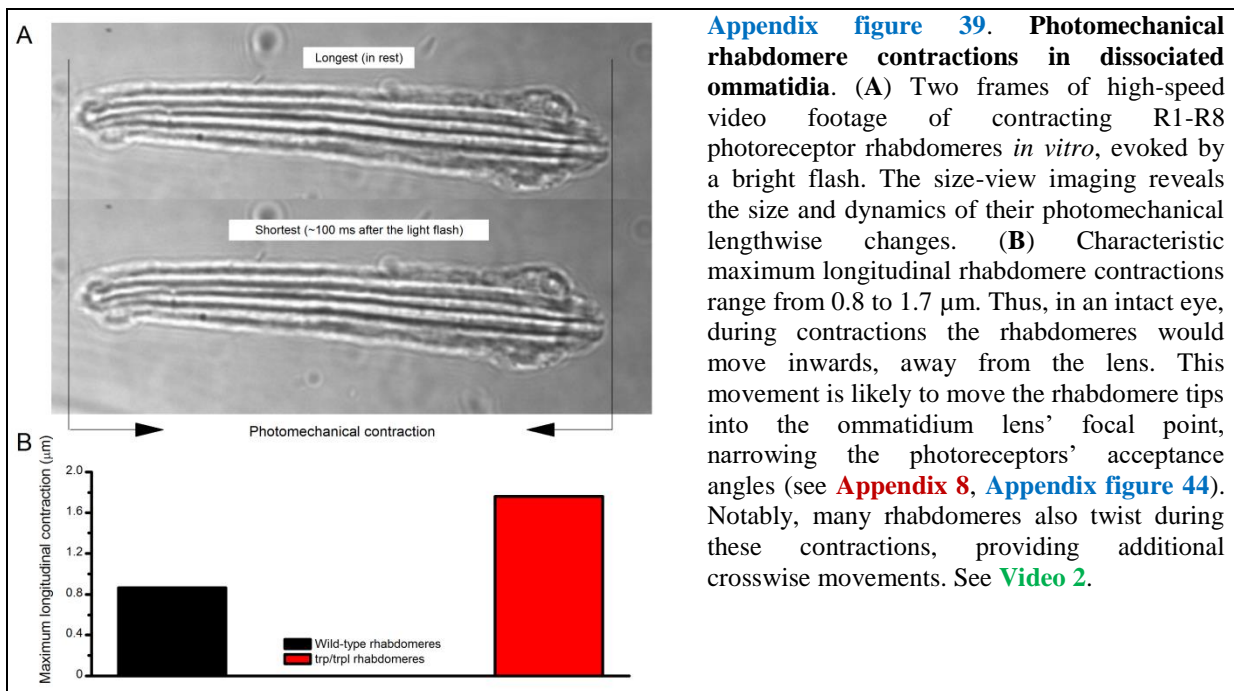
7 Only in 2 out of 21 tested *Drosophila* eyes, the rhabdomeres moved unmistakably (twitched) to a very  
8 dim 10 ms blue/green LED flash, in which intensity was reduced ~200,000-fold by neutral density  
9 filters. Therefore, in these two positive occasions: (i) the resulting response must have been quantal  
10 with (ii) the 10 ms flash maximally containing ~1-3 absorbed photons. Furthermore, because this  
11 flash only succeeded in ~1/10 eyes, its average maximum intensity could only be  $\leq 3/10$  photons/10  
12 ms, *i.e.*  $\leq 0.03$  photons/ms. This means that the brightest flash ( $\log I(0)$ ), which was not filtered, could  
13 maximally contain  $\leq 6,000$  photons/ms, or  $\leq 6$  million photons/s, making the used light intensity range  
14 natural and directly comparable to that used for the intracellular recordings (**Figures 1-2** and **6-9**).

15 This reasoning is in line with the similar LED driver settings used in all the experiments, and  
16 the similar  $V/\log(I)$  and  $(\mu m)/\log(I)$  functions, which resulted from these experiments.

### 18 ***In vitro* rhabdomere movements**

19 As further controls, we measured photomechanical R1-R8 rhabdomere contractions of freshly  
20 dissociated ommatidia (Hardie & Franze, 2012) to green (480 nm) light flashes using high-speed  
21 video recordings with infrared 850 nm background illumination (**Appendix figure 39**). The benefit of  
22 this *in vitro* method was that it provided a clear side-view of the tested wild-type and mutant  
23 rhabdomeres, enabling us to estimate their axial (longitudinal inward) contraction component; or how  
24 much the rhabdomere tip moved away from the ommatidium lens (**Video 2**). *In vivo*, such fast  
25 lengthwise light-sensor movements should contribute to R1-R6 photoreceptors' transiently narrowing  
26 receptive fields (see **Appendix 8**).

27 We found that after dark-adaptation bright flashes could evoke 0.8-1.7  $\mu m$  longitudinal  
28 rhabdomere contractions. These were characteristically accompanied by synchronous (about equally  
29 large) crosswise movement (or twist), which likely forms the basis of the sideways rhabdomere  
30 displacement; seen during the *in vivo* recordings (*e.g.* **Appendix figure 30D**).



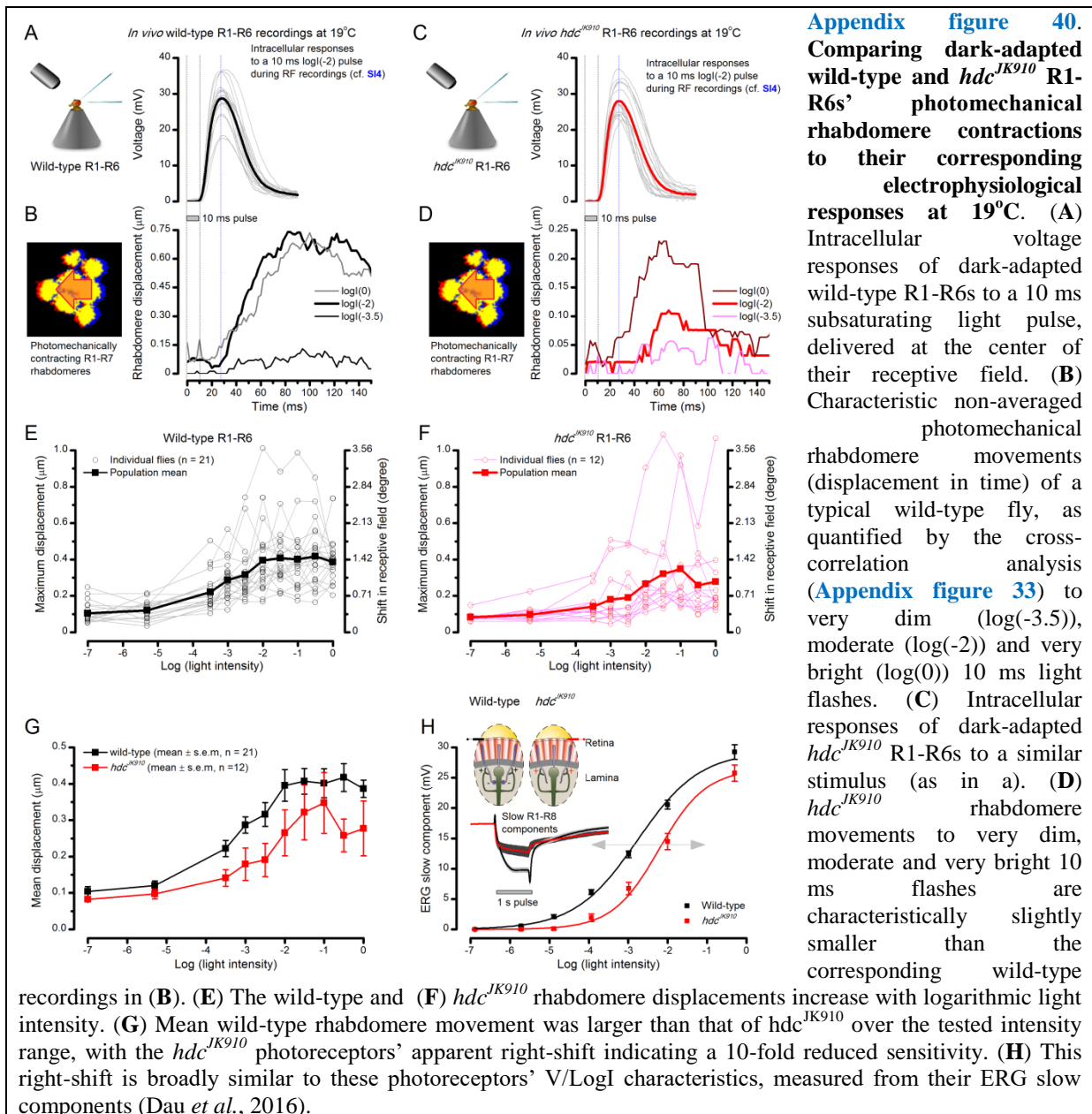
### 32 **Photomechanical rhabdomere movements vs. R1-R6s' voltage responses**

1 We next compared intracellular wild-type and  $hdc^{JK910}$  R1-R6 voltage outputs, evoked by 10 ms light  
 2 flashes after brief dark-adaptation, to their characteristic rhabdomere movements (**Appendix figure**  
 3 **40A-D**). R1-R6 output and rhabdomere motion exhibited broadly comparable delays (or dead-time),  
 4 but overall the rhabdomeres moved considerably slower than how their voltage was changing (*cf.* the  
 5 thick black traces in **A-B**, and the thick red traces in **C-D** for similar flash intensities). The voltage  
 6 responses peaked 25-30 ms from the light onset, and the rhabdomere movements 40-120 ms later. At  
 7 this point, the photoreceptors had almost repolarized back to their dark resting potential (indicated by  
 8 zero ordinate). Moreover, the recordings suggested that for a given flash  $hdc^{JK910}$  rhabdomeres  
 9 typically moved less and returned faster to their original positions than their wild-type counterparts.

10 To further characterize their light-dependent differences, we plotted the maximum wild-type  
 11 and  $hdc^{JK910}$  rhabdomere movements of many flies against the corresponding flash intensities over the  
 12 whole tested light range. The analysis revealed that:

- 13 • Both wild-type and  $hdc^{JK910}$  rhabdomere movements increased with flash intensity (**Appendix**  
 14 **figures 40E-F**), following a characteristic sigmoidal displacement/logI-relationship.

15



16

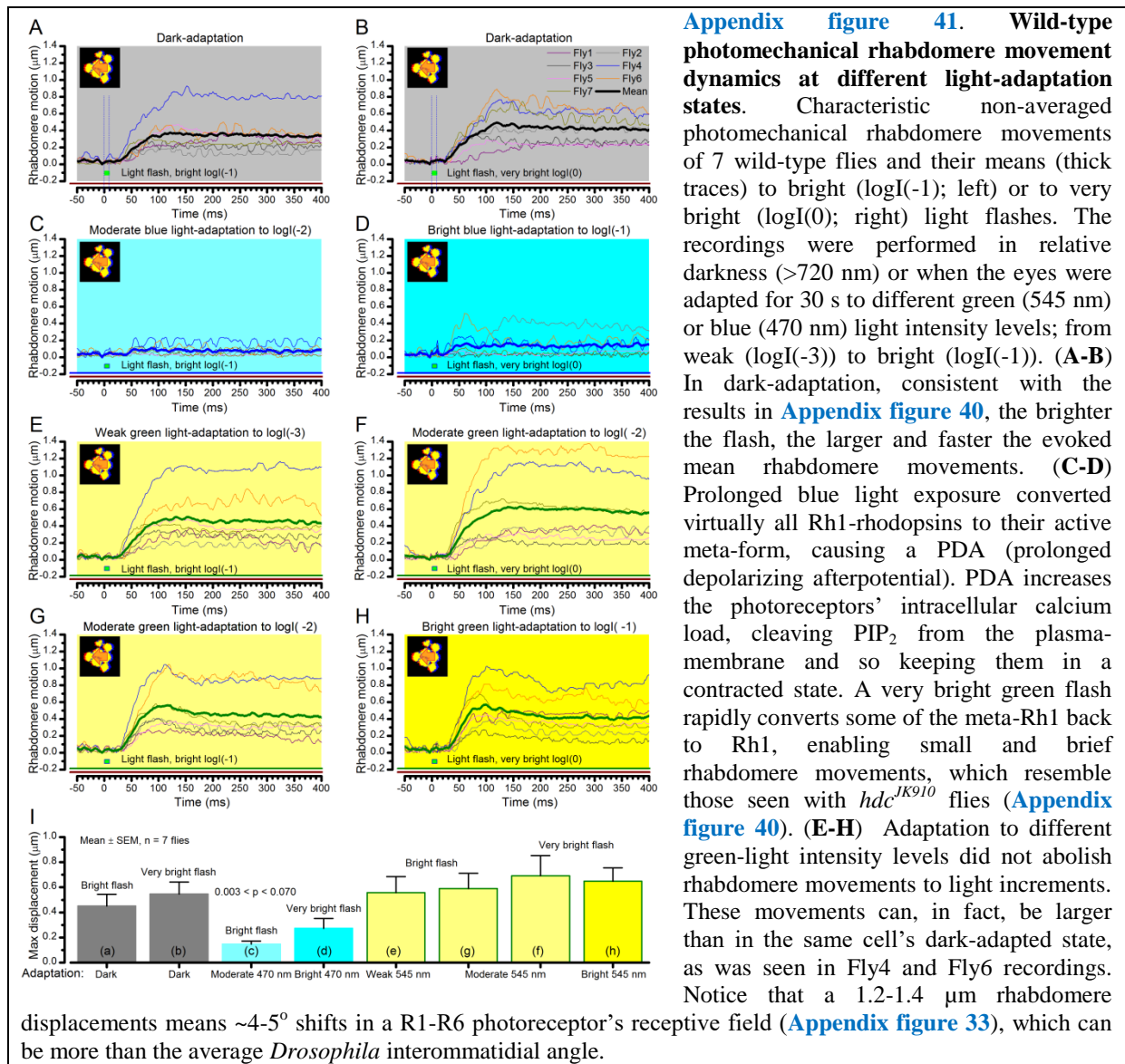
- 1 • The average  $hdc^{JK910}$  rhabdomere movements were smaller than those in wild-type eyes. In  
2 part, this could result from  $hdc^{JK910}$  R1-R6s being smaller than their wild-type counterparts,  
3 and embedded deeper inside the ommatidia. As their rhabdomere diameters are ~4% smaller  
4 than those of the wild-type (**Appendix 5**), their length should also be reduced proportionally;  
5 with the average wild-type R1-R6 being ~100  $\mu\text{m}$  tall,  $hdc^{JK910}$  R1-R6s should be ~4  $\mu\text{m}$   
6 shorter. Accordingly, by using the z-axis micromanipulator (see above), we measured *in situ*  
7 (rest) that  $hdc^{JK910}$  rhabdomere tips were 3.5  $\mu\text{m}$  further away from the lens than the wild-type  
8 tips ( $hdc^{JK910}$ :  $27.4 \pm 1.2 \mu\text{m}$ ; wild-type:  $23.9 \pm 1.2 \mu\text{m}$ ; n = 6 ommatidia, 6 flies).  
9 •  $hdc^{JK910}$  rhabdomere contractions further implied reduced sensitivity (**Appendix figure 40G**),  
10 seen as a 10-fold right-shift in their displacement/logI-curve in respect to the wild-type data.  
11 • Interestingly, this sensitivity difference resembles that seen between the wild-type and  
12  $hdc^{JK910}$  ERGs (**Appendix figure 40H**). We have recently provided compelling evidence that  
13 the missing histaminergic (inhibitory) neurotransmission from  $hdc^{JK910}$  photoreceptors to  
14 interneurons (LMCs and amacrine cells) causes a tonic excitatory synaptic feedback to R1-  
15 R6s, depolarizing them ~5 mV above the normal wild-type dark resting potential (Dau *et al.*,  
16 2016). Thus,  $hdc^{JK910}$  R1-R6s should experience a tonic  $\text{Ca}^{2+}$  influx and be permanently in a  
17 more “light-adapted” state. Here, our results suggested that  $\text{Ca}^{2+}$  overload may desensitize the  
18 biophysical machinery that moves the rhabdomeres, reducing its dynamic range.  
19

### 20 **Light-adapted rhabdomere motion reflects rhodopsin/meta-rhodopsin balance**

21 Given the slightly reduced back-to-front rhabdomere mobility of  $hdc^{JK910}$  photoreceptors, we next  
22 asked whether prolonged light-adaptation itself would reduce wild-type photoreceptors’ rhabdomere  
23 movement. To study this question, we examined how the rhabdomeres in seven individual flies  
24 responded to different light impulses at different adaptation states.

25 First, to obtain the baseline responses in each fly eye, we recorded their rhabdomere  
26 movements to a bright and a very bright full-field green-blue flash after 30 s of dark-adaption  
27 (**Appendix figures 41A and B**, respectively). As before, we found that the brighter the light flash, the  
28 larger and the faster their rhabdomere movements were on average.

29 Interestingly, however, when the flies were adapted to a moderate or bright blue (470 nm)  
30 light field for 30 s, which converts most (if not all) rhodopsin Rh1 to its active meta-form (causing  
31 PDA, prolonged depolarizing afterpotential), the flashes now evoked only weak or no rhabdomere  
32 movement (**Appendix figure 41C-D**). Such reduced mobility somewhat resembled that in some  
33  $hdc^{JK910}$  rhabdomeres (**Appendix figure 40D**). These observations can be explained, at least in part,  
34 with the basic molecular model proposed for rhabdomere contraction (Hardie & Franze, 2012). Here,  
35 meta-rhodopsin would continuously activate G-protein and in turn phospholipase C (PLC). PLC  
36 would then cleave most  $\text{PIP}_2$  off the microvillar membrane, causing a tonic photoreceptor contraction,  
37 which facilitates light-gated channel openings and thus increases  $\text{Ca}^{2+}$  influx. But because a 10 ms  
38 bright green (545 nm) light pulse would convert only some fraction of meta-rhodopsin back to its  
39 non-activated form, this effect would be small proportionally, and could only partially rescue the  
40 rhabdomere contractibility.  
41



1  
2 **Rhabdomere contractions resensitize refractory sampling units**  
3 On the other hand, under more natural green light-adaptation (Appendix figure 41E-H), the eyes'  
4 normal back-to-front rhabdomere contractibility to light increments was retained, and sometimes even  
5 increased, in respect to their dark-adapted baseline responses (Appendix figure 41A, B).  
6 Consequently in every fly eye (7/7), the rhabdomeres moved more when green-adapted than when  
7 moderately blue light-adapted (Appendix figure 41C), as quantified by their flash-induced maximum  
8 displacements (Appendix figure 41I).

9 These results indicate that in normal spectrally-broad natural environments, light increments  
10 (positive contrasts) will evoke fast evasive rhabdomere movements, steering them away from pointing  
11 directly to a bright light source. This novel photomechanical adaptation should together with the  
12 slower screening pigment migration (intracellular pupil mechanism, Appendix 2) help to recover  
13 (resensitize) a rhabdomere's refractory sampling units (30,000 microvilli). Thus, the rhabdomere  
14 movements likely participate in optimizing photon sampling for maximum information capture  
15 (Appendixes 1-2). This further means that a rhabdomere's state of contraction is constantly being  
16 reset to the ongoing light input, providing the capacity to respond to the next stimulus increment.  
17 Therefore, although being slower, in many sense, *Drosophila* photoreceptors' mechanical adaptation  
18 resembles the inner ear hair-cells' adaptive resensitization (Howard *et al.*, 1988; Corey *et al.*, 2004).

## Appendix 8: Microsaccadic sampling hypothesis for resolving fast-moving objects

### Overview

This appendix describes a new ‘microsaccadic sampling’-hypothesis that predicts a *Drosophila* photoreceptor’s voltage responses to moving dots, and provides important background information about the experimental and theoretical results presented in [Figures 7-9](#).

In this appendix:

- We use our biophysical *Drosophila* R1-R6 model ([Appendix 1](#)), with different degrees of photomechanical rhabdomere movements modulating light input ([Appendix 7](#)), to simulate photoreceptor voltage output to moving bright dots that cross its receptive field in different directions, speeds and inter-distances.
- By comparing the model simulations to intracellular recordings, we reveal the likely biomechanics that allow R1-R6s to resolve adjacent dots at saccadic velocities ([Appendix 6](#)).
- We show that when a rhabdomere contracts away from the ommatidium lens’s focal point, its receptive field must move and narrow dynamically. Together these processes actively reshape both the light input and photoreceptor output to separate and sharpen neighboring visual objects in time, improving their resolvability.
- Crucially, with such photomechanical light input modulation, the model photoreceptor output closely approximates that of the real R1-R6s, as recorded to two moving bright dots crossing their receptive fields at different speeds ([Figures 7-9](#); [Appendix 6](#)).
- Hence, with refractory photon sampling and photomechanical rhabdomere movements, we can correctly predict and convincingly explain visual acuity of R1-R6s to moving objects.

### Modeling a R1-R6’s receptive field dynamics to moving dots

Based on the combined results in [Appendix 1-7](#), we develop a new ‘microsaccadic sampling’-hypothesis, which predicts how photomechanical rhabdomere contractions (microsaccades) move and narrow *Drosophila* R1-R6 photoreceptors’ receptive fields (RFs) to resolve fast-moving objects. We present extensive analytical and experimental evidence to show how these mechanisms operate with the photoreceptors’ refractory information sampling to reduce light-adaptation and to increase the spatiotemporal resolution of their voltage responses, improving visual acuity.

Using the results in [Appendix 1-7](#), we can now work out the biomechanics, which allow a R1-R6 to resolve two close bright dots crossing its receptive field at saccadic speeds. We do this systematically by comparing the output of our biophysical model (Song *et al.*, 2012; Song & Juusola, 2014; Juusola *et al.*, 2015) ([Appendix 1](#)), in which input is modulated by different degrees of rhabdomere photomechanics ([Appendix figure 42A-C](#)), to the corresponding recorded real R1-R6 output ([Appendix figure 42D](#)). Specifically, we consider three input modulation models:

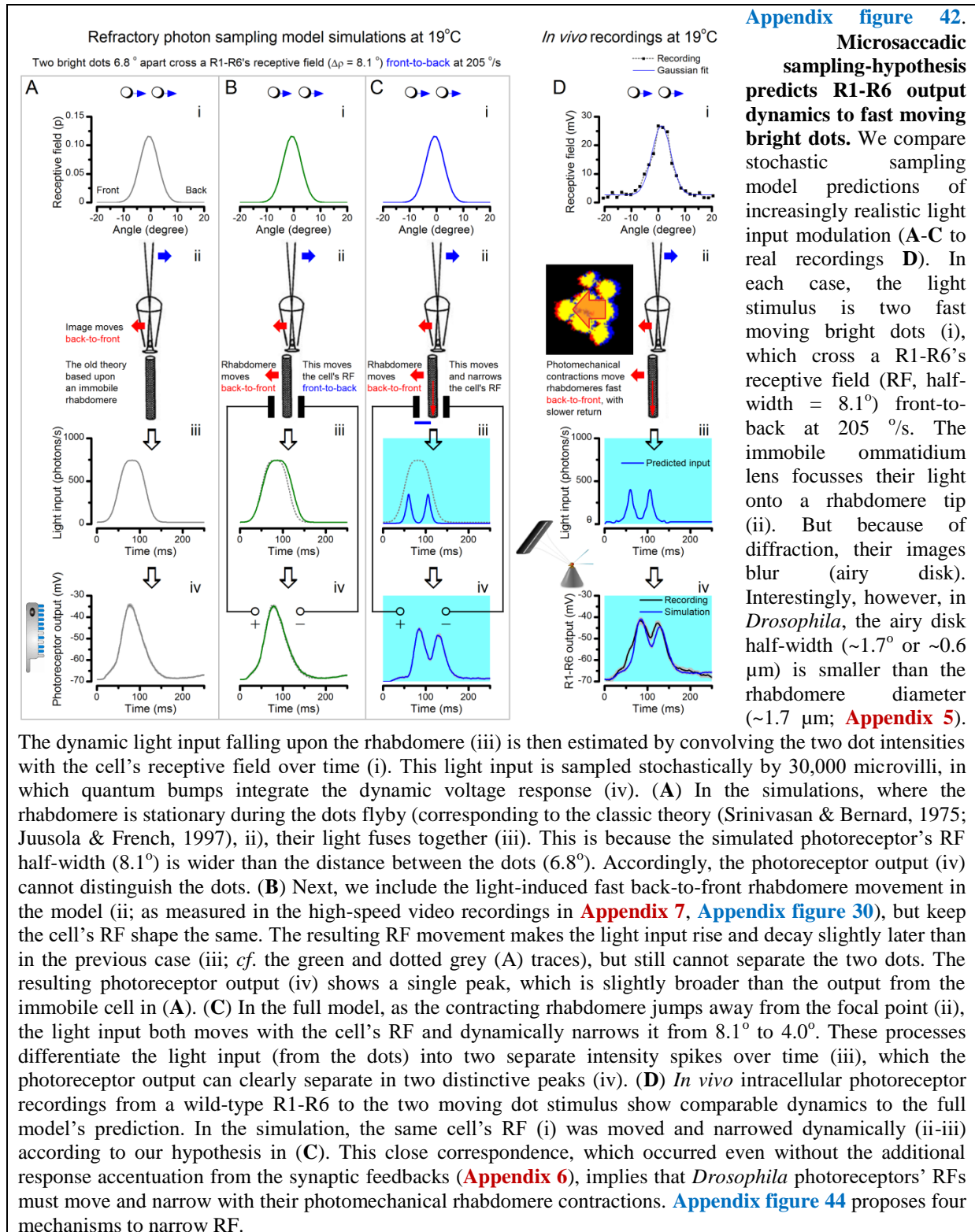
- A. Stationary rhabdomere model (receptive field is fixed)**
- B. Photomechanical rhabdomere model (receptive field moves)**
- C. Photomechanical rhabdomere model (receptive field moves and narrows)**

In the following, to make these different models ([A-C](#)) directly comparable, we first present the findings for two bright dots, which cross the receptive field at 205 °/s ([Appendix figure 42](#)), before generalizing the results for a vast range of stimuli and giving more examples. Note that these simulations and recordings were performed at 19-20 °C. Later on in this appendix, we show how at the *Drosophila*’s preferred temperature range (24-25 °C) (Sayeed & Benzer, 1996) these dynamics are naturally faster (Juusola & Hardie, 2001b) and improve visual acuity further.

**A. Stationary rhabdomere model (receptive field is fixed).** This approach is broadly analogous to the classic theory ([Appendix 4](#) and [Appendix 6](#)). It was implemented in four steps ([Appendix figure 42A](#)):

- (i) Two bright dots, which were 6.8° apart, crossed a R1-R6’s RF ( $\Delta\theta = 8.1^\circ$ ) front-to-back at the saccadic speed of 205 °/s.
- (ii) Concurrently, the ommatidium lens focused their light onto a rhabdomere tip.

- 1 (iii) The resulting dynamic light input at the rhabdomere tip was a convolution of the two dot  
 2 intensities with the cell's receptive field over time (Srinivasan & Bernard, 1975; Juusola &  
 3 French, 1997).  
 4 (iv) The light input (photons/s) drove the photon sampling and refractory quantum bump (QB)  
 5 production of 30,000 microvilli (Song *et al.*, 2012; Song & Juusola, 2014; Juusola *et al.*,  
 6 2015), which formed the rhabdomere. The resulting macroscopic photoreceptor output  
 7 (Hardie & Juusola, 2015) dynamically integrated the QBs.  
 8



Characteristically in this approach, input modulation reduced to a single peak as the RF convolution fused the light from the two dots together (iii). This made them irresolvable to the discrete photon sampling (iv). Specifically here, light input could not separate the two dots because the given receptive field half-width ( $8.1^\circ$ ) was wider than the distance between the dots ( $6.8^\circ$ ). The resulting model output, thus, failed to capture the resolvability of the real R1-R6 output (**Appendix figure 42D**, iv).

Markedly, the model prediction (**Appendix figure 42A**, iv) much resembled those of the deterministic Volterra-models, in which similarly broad RFs were used in the calculations (see **Appendix 6**).

**B. Photomechanical rhabdomere model (receptive field moves).** In this case (**Appendix figure 42B**), we kept the cell's receptive field shape the same (i;  $\Delta\rho = 8.1^\circ$ ) but included the light-induced fast horizontal (back-to-front) rhabdomere movement in the model (ii). The given model parameters (**Table 8**) were fixed to closely approximate the experimentally observed rhabdomere movement dynamics (see **Appendix 7**). Here, the following deductions were made:

- Each photoreceptor contracted independently to light. Although this movement is linked to the synchronous contractions of its neighbors inside the same ommatidium, such cooperativity makes no difference to the model.
- Rhabdomere movement started 8 ms after the first dot reached the outer rim of a photoreceptor's receptive field, called the trigger zone. This delay matched both the delay in R1-R6 output (**Appendix 7: Appendix figure 40A**) and the apparent dead-time in AFM data (Hardie & Franze, 2012) to a bright light flash (**Appendix 7: Appendix figure 38J**). The trigger zone was  $14.6^\circ$  from the photoreceptor receptive field center, matching the typical spatial threshold where dark-adapted wild-type R1-R6s responded faintly to subsaturating peripheral light flashes (**Appendix 4, Figure 7-figure supplement 1A**).
- Maximum horizontal rhabdomere movement was set to be  $0.58\ \mu\text{m}$ , corresponding to a  $1.6^\circ$  shift in its receptive field. This value is close to the measured average of the maximum light-induced rhabdomere movements in wild-type fly ommatidia (**Appendix 7, Figure 8D**).
- Rhabdomere movements had two phases. In the 1<sup>st</sup> phase, a rhabdomere moved  $1.6^\circ$  in back-to-front direction for 100 ms, reaching its maximum displacement. This caused a receptive field to shift in the opposite,  $\alpha$  (front-to-back) direction. Importantly, the 1<sup>st</sup> phase could not be disturbed. In the 2<sup>nd</sup> phase: the rhabdomere slowly returned to the original position in 500 ms. The 2<sup>nd</sup> phase could be disturbed. Both the phases followed linear motion.

**Table 8. Parameters for modeling a R1-R6's receptive field (RF) dynamics caused by its rhabdomere contraction**

Trigger zone: <b>trig</b>	Starting RF half-width: $\Delta\rho_{\text{start}}$	Delay before rhabdomere motion: <b>lag</b>	Rhabdomere motion: (time-to-peak) <b>Phase 1</b>	Resulting parallel RF shift: $\text{RF}_{\text{shift}}$	RF shift direction: $\alpha$ (front-to-back)	Rhabdomere motion: <b>Phase 2</b>	Ending RF half-width: $\Delta\rho_{\text{end}}$
$14.6^\circ$	$8.1^\circ$	8 ms	100 ms	$1.6^\circ$	0	500 ms	$4.0^\circ$

As in the first case, the moving receptive field model (**Appendix figure 42B**) was implemented for the same stimulus in four steps (i-iv):

- Two bright dots,  $6.8^\circ$  apart, crossed a photoreceptor's RF ( $\Delta\rho = 8.1^\circ$ ) front-to-back at the saccadic speed of 205 °/s.
- The ommatidium lens focused their light onto a rhabdomere tip. But here, after 8 ms delay, the rhabdomere started to move back-to-front as it contracted photomechanically.
- The resulting dynamic light input was, therefore, a convolution of the two dot intensities and the cell's receptive field, which moved at different speeds in the same direction (front-to-back).
- The light input drove the photon sampling and refractory QB production of 30,000 microvilli, while the resulting macroscopic photoreceptor output summed up the QBs.

1  
2 We found that the resulting receptive field movement caused (iii) the light input rise and  
3 decay slightly later than when the rhabdomere was immobile (*cf.* green and dotted grey traces).  
4 However, because the two dots were close and crossed the cell's receptive field fast, the given co-  
5 directional receptive field motion failed to separate the light from them. Thus, (iv) the resulting  
6 photoreceptor output showed a single peak, which was slightly broader than the output from the  
7 immobile model.

8  
9 **C. Photomechanical rhabdomere model (receptive field moves and narrows).** There is a large  
10 disparity between the measured (**Appendix 4**:  $\Delta\rho = 7.00 - 11.65^\circ$ ) and the optical waveguide theory  
11 derived (Stavenga, 2003b) ( $\Delta\rho = 3.5 - 5.3^\circ$ ) acceptance angles of dark-adapted R1-R6s. Even Snyder's  
12 simple formula (Snyder, 1977) (**Appendix 4**: Eq. A4.3), which overestimates (van Hateren, 1984;  
13 Stavenga, 2003b)  $\Delta\rho$  from the measured *Drosophila* ommatidium optical dimensions, gives a  
14 theoretical upper bound ( $\Delta\rho < 5^\circ$ ) that is smaller than the smallest intracellularly measured values.

$$\Delta\rho = \left( \sqrt{\left(\frac{0.545}{16}\right)^2 + \left(\frac{1.7}{21.36}\right)^2} \right) \times \frac{180}{\pi} = 4.9601^\circ$$

$$\Delta\rho = \left( \sqrt{\left(\frac{0.545}{17}\right)^2 + \left(\frac{1.7}{21.36}\right)^2} \right) \times \frac{180}{\pi} = 4.9161^\circ$$

15 These upper bounds for green light (545 nm) were obtained for the smallest and largest ommatidium  
16 lens (16-17  $\mu\text{m}$ ) with average rhabdomere diameter EM measurements (1.7  $\mu\text{m}$ ) (**Appendix 5**), using  
17 the experimentally estimated focal length (21.36  $\mu\text{m}$ ) (Gonzalez-Bellido *et al.*, 2011).

18 Moreover, interestingly, Götz estimated from *Drosophila* optomotor behavior, using the early  
19 flight simulator system (Götz, 1964), that in bright illumination R1-R6  $\Delta\rho$  would be  $3.5^\circ$ .

20 To resolve the paradox between the conflicting experimental and theoretical  $\Delta\rho$ -estimates,  
21 which in the past were based upon histological measurements of fixed/stained (dead/immobile) retinal  
22 structures, we hypothesized that the photomechanical rhabdomere contractions not only move a  
23 photoreceptor's RF but also dynamically narrow it (**Appendix figure 42C**). What is more, we  
24 reasoned that the RF narrowing should depend upon stimulus history; the cell's ongoing light  
25 exposure. Therefore, our specific prediction was that when moving bright dot stimuli entered a R1-  
26 R6's RF, the resulting dynamic input modulation would transiently sharpen R1-R6 output, improving  
27 its temporal resolution.

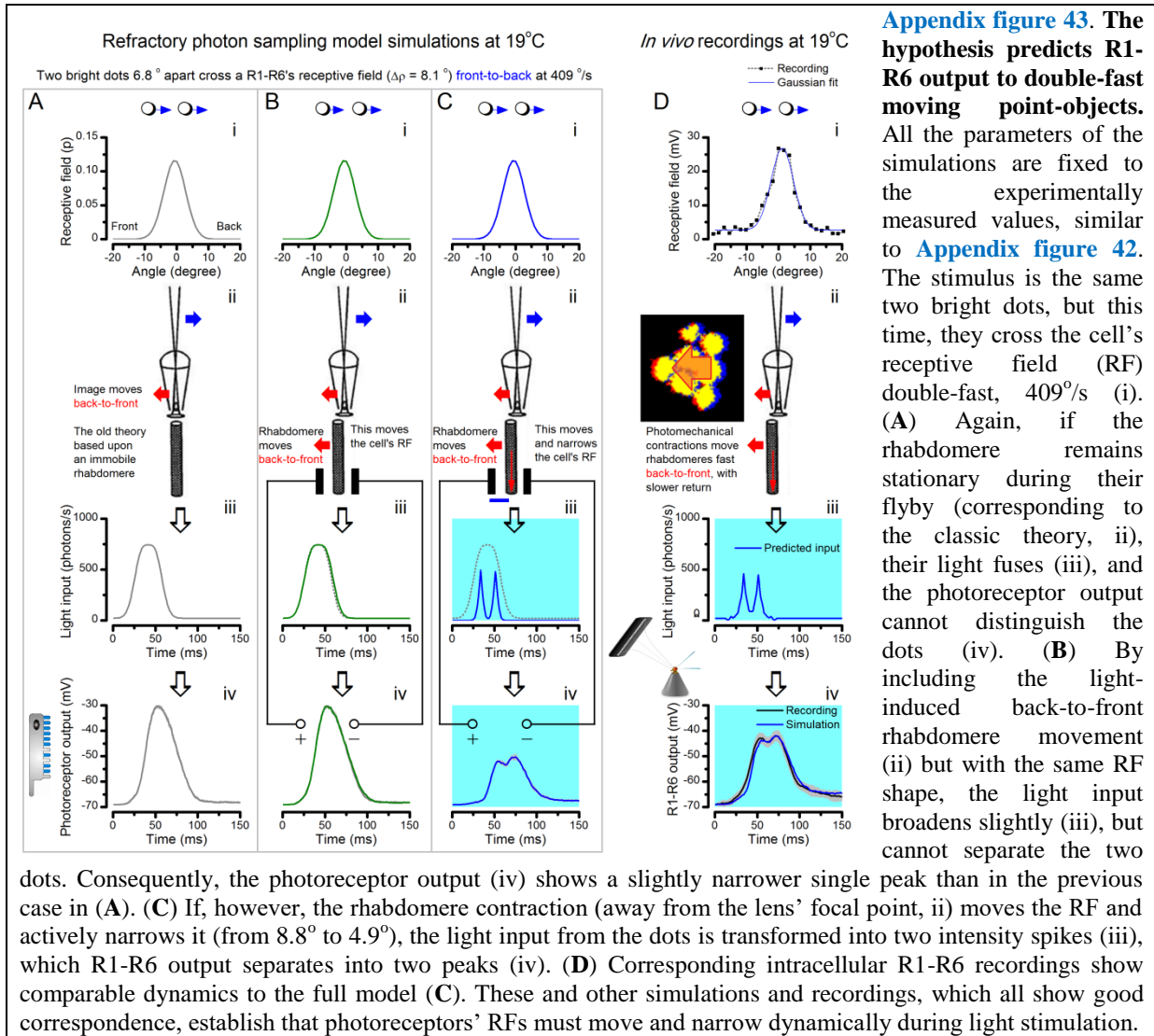
28 Again, the feasibility of the hypothesis was assessed by analyzing and comparing the  
29 resulting biophysical model output to real R1-R6 recordings. The model was implemented in four  
30 steps (**Appendix figure 42C**):

- 31 (i) Two bright dots,  $6.8^\circ$  apart, crossed a photoreceptor's RF ( $\Delta\rho = 8.1^\circ$ ) front-to-back at the  
32 saccadic speed of 205  $^\circ/\text{s}$ .
- 33 (ii) The ommatidium lens focused their light onto a rhabdomere tip. After 8 ms delay, the  
34 rhabdomere started to move back-to-front as it contracted photomechanically. And now, with  
35 this movement, its acceptance angle,  $\Delta\rho$ , also narrowed transiently, from  $8.1^\circ$  to  $4.0^\circ$  (**Table**  
36 **8**). In the model, the further away the rhabdomere moved from its starting position at the focal  
37 plane, the more its receptive field narrowed (or skewed).
- 38 (iii) The resulting dynamic light input was, therefore, a convolution of the two dot intensities and  
39 the cell's RF, which narrowed and moved at different speeds in the same direction (front-to-  
40 back).
- 41 (iv) The light input drove the microvillar photon sampling and refractory QB production, which  
42 were summed up over the whole rhabdomere to a macroscopic photoreceptor voltage output.

43  
44 Importantly, the predicted photoreceptor output showed now two distinct peaks, indicating that the  
45 two dots (iv) were resolved neurally. Moreover, the simulations closely resembled the recordings to  
46 the similar stimulus (*cf.* **Appendix figure 42C to D**).

47 In another test (**Appendix figure 42D**), we estimated the same R1-R6's light input (iii) from  
48 its RF (i; through programmed look-up table operations, see **Appendix figure 22**) and used this to

1 predict its output (iv; blue dotted trace). We discovered that the simulated output was indeed similar  
 2 to the cell's actual recorded output to the same stimulus (black trace), with the timing of their two  
 3 peaks matching closely. This close dynamic correspondence between the simulations and recordings  
 4 was robust and reproducible in different tested stimulus conditions (**Appendix figure 43C-D**),  
 5 meaning that the given model structure likely incorporated the basic biophysical mechanisms that R1-  
 6 R6s use in encoding moving stimuli.  
 7



8  
 9 In summary, for the biophysical model to match up the real R1-R6 cells in resolving two bright  
 10 moving dots, its receptive field must move and transiently narrow from its original size (**Appendix 4:**  
 11  $\Delta\rho_{\text{start}} = 7.00 - 11.65^\circ$ ) to the size predicted by the optical waveguide theory ( $\Delta\rho_{\text{end}} = 3.5 - 5.3^\circ$ ).  
 12 Moreover, within this dynamic  $\Delta\rho$  change range, the resulting model outputs become realistic and  
 13 robust. Using this modeling approach, we could appropriately predict the real photoreceptors' voltage  
 14 responses to the different moving dot stimuli (**Appendix 6**), irrespective of the tested dot speed,  
 15 direction (front-to-back or back-to-front) and inter-dot distance. For example, by replacing the mean  
 16 measured rhabdome displacements with some of the larger values (**Appendix 7**), the simulations  
 17 resolved moving dots similarly well to the recordings even at very high stimulus speeds 400-800°/s.

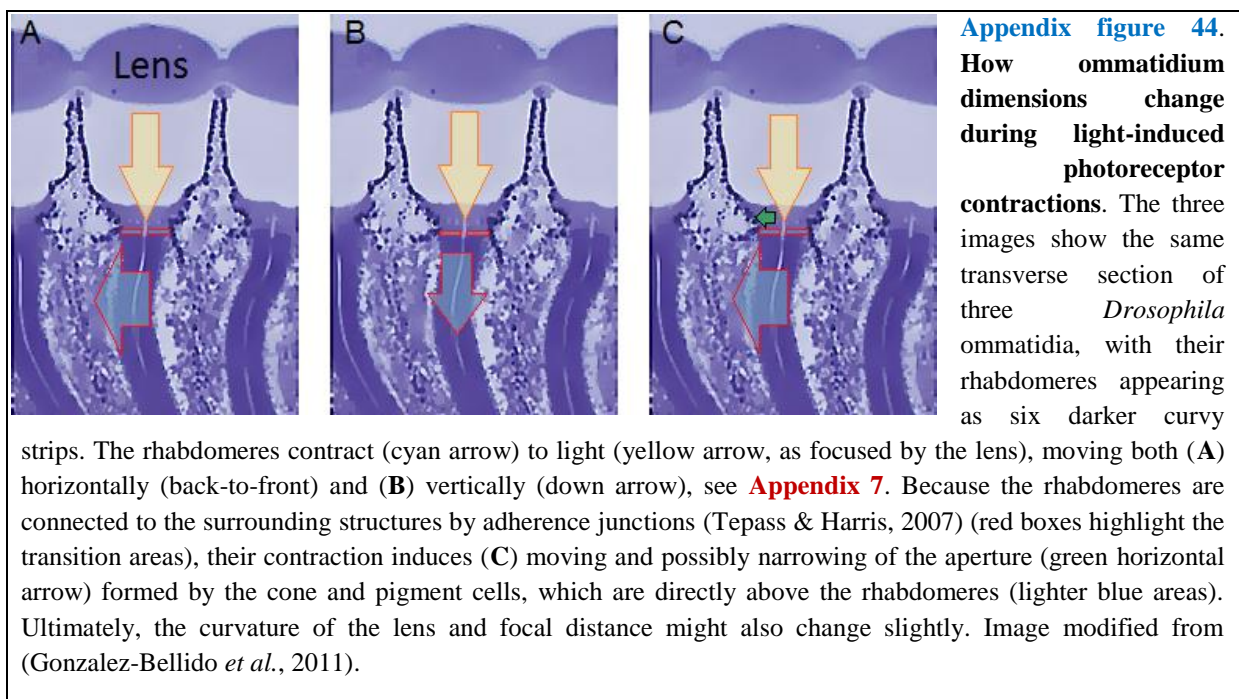
18 From the neural coding point of view, this broad agreement between our 'microsaccadic  
 19 sampling'-hypothesis and the experiments makes it almost certain that photomechanical rhabdome  
 20 contractions (**Appendix 7**) move and narrow R1-R6 photoreceptors' RFs to enhance visual acuity.  
 21 But from the viewpoint of reducing light-adaptation, these processes seem like by-products of a  
 22 simple evasive action, which steers the rhabdome away from pointing directly to the light source (to

1 recover more refractory microvilli; see **Appendix 2**). Nevertheless, while elementary optics makes it  
2 clear why a horizontal rhabdomere motion must move a R1-R6's receptive field in the opposite way,  
3 it is harder to see what physical mechanisms could narrow it. We next consider four potential  
4 processes within the ommatidium lens system that could just do this.

### 6 **What could cause the receptive field narrowing during moving light stimuli?**

7 Four hypothetical mechanisms, together or separately, could explain the required RF narrowing:

- 8 1. When a rhabdomere moves back-to-front (**Appendix figure 44A**), it moves away from  
9 the center axis, which remains fixed because the ommatidium lens system does not move  
10 (see **Appendix 7**, **Appendix figure 36**). Therefore, as the rhabdomere tip moves  
11 horizontally (**Video 3**), the light input point-spread function (airy disc) should fall only  
12 partly upon it. This may clip or skew the rhabdomere's RF (acceptance angle,  $\Delta\rho$ ),  
13 narrowing it.
- 14 2. Besides moving rhabdomeres horizontally (**Appendix 7**), photomechanical photoreceptor  
15 contractions also move them 0.5-1.7  $\mu\text{m}$  inwards (**Video 2**; **Appendix figure 44B**). In a  
16 dark-adapted state, the rhabdomeres are elongated towards the lens with their tips  
17 possibly not being at the focal point. Hence, in this position, the rhabdomeres should  
18 collect light from broader angles (**Appendix 4**, from the brief test pulses: **Appendix**  
19 **figure 17**), and partially recover (re-elongate) before the next pulse comes. But during  
20 more continuous light stimulus, their contraction pulls their tips inwards, towards the  
21 possible focal point of the lens, which could narrow  $\Delta\rho$  towards its theoretical values  
22 (3.5-5.3°).
- 23 3. Rhabdomere tips are linked by adherence junctions to the cone cells (above them) and  
24 pigment cells (at their upper corners) (Tepass & Harris, 2007) (**Appendix figure 44C**).  
25 When the rhabdomeres contract these connections likely pull the pigment cells above,  
26 generating a dynamic aperture (**Video 4**), which moves and possibly tightens, to narrow  
27  $\Delta\rho$  (see **Appendix 7**, **Appendix figure 36**).  
28



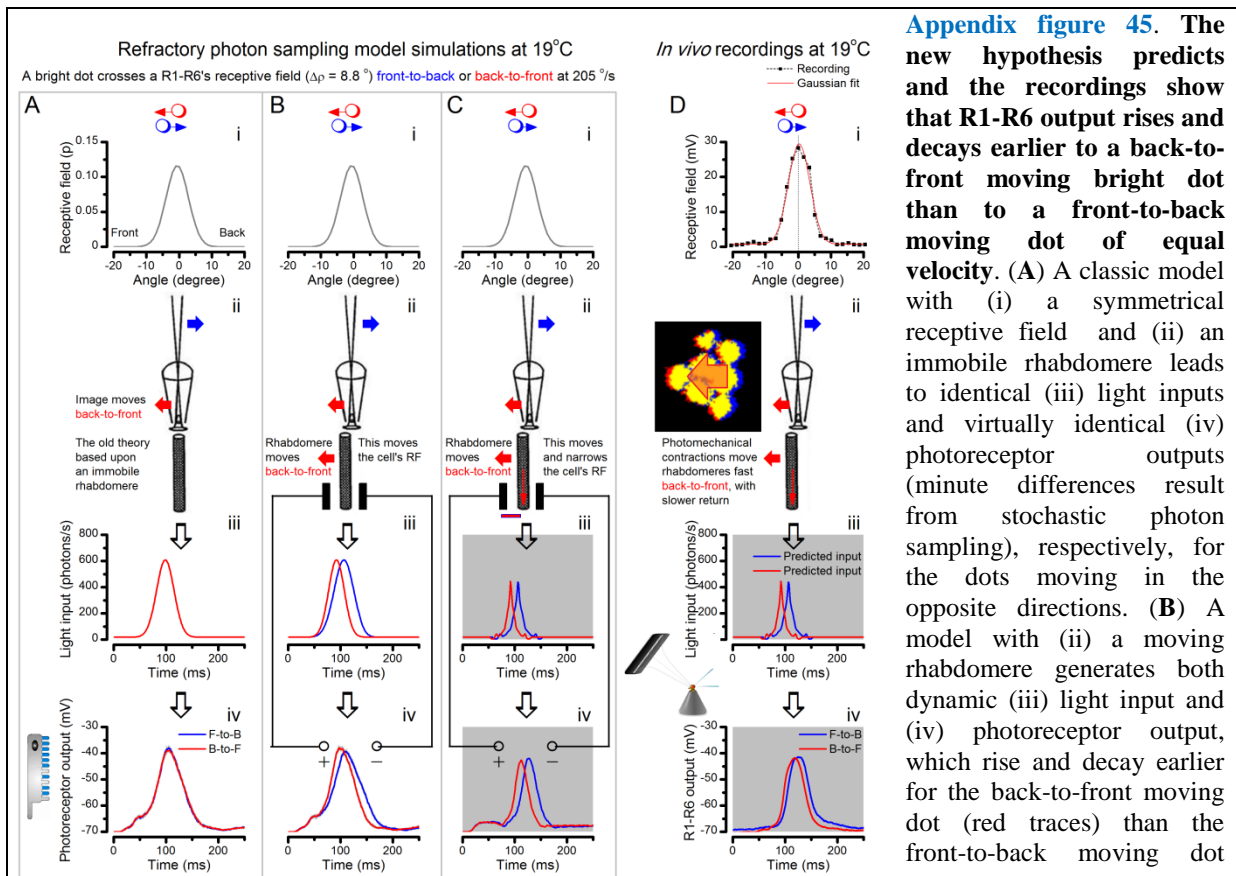
- 29
- 30
- 31 4. In dark-adaptation, the waveguide crosstalk between neighboring rhabdomeres could broaden  
32 their receptive fields. But light-induced horizontal rhabdomere movement may eliminate the  
33 crosstalk between the neighbors, narrowing  $\Delta\rho$  towards the theoretical values (3.5-5.3°).  
34

### 34 **Specific predictions of our new hypothesis and their experimental validations**

1 The microsaccadic sampling-hypothesis, as implemented by our biophysically realistic photoreceptor  
 2 model (**Appendix 1**) with combined photomechanical rhabdomere dynamics, makes important  
 3 predictions about the coding benefits of moving and narrowing R1-R6 receptive fields that can be  
 4 tested experimentally.

5 The 1<sup>st</sup> prediction is that, for a given stimulus or saccadic velocity, R1-R6 output to a back-to-  
 6 front moving bright dot should appear before the output to a front-to-back moving dot. This is because  
 7 the back-to-front moving dot should enter and exit a contracting photoreceptor's front-back moving  
 8 receptive field earlier; whereas the dot moving in the opposite direction should stay marginally longer  
 9 inside its RF. **Appendix figure 45** compares the theoretical predictions (output simulations) of the  
 10 same three models as earlier (**A**, **B** and **C**; their details are above) and corresponding exemplary  
 11 intracellular recordings (**D**) for these two stimuli.

12 Both the full model simulations (**C**) and many recordings (**D**) indicate that this prediction is  
 13 indeed what happens for a R1-R6 with a symmetrical RF (i). The responses (red traces) to back-to-  
 14 front moving dots rise and decay faster than the responses (blue traces) to front-to-back moving dots.  
 15 Similar response dynamics of another intracellular recording series from another R1-R6 are  
 16 highlighted in **Appendix 6** (**Appendix figure 25**). Notice, however, that these results are explicitly  
 17 true for symmetrical receptive fields. If, on the other hand, a R1-R6's RF was asymmetrical - say,  
 18 profoundly skewed towards the front of the eye, then its response to the front-to-back moving dot  
 19 might, in fact, rise earlier, or there could be little difference between the responses. Thus, it is the  
 20 mathematical relationship between the scale of RF asymmetry and the scale of the rhabdomere  
 21 back-to-front movement, which ultimately sets whether a front-to-back or back-to-front stimulus  
 22 would win. Notice also that dynamic photomechanical rhabdomere movements and eye muscle  
 23 activity make RF recordings difficult to perform, and consequently, experimental inaccuracies and  
 24 limitations can influence the results. Thus, some of the natural variations in the recordings may result  
 25 from imprecise stimulation control. For example, imperfect positioning of a 25 light-point stimulus  
 26 array - either off-center of a cell's receptive field or if not aligned perfectly parallel in respect to the  
 27 eye's back-to-front axis - could bias a recording (more about this variation and the cell numbers in  
 28 **Appendix 6**).  
 29

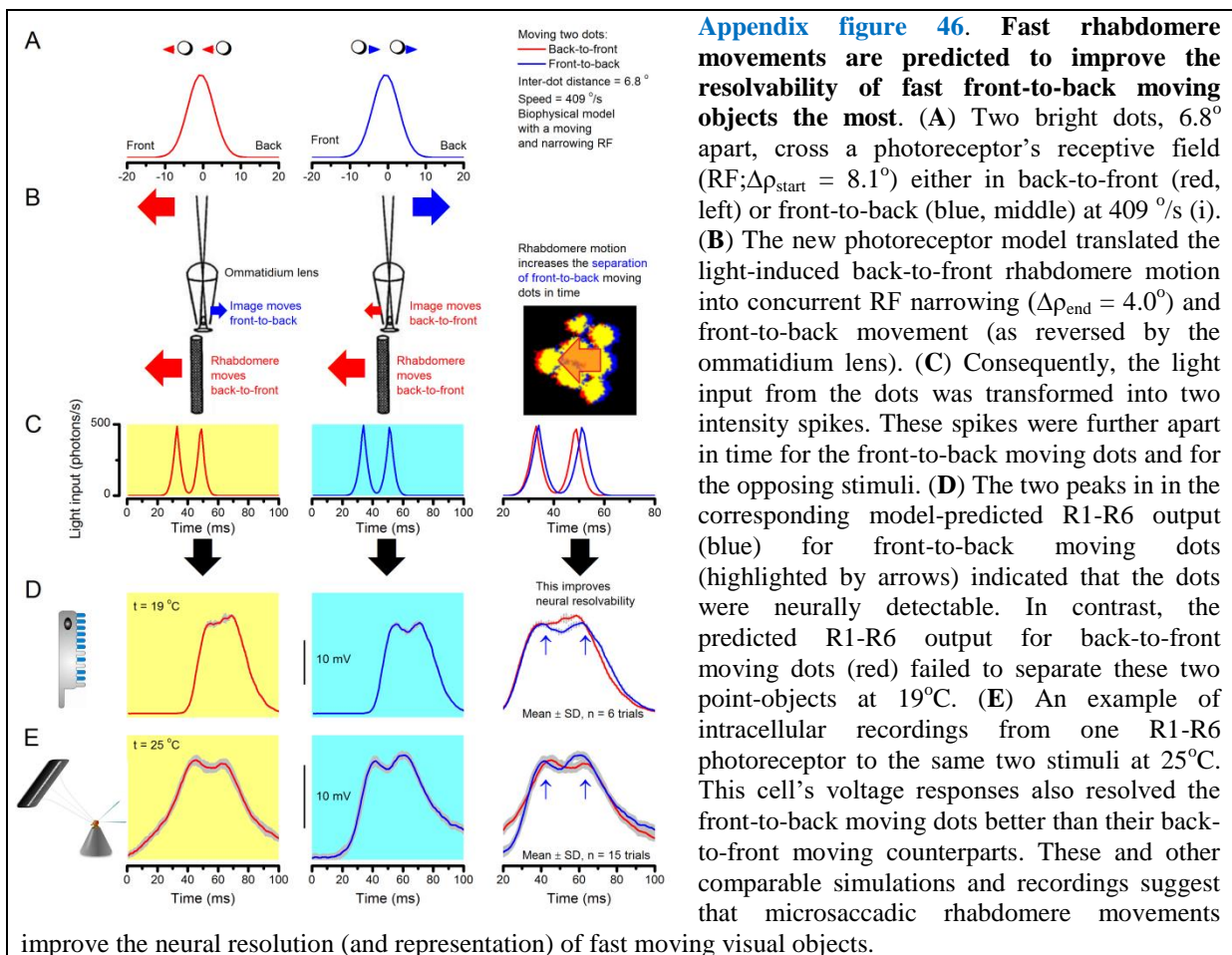


(blue traces). (C) Our full model with rhabdomere contraction dynamics that move and narrow its receptive field. This makes the light input and photoreceptor output rise and decay faster than in the other two models, with the back-to-front waveforms leading the front-to-back counterparts. (D) The intracellular responses of a R1-R6 photoreceptor to the given two dot stimuli, as recorded *in vivo*, show similar dynamics to the full model in (C) with its back-to-front signals (red) leading the front-to-back signals (blue).

1  
2  
3  
4  
5  
6  
7  
8  
9  
10  
11  
12  
13  
14  
15  
16  
17  
18  
19  
20

Interestingly, for both opposing object directions, the narrowing of a R1-R6's receptive field (Appendix figure 45C-D) makes its voltage responses briefer than what would be the case without this process (A-B). Therefore, the resulting faster temporal photoreceptor output dynamics combat the effects of motion blur, supporting the theoretical and experimental results in Appendix 6 (Appendix figure 29).

The 2<sup>nd</sup> prediction is that, for high (saccadic) speeds, R1-R6s resolve two front-to-back moving bright dots better than when these move back-to-front (Appendix figure 46). Thus, the normal back-to-front rhabdomere movement should improve the fly eye's spatiotemporal resolution during fast forward locomotion or object motion. This is indeed what we saw in the full model simulations (Appendix figure 46D) and in some stable experimental recordings (Appendix figure 46E). Because of the back-to-front rhabdomere movement, which was inverted by the ommatidium lens, the light input (Appendix figure 46C) for two front-to-back moving dots were separated further apart as intensity spikes (blue trace) than that for the opposite motion (red). Consequently, the resolvability in the resulting R1-R6 output (Appendix figure 46D) also became greater for front-to-back moving stimuli. This of course further meant that in comparison to the case of the immobile rhabdomere with the same narrow acceptance angle ( $\Delta\rho = 4^\circ$ ), the neural resolvability of the back-to-front moving rhabdomere, which kept the same stimulus longer within its receptive field, would be still better.



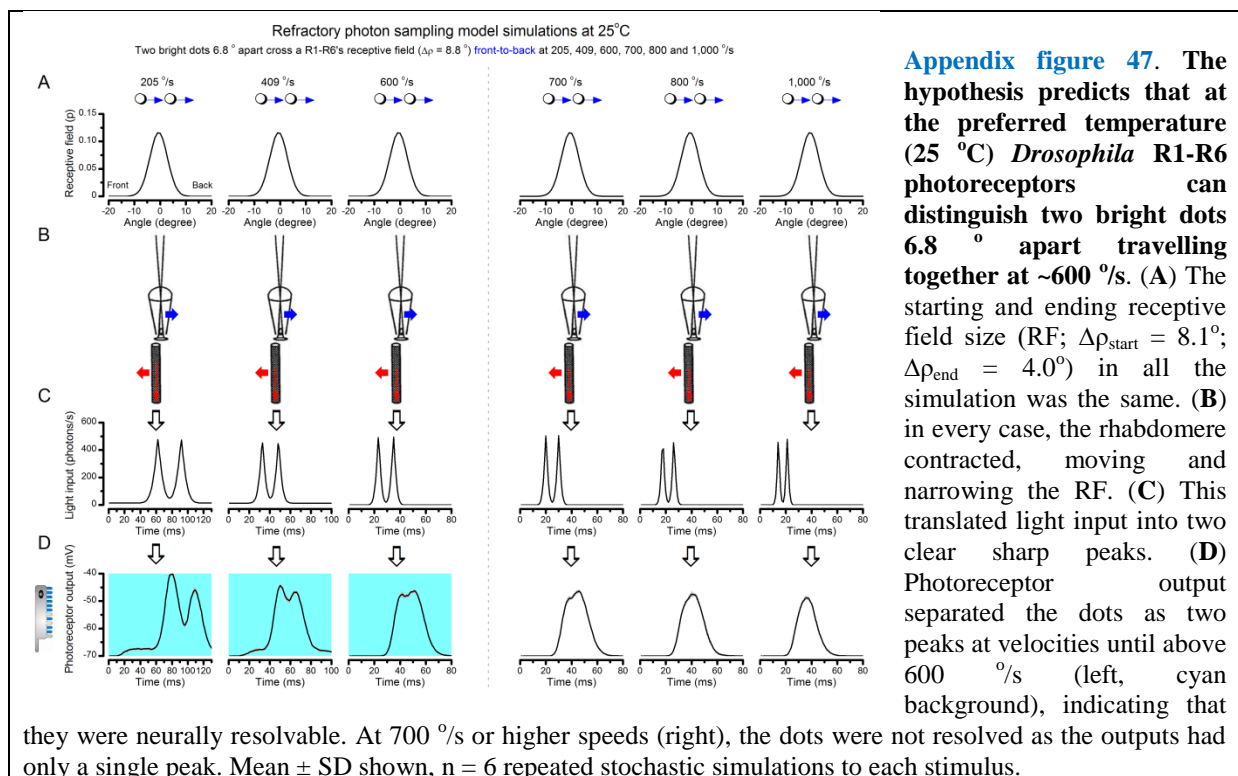
21  
22

## Photoreceptors resolve moving object up to high body-saccadic speeds

1 We next used the complete photoreceptor model (above) to estimate how well a typical R1-R6  
 2 photoreceptor can resolve two bright dots, which are less than the average acceptance angle ( $\Delta\rho$ )  
 3 apart, moving together at increasingly fast (saccadic) velocities. This time, however, the simulations  
 4 were performed at the flies' preferred temperature (Sayeed & Benzer, 1996) of 25 °C, rather than at  
 5 19°C (as in the previous data). We have shown earlier that warming accelerates R1-R6s'  
 6 phototransduction dynamics and refractory microvilli recovery (Juusola & Hardie, 2001b; Song *et al.*,  
 7 2012; Song & Juusola, 2014). Because the resulting increase in their sample (quantum bump)  
 8 rate changes improves information transfer rate (Juusola & Hardie, 2001b; Song *et al.*, 2012; Song &  
 9 Juusola, 2014), we expect here that their output to moving dots should also show improved  
 10 resolvability. We later compare these estimates to the measured head/body-saccade speeds of freely  
 11 locomoting *Drosophila* (Fry *et al.*, 2003; Geurten *et al.*, 2014).

12 **Appendix figure 47** shows the simulated light input (**C**) and photoreceptor output (**D**) to the  
 13 dots (6.8° apart) crossing a R1-R6 photoreceptor's RF ( $\Delta\rho_{\text{start}} = 8.1^\circ$ ,  $\Delta\rho_{\text{end}} = 4.0^\circ$ ) in front-to-back  
 14 direction at 205 (left), 409, 600, 700, 800 and 1,000°/s (right). We found that the slower the dots  
 15 moved (**A**), the better the predicted photoreceptor output distinguished them as two separate events  
 16 (peaks) in time (**D**). Remarkably, the output resolved the dots at speeds until ~600 °/s (cyan  
 17 background). As a neural threshold for representing sub-RF details, this image speed is indeed very  
 18 high. It means that *Drosophila* should lose little neural image detail during its normal saccadic body  
 19 rotations during walking; the measured rotation speed range is ~200-800 °/s (Geurten *et al.*, 2014).

20 At the higher speeds, the two response peaks fused into one. Notice that because the predicted  
 21 light input (as modulated by the rhabdome contraction) resolved the dots even at 1,000 °/s  
 22 (**Appendix figure 47C**), the resolution limit in the photoreceptor output (**Appendix figure 47D**)  
 23 resulted from its intrinsic signal integration time limit; for the given (experimentally measured)  
 24 quantum bump size, latency and refractoriness distributions (Juusola & Hardie, 2001a; Song *et al.*,  
 25 2012; Song & Juusola, 2014). Notice also how the response amplitude and half-width were reduced  
 26 more the faster the dots crossed the receptive field. Thus, the rhabdome then simply captured and  
 27 integrated fewer photons in a given time unit.  
 28



29  
 30 **Prediction that R1-R6s encode hyperacute images in space-time**  
 31 Given that R1-R6 output shows unexpectedly high acuity even at very fast saccadic velocities  
 32 (**Appendix figure 47**), we asked how well these cells could in fact resolve slower moving point-

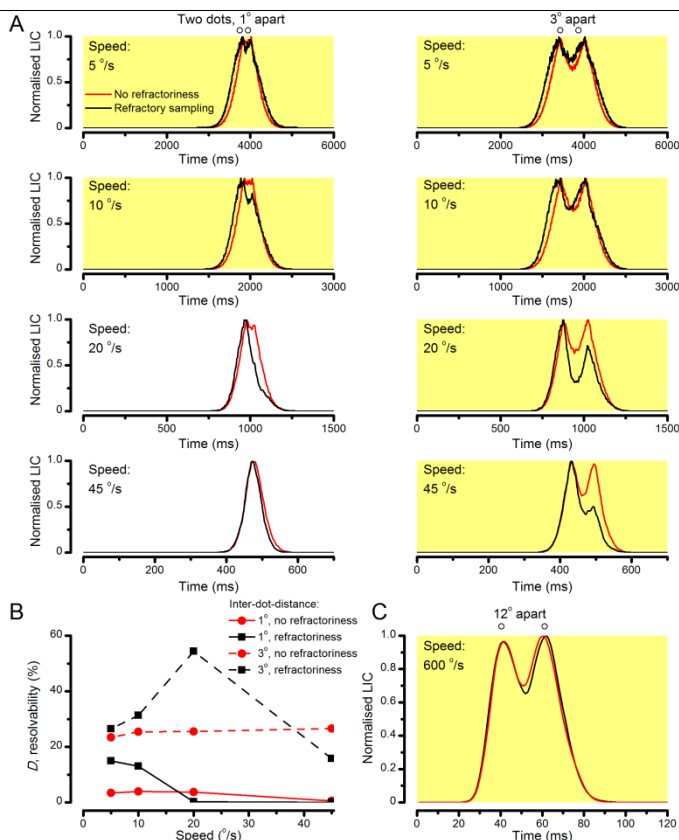
1 objects. Could a normal R1-R6 encode image details, which were less than the average  
 2 interommatidial angle apart? That is, could *Drosophila* actually see the world in finer resolution than  
 3 their compound eyes maximum sensor (or pixel) spacing, which is the limit predicted by the classic  
 4 optical theory (Land, 1997)?

5 We tested this hypothesis theoretically by using the full ‘microsaccadic sampling’-model  
 6 (Figure 9). In these simulations, two bright dots were now either 1°, 2°, 3° or 4° apart. Thus the dot  
 7 spacing was less than the *Drosophila* compound eye’ average interommatidial angle ( $\Delta\phi \sim 4.5\text{-}5^\circ$ ).  
 8 The dots were then moved across a R1-R6 photoreceptor’s RF ( $\Delta\rho_{\text{start}} = 8.1^\circ$ ;  $\Delta\rho_{\text{end}} = 4.0^\circ$ ) at different  
 9 speeds, ranging from 5 (slow gaze fixation) to 400 °/s (very fast body saccade).

10 The model predicted that a typical R1-R6 photoreceptor would resolve the dots in hyperacute  
 11 details (Figure 9) over a broad range of velocities. These theoretical predictions were broadly  
 12 confirmed by intracellular recordings (Figure 9-figure supplement 1), whilst flight simulator  
 13 experiments verified that *Drosophila* indeed have hyperacute vision (Figure 10).

### 15 Refractory sampling improves hyperacute motion vision

16 To quantify how refractory photon sampling contributes to the sharpening of the macroscopic  
 17 responses during moving hyperacute 2-dot stimuli, we further compared the outputs of two different  
 18 photoreceptor models for the same stimuli (Appendix figure 48), with the brightness as in Appendix  
 19 figure 42. For both cases, the resulting dynamic light input – reflecting the narrowing and moving  
 20 receptive field, as caused by photomechanical rhabdomere contraction - was the same, but the  
 21 models’ photon sampling differed. The test model had 30,000 stochastically operating refractory  
 22 microvilli and the control was a comparable mock model, which converted every incoming photon  
 23 into a quantum bump.



Appendix figure 48. Refractory sampling enhances neural resolution for different aspects of hyperacute images. (A) Examples of simulated macroscopic light-induced current responses (normalized LICs) of two different photoreceptor models. Both models have 30,000 microvilli. In the 1<sup>st</sup> model (red), every photon causes a quantum bump; hence, its photon sampling has no refractoriness. In the 2<sup>nd</sup> model (black), photon sampling is refractory. Both models are stimulated with the same moving two bright dots, with their actual light inputs being first modulated by photomechanical rhabdomere contractions (following the microsaccadic sampling hypothesis). Based on the tests with different velocities and inter-dot-distances, refractoriness consistently causes a phase lead in LIC responses. (B) Refractoriness improves response resolution for hyperacute stimuli (inter-dot-distance <4.5°) at slow velocities ( $\leq 20$  °/s). The resolvability,  $D$ , of the recordings and simulations, was determined by Rayleigh criterion (cf. Figure 7C). (C) An example of how refractoriness can enhance response resolution for larger stimulus separations at high saccadic velocities. The difference from the lower peak

to the trough is larger in the black trace (refractory photon sampling) than in the red trace (complete photon sampling).

25 Firstly, we found that the refractory sampling consistently improved the response resolution  
 26 beyond that of the control for bright hyperacute dots (inter-dot-distance <4.5°) at slow velocities ( $\leq 20$   
 27

1 %/s) (**Appendix figure 48A-B**). Thus, refractoriness enhances neural image resolution during slow  
2 self-motion or when high-resolution objects move slowly. Its effects were particularly well seen in the  
3 differing rising phases of the normalized light-induced current (LIC) responses of the two models.  
4 With the slow moving stimuli, the rising responses of the refractory sampling model (black traces)  
5 always led those of the non-refractory model (red).

6 Additionally, in other trials, we found that when the dots were more than the average  
7 acceptance angle apart ( $\Delta\rho_{\text{start}} \geq 9.5^\circ$ ) but moved across a R1-R6 photoreceptor's receptive field at  
8 very fast saccadic speeds ( $\geq 400$  %/s), the refractoriness often enhanced neural image resolution  
9 beyond that of the controls (**Appendix figure 48C**). This observation is consistent with our previous  
10 finding that stochastic refractoriness of light-activated microvilli exerts a memory of past events in  
11 bump integration (Song & Juusola, 2014). This memory accentuates certain stimulus features relative  
12 to others so that a R1-R6 samples information from different inter-dot-distance/speed-combinations  
13 differently. Ultimately, it could well be that the real R1-R6s' refractory photon sampling statistics are  
14 adapted (through their visual lifestyle) to the statistics of moving high-resolution natural images. Of  
15 course, here, the used 2-dot stimuli and the models, which were isolated from the lamina network  
16 feedbacks, are too simple to fully explore such statics and the intricacies of hyperacute *Drosophila*  
17 vision.

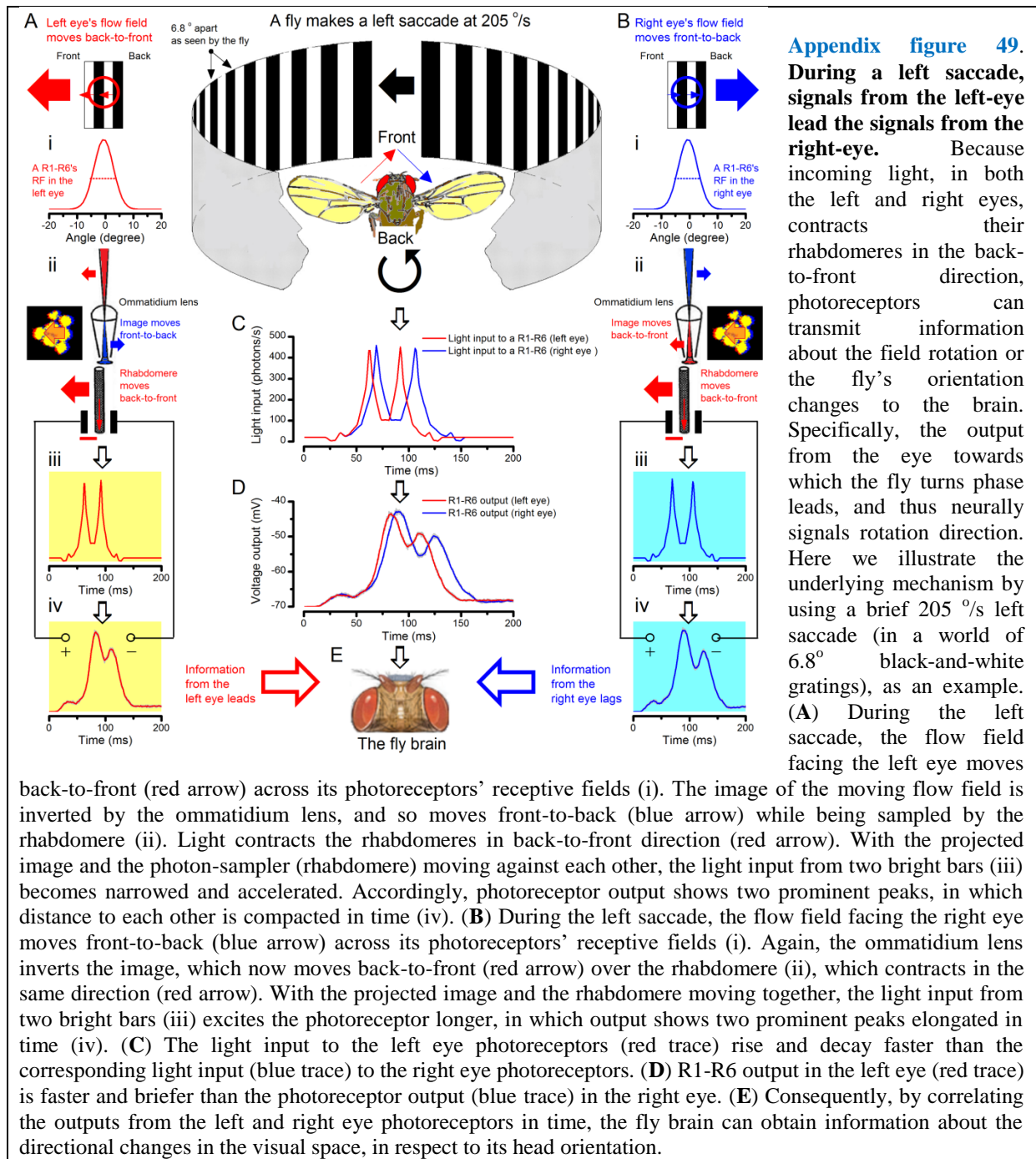
### 18 19 **Horizontal vs. vertical motion hyperacuity**

20 The two most important biophysical factors of *Drosophila* photoreceptors, which lead to motion  
21 hyperacuity - whereupon space is encoded in time - are their sufficiently narrow receptive fields  
22 ( $\Delta\rho_{\text{end}} < 5^\circ$ ) and refractory photon sampling (quantum bump dynamics). Therefore, theoretically, as  
23 R1-R6s' receptive fields should narrow when an object crosses them, irrespective of its motion  
24 direction; *Drosophila* is expected to have hyperacute vision for both horizontal and vertical motion.

25 However, as we considered in **Appendix figure 45**, R1-R6 photoreceptors' neural  
26 resolvability should be the best for front-to-back moving objects. In this case, due to their back-to-  
27 front sweeping rhabdomeres, R1-R6s' receptive field can broaden slightly in horizontal direction.  
28 This dynamic may in part contribute to the curious observation that L2 monopolar cell terminals'  
29 receptive fields (in the medulla) are anisotropic, elongated in horizontal (yaw) direction and narrower  
30 in vertical (pitch) direction, as measured by calcium-imaging experiments (Freifeld *et al.*, 2013).

### 31 32 **Mirror symmetric contractions may also provide navigational heading signal**

33 As we showed in **Appendix 7**, light increments evoke mirror symmetric back-to-front rhabdomere  
34 movements in the left and right fly eye. Interestingly, during fast saccadic body rotations, this  
35 phenomenon could surprisingly help a fly's visual orientation (**Appendix figure 49**). The  
36 microsaccadic sampling-hypothesis predicts that image rotation causes a phasic difference in  
37 photoreceptor outputs between the left and the right eye, with the signals always arriving slightly  
38 faster from the eye, towards which the fly rotates. Because this difference depends upon the rotation  
39 speed, it could be used for signaling changes in the fly's heading direction or to improve visual  
40 navigation. For example, when flying across more homogenous surroundings, such as an open field  
41 with few distinctive visual landmarks, the central brain could use saccadic turns to recalibrate the fly's  
42 head-direction in its internal world map near instantaneously; matching the intended direction to the  
43 new direction, as pointed by the global phase difference between the left and right eye signals.



1  
2

## 1 **Appendix 9: Microsaccadic rhabdomere movements and R1-R6s' information capture**

### 3 **Overview**

4 This appendix describes how photomechanical rhabdomere movements affect *Drosophila* R1-R6  
5 photoreceptors' information capture, compares microsaccadic information sampling of dark and  
6 bright objects and provides useful background information about the experimental and theoretical  
7 results presented in **Figures 1-9**.

9 In this appendix:

- 10 • We explain why and how rhabdomere movement noise influences R1-R6 output mostly at  
11 low frequencies, causing relatively little information loss.
- 12 • We test and compare how microsaccadic sampling affects encoding of bursty bright or *dark*  
13 image contrasts, using intracellular recordings.
- 14 • We further examine how well R1-R6s encode two *dark* moving point-objects (dots), and  
15 compare these recordings with those to corresponding bright moving dots.
- 16 • The results confirm that *Drosophila* R1-R6 photoreceptors resolve both bright and dark  
17 moving hyperacute patterns ( $<$  interommatidial angle,  $\Delta\phi \sim 4.5\text{-}5^\circ$ ), and can respond to bright  
18 or dark point-objects, which are less than their acceptance angles ( $\Delta\rho \sim 9.5^\circ$ ) apart, even at  
19 high saccadic velocities. Thus, microsaccadic sampling hypothesis provides a robust  
20 functional explanation for *Drosophila*'s hyperacute vision (**Appendix 10**).
- 21 • The results support the idea that a fly's optimal viewing strategy would involve fixating on  
22 dark features, which recover refractory microvilli, and then shifting gaze to bright features, to  
23 maximize information capture. This of course would require that it can neurally shift attention  
24 (across the eyes) to visual objects of interest, as some results suggest (Tang *et al.*, 2004; van  
25 Swinderen, 2007; Tang & Juusola, 2010; Paulk *et al.*, 2014; Seelig & Jayaraman, 2015).

### 27 **Microsaccades accentuate high-frequency resolution but generate low-frequency noise**

28 Photomechanical rhabdomere contractions (microsaccades; **Appendix 7**) can maximally shift the  
29 center of a R1-R6 photoreceptor's receptive field by  $\sim 5^\circ$ , and through this self-induced light input  
30 modulation (**Figure 8**) cause variations (noise) in its voltage output. Such "rhabdomere movement  
31 noise" is inevitable if the photoreceptor signal is classified and estimated as the average of the  
32 repeated responses, just as we did in the performance calculations (*e.g.* **Figure 2**).

33 The condition itself bears resemblance to taking snapshots of a stationary scene from different  
34 positions and averaging these. The mean image shows an obvious smear, even if the positions were  
35 only a fraction of a photoreceptor's receptive field ("pixel") apart. However, during repeated light  
36 stimulation, the rhabdomere movements adapt rapidly (**Figure 8E**, **Figure 2-figure supplement 2**),  
37 with this noise affecting less the subsequent performance estimates. Thus, when quantifying the  
38 photoreceptor performance to repeated light intensity time series stimulation (*e.g.* **Figure 2**), we  
39 removed the first 3-10 responses, in which these movements had the largest effect. In the recordings,  
40 this noise would then be rather constant across the collected responses.

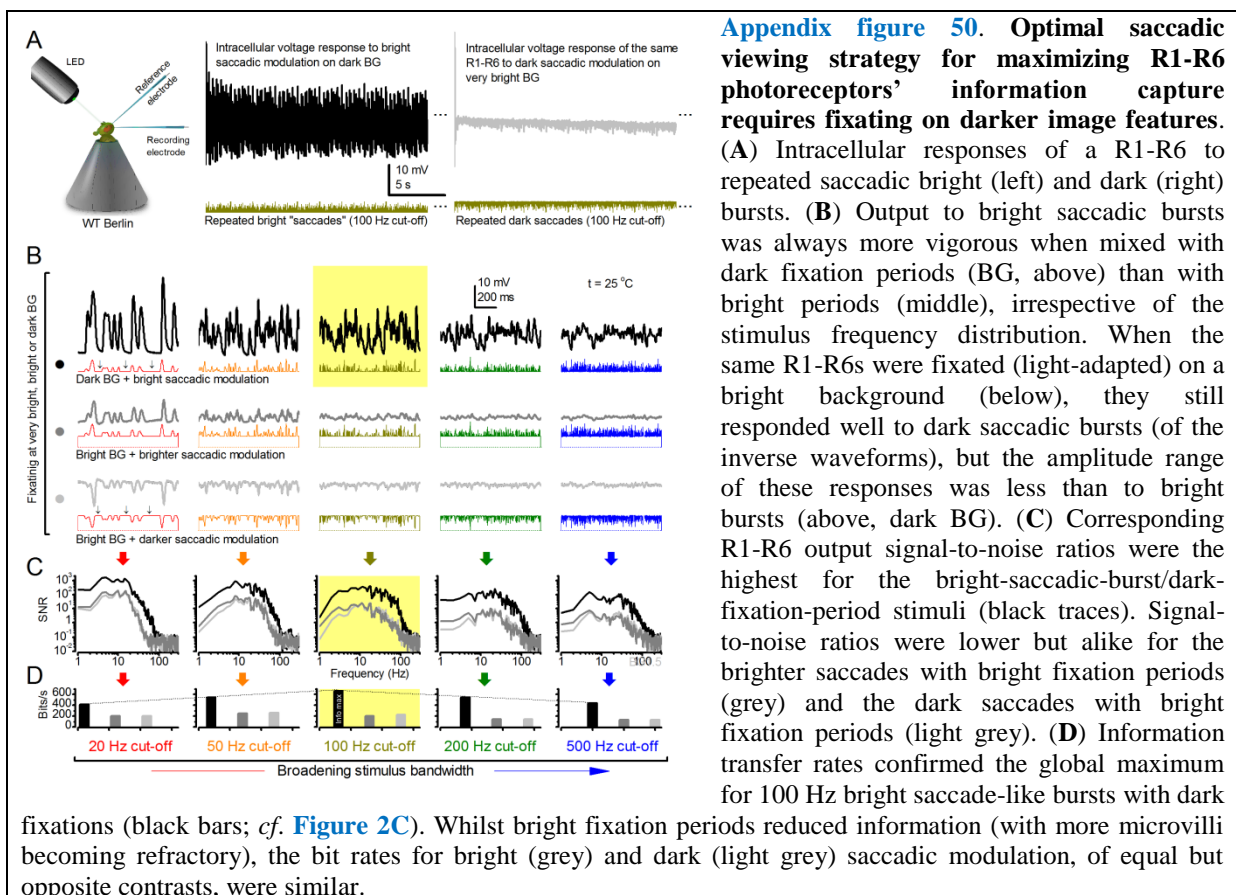
41 Rhabdomere movement noise is missing from the simulated R1-R6 output (**Figures 8-9**).  
42 Therefore, given that the stochastic photoreceptor model's transduction noise is adapted to the mean  
43 light intensity (**Appendix 2**), similarly to that of the recordings (**Figure 2-figure supplement 2A-B**),  
44 we could isolate it as the difference between the recorded and simulated R1-R6 output (**Figure 2-**  
45 **figure supplement 2C-D**). The analysis suggests that rhabdomere movement noise affects mostly  
46 low-frequency R1-R6 output, reducing its signal-to-noise ratio, and importantly, it effectively matches  
47 the rhabdomere jitter in high-speed video footage (**Figure 2-figure supplement 2E, F**).

48 The contractions deviate the rhabdomere from directly facing the light source, reducing  
49 photon influx especially during bright stimulation (**Figures 8C-D**). Such evasive action, however, has  
50 surprisingly little detrimental effect on the R1-R6s' information transfer. This is because bright  
51 stimulation ( $>10^6$  photons/s) contains too much light to be transduced by 30,000 microvilli into  
52 quantum bumps, and R1-R6s actively screen off excess photons to maximize information in their  
53 voltage output. In **Appendix 2**, we showed that R1-R6s' photomechanical adaptations (the  
54 contractions and intracellular pupil mechanism) are jointly optimized with refractory sampling (to

1 modulate quantum efficiency (Song *et al.*, 2012; Song & Juusola, 2014)) for maximal information  
 2 intake at different stimulus conditions. Moreover, owing to bump adaptation and microvilli  
 3 refractoriness, which accentuate light fast changes in macroscopic voltage output (Song *et al.*, 2012;  
 4 Song & Juusola, 2014; Juusola *et al.*, 2015) (*e.g.* (Song & Juusola, 2014): Figures 9-10, improving  
 5 high-frequency resolution), slower signals in return become compressed. Importantly, this low-  
 6 frequency response range (<~10Hz), where also rhabdomere movement noise mostly resides (**Figure**  
 7 **2-figure supplement 2D**), carries relatively little information (Song & Juusola, 2014) (about the  
 8 behaviorally more relevant faster changes in the world).

### 9 **Are saccades and fixations optimized to microsaccadic sampling?**

11 Recordings and simulations (**Figures 1-2**) showed unequivocally that R1-R6s information capture is  
 12 maximized for high-frequency saccade-like bursts with dark fixation intervals. This suggests that the  
 13 optimal daytime viewing strategy would be to fixate on dark features in the visual scenes, as this  
 14 recovers refractory microvilli, and then rapidly move gaze to over bright features, as this increases  
 15 quantum bump (sample) rate changes and thus information capture in time. And indeed, in behavioral  
 16 experiments, *Drosophila* readily fixates on and track dark objects, such as vertical bars (Götz, 1980;  
 17 Tang & Juusola, 2010; Bahl *et al.*, 2013). But because the fly eye photoreceptors sample a continuous  
 18 panoramic view of the world, many of them - at any one time - would unavoidably face bright  
 19 contrasts, which reduce their sensitivity even when their photomechanical adaptations (**Appendix 2**)  
 20 operate maximally. We therefore also tested by intracellular R1-R6 recordings how encoding of  
 21 dynamic bright or dark contrast changes may differ.



23 **Appendix figure 50A** shows examples of consecutive responses recorded from a R1-R6 to repeated  
 24 high-frequency saccadic bright or dark contrast bursts (with 100 Hz cut-off). Expectedly, following  
 25 the stochastic adaptive visual information sampling theory (**Appendixes 1-2**), the responses to bright  
 26 (positive) contrasts after dark “fixation” periods (background, BG) were significantly larger than  
 27 those to dark (negative) contrasts after bright “fixation” periods. Notice, however, that although in  
 28

1 terms of absolute light intensity ( $I$ ) changes (or peak-to-peak amplitude modulation) the two stimuli  
2 were equal, the negative bursts had smaller absolute contrast values ( $c = \frac{\Delta I}{I}$ ) than the positive ones.  
3 This is because the darkening bursts reached their absolute contrast maximum (darkness, -1) only  
4 occasionally, whereas the corresponding brightening bursts reached higher absolute contrasts ( $>1$ ;  
5 owing to their lower mean light intensity).

6 To counter this bias, we used three sets of stimuli to examine individual R1-R6s' response  
7 dynamics to both positive and negative bursts of equal or different contrast distributions (**Appendix**  
8 **figure 50B**). First (top row), the photoreceptors were stimulated with positive contrast bursts (peak-  
9 to-peak modulation = 1 intensity units), which contained high-frequency saccade-like events on a dark  
10 background, having different cut-off frequencies (from 20 to 500 Hz, as in **Figure 1**). In the 2<sup>nd</sup> set  
11 (middle), the same stimuli were superimposed on a bright background (1 unit). Finally (bottom), the  
12 stimulus modulation was inverted (to negative contrast bursts) and superimposed on the same bright  
13 background (1 unit). Thus, for the 2<sup>nd</sup> and 3<sup>rd</sup> sets, the stimulus contrasts were equal but opposite.

14 We found (again in agreement with the theory) that whilst the responses were always the  
15 largest to positive contrast bursts on a dark background, the corresponding responses to the positive  
16 and negative contrast bursts on bright background, although smaller, were about the same size  
17 (**Appendix figure 50B**). Since we further know that the larger responses contain more quantum  
18 bumps (**Figure 2**), with the average bumps light-adapting to about the same size (e.g. **Figure 2-figure**  
19 **supplement 2A-B**), the responses' signal-to-noise ratios (**Appendix figure 50C**) and information  
20 transfer rates (**Appendix figure 50D**) were predictable. R1-R6s' signaling performance was the  
21 greatest to the larger positive contrast bursts on a dark background (black), and more than halved to  
22 the smaller corresponding positive (grey) and negative (light grey) contrast bursts over the test  
23 bandwidths. Notably, the responses to the opposite but equal positive and negative contrast bursts  
24 carried effectively equal information contents, underscoring the importance of contrast invariance at  
25 the primary visual encoding stage (Juusola, 1993; Song *et al.*, 2012; Juusola *et al.*, 2015).

26 Therefore, given the fast speed of adaptation (microvilli refractoriness and dynamic quantum  
27 bump size modulation) and its photomechanical counterbalancing (**Appendixes 2, 7**), the sensitivity  
28 of neighboring photoreceptors across the eyes can differ greatly at any one moment, depending upon  
29 whether they face dark or bright contrasts. This realization also implies that when a fly moves its gaze  
30 in saccades, the dark and bright spatial contrast differences in the world should be automatically  
31 translated into large temporal contrast changes between the neighboring retinotopic image pixels  
32 (neuro-ommatidia). Enhancement of local differences and similarities in neural images by  
33 spatiotemporal synaptic (Zheng *et al.*, 2006; Freifeld *et al.*, 2013) and gap-junctional (Wardill *et al.*,  
34 2012) co-processing (including network adaptation (Nikolaev *et al.*, 2009; Zheng *et al.*, 2009)) across  
35 the first optic ganglia, the lamina and medulla, should further improve object detection and fly vision.

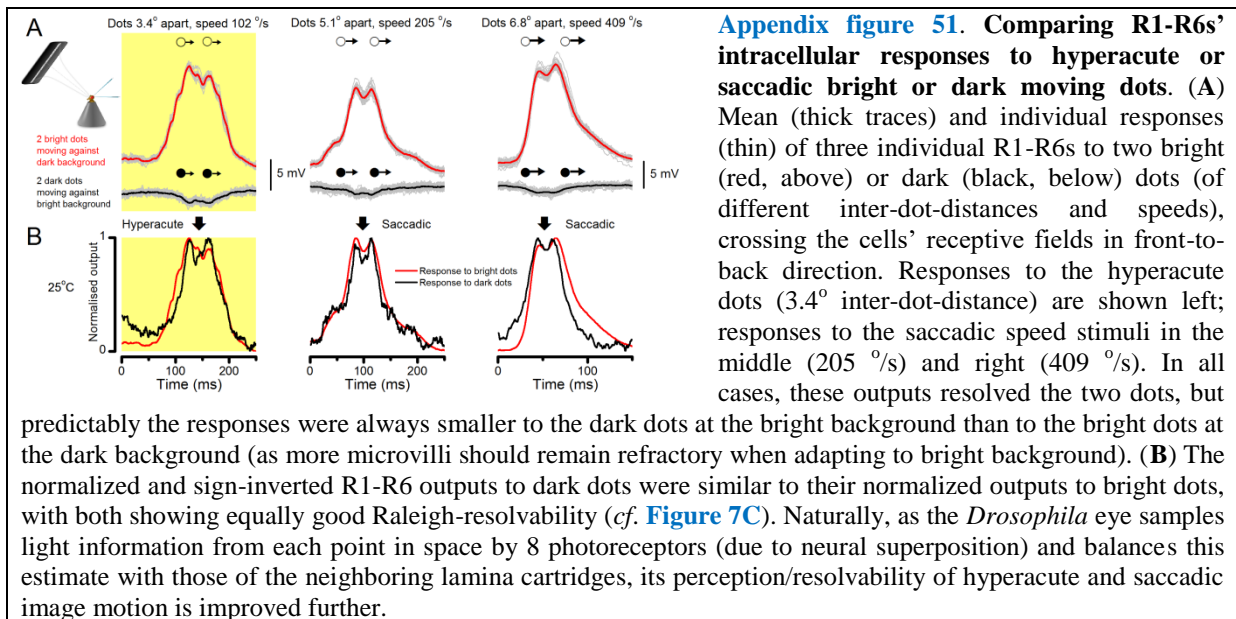
### 37 **Microsaccadic sampling of bright or dark moving point-objects**

38 Natural scenes are rich with dark features: shadows, object boundaries, surfaces of lesser reflectance  
39 etc., which have shaped visual circuit functions, perception and behaviors (Barlow, 1961; Yeh *et al.*,  
40 2009; Joesch *et al.*, 2010; Ratliff *et al.*, 2010; Kremkow *et al.*, 2014; Song & Juusola, 2014).  
41 Consequently, a fly's self-motion generates both dark and bright moving features travelling across its  
42 eyes. We have shown that R1-R6s can resolve fast-moving and hyperacute bright dots (**Figures 7-9**  
43 and **Figure 9-figure supplement 1**). But how well can these cells resolve dark moving dots?

44 We studied this question with the 25 light-point stimulus array (explained in **Appendix 4** and  
45 **Appendix 6**). As before, the stimulus array was first carefully placed at the studied R1-R6's receptive  
46 field center, but this time, all the light-points were switched on, and we generated two travelling dark  
47 points of specified speeds and interdistances. As during these experiments the cells were light-adapted  
48 (depolarized) by the lit stimulus array, the two moving dark dots evoked hyperpolarizing responses.

49 **Appendix figure 51A** shows R1-R6s' characteristic responses to two dark (black traces) and  
50 bright (red) dots of specific speeds (102, 205 and 409 °/s) and interdistances (3.4, 5.1 and 6.8° apart),  
51 recorded from the same cells. In all these cases, the hyperpolarizing responses resolved the two dots,  
52 generating two troughs separated by a peak, but these responses were considerably smaller than those  
53 to the corresponding bright dots. However, when normalized, the photoreceptors' relative neural  
54 resolvability of the dark dots matched that of the bright dots (**Appendix figure 51B**).

1 Thus, in concordance with the behavioral experiments (**Figure 10**), these and other  
 2 intracellular recordings established that *Drosophila* R1-R6 photoreceptors see both bright and dark  
 3 moving hyperacute patterns ( $<$  interommatidial angle,  $\Delta\phi \sim 4.5\text{-}5^\circ$ ), and can resolve point-objects,  
 4 which are less than their acceptance angles ( $\Delta\rho \sim 9.5^\circ$ ) apart, even at high saccadic velocities.  
 5



### 6 **Microsaccadic sampling hypothesis and efficient coding**

7 Our results indicate that R1-R6 photoreceptors' information transfer adapts to the context of stimulus  
 8 statistics; with refractory microvilli, fast quantum bump adaptation (Henderson *et al.*, 2000; Juusola &  
 9 Hardie, 2001a; Song *et al.*, 2012) and photomechanical microsaccades maximizing encoding of phasic  
 10 information from high-contrast bursts. Remarkably, the extraction of phasic stimulus features, which  
 11 characterize object boundaries and line elements in visual scenes, already starts during sampling and  
 12 integration of visual information in the microvilli, at the first visual processing stage. The darker  
 13 periods in stimuli relieve the effects of microvilli refractoriness, enabling greater sensitivity: more and  
 14 slightly larger samples (quantum bumps) can be generated transiently to the next light change (**Figure**  
 15 **1**). This increases the signal-to-noise ratio of the integrated macroscopic response, especially in its  
 16 phasic (fast rising/decaying) components (**Appendix 3**, **Appendix figure 10**). However, unlike later  
 17 information processing in the network, during which presynaptic inputs are often translated to  
 18 postsynaptic spike-bursts of high sparseness for specific features, the neural code of photoreceptors  
 19 must consider all stimulus features together. It adapts to allocate information in high-contrast bursts  
 20 into continuous Gaussian broadband voltage signals (**Figures 2A-B**), utilizing the output range  
 21 optimally.  
 22

23 In the viewpoint of efficient coding, stochastic refractory sampling, fast quantum bump  
 24 adaptation and photomechanical contractions benefit vision in three important ways:

- 25 • They exchange redundant information in mean voltage to more useful information in relative  
 26 modulation, enabling photoreceptors to encode reliable estimates of the world within their  
 27 limited output ranges, despite strongly and quickly changing intensities.
- 28 • They lower the metabolic cost of information with fewer bumps integrating a lower  
 29 membrane potential, consuming less ATP (Song & Juusola, 2014).
- 30 • And when linked to bursty saccadic head/body movements, they increase high-frequency  
 31 information capture from the world and reduce motion blur.

32 These results further imply that saccadic behaviors enable the fly eye to convey to the fly brain a far  
 33 more efficient and accurate neural image of the variable world than what was believed before. Thus,  
 34 saccades not only contribute to gaze-stabilization (Land, 1973; Fox & Frye, 2014), which historically  
 35 is considered to be their major function (Land, 1999), but they also “burstify” light input for efficient  
 36 and accurate sampling.

## 1 **Appendix 10: *Drosophila* behavior in a flight simulator system confirms hyperacute vision**

### 3 **Overview**

4 This appendix describes the used optomotor behavioral paradigm in a classic *Drosophila* flight  
5 simulator system to study visual resolution, and provides important background information about the  
6 experimental and theoretical results presented in **Figure 10** in the main paper.

8 In this appendix:

- 9 • We test in open-loop conditions whether wild-type *Drosophila* can generate yaw-torque  
10 (optomotor responses) to hyperacute vertical black-and-white stripe-scenes that rotate  
11 clockwise and counterclockwise at 45 °/s.
- 12 • Our results clearly indicate that wild-type *Drosophila* have hyperacute vision (seeing finer  
13 image details than the average interommatidial angle,  $\Delta\phi \sim 4.5$ , of their compound eyes), with  
14 the measured behavioral responses closely following the prediction of our new  
15 ‘microsaccadic sampling’-hypothesis (see **Appendix 8**).

### 17 **Testing *Drosophila* visual behavior in flight simulator system**

18 Wild-type "Berlin" *Drosophila* were raised on standard food medium at 25°C and 60% relative  
19 humidity with a 12-h light and 12-h dark cycle, with light on at 8 a.m. In the experiments, we used 2-  
20 to 3-day-old female flies. Under cold-anesthesia (lasting < 3 min), a small copper-wire hook was fixed  
21 with a droplet of UV-light sensitive glue (Loctite) between each fly's head and thorax. After  
22 preparation, flies were left to familiarize themselves with their hooks overnight in single vials, which  
23 provided them water and sucrose.

24 A custom-built, computer controlled flight simulator system (Wardill *et al.*, 2012) was used to  
25 study *Drosophila*'s optomotor behavior. A tethered *Drosophila* was connected to the torque-meter  
26 (Tang & Guo, 2001) by a small clamp holding the copper-wire hook, which fixed the fly's head in a  
27 rigid position and orientation, but allowed stationary flight (Götz, 1964; Heisenberg & Buchner,  
28 1977). The torque meter transduced yaw torque into electrical voltage.

29 A fly, tethered from the torque meter, was lowered by a mechanical micromanipulator in the  
30 center of a white featureless plastic hollow cylinder (a diffuser). Inside it, we placed high-resolution  
31 visual patterns (bars, stripe patterns, etc.), which were laser-printed on a transparent film, forming a  
32 360° panorama around the fly's long axis. The panorama could be rotated around its vertical axis by a  
33 servomotor. Outside, the diffuse cylinder faced a surrounding ring-shaped light-tube (special full-  
34 band: 350-900 nm) that provided uniform illumination on the panorama. The light intensity during the  
35 panoramic motion stimulation, although bright, was always less (0.5-1.5 log-intensity units) than the  
36 direct stimuli used in the intracellular recordings (*cf.* **Figure 1**).

### 38 **Open-loop experiments**

39 Inside the flight simulator, a flying fly saw a continuous (360°) stripe-scene (black-and-white bars) of  
40 predetermined spectral and spatial resolution, which was free of motion artefacts, flashing or aliasing.  
41 After one second of viewing the still scene, it was spun to right (clockwise) by a linear stepping motor  
42 for two seconds, stopped for two seconds, before rotating to left (counterclockwise) for two seconds,  
43 and stopped again for a second. This eight-second stimulus was repeated 10-25 times and each trial,  
44 together with the fly's coincident yaw torque responses, was sampled at 1 kHz and stored in a PC's  
45 hard-drive for later analysis, using custom-written software (Biosyst) (Juusola & Hardie, 2001a).  
46 Presumably to stabilize gaze, flies tend to follow the scene rotations, generating yaw torque responses  
47 (optomotor responses to right or left), the strength of which is believed to reflect the strength of their  
48 motion perception (Götz, 1964; Heisenberg & Buchner, 1977; Wardill *et al.*, 2012). The fixed  
49 stimulus parameters for moving stripe scenes, as shown in the figures, were: azimuth  $\pm 360^\circ$ ; elevation  
50  $\pm 45^\circ$ ; velocity, 45, 50, 200 or 300 °/s; contrast, 1.0, as seen by the fly. **Figure 10A** show the averages  
51 ( $n = 9$  flies) of the mean optomotor responses ( $n = 22-35$  trials for each fly).

52 We first tested optomotor responses of wild-type flies to black-and-white stripe-scenes  
53 (spectral full-width: 380-900 nm) of three different spatial resolutions (wavelength: 1.16°, 2.88° and  
54 14.4°), **rotating at 45°/s**, as shown in **Figures 10A-C**. To verify that air flow, or some hidden features  
55 in the stimulus panorama, was not affecting optomotor responses, we used the white diffuser cylinder

1 alone, which showed no clear contrast to human eye, as the control stimulus. These control field  
2 rotation experiments were repeated using the same flies (**Figure 10-figure supplement 1**). We found  
3 by that the white control stimulus did not evoke torque responses.

4 We also tested optomotor responses of five flies to 3.9° (hyperacute) and 14.4° (control)  
5 wavelength panoramic stripe-scenes, rotating at 50, 200 and 300 °/s (**Figures 10D-F**). The results were  
6 consistent with the predictions of the full photoreceptor model (*cf.* **Figure 9A**, two dots 4° apart),  
7 which incorporated both the refractory photon sampling and photomechanical rhabdomere motion  
8 dynamics.

9  
10 *Quantifying optomotor behavior.* The optomotor responses of individual flies to the same repeated  
11 field rotations vary in strength and repeatability (**Figure 10-figure supplement 1A**), but their visual  
12 performance to different spatial resolution stripe scenes is clearly different. These differences can be  
13 quantified by measuring the mean torque response of a single fly to stimulus repetitions and by  
14 averaging the mean responses of the many flies of the same stripe scene resolution (**Figure 10-figure**  
15 **supplement 1B**; here 9). This reduces noise and non-systematic (arbitrary) trends of single  
16 experiments, revealing the underlying response strength and optomotor behavior characteristics.  
17 These population responses are shown in **Figure 10** for a straightforward comparison.

18 In open-loop experiments, a fly's torque response returns gradually to baseline after the  
19 optomotor stimulus stops, but this can take seconds (varying with individual flies). Accordingly, in  
20 our experiments, which contain only brief 2-s-long inter-stimulus-intervals, the torque responses  
21 typically recover only fractionally (10-70%) during these still periods toward the baseline. Therefore,  
22 for comparing the optomotor behavior different stripe scene resolutions, we used the maximum range  
23 (or peak-to-peak) of the torque response, evoked by the combined leftward and rightward field  
24 rotation stimulus. The maximum range and variability in the torque responses to the same optomotor  
25 stimulus are shown with controls in **Figure 10-figure supplement 1C** and **D**, respectively.

26 Markedly, the optomotor responses to hyperacute stripe-scenes were not caused by aliasing.  
27 This is because perceptual aliasing (such as the wagon-wheel effect or Moiré patterns), if induced by  
28 the rotating hyperacute scenes, would have been perceived as slowed down image rotation, eventually  
29 reversing to the opposite direction (the reverse rotation effect). And thus, if the tested flies had seen  
30 such motion patterns, they would have consequently followed them slower and rotated against the real  
31 scene rotation direction. Such optomotor behavior was never observed in our experiments.

### 32 33 **Why did the previous behavioral studies not find hyperacute vision?**

34 In 1976, Buhner probed *Drosophila*'s visual acuity by stimulating the upper frontal part in one of its  
35 eyes with small local moving grating patterns (covering about 50 ommatidia) while a fly walked on  
36 track-ball (Buchner, 1976). Notably, the aim of his study was not to find the finest resolution what a  
37 *Drosophila* can resolve but instead to deduce the likely columnar organization of its directionally  
38 sensitive elementary motion detectors from a fixed fly's tendency to follow moving stimulus patterns.  
39 Thus, this was also an open-loop paradigm, but the used microscope-mediated local grating  
40 stimulation was very different from the global hyperacute panoramic visual scenes of our study.  
41 Specifically, we note that in Buchner's study:

- 42 • Visual acuity was not tested below the interommatidial angle ( $\Delta\phi \sim 4.5$ ); with the overall  
43 results deduced by eliminating the presumed boundary elements and contrast attenuation from  
44 the data.
- 45 • The used mean stimulus light intensity (luminance; 16 cd/m<sup>2</sup>) was low. Therefore, the  
46 resulting image grating at the level of individual photoreceptors would have been dim and  
47 spatiotemporal signal-to-noise ratio of light input and photoreceptor output low. Based on our  
48 intracellular data (Juusola & Hardie, 2001a; Song *et al.*, 2012), this dim light intensity would  
49 have made it practically impossible for R1-R6 photoreceptors to resolve very fine (or  
50 hyperacute) visual patterns.
- 51 • The sensitivity and the time resolution of the used trackball system (Buchner, 1976) seem  
52 significantly less than in our bespoke torque meter (Tang *et al.*, 2004), requiring extensive  
53 data averaging. This would have made it more difficult for the trackball system to resolve the  
54 weaker (small amplitude) behavioral responses to fine spatial contrast changes (**Figure 10A**).

1 More recently, because of the historical belief that interommatidial angle limits a fly's visual acuity,  
2 many experimentalists have started using coarse LED-matrixes, typically with 4.5-5° maximum  
3 resolution, to probe visual learning and optomotor responses. As our study here shows, these kinds of  
4 visual stimuli are very different from the panoramic high-resolution printed scenes with thin  
5 continuous lines and symbols and thus are expected evoke quite different neural responses.

## References

- 1  
2 About Tayoun AN, Li XF, Chu B, Hardie RC, Juusola M & Dolph PJ. (2011). The *Drosophila* SK  
3 channel (dSK) contributes to photoreceptor performance by mediating sensitivity control at  
4 the first visual network. *J Neurosci* **31**, 13897-13910.
- 5 Agi E, Langen M, Altschuler SJ, Wu LF, Zimmermann T & Hiesinger PR. (2014). The evolution and  
6 development of neural superposition. *J Neurogenet* **28**, 216-232.
- 7 Ahissar E & Arieli A. (2001). Figuring space by time. *Neuron* **32**, 185-201.
- 8 Anderson JC & Laughlin SB. (2000). Photoreceptor performance and the co-ordination of achromatic  
9 and chromatic inputs in the fly visual system. *Vision Res* **40**, 13-31.
- 10 Asyali MH & Juusola M. (2005). Use of Meixner functions in estimation of Volterra kernels of  
11 nonlinear systems with delay. *Ieee T Bio-Med Eng* **52**, 229-237.
- 12 Atick JJ. (1992). Could information-theory provide an ecological theory of sensory processing.  
13 *Network-Comp Neural* **3**, 213-251.
- 14 Bahl A, Ammer G, Schilling T & Borst A. (2013). Object tracking in motion-blind flies. *Nat Neurosci*  
15 **16**, 730-738.
- 16 Barlow H, B. (1961). Possible principles underlying the transformation of sensory messages. In  
17 *Sensory communication*, ed. Rosenblith WA. MIT, Cambridge.
- 18 Barlow HB. (1952). The size of ommatidia in apposition eyes. *J Exp Biol* **29**, 667-674.
- 19 Behnia R, Clark DA, Carter AG, Clandinin TR & Desplan C. (2014). Processing properties of ON and  
20 OFF pathways for *Drosophila* motion detection. *Nature* **512**, 427-430.
- 21 Berry MJ, Brivanlou IH, Jordan TA & Meister M. (1999). Anticipation of moving stimuli by the  
22 retina. *Nature* **398**, 334-338.
- 23 Blaj G & van Hateren JH. (2004). Saccadic head and thorax movements in freely walking blowflies. *J*  
24 *Comp Physiol A* **190**, 861-868.
- 25 Boschek CB. (1971). Fine structure of peripheral retina and lamina ganglionaris of fly, *Musca*  
26 *domestica*. *Z Zellforsch Mik Ana* **118**, 369-409.
- 27 Braitenberg V & Debbage P. (1974). Regular net of reciprocal synapses in visual system of fly,  
28 *Musca Domestica*. *J Comp Physiol* **90**, 25-31.
- 29 Brenner E & Smeets JBJ. (2000). Motion extrapolation is not responsible for the flash-lag effect.  
30 *Vision Res* **40**, 1645-1648.
- 31 Brinkworth RSA, Mah EL, Gray JP & O'Carroll DC. (2008). Photoreceptor processing improves  
32 salience facilitating small target detection in cluttered scenes. *J Vision* **8**.
- 33 Britt SG, Feiler R, Kirschfeld K & Zuker CS. (1993). Spectral tuning of rhodopsin and metarhodopsin  
34 *in vivo*. *Neuron* **11**, 29-39.
- 35 Buchner E. (1976). Elementary movement detectors in an insect visual system. *Biol Cybern* **24**, 85-  
36 101.
- 37 Burg MG, Sarthy PV, Koliantz G & Pak WL. (1993). Genetic and molecular identification of a  
38 *Drosophila* histidine-decarboxylase gene required in photoreceptor transmitter synthesis.  
39 *Embo J* **12**, 911-919.
- 40 Burkhardt D. (1977). Vision of insects. *J Comp Physiol* **120**, 33-50.
- 41 Burton BG & Laughlin SB. (2003). Neural images of pursuit targets in the photoreceptor arrays of  
42 male and female houseflies *Musca domestica*. *J Exp Biol* **206**, 3963-3977.
- 43 Burton BG, Tatler BW & Laughlin SB. (2001). Variations in photoreceptor response dynamics across  
44 the fly retina. *J Neurophysiol* **86**, 950-960.
- 45 Chiappe ME, Seelig JD, Reiser MB & Jayaraman V. (2010). Walking modulates speed sensitivity in  
46 *Drosophila* motion vision. *Curr Biol* **20**, 1470-1475.
- 47 Corey DP, Garcia-Anoveros J, Holt JR, Kwan KY, Lin SY, Vollrath MA, Amalfitano A, Cheung  
48 ELM, Derfler BH, Duggan A, Geleoc GSG, Gray PA, Hoffman MP, Rehm HL, Tamasauskas  
49 D & Zhang DS. (2004). TRPA1 is a candidate for the mechanosensitive transduction channel  
50 of vertebrate hair cells. *Nature* **432**, 723-730.
- 51 Cover T & Thomas J. (1991). *Elements of Information Theory*. John Wiley & Sons, Inc., New York.
- 52 Dau A, Friederich U, Dongre S, Li X, Bollepalli MK, Hardie RC & Juusola M. (2016). Evidence for  
53 dynamic network regulation of *Drosophila* photoreceptor function from mutants lacking the  
54 neurotransmitter histamine. *Frontiers in Neural Circuits* **10**.

- 1 Dippe MAZ & Wold EH. (1985). Antialiasing through stochastic sampling. *Computer Graphics* **19**,  
2 69-78.
- 3 Ditchburn RW & Ginsborg BL. (1952). Vision with a stabilized retinal image. *Nature* **170**, 36-37.
- 4 Donner K & Hemilä S. (2007). Modelling the effect of microsaccades on retinal responses to  
5 stationary contrast patterns. *Vision Res* **47**, 1166-1177.
- 6 Dubs A. (1982). The spatial integration of signals in the retina and lamina of the fly compound eye  
7 under different conditions of luminance. *J Comp Physiol* **146**, 321-343.
- 8 Dubs A, Laughlin SB & Srinivasan MV. (1981). Single photon signals in fly photoreceptors and 1st  
9 order interneurons at behavioral threshold. *J Physiol-London* **317**, 317-334.
- 10 Eckert H & Bishop LG. (1975). Nonlinear dynamic transfer characteristics of cells in peripheral  
11 visual pathway of flies. 1. retinula cells. *Biol Cybern* **17**, 1-6.
- 12 Eguchi E & Horikoshi T. (1984). Comparison of stimulus-response (V-Log-I) functions in 5 types of  
13 *lepidopteran* compound eyes (46 species). *J Comp Physiol* **154**, 3-12.
- 14 Elyada YM, Haag J & Borst A. (2009). Different receptive fields in axons and dendrites underlie  
15 robust coding in motion-sensitive neurons. *Nat Neurosci* **12**, 327-332.
- 16 Field DJ. (1987). Relations between the statistics of natural images and the response properties of  
17 cortical cells. *J Opt Soc Am A* **4**, 2379-2394.
- 18 Field GD, Gauthier JL, Sher A, Greschner M, Machado TA, Jepsen LH, Shlens J, Gunning DE,  
19 Mathieson K, Dabrowski W, Paninski L, Litke AM & Chichilnisky EJ. (2010). Functional  
20 connectivity in the retina at the resolution of photoreceptors. *Nature* **467**, 673-677.
- 21 Fox JL & Frye MA. (2014). Figure-ground discrimination behavior in *Drosophila*. II. Visual  
22 influences on head movement behavior. *J Exp Biol* **217**, 570-579.
- 23 Franceschini N. (1998). Combined optical, neuroanatomical, electrophysiological and behavioural  
24 studies of signal processing in the fly compound eye. In *Biocybernetics of Vision: Integrative*  
25 *mechanisms and Cognitive Processes*, ed. Taddei-Ferretti C, pp. 341-361. World Scientific,  
26 Singapore.
- 27 Franceschini N & Chagneux R. (1994). Retinal movements in freely walking flies. In *Gottingen*  
28 *Neurobiology Report*, ed. Elsner N & Breer H. Georg Thieme Verlag, Stuttgart.
- 29 Franceschini N & Chagneux R. (1997). Repetitive scanning in the fly compound eye. In *Gottingen*  
30 *Neurobiology Report*, ed. Wässle H & Eisner N, pp. 279. Georg Thieme Verlag, Stuttgart.
- 31 Franceschini N, Chagneux R & Kirschfeld K. (1995). Gaze control in flies by co-ordinated action of  
32 eye muscles. In *Gottingen Neurobiology Report*, ed. Elsner N & Menzel R, pp. 401. Georg  
33 Thieme Verlag, Stuttgart.
- 34 Franceschini N, Chagneux R, Kirschfeld K & Mucke A. (1991). Vergence eye movements in flies. In  
35 *Gottingen Neurobiology Report*, ed. Elsner N & Penzlin H. Georg Thieme Verlag, Stuttgart.
- 36 Franceschini N, Hu Y, Reiner AP, Buyske S, Nalls M, Yanek LR, Li Y, Hindorff LA, Cole SA,  
37 Howard BV, Stafford JM, Carty CL, Sethupathy P, Martin LW, Lin DY, Johnson KC, Becker  
38 LC, North KE, Dehghan A, Bis JC, Liu Y, Greenland P, Manson JE, Maeda N, Garcia M,  
39 Harris TB, Becker DM, O'Donnell C, Heiss G, Kooperberg C & Boerwinkle E. (2014).  
40 Prospective associations of coronary heart disease loci in African Americans using the  
41 MetaboChip: the PAGE study. *Plos One* **9**, e113203.
- 42 Franceschini N & Kirschfeld K. (1971a). Optical study *in vivo* of photoreceptor elements in  
43 compound eye of *Drosophila*. *Kybernetik* **8**, 1-13.
- 44 Franceschini N & Kirschfeld K. (1971b). Phenomena of pseudopupil in the compound eye of  
45 *Drosophila*. *Kybernetik* **9**, 159-182.
- 46 Franceschini N & Kirschfeld K. (1976). Automatic-control of light flux in compound eye of *diptera* -  
47 spectral, statical, and dynamical properties of mechanism. *Biol Cybern* **21**, 181-203.
- 48 Freifeld L, Clark DA, Schnitzer MJ, Horowitz MA & Clandinin TR. (2013). GABAergic lateral  
49 interactions tune the early stages of visual processing in *Drosophila*. *Neuron* **78**, 1075-1089.
- 50 French AS, Korenberg MJ, Jarvilehto M, Kouvalainen E, Juusola M & Weckstrom M. (1993). The  
51 dynamic nonlinear behavior of fly photoreceptors evoked by a wide-range of light intensities.  
52 *Biophys J* **65**, 832-839.
- 53 Friederich U, Coca D, Billings S & Juusola M. (2009). Data modelling for analysis of adaptive  
54 changes in fly photoreceptors. *Lect Notes Comput Sc* **5863**, 34-48.

- 1 Fry SN, Sayaman R & Dickinson MH. (2003). The aerodynamics of free-flight maneuvers in  
2 *Drosophila*. *Science* **300**, 495-498.
- 3 Gemperlein R & Mccann GD. (1975). Study of response properties of retinula cells of flies using  
4 nonlinear identification theory. *Biol Cybern* **19**, 147-158.
- 5 Geurten BRH, Jahde P, Corthals K & Gopfert MC. (2014). Saccadic body turns in walking  
6 *Drosophila*. *Front Behav Neurosci* **8**.
- 7 Golub GH & Reinsch C. (1970). Singular value decomposition and least squares solutions. *Numer*  
8 *Math* **14**, 403-420.
- 9 Gonzalez-Bellido PT. (2009). Photoreceptor spatial performance of the fruit fly *Drosophila*  
10 *melanogaster* and the killer fly *Coenosia attenuata*. In *PhD theses in Biomedical Science*, pp.  
11 111. the University of Sheffield, Sheffield.
- 12 Gonzalez-Bellido PT, Wardill TJ & Juusola M. (2011). Compound eyes and retinal information  
13 processing in miniature dipteran species match their specific ecological demands. *P Natl Acad*  
14 *Sci USA* **108**, 4224-4229.
- 15 Götz KG. (1964). Optomotor investigation of the visual system of some eye mutations of the  
16 *Drosophila* fruit fly. *Kybernetik* **2**, 77-91.
- 17 Götz KG. (1980). Visual guidance in *Drosophila*. *Basic Life Science* **16**, 391-407.
- 18 Greiner B, Ribí WA & Warrant EJ. (2005). A neural network to improve dim-light vision? Dendritic  
19 fields of first-order interneurons in the nocturnal bee *Megalopta genalis*. *Cell Tissue Res* **322**,  
20 313-320.
- 21 Haag J, Wertz A & Borst A. (2010). Central gating of fly optomotor response. *P Natl Acad Sci USA*  
22 **107**, 20104-20109.
- 23 Hardie RC. (1979). Electrophysiological analysis of fly retina. 1. Comparative properties of R1-6 and  
24 R7 and 8. *J Comp Physiol* **129**, 19-33.
- 25 Hardie RC. (1984). Properties of Photoreceptor-R7 and Photoreceptor-R8 in Dorsal Marginal  
26 Ommatidia in the Compound Eyes of *Musca* and *Calliphora*. *J Comp Physiol* **154**, 157-165.
- 27 Hardie RC. (1985). Functional organization of the fly retina. In *Progress in Sensory Physiology*, ed.  
28 Ottoson D, pp. 1-79. Springer, New York.
- 29 Hardie RC, Franceschini N, Ribí W & Kirschfeld K. (1981). Distribution and properties of sex-  
30 specific photoreceptors in the fly *Musca domestica*. *J Comp Physiol* **145**, 139-152.
- 31 Hardie RC & Franze K. (2012). Photomechanical responses in *Drosophila* photoreceptors. *Science*  
32 **338**, 260-263.
- 33 Hardie RC & Juusola M. (2015). Phototransduction in *Drosophila*. *Current opinion in neurobiology*  
34 **34C**, 37-45.
- 35 Heisenberg M. (1971). Separation of receptor and lamina potentials in electroretinogram of normal  
36 and mutant *Drosophila*. *J Exp Biol* **55**, 85-100.
- 37 Heisenberg M & Buchner E. (1977). Role of retinula cell-types in visual behavior of *Drosophila*  
38 *melanogaster*. *J Comp Physiol* **117**, 127-162.
- 39 Henderson SR, Reuss H & Hardie RC. (2000). Single photon responses in *Drosophila* photoreceptors  
40 and their regulation by Ca<sup>2+</sup>. *J Physiol-London* **524**, 179-194.
- 41 Hengstenberg R. (1971). Eye muscle system of housefly *Musca domestica*. 1. Analysis of clock  
42 spikes and their source. *Kybernetik* **9**, 56-&.
- 43 Hofstee CA & Stavenga DG. (1996). Calcium homeostasis in photoreceptor cells of *Drosophila*  
44 mutants *inaC* and *trp* studied with the pupil mechanism. *Visual Neurosci* **13**, 257-263.
- 45 Honkanen A, Takalo J, Heimonen K, Vahasoyrinki M & Weckstrom M. (2014). Cockroach  
46 optomotor responses below single photon level. *J Exp Biol* **217**, 4262-4268.
- 47 Hornstein EP, O'Carroll DC, Anderson JC & Laughlin SB. (2000). Sexual dimorphism matches  
48 photoreceptor performance to behavioural requirements. *P Roy Soc B-Biol Sci* **267**, 2111-  
49 2117.
- 50 Horridge GA, Mimura K & Hardie RC. (1976). Fly photoreceptors. 3. Angular sensitivity as a  
51 function of wavelength and limits of resolution. *Proc R Soc Ser B-Bio* **194**, 151-177.
- 52 Howard J, Blakeslee B & Laughlin SB. (1987). The intracellular pupil mechanism and photoreceptor  
53 signal-noise ratios in the fly *Lucilia cuprina*. *Proc R Soc Ser B-Bio* **231**, 415-435.
- 54 Howard J, Roberts WM & Hudspeth AJ. (1988). Mechano-electrical transduction by hair-cells. *Annu*  
55 *Rev Biophys Bio* **17**, 99-124.

- 1 Hu W, Wang TT, Wang X & Han JH. (2015). I-h channels control feedback regulation from amacrine  
2 cells to photoreceptors. *Plos Biol* **13**.
- 3 Järvilehto M & Zettler F. (1973). Electrophysiological-histological studies on some functional  
4 properties of visual cells and second-order neurons of an insect retina. *Z Zellforsch Mik Ana*  
5 **136**, 291-306.
- 6 Joesch M, Schnell B, Raghu SV, Reiff DF & Borst A. (2010). ON and OFF pathways in *Drosophila*  
7 motion vision. *Nature* **468**, 300-304.
- 8 Juusola M. (1993). Linear and nonlinear contrast coding in light-adapted blowfly photoreceptors. *J*  
9 *Comp Physiol A* **172**, 511-521.
- 10 Juusola M, Dau A, Zheng L & Rien D. (2016). Electrophysiological method for recording  
11 intracellular voltage responses of *Drosophila* photoreceptors and interneurons to light stimuli  
12 in vivo. *Journal of Visualized Experiments*, e54142.
- 13 Juusola M & de Polavieja GG. (2003). The rate of information transfer of naturalistic stimulation by  
14 graded potentials. *J Gen Physiol* **122**, 191-206.
- 15 Juusola M & French AS. (1997). Visual acuity for moving objects in first- and second-order neurons  
16 of the fly compound eye. *J Neurophysiol* **77**, 1487-1495.
- 17 Juusola M & Hardie RC. (2001a). Light adaptation in *Drosophila* photoreceptors: I. Response  
18 dynamics and signaling efficiency at 25 degrees C. *J Gen Physiol* **117**, 3-25.
- 19 Juusola M & Hardie RC. (2001b). Light adaptation in *Drosophila* photoreceptors: II. Rising  
20 temperature increases the bandwidth of reliable signaling. *J Gen Physiol* **117**, 27-41.
- 21 Juusola M, Kouvalainen E, Järvilehto M & Weckstrom M. (1994). Contrast gain, signal-to-noise ratio,  
22 and linearity in light-adapted blowfly photoreceptors. *J Gen Physiol* **104**, 593-621.
- 23 Juusola M, Niven JE & French AS. (2003). Shaker K<sup>+</sup> channels contribute early nonlinear  
24 amplification to the light response in *Drosophila* photoreceptors. *J Neurophysiol* **90**, 2014-  
25 2021.
- 26 Juusola M & Song Z. (2017). How a fly photoreceptor samples light information in time. *J Physiol*.
- 27 Juusola M, Song Z & Hardie RC. (2015). Biophysics of insect phototransduction. In *Encyclopedia of*  
28 *Computational Neuroscience*, pp. 2359-2376. Springer, New York.
- 29 Juusola M, Uusitalo RO & Weckstrom M. (1995a). Transfer of graded potentials at the photoreceptor  
30 interneuron synapse. *J Gen Physiol* **105**, 117-148.
- 31 Juusola M, Weckstrom M, Uusitalo RO, Korenberg MJ & French AS. (1995b). Nonlinear models of  
32 the first synapse in the light-adapted fly retina. *J Neurophysiol* **74**, 2538-2547.
- 33 Kirschfeld K & Franceschini N. (1969). A mechanism for directing flow of light in rhabdomeres of  
34 complex eyes in *Musca*. *Kybernetik* **6**, 13-22.
- 35 Klaus A & Warrant EJ. (2009). Optimum spatiotemporal receptive fields for vision in dim light. *J*  
36 *Vision* **9**.
- 37 Korenberg MJ, Bruder SB & Mcilroy PJ. (1988). Exact orthogonal kernel estimation from finite data  
38 records - Extending wiener identification of nonlinear systems. *Ann Biomed Eng* **16**, 201-214.
- 39 Korenberg MJ, Juusola M & French AS. (1998). Two methods for calculating the responses of  
40 photoreceptors to moving objects. *Ann Biomed Eng* **26**, 308-314.
- 41 Korenberg MJ & Paarmann LD. (1989). Applications of fast orthogonal search - time-series analysis  
42 and resolution of signals in noise. *Ann Biomed Eng* **17**, 219-231.
- 43 Krekelberg B & Lappe M. (2001). Neuronal latencies and the position of moving objects. *Trends*  
44 *Neurosci* **24**, 335-339.
- 45 Kremkow J, Jin J, Kombar SJ, Wang Y, Lashgari R, Li X, Jansen M, Zaidi Q & Alonso JM. (2014).  
46 Neuronal nonlinearity explains greater visual spatial resolution for darks than lights. *Proc*  
47 *Natl Acad Sci U S A*.
- 48 Kuang X, Poletti M, Victor JD & Rucci M. (2012a). Encoding space in time during active fixation.  
49 *Perception* **41**, 162-163.
- 50 Kuang XT, Poletti M, Victor JD & Rucci M. (2012b). Temporal encoding of spatial information  
51 during active visual fixation. *Curr Biol* **22**, 510-514.
- 52 Land MF. (1973). Head movement of flies during visually guided flight. *Nature* **243**, 299-300.
- 53 Land MF. (1997). Visual acuity in insects. *Annu Rev Entomol* **42**, 147-177.

- 1 Land MF. (1998). Compound eye structure: Matching eye to environment. In *Adaptive Mechanisms in*  
2 *the Ecology of Vision*, ed. Archer S, Djamgoz MB, Loew E & Partridge JC, pp. 51-72.  
3 Kluwer Academic Publishers, London.
- 4 Land MF. (1999). Motion and vision: why animals move their eyes. *J Comp Physiol A* **185**, 341-352.
- 5 Laufer G. (1996). *Introduction to optics and lasers in engineering*. Cambridge University Press
- 6 Laughlin SB. (1989). The role of sensory adaptation in the retina. *J Exp Biol* **146**, 39-62.
- 7 Laughlin SB. (1992). Retinal information capacity and the function of the pupil. *Ophthal Physl Opt*  
8 **12**, 161-164.
- 9 Laughlin SB & Hardie RC. (1978). Common strategies for light adaptation in the peripheral visual  
10 systems of fly and dragonfly. *J Comp Physiol* **128**, 319-340.
- 11 Laughlin SB, van Steveninck RRD & Anderson JC. (1998). The metabolic cost of neural information.  
12 *Nat Neurosci* **1**, 36-41.
- 13 Laughlin SB & Weckstrom M. (1993). Fast and slow photoreceptors - a comparative study of the  
14 functional diversity of coding and conductances in the *diptera*. *J Comp Physiol A* **172**, 593-  
15 609.
- 16 Lawson CL & Hanson RJ. (1974). *Solving least squares problems*. SIAM.
- 17 Luke GP, Wright CHG & Barrett SF. (2012). A multiaperture bioinspired sensor with hyperacuity.  
18 *Ieee Sens J* **12**, 308-314.
- 19 Maimon G, Straw AD & Dickinson MH. (2010). Active flight increases the gain of visual motion  
20 processing in *Drosophila*. *Nat Neurosci* **13**, 393-399.
- 21 Marmarelis PZ & Mccann GD. (1973). Development and application of white-noise modeling  
22 techniques for studies of insect visual nervous-system. *Kybernetik* **12**, 74-89.
- 23 Martinez-Conde S, Otero-Millan J & Macknik SL. (2013). The impact of microsaccades on vision:  
24 towards a unified theory of saccadic function. *Nat Rev Neurosci* **14**, 83-96.
- 25 Matic T & Laughlin SB. (1981). Changes in the intensity-response function of an insects  
26 photoreceptors due to light adaptation. *J Comp Physiol* **145**, 169-177.
- 27 Meinertzhagen IA & Oneil SD. (1991). Synaptic organization of columnar elements in the lamina of  
28 the wild-type in *Drosophila melanogaster*. *J Comp Neurol* **305**, 232-263.
- 29 Melzig J, Buchner S, Wiebel F, Wolf R, Burg M, Pak WL & Buchner E. (1996). Genetic depletion of  
30 histamine from the nervous system of *Drosophila* eliminates specific visual and  
31 mechanosensory behavior. *J Comp Physiol A* **179**, 763-773.
- 32 Melzig J, Burg M, Gruhn M, Pak WL & Buchner E. (1998). Selective histamine uptake rescues  
33 photo- and mechanoreceptor function of histidine decarboxylase-deficient *Drosophila* mutant.  
34 *J Neurosci* **18**, 7160-7166.
- 35 Mimura K. (1981). Receptive-field patterns in photoreceptors of the fly. *J Comp Physiol* **141**, 349-  
36 362.
- 37 Minke B. (2012). The history of the prolonged depolarizing afterpotential (PDA) and its role in  
38 genetic dissection of *Drosophila* phototransduction. *J Neurogenet* **26**, 106-117.
- 39 Nijhawan R. (1994). Motion extrapolation in catching. *Nature* **370**, 256-257.
- 40 Nijhawan R. (2002). Neural delays, visual motion and the flash-lag effect. *Trends Cogn Sci* **6**, 387-  
41 393.
- 42 Nikolaev A, Zheng L, Wardill TJ, O'Kane CJ, de Polavieja GG & Juusola M. (2009). Network  
43 adaptation improves temporal representation of naturalistic stimuli in *Drosophila* eye: II  
44 mechanisms. *Plos One* **4**.
- 45 Nilsson DE. (1989). Optics and evolution of the compound eye. In *Facets of vision*, ed. Stavenga DG  
46 & Hardie RC. Springer, Berlin.
- 47 Nilsson DE & Ro AI. (1994). Did neural pooling for night-vision lead to the evolution of neural  
48 superposition eyes. *J Comp Physiol A* **175**, 289-302.
- 49 Niven JE, Anderson JC & Laughlin SB. (2007). Fly photoreceptors demonstrate energy-information  
50 trade-offs in neural coding. *Plos Biol* **5**, 828-840.
- 51 Niven JE, Vähäsöyrinki M, Juusola M & French AS. (2004). Interactions between light-induced  
52 currents, voltage-gated currents, and input signal properties in *Drosophila* photoreceptors. *J*  
53 *Neurophysiol* **91**, 2696-2706.

- 1 Niven JE, Vähäsöyrinki M, Kauranen M, Hardie RC, Juusola M & Weckström M. (2003). The  
2 contribution of Shaker K<sup>+</sup> channels to the information capacity of *Drosophila* photoreceptors.  
3 *Nature* **421**, 630-634.
- 4 Paulk AC, Stacey JA, Pearson TWJ, Taylor GJ, Moore RJD, Srinivasan MV & van Swinderen B.  
5 (2014). Selective attention in the honeybee optic lobes precedes behavioral choices. *P Natl*  
6 *Acad Sci USA* **111**, 5006-5011.
- 7 Pick B & Buchner E. (1979). Visual movement detection under light-adaptation and dark-adaptation  
8 in the fly, *Musca domestica*. *J Comp Physiol* **134**, 45-54.
- 9 Poletti M, Listorti C & Rucci M. (2013). Microscopic eye movements compensate for  
10 nonhomogeneous vision within the fovea. *Curr Biol* **23**, 1691-1695.
- 11 Ratliff CP, Borghuis BG, Kao YH, Sterling P & Balasubramanian V. (2010). Retina is structured to  
12 process an excess of darkness in natural scenes. *P Natl Acad Sci USA* **107**, 17368-17373.
- 13 Reynolds ES. (1963). Use of lead citrate at high pH as an electron-opaque stain in electron  
14 microscopy. *J Cell Biol* **17**, 208-212.
- 15 Ribi WA. (1978). Gap junctions coupling photoreceptor axons in the 1<sup>st</sup> optic ganglion of the fly. *Cell*  
16 *Tissue Res* **195**, 299-308.
- 17 Riggs LA & Ratliff F. (1952). The effects of counteracting the normal movements of the eye. *J Opt*  
18 *Soc Am* **42**, 872-873.
- 19 Rivera-Alba M, Vitaladevuni SN, Mischenko Y, Lu ZY, Takemura SY, Scheffer L, Meinertzhagen  
20 IA, Chklovskii DB & de Polavieja GG. (2011). Wiring economy and volume exclusion  
21 determine neuronal placement in the *Drosophila* brain. *Curr Biol* **21**, 2000-2005.
- 22 Roebroek JGH & Stavenga DG. (1990). Insect pupil mechanisms. 4. Spectral characteristics and light-  
23 intensity dependence in the blowfly, *Calliphora erythrocephala*. *J Comp Physiol A* **166**, 537-  
24 543.
- 25 Rucci M, Iovin R, Poletti M & Santini F. (2007). Miniature eye movements enhance fine spatial  
26 detail. *Nature* **447**, 851-854.
- 27 Rucci M & Victor JD. (2015). The unsteady eye: an information-processing stage, not a bug. *Trends*  
28 *Neurosci* **38**, 195-206.
- 29 Sayeed O & Benzer S. (1996). Behavioral genetics of thermosensation and hygrosensation in  
30 *Drosophila*. *P Natl Acad Sci USA* **93**, 6079-6084.
- 31 Schetzen M. (1980). *The Volterra and Wiener theories of nonlinear systems*.
- 32 Schilstra C & van Hateren JH. (1998). Stabilizing gaze in flying blowflies. *Nature* **395**, 654.
- 33 Schilstra C & Van Hateren JH. (1999). Blowfly flight and optic flow I. Thorax kinematics and flight  
34 dynamics. *J Exp Biol* **202**, 1481-1490.
- 35 Seelig JD & Jayaraman V. (2015). Neural dynamics for landmark orientation and angular path  
36 integration. *Nature* **521**, 186-191.
- 37 Shannon CE. (1948). A mathematical theory of communication. *At&T Tech J* **27**, 379-423.
- 38 Shaw SR. (1975). Retinal resistance barriers and electrical lateral inhibition. *Nature* **255**, 480-483.
- 39 Shaw SR. (1984). Early visual processing in insects. *J Exp Biol* **112**, 225-251.
- 40 Shaw SR, Frohlich A & Meinertzhagen IA. (1989). Direct connections between the R7/8 and R1-6  
41 photoreceptor subsystems in the *dipteran* visual system. *Cell Tissue Res* **257**, 295-302.
- 42 Sinakevitch I & Strausfeld NJ. (2004). Chemical neuroanatomy of the fly's movement detection  
43 pathway. *J Comp Neurol* **468**, 6-23.
- 44 Skorupski P & Chittka L. (2010). Differences in photoreceptor processing speed for chromatic and  
45 achromatic vision in the bumblebee, *Bombus terrestris*. *J Neurosci* **30**, 3896-3903.
- 46 Smakman JGJ & Stavenga DG. (1987). Angular sensitivity of blowfly photoreceptors - broadening by  
47 artificial electrical coupling. *J Comp Physiol A* **160**, 501-507.
- 48 Smakman JGJ, Vanhateren JH & Stavenga DG. (1984). Angular sensitivity of blowfly photoreceptors  
49 - intracellular measurements and wave-optical predictions. *J Comp Physiol* **155**, 239-247.
- 50 Snyder AW. (1977). Acuity of compound Eyes - physical limitations and design. *J Comp Physiol* **116**,  
51 161-182.
- 52 Snyder AW & Miller WH. (1977). Photoreceptor diameter and spacing for highest resolving power. *J*  
53 *Opt Soc Am* **67**, 696-698.
- 54 Snyder AW, Stavenga DG & Laughlin SB. (1977). Spatial information capacity of compound eyes. *J*  
55 *Comp Physiol* **116**, 183-207.

- 1 Song Z & Juusola M. (2014). Refractory sampling links efficiency and costs of sensory encoding to  
2 stimulus statistics. *J Neurosci* **34**, 7216-7237.
- 3 Song Z, Postma M, Billings SA, Coca D, Hardie RC & Juusola M. (2012). Stochastic, adaptive  
4 sampling of information by microvilli in fly photoreceptors. *Curr Biol* **22**, 1371-1380.
- 5 Song Z, Zhou Y & Juusola M. (2016). Random photon absorption model elucidates how early gain  
6 control in fly photoreceptors arises from quantal sampling. *Frontiers in computational  
7 neuroscience* **10**, 61.
- 8 Srinivasan MV. (1985). Shouldnt directional movement detection necessarily be color-blind. *Vision  
9 Res* **25**, 997-1000.
- 10 Srinivasan MV & Bernard GD. (1975). Effect of motion on visual acuity of compound Eye -  
11 theoretical analysis. *Vision Res* **15**, 515-525.
- 12 Srinivasan MV & Dvorak DR. (1980). Spatial processing of visual information in the movement-  
13 detecting pathway of the fly - characteristics and functional significance. *J Comp Physiol* **140**,  
14 1-23.
- 15 Srinivasan MV, Laughlin SB & Dubs A. (1982). Predictive coding - a fresh view of inhibition in the  
16 retina. *Proc R Soc Ser B-Bio* **216**, 427-459.
- 17 Stavenga DG. (2003a). Angular and spectral sensitivity of fly photoreceptors. I. Integrated facet lens  
18 and rhabdomere optics. *Journal of Comparative Physiology a-Neuroethology Sensory Neural  
19 and Behavioral Physiology* **189**, 1-17.
- 20 Stavenga DG. (2003b). Angular and spectral sensitivity of fly photoreceptors. II. Dependence on facet  
21 lens F-number and rhabdomere type in *Drosophila*. *Journal of Comparative Physiology a-  
22 Neuroethology Sensory Neural and Behavioral Physiology* **189**, 189-202.
- 23 Stavenga DG. (2004a). Angular and spectral sensitivity of fly photoreceptors. III. Dependence on the  
24 pupil mechanism in the blowfly *Calliphora*. *Journal of Comparative Physiology a-  
25 Neuroethology Sensory Neural and Behavioral Physiology* **190**, 115-129.
- 26 Stavenga DG. (2004b). Visual acuity of fly photoreceptors in natural conditions - dependence on UV  
27 sensitizing pigment and light-controlling pupil. *J Exp Biol* **207**, 1703-1713.
- 28 Stockl AL, O'Carroll DC & Warrant EJ. (2016). Neural summation in the hawkmoth visual system  
29 extends the limits of vision in dim light. *Curr Biol* **26**, 821-826.
- 30 Tang SM & Guo A. (2001). Choice behavior of *Drosophila* facing contradictory visual cues. *Science*  
31 **294**, 1543-1547.
- 32 Tang SM & Juusola M. (2010). Intrinsic activity in the fly brain gates visual information during  
33 behavioral choices. *Plos One* **5**.
- 34 Tang SM, Wolf R, Xu SP & Heisenberg M. (2004). Visual pattern recognition in *Drosophila* is  
35 invariant for retinal position. *Science* **305**, 1020-1022.
- 36 Teich MC, Saleh BEA & Perina J. (1984). Role of primary excitation statistics in the generation of  
37 antibunched and sub-Poisson light. *J Opt Soc Am B* **1**, 366-389.
- 38 Tepass U & Harris KP. (2007). Adherens junctions in *Drosophila* retinal morphogenesis. *Trends Cell  
39 Biol* **17**, 26-35.
- 40 Uusitalo RO, Juusola M & Weckstrom M. (1995). Graded responses and spiking properties of  
41 identified first-order visual interneurons of the fly compound eye. *J Neurophysiol* **73**, 1782-  
42 1792.
- 43 Vähäsöyrinki M, Niven JE, Hardie RC, Weckström M & Juusola M. (2006). Robustness of neural  
44 coding in *Drosophila* photoreceptors in the absence of slow delayed rectifier K<sup>+</sup> channels. *J  
45 Neurosci* **26**, 2652-2660.
- 46 van Hateren JH. (1984). Waveguide theory applied to optically measured angular sensitivities of fly  
47 photoreceptors. *J Comp Physiol* **154**, 761-771.
- 48 van Hateren JH. (1986). Electrical coupling of neuro-ommatidial photoreceptor cells in the blowfly. *J  
49 Comp Physiol A* **158**, 795-811.
- 50 van Hateren JH. (1992a). Real and optimal neural images in early vision. *Nature* **360**, 68-70.
- 51 van Hateren JH. (1992b). Theoretical predictions of spatiotemporal receptive-fields of fly LMCs, and  
52 experimental validation. *J Comp Physiol A* **171**, 157-170.
- 53 van Hateren JH. (1992c). A theory of maximizing sensory information. *Biol Cybern* **68**, 23-29.
- 54 van Hateren JH. (1993a). 3 modes of spatiotemporal preprocessing by eyes. *J Comp Physiol A* **172**,  
55 583-591.

- 1 van Hateren JH. (1993b). Spatiotemporal contrast sensitivity of early vision. *Vision Res* **33**, 257-267.
- 2 van Hateren JH. (1997a). Processing of natural time series of intensities by the visual system of the  
3 blowfly. *Vision Res* **37**, 3407-3416.
- 4 van Hateren JH. (1997b). Processing of natural time series of intensities in the early visual system of  
5 the blowfly. *Perception* **26**, 6-7.
- 6 van Hateren JH & Schilstra C. (1999). Blowfly flight and optic flow II. Head movements during  
7 flight. *J Exp Biol* **202**, 1491-1500.
- 8 van Steveninck RRD & Laughlin SB. (1996). The rate of information transfer at graded-potential  
9 synapses. *Nature* **379**, 642-645.
- 10 van Swinderen B. (2007). Attention-like processes in *Drosophila* require short-term memory genes.  
11 *Science* **315**, 1590-1593.
- 12 Vasiliauskas D, Mazzoni EO, Sprecher SG, Brodetskiy K, Johnston RJ, Lidder P, Vogt N, Celik A &  
13 Desplan C. (2011). Feedback from rhodopsin controls rhodopsin exclusion in *Drosophila*  
14 photoreceptors. *Nature* **479**, 108-112.
- 15 Victor JD. (1992). Nonlinear systems analysis in vision: Overview of kernel methods. In *Nonlinear*  
16 *vision: Determination of neural receptive fields, function, and networks*, pp. 1-37. CRC.
- 17 Vigier P. (1907a). On the photoreceptive endings in the compound eyes of *Muscids*. *Cr Hebd Acad*  
18 *Sci* **145**, 532-536.
- 19 Vigier P. (1907b). The reception of light stimulant in the compound eyes of insects, particularly the  
20 Muscidae. *Cr Hebd Acad Sci* **145**, 633-636.
- 21 Viollet S. (2014). Vibrating makes for better seeing: from the fly's micro-eye movements to  
22 hyperacute visual sensors. *Frontiers in Bioengineering and Biotechnology* **2**, 1-8.
- 23 Wardill TJ, List O, Li XF, Dongre S, McCulloch M, Ting CY, O'Kane CJ, Tang SM, Lee CH, Hardie  
24 RC & Juusola M. (2012). Multiple spectral inputs improve motion discrimination in the  
25 *Drosophila* visual system. *Science* **336**, 925-931.
- 26 Warrant E & McIntyre P. (1992). The trade-off between resolution and sensitivity in compound eyes.  
27 In *Nonlinear vision*, pp. 391-421.
- 28 Warrant E & Nilsson DE. (2006). *Invertebrate vision*. Cambridge University Press, Cambridge.
- 29 Warrant E, Porombka T & Kirchner WH. (1996). Neural image enhancement allows honeybees to see  
30 at night. *P Roy Soc B-Biol Sci* **263**, 1521-1526.
- 31 Warrant EJ. (1999). Seeing better at night: life style, eye design and the optimum strategy of spatial  
32 and temporal summation. *Vision Res* **39**, 1611-1630.
- 33 Warrant EJ & McIntyre PD. (1993). Arthropod eye design and the physical limits to spatial resolving  
34 power. *Prog Neurobiol* **40**, 413-461.
- 35 Washizu Y, Burkhardt D & Streck P. (1964). Visual field of single retinula cells and interommatidial  
36 inclination in the compound eye of the blowfly *Calliphora erythrocephala*. *Z Vergl Physiol*  
37 **48**, 413-428.
- 38 Wernet MF, Velez MM, Clark DA, Baumann-Klausener F, Brown JR, Klovstad M, Labhart T &  
39 Clandinin TR. (2012). Genetic dissection reveals two separate retinal substrates for  
40 polarization vision in *Drosophila*. *Curr Biol* **22**, 12-20.
- 41 Wijngaard W & Stavenga DG. (1975). Optical crosstalk between fly rhabdomeres. *Biol Cybern* **18**,  
42 61-67.
- 43 Williams DS. (1982). Rhabdom size and photoreceptor membrane turnover in a *Muscoid* fly. *Cell*  
44 *Tissue Res* **226**, 629-639.
- 45 Wilson M. (1975). Angular sensitivity of light and dark adapted locust retinula cells. *J Comp Physiol*  
46 **97**, 323-328.
- 47 Wong F, Knight BW & Dodge FA. (1982). Adapting bump model for ventral photoreceptors of  
48 *Limulus*. *J Gen Physiol* **79**, 1089-1113.
- 49 Yang HH, St-Pierre F, Sun XL, Ding XZ, Lin MZ & Clandinin TR. (2016). Subcellular imaging of  
50 voltage and calcium signals reveals neural processing *in vivo*. *Cell* **166**, 245-257.
- 51 Yeh CI, Xing DJ & Shapley RM. (2009). "Black" responses dominate macaque primary visual cortex  
52 V1. *J Neurosci* **29**, 11753-11760.
- 53 Yellott JI. (1982). Spectral-analysis of spatial sampling by photoreceptors - topological disorder  
54 prevents aliasing. *Vision Res* **22**, 1205-1210.
- 55 Zettler F & Järvilehto M. (1972). Lateral inhibition in an insect eye. *Z Vergl Physiol* **76**, 233-244.

- 1 Zheng L, de Polavieja GG, Wolfram V, Asyali MH, Hardie RC & Juusola M. (2006). Feedback  
2 network controls photoreceptor output at the layer of first visual synapses in *Drosophila*. *J*  
3 *Gen Physiol* **127**, 495-510.
- 4 Zheng L, Nikolaev A, Wardill TJ, O'Kane CJ, de Polavieja GG & Juusola M. (2009). Network  
5 adaptation improves temporal representation of naturalistic stimuli in *Drosophila* eye: I  
6 dynamics. *Plos One* **4**.
- 7 Zurek DB & Nelson XJ. (2012). Hyperacute motion detection by the lateral eyes of jumping spiders.  
8 *Vision Res* **66**, 26-30.  
9